Synthesis, characterization, magnetic and photocatalytic properties of substituted rare earth perovskite-like ferrites

by

Ibrahim Abdulkadir

Submitted in fulfilment of the academic degree of Doctor of Philosophy in the School of Chemistry and Physics, University of KwaZulu-Natal, Durban

December 2014

ABSRACT

The present investigation deals with the synthesis of iron-based materials, namely, hematite and rare earth perovskite-like solid solutions, their structural characterization, and a study of their magnetic and photocatalytic activities.

These materials are of interest because their nanoparticles have been shown to display intriguing properties which are drastically different from the bulk that could be of interest in various technological fields such as memory and recording devices. They have a band gap that allows them absorb in the visible region of the electromagnetic spectrum and thus can utilise light in the visible region for photodegradation of organic pollutants.

Samples of α-Fe_2O_3 nanoparticles were synthesized by three methods: through the co-precipitation route in cetyltrimethylammonium bromide (Hem_PR), via a citric acid sol-gel method (Hem_SG) and a modified sol-gel method in Tween 20 (Hem_TW). Each sample was annealed at three different temperatures (400, 500 and 600 °C).

The rare earth perovskite-like ferrites with general formular $(RE_{0.5}Bi_{0.2}X_{0.2}Mn_{0.1})FeO_{(3-\delta)}$ (RE = La^{3+}, Nd^{3+} and Eu^{3+}, X = Ca^{2+}, Sr^{2+} and Ba^{2+}) were synthesized through a modified Pechini-type sol-gel method and annealed at different temperatures. A number of techniques (which include PXRD, SEM, HRTEM, FTIR, BET, Mössbauer spectroscopy and photoluminescence spectroscopy (PL)) were used to characterize all the powders. The photocatalytic activities of the powders were then tested on a model dye, rhodamine B in aqueous solution.

α-Fe_2O_3 nano-rods were obtained from the co-precipitation route, while the citric acid and Tween 20 routes both produced polycrystalline nanoparticles. However, Tween 20

was able to control the growth in particle sizes of the crystals. Hem_TW showed the smallest particle size and highest BET surface area, saturation magnetization and photocatalytic activity.

The perovskite-like materials crystallized in either an orthorhombic or a rhombohedral lattice with phase purity increasing at higher calcination temperatures. The BET specific surface area range was between 2 and 27 m^2 g^{-1} and the particle size range was 16-40 nm. Vibrating sample magnetometer (VSM) measurements showed that the powders are weakly ferromagnetic with very high coercive fields at high annealing temperatures. Coercive fields of up to 5.70 kOe were obtained. Photoluminescence spectroscopy showed that the powders were all active in the visible region. The photocatalytic activities of the powders were then tested on a model dye, rhodamine B in solution in the presence of H_2O_2. Powders annealed at 700 °C and above showed good photocatalytic activities with decolourization and mineralization efficiencies as high as 99 and 80 % respectively recorded. The observed trend in photo-activity with respect to the alkaline earth metal substitution is Ca > Sr > Ba in all the series of the synthesized perovskites. These powders therefore show promise as good materials for use as photocatalysts for removing pollutants from water and the improved magnetic properties might be of interest in the field of recording and other magnetic devices.

PREFACE

The experimental work described in this thesis was carried out in the School of Chemistry and Physics, University of KwaZulu-Natal, Durban, from September 2011 to December 2014, under the supervision of Professors Sreekantha B. Jonalaggadda and Bice S. Martincigh.

These studies represent original work by the author and have not been submitted in any form for any degree or diploma to any tertiary institution. Where use has been made of the work of others it is duly acknowledged in the text.

DECLARATION 1 - PLAGIARISM

I, Ibrahim Abdulkadir, declare that

1. The research in this thesis, except where otherwise indicated, is my original research.
2. This thesis has not been submitted for any degree or examination at any other university.
3. This thesis does not contain other persons data, picture, graphs, or other information, unless specifically acknowledged as being sourced from other persons.
4. This thesis does not contain other persons writing, unless specifically acknowledged as being sourced from other researchers. Where other written sources have been quoted, then:
   a. Their words have been rewritten but the general information attributed to them has been referenced.
   b. Where their exact words have been used, then their writing has been placed in italics inside a quotation marks, and referenced.

5 This thesis does not contain text, graphics or tables copied and pasted from the internet, unless specifically acknowledged, and the source being detailed in the thesis and in the references section.

Signed:_____

DECLARATION 2 – PUBLICATIONS

Details of contributions to publications that form part and/or include research presented in this thesis.

1. **Ibrahim Abdulkadir**, Hafiz M.I. Abdallah, Bice S. Martincigh and Sreekantha B. Jonnalagadda (2014). The effect of synthesis method on the structure and magnetic and photocatalytic properties of α-Fe_2O_3. (Manuscript under review). Materials Science Bulletin: (Contribution: IA designed the experimental procedure, carried out the synthesis, characterization and other experiments and wrote the draft manuscript. BSM and SBJ supervised every step of the work. HMIA collected and helped with the interpretation of the hematite Mössbauer spectra.)

2. **Ibrahim Abdulkadir**, Bice S. Martincigh, and Sreekantha B. Jonnalagadda (2014). Synthesis, characterization and photocatalytic activities of perovskite-like $Nd_{0.5}(Bi_{0.2}X_{0.2}Mn_{0.1})$ $FeO_{3-\delta}$ (X = Ca, Sr and Ba). (Contribution: IA designed the experimental procedure, carried out the synthesis, characterization and other experiments. BSM and SBJ supervised every step of the work.)

3. **Ibrahim Abdulkadir,** Bice S. Martincigh, and Sreekantha B. Jonnalagadda (2014). Synthesis characterization and photocatalytic activities of substituted EBFO perovskite-like materials. (Contribution: IA designed the experimental procedure, carried out the synthesis, characterization and other experiments. BSM and SBJ supervised every step of the work.)

4. **Ibrahim Abdulkadir**, Bice S. Martincigh, and Sreekantha B. Jonnalagadda (2014). Synthesis and the effect of annealing temperature on the structural, magnetic and photocatalytic properties of $(La_{0.5}Bi_{0.2}Sr_{0.2}Mn_{0.1})FeO_{(3-\delta)}$. (Contribution: IA designed the experimental procedure, carried out the synthesis, characterization and other experiments. BSM and SBJ supervised every step of the work.)

5. **Ibrahim Abdulkadir**, Bice S. Martincigh, and Sreekantha B. Jonnalagadda (2014). Synthesis and the effect of annealing temperature on the structural, magnetic and photocatalytic properties of $(La_{0.5}Bi_{0.2}Ba_{0.2}Mn_{0.1})FeO_{(3-\delta)}$. (Contribution: IA designed the experimental procedure, carried out the synthesis, characterization and other experiments. BSM and SBJ supervised every step of the work.)

6. **Ibrahim Abdulkadir**, Bice S. Martincigh, and Sreekantha B. Jonnalagadda (2014). Synthesis and effect of annealing temperature on the structural, magnetic and photocatalytic properties of $(La_{0.5}Bi_{0.2}Ca_{0.2}Mn_{0.1})FeO_{(3-\delta)}$. (Contribution: IA designed the experimental procedure, carried out the synthesis, characterization and other experiments. BSM and SBJ supervised every step of the work.)

LIST OF CONFERENCE PRESENTATIONS

1 **Ibrahim Abdulkadir,** Bice S. Martincigh, and Sreekantha B. Jonnalagadda: **.** Synthesis, characterization and photocatalytic activities of perovskite-like $Nd_{0.5}(Bi_{0.2}X_{0.2}Mn_{0.1})\ FeO_{3-\delta}$ (X = Ca, Sr and Ba). Powder Diffraction Conference and workshop, University of Witwatersrand, Johannesburg South Africa. 27-31 January 2014. (Oral presentation).

2 **Ibrahim Abdulkadir,** Bice S. Martincigh, and Sreekantha B. Jonnalagadda: **.** Synthesis, characterization and photocatalytic activities of perovskite-like $Nd_{0.5}(Bi_{0.2}X_{0.2}Mn_{0.1})\ FeO_{3-\delta}$ (X = Ca, Sr and Ba). University of KwaZulu-Natal, College of Agriculture, Engineering and Science Postgraduate Research Day, Howard College, South Africa, 1 November 2013. (Oral presentation).

3 **Ibrahim Abdulkadir,** Bice S. Martincigh, and Sreekantha B. Jonnalagadda: A comparison of different synthetic methods for the preparation of hematite nanoparticles. 16th Biennual SACI Inorganic Chemistry Conference incorporating the Carman Physical Chemistry Symposium, Durban, South Africa, 30 June – 4 July 2013. (Poster presentation).

4 **Ibrahim Abdulkadir,** Bice S. Martincigh, and Sreekantha B. Jonnalagadda: The synthesis of stable iron-based catalyst which were active in the visible region of the solar spectrum. University of KwaZulu-Natal, College of Agriculture, Engineering and Science Postgraduate Research Day, Pietermaritzburg, South Africa, 29 October 2012. (Poster presentation).

ACKNOWLEDGEMENTS

I would like to express my sincere and profound gratitude to:

- My supervisors, Prof. SB Jonalaggadda and Prof. BS Martincigh. Their support, encouragement and guidance throughout the duration of my studies are highly appreciated.
- The authorities of the Ahmadu Bello University Zaria and the Tertiary Education Trust Funds (TETFUND) for granting me study leave, and also for their financial support throughout the duration of my studies.
- The College of Agriculture, Engineering and Sceince at the University of KwaZulu-Natal for the award of a bursary and a Doctoral Schorlarship.
- Dr Thomas Moyo of the Condensed Physics Group for his assistance with the VSM and Mössbauer spectrometer. Dr Hafiz Abdallah for helping with the interpretation of the Mössbauer results for the hematite nanoparticles.
- The technical staff of the School of Chemistry and Physics for their help with use of laboratories and instruments. In particular I would like to thank Mrs Vashty Reddy for her assistance with the Instruments in the analytical chemistry laboratory and Mr Neal Broomhead for his assistance with the TGA and FTIR instruments.
- My parents, my brothers and sisters for their advice and prayers.
- My wife for patience, prayers and kind words.
- To God for giving me the strength to go through this program.

TABLE OF CONTENTS

Abstract (i)

Preface (iii)

Plagiarism (iv)

Publications (v)

List of presentations (vii)

Acknowledgements (viii)

Table of contents (ix)

List of abbreviations (xvii)

Chapter 1: Introduction (1)

1 Background (1)

1.1 Aim and objectives of work (3)

1.2 Structure of thesis (4)

References (7)

Chapter 2: Literature review (10)

2.1 Advanced oxidation processes (10)

2.2 Photoinduced processes (11)

2.3 Synthesis of functional materials (13)

2.3.1 Co-precipitation (13)

2.3.2 Hydrothermal/solvothermal methods (13)

2.3.3 Microemulsion method (14)

2.3.4 Sol-gel method (14)

2.3.5 Combustion synthesis (15)

2.3.6 Mechanochemical method (16)

2.4 Characterization of photocatalytic materials (16)

2.4.1 Powder X-ray diffraction (16)

2.4.2 Electron microscopy (17)

2.4.3 Mössbauer spectroscopy (19)

2.4.4 Fourier transform infrared microscopy (19)

2.4.5 Photoluminescence spectroscopy (20)

2.4.6 Vibrating sample magnetometer (21)

2.4.7 Surface area measurements (21)

2.5 Literature review (22)

2.5.1 Synthesis (22)

2.5.2 Magnetic and photocatalytic properties (30)

2.5.2.1 Hematite (30)

2.5.2.2 Perovskites (33)

References (39)

Chapter 3: The effect of synthesis method on the structure and magnetic properties of α-Fe_2O_2 (46)

Abstract (47)

3.1 Introduction (48)

3.2 Experimental (49)

3.2.1 Materials (49)

3.2.2 Synthesis (49)

3.2.2.1 Co-precipitation (49)

3.2.2.2 Sol-gel method 1 (50)

3.2.2.3 Sol-gel method 2 (50)

3.2.3 Characterization (51)

3.3 Results and discussion (52)

3.3.1 Phase purity and crystallinity (52)

3.3.2 Structural characteristics (55)

3.3.3 Morphology (57)

3.3.4 Surface area and porosity (59)

3.3.5 Magnetic properties (60)

3.3.6 Mössbauer spectroscopy (63)

3.3.7 Photocatalytic activities (67)

3.3.7.1 Mechanism of photodegradation (70)

3.4 Conclusions (71)

References (72)

Chapter 4: Synthesis, characterization and photocatalytic activities of perovskite-like $Nd_{0.5}(Bi_{0.2}X_{0.2}Mn_{0.1})\ FeO_{3-\delta}$ (X = Ca, Sr and Ba) (75)

Abstract (76)

4.1 Introduction (77)

4.2 Experimental (78)

4.2.1 Materials (78)

4.2.2 Synthesis of $Nd_{0.5}(Bi_{0.2}X_{0.2}Mn_{0.1})\ FeO_{3-\delta}$ (78)

4.2.3 Characterisation (79)

4.2.4 Photocatalytic activity (80)

4.3 Results and discussion (81)

4.3.1 Morphology (82)

4.3.2 Crystal phase characterisation (84)

4.3.3 Surface Characterization (87)

4.3.4 Surface areas and pore sizes (88)

4.3.5 Magnetic properties (90)

4.3.6 Mössbauer spectroscopy analysis (92)

4.3.7 Photoluminescence measurements (94)

4.3.8 Photocatalytic screening (96)

4.3.8.1 Effect of amount of photocatalyst (99)

4.3.8.2 Effect of pH (101)

4.3.8.3 Effect of peroxide concentration (102)

4.3.8.4 Effect of dye concentration (104)

4.3.8.5 Chemical oxygen demand (105)

4.3.9 Mechanism (106)

4.4 Conclusions (107)

References (109)

Chapter 5: Synthesis, characterization and photocatalytic activities of substituted REBFO perovskite-like materials (111)

Abstract (112)

5.1 Introduction (113)

5.2 Experimental (114)

5.2.1 Materials (114)

5.2.2 Synthesis of $(Eu_{0.5}Bi_{0.2}Mn_{0.1})FeO_{3-\delta}$ (114)

5.2.3 Characterization (115)

5.2.4 Photocatalytic screening (116)

5.3 Results and discussion (116)

5.3.1 Phase purity and crystallinity (117)

5.3.2 Microstructural characterization (120)

5.3.3 Surface characterization (121)

5.3.4 Surface area and porosity (122)

5.3.5 Magnetic properties (123)

5.3.6 Photoluminescence spectroscopy (126)

5.3.7 Photocatalytic screening (127)

5.3.7.1 Effect of annealing temperature on efficiency (127)

5.3.7.2 Effect of photocatalyst loading (129)

5.3.7.3 Effect of solution pH on rate of decomposition (130)

5.3.7.4 Effect of RhB concentration on rate of decomposition (132)

5.3.7.5 Mineralization (133)

5.3.8 Mechanism (134)

5.4 Conclusions (134)

References (136)

Chapter 6: Synthesis and the effect of annealing temperature on the structural, magnetic and photocatalytic properties of $(La_{0.5}Bi_{0.2}Sr_{0.2}Mn_{0.1})FeO_{(3-\delta)}$ (138)

Abstract (139)

6.1 Introduction (140)

6.2 Experimental (141)

6.2.1 Materials (141)

6.2.2 Synthesis of $(La_{0.5}Bi_{0.2}Sr_{0.2}Mn_{0.1})FeO_{(3-\delta)}$ (142)

6.2.3 Characterization (142)

6.2.4 Photocatalytic screening (143)

6.3 Results and discussion (144)

6.3.1 Phase purity and crystallinity (144)

6.3.2 BET surface area and porosity (146)

6.3.3 Surface characterization (148)

6.3.4 Thermal stability (149)

6.3.5 Magnetic properties (151)

6.3.6 Microstructural characterization (153)

6.3.7 Photoluminescence spectroscopy (154)

6.3.8 Photocatalytic screening (156)

6.3.9 Mineralization (159)

6.4 Conclusions (160)

References (162)

Chapter 7: Synthesis and the effect of annealing temperature on the structural, magnetic and photocatalytic properties of $(La_{0.5}Bi_{0.2}Ba_{0.2}Mn_{0.1})FeO_{(3-\delta)}$ (164)

Abstract (165)

7.1 Introduction (166)

7.2 Experimental (167)

7.2.1 Materials (167)

7.2.2 Synthesis of $(La_{0.5}Bi_{0.2}Ba_{0.2}Mn_{0.1})FeO_{(3-\delta)}$ (167)

7.2.3 Characterization (168)

7.2.4 Photocatalytic screening (169)

7.3 Results and discussion (169)

7.3.1 Phase characterisation (170)

7.3.2 Microstructural characterization (172)

7.3.3 BET surface area and porosity (173)

7.3.4 Thermal stability (175)

7.3.5 Surface characterization (176)

7.3.6 Magnetic properties (177)

7.3.7 Photoluminescence spectroscopy (180)

7.3.8 Photocatalytic screening (181)

7.3.8.1 Mineralization of RhB dye solution (183)

7.3.8.2 Mechanism of RhB degradation (185)

7.4 Conclusions (185)

References (187)

Chapter 8: Synthesis and effect of annealing temperature on the structural, magnetic and photocatalytic properties of ($La_{0.5}Bi_{0.2}Ca_{0.2}Mn_{0.1}$)$FeO_{(3-\delta)}$ (189)

Abstract (190)

8.1 Introduction (191)

8.2 Experimental (192)

8.2.1 Materials (192)

8.2.2 Synthesis of ($La_{0.5}Bi_{0.2}Ba_{0.2}Mn_{0.1}$)$FeO_{(3-\delta}$ (192)

8.2.3 Characterization (193)

8.2.4 Photocatalytic screening (194)

8.3 Results and discussion (194)

8.3.1 Crystal phase characterisation (195)

8.3.2 Morphology (197)

8.3.3 BET surface areas (198)

8.3.4 Surface characterization (201)

8.3.5 Thermal stability (202)

8.3.6 Magnetic properties (203)

8.3.7 Photoluminescence (205)

8.3.8 Photocatalytic screening (207)

8.3.8.1 Mineralization of the RhB dye (209)

8.3.8.2 Mechanism of the photodegradation process (211)

8.4 Conclusions (212)

References (213)

Chapter 9: Summary and conclusion (215)

9.1 Summary (215)

9.2 Conclusions (221)

9.3 Further work (222)

Appendix: Supplementary materials (223)

List of abbreviations

AFM	Antiferromgnetic
AOP	Advanced oxidation processes
ATR	Attenuated total reflectance
BET	Brunaur-Emmet-Teller
B_{hf}	Hyperfine magnetic field
CB	Conduction band
COD	Chemical oxygen demand
CTAB	Cetyl trimethylammonium bromide
D	Crystallite sizes
E_A	Activation energy
E_{em}	Emission energy
E_{ex}	Excitation energy
e^-	Electron
FM	Ferromagnetic
FTIR	Fourier transform infrared
G	Grain sizes
H_C	Coercive field
HRTEM	High resolution transmission electron microscope
HS	High spin
h^+	Hole
$IS(\delta)$	Isomer shift
IUPAC	International Union of Pure and Applied Chemistry
k	Scherrer constant
K	Kelvin temperature
M_S	Saturation magnetization

M_R	Remanent magnetization
PC	Photocatalyst
PL	Photoluminescence
PSD	Pore size distribution
PXRD	Powder X-ray diffraction
RhB	Rhodamine B
SEM	Scanning electron microscopy
SSA	Specific surface area
TEM	Transmission electron microscopy
T_A	Annealing temperature
T_M	Morin temperature
T_N	Neel temperature
UV	Ultra violet
VB	Valence band
VSM	Vibrating sample magnetometer
WF	Weak ferromagnetic

Chapter 1

Introduction

Nanomaterials have recently generated significant interest due to the physical and chemical properties they exhibit, which are dependent on their sizes and morphology [1-4]. Some of these physical and chemical properties have made nanomaterials useful in various fields of advanced technologies ranging from electronic and magnetic devices in medicine [5, 6] and communication [7], to devices used in environmental remediation [8, 9], catalysis [10] and renewable energy [11]. Interest has also been shown in the photocatalytic properties of nanostructured semiconductors and novel solid solutions [12, 13].

Iron oxides are the most ubiquitous metal oxides of technological importance, with sixteen known polymorphs. The most stable and, therefore, the most widespread of which are goethite (α-FeOOH) and hematite (α-Fe_2O_3) [14, 15]. Hematite, which is n-type semiconductor with an energy band gap of 2.1 eV, crystallizes in a rhombohedral structure (similar to corundum (Al_2O_3)) with a space group of R3c [16]. It is antiferromagnetic, or weakly ferromagnetic with a maximum magnetization value of 0.3 emu g^{-1} [17] The ferromagnetism in hematite arises as a result of canting of electron spin from anti-parallel alignment [18-20] and when doped or prepared in nanoparticulate size exhibits novel properties [3, 4, 21-27]. These properties coupled with its stability, low cost, corrosion resistance, non-toxicity and environmental compatibility [1, 18, 28], makes it suitable for applications in diverse areas such as catalysis [29, 30], pigments [31, 32], photoelectrochemical water splitting [33-35], gas

sensors [36], and optical [37, 38] and biomedical devices [39]. Therefore, there is much interest in doping or controlling the size and shape of hematite nanoparticles.

Perovskites, on the other hand, are a large family of multifunctional materials with the general formula ABO_3 (where A^{3+} is a large rare earth or transition metal ion and B^{3+} is a smaller transition metal ion) and are mostly weakly ferromagnetic. The perovskite structure is flexible and can accommodate almost all the elements on the periodic table. The most important factor that describes the formability and structure of perovskites is the ionic radius of the A- and B-site ions and this is expressed in terms of the tolerance factor, obtained from the Goldschmidts equation given by $t = (r_A + r_O)/\sqrt{2}(r_B + r_O)$, where t is the tolerance factor, r_A is the radius of the A-site ion, r_B is the radius of the B-site ion and r_O is the radius of oxygen. The ideal perovskite structure is cubic with a space group *Pm3m* and a t factor value of 1. A deviation from this t value indicates distortion in the crystal lattice [40] (when t lies between 0.75 and 1 an orthorhombic structure with space group *Pnma* or *Pbnm* is indicated, while a t value between 1 and 1.032 indicates a tilt towards a hexagonal structure, with space group *R3c*).

Heavy doping of hematite could result in the substitution of Fe^{3+}, giving rise to a perovskite-like material known as orthoferrite [41]. The perovskite-like materials ($AFeO_3$) form an interesting class of multiferroic perovskite-like materials and $BiFeO_3$ has been the poster child of this group of materials in this regard [42-45]. Some rare earth based orthoferrites (i.e., $REFeO_3$) have also been shown to posses very intriguing catalytic, photocatalytic [46], magnetic [47], electric, and magneto-optical properties [48, 49]. Partial substitution of the ion on the A- or B-site of a perovskite-like material by carefully selected ions with varying physical and/or chemical properties could drastically alter the properties of the materials and make them more robust for

application in the technological field of interest as applied in this research work. For example, introducing a transition metal with a lone pair of electrons can impart ferroelectricity on the material [50, 51]. This flexibility for various substitutions have imparted on this class of materials the potential for application in a plethora of advanced technologies.

Efficient photocatalytic perovskite-like materials for degradation of organic molecules such as $NaTaO_3$, $KTaO_3$ and $SrTiO_3$ utilize ultraviolet (UV) light for this purpose [52, 53]. Dopants have been added in the synthesis of these materials in order to try to reduce the energy bandgap to allow for the utilization of visible light and reap more benefits from the light spectrum [53-56]. As stated earlier hematite and the perovskite-like ferrites have bandgaps that fall within the required range for visible light utilisation [57-59] and therefore it is of interest to study these materials and their properties futher for possible application in photocatalysis.

1.1 Aim and objectives of this work

The main focus of this work was to synthesize and characterize nanoparticles of some hematite powders and substituted perovskite-like solid solutions with general formular $L_nBi_{0.2}A_{0.2}Mn_{0.1}FeO_{(3-\delta)}$ (where L_n = La, Nd and Eu, and A = Ca, Sr and Ba) with enhanced magnetic properties and apply these materials in the photocatalytic degradation of organic dyes. To this end, co-precipitation and sol-gel (one in citric acid and the other in Tween 20) methods were used to prepare nanoparticles of hematite.

A slightly modified Pechini-type sol-gel method was used to prepare $LnBi_{0.2}A_{0.2}Mn_{0.1}FeO_{(3-\delta)}$. These materials were annealed at different temperatures to discern the effect of calcination temperature on the resultant properties. All these

materials were analysed for their morphology (SEM, TEM), structure (PXRD, FTIR), Fe^{3+} distribution (Mössbauer spectroscopy), and magnetic properties (VSM).

Their activities as photocatalysts were tested on the organic dye RhB on their own or with the addition of H_2O_2.

1.2 Structure of thesis

This thesis is written in manuscript format and consequently consist of a series of stand-alone chapters.

Chapter 2 contains the literature review and background information to this study. It covers a description of advanced oxidation processes (AOP) and the mechanism of free radical generation, the chemical routes for synthesis of functional nanomaterials, instrumentation used for material characterisation, a discussion on the magnetic and photocatalytic properties of hematite and perovskites and a review of published work on synthesis, magnetic and photocatalytic properties of hematite and perovskites.

Chapter 3 describes the synthesis and characterisation of hematite nanoparticles that have been synthesized via three different synthesis routes, namely, co-precitation, a citric acid sol-gel route in citric acid and a sol-gel route in Tween 20. The structure and magnetic properties of these materials were characterised and their efficiency in the photodegradation of rhodamine B was investigated and discussed.

Chapter 4 describes the synthesis and characterization of a perovskite-like solid solution $(L_{n0.5}Bi_{0.2}A_{0.2}Mn_{0.1})FeO_{3-\delta}$ (where L_n = Nd, A = Ca, Sr and Ba and δ is a fraction which indicates deficiency in the oxygen content of the powders). The evolution of the pure perovskite phase, lattice parameter, BET specific surface area (SSA) were investigated

and discussed with respect to the variations in A. The effect of annealing temperature on the magnetic properties in relation to the saturated magnetization and coercive field were investigated and discussed. The optical activities of the materials were also investigated and compared. A comparison of the photocatalytic properties of these materials with respect to annealing temperature on RhB dye were also investigated and discussed.

Chapter 5 describes the synthesis and characterization of perovskite-like solid solutions $(Ln_{0.5}Bi_{0.2}A_{0.2}Mn_{0.1})FeO_{3-\delta}$ (where Ln = Eu, and A = Ca, Sr and Ba) in which Nd in the previous series is now replaced by Eu and the Group II cations is varied as before. The annealing temperatures were readjusted to 600, 700, 800 and 900 °C. The evolution of the pure perovskite phase, lattice parameter, BET specific surface area (SSA) were investigated and discussed with respect to the variations in A. The effect of annealing temperature on the magnetic properties in relation to the saturated magnetization and coercive field was investigated and discussed. The optical activities of the materials were also investigated and compared. A comparison of the photocatalytic properties of these materials with respect to annealing temperature on RhB dye was also investigated and discussed.

Chapter 6 describes the synthesis and characterization of a perovskite-like solid solution $La_{0.5}Bi_{0.2}Sr_{0.2}Mn_{0.1}FeO_{3-\delta}$. Here the rare earth metal was replaced with La and the only Group II metal used was Sr. The materials were calcined at temperatures of 400, 500, 600 700, 800 and 900 °C. This allowed the monitoring of the evolution of the pure perovskite phase, the variation of the lattice parameters and the BET specific surface area (SSA) with annealing temperature, were investigated and thoroughly discussed. The effect of annealing temperature on the magnetic properties in relation to the

saturation magnetization and coercive field was investigated and discussed. The photocatalytic properties of these materials with respect to annealing temperature on RhB dye were also investigated and discussed.

Chapter 7 describes the synthesis and characterization of a perovskite-like solid solution $La_{0.5}Bi_{0.2}Ba_{0.2}Mn_{0.1}FeO_{3-\delta}$ where the Sr in the previous material was replaced with Ba. Here also the evolution of the pure perovskite phase, lattice parameter, BET specific surface area (SSA) were investigated and thoroughly discussed. The effect of annealing temperature on the magnetic properties in relation to the saturated magnetization and coercive field were investigated and discussed. The photocatalytic properties of these materials with respect to annealing temperature on RhB dye were also investigated and discussed.

Chapter 8 describes the synthesis and characterization of a third La substituted perovskite-like solid solution in which the Group II metal cation of the previous material has been replaced with a Ca to form $La_{0.5}Bi_{0.2}Ca_{0.2}Mn_{0.1}FeO_{3-\delta}$. Again, the evolution of the pure perovskite phase, lattice parameter, Brunauer-Emmett-Teller (BET) specific surface area (SSA) were investigated and thoroughly discussed. The effect of annealing temperature on the magnetic and photocatalytic properties of these materials on RhB dye were also investigated and discussed.

Chapter 9 contains the summary of the work and results obtained from Chapters 3 through to 8 and the conclusions drawn from the research work thus far and suggestions for further work.

References

[1] Y. Xu, S. Yang, G. Zhang, Y. Sun, D. Gao, Y. Sun, Materials Letters 65 (2011) 1911-1914.
[2] L. Liu, H.-Z. Kou, W. Mo, H. Liu, Y. Wang, The Journal of Physical Chemistry B 110 (2006) 15218-15223.
[3] J. Lian, X. Duan, J. Ma, P. Peng, T. Kim, W. Zheng, ACS Nano 3 (2009) 3749-3761.
[4] X. Gou, G. Wang, X. Kong, D. Wexler, J. Horvat, J. Yang, J. Park, Chemistry – A European Journal 14 (2008) 5996-6002.
[5] M. Mahmoudi, S. Sant, B. Wang, S. Laurent, T. Sen, Advanced Drug Delivery Reviews 63 (2011) 24-46.bybbh
[6] S. Hanessian, J.A. Grzyb, F. Cengelli, L. Juillerat-Jeanneret, Bioorganic & Medicinal Chemistry 16 (2008) 2921-2931.
[7] M.S. Islam, V. Logeeswaran, Communications Magazine, IEEE 48 (2010) 112-120.
[8] M.S. Mauter, M. Elimelech, Environmental Science & Technology 42 (2008) 5843-5859.
[9] G. Aragay, A. Merkoçi, Electrochimica Acta 84 (2012) 49-61.
[10] Z.-Y. Zhou, N. Tian, J.-T. Li, I. Broadwell, S.-G. Sun, Chemical Society Reviews 40 (2011) 4167-4185.
[11] X. Chen, C. Li, M. Graetzel, R. Kostecki, S.S. Mao, Chemical Society Reviews 41 (2012) 7909-7937.
[12] A. Kubacka, M. Fernandez-Garcia, G. Colon, Chemical Reviews 112 (2011) 1555-1614.
[13] M.R. Hoffmann, S.T. Martin, W. Choi, D.W. Bahnemann, Chemical Reviews 95 (1995) 69-96.
[14] W.R. Fischer, U. Schwertmann, Clays and Clay Minerals 23 (1975) 33-34,.
[15] C. Colombo, G. Palumbo, A. Ceglie, R. Angelico, Journal of Colloid and Interface Science 374 (2012) 118-126.
[16] R.D. Rodriguez, D. Demaille, E. Lacaze, J. Jupille, C. Chaneac, J.-P. Jolivet, The Journal of Physical Chemistry C 111 (2007) 16866-16870.
[17] A.S. Teja, P.-Y. Koh, Progress in Crystal Growth and Characterization of Materials 55 (2009) 22-45.
[18] M. Tadić, N. Čitaković, M. Panjan, Z. Stojanović, D. Marković, V. Spasojević, Journal of Alloys and Compounds 509 (2011) 7639-7644.
[19] L.C. Sánchez, J.D. Arboleda, C. Saragovi, R.D. Zysler, C.A. Barrero, Physica B: Condensed Matter 389 (2007) 145-149.
[20] J. Jacob, M. Abdul Khadar, Journal of Magnetism and Magnetic Materials 322 (2010) 614-621.
[21] X. Zhang, H. Li, S. Wang, F.-R.F. Fan, A.J. Bard, The Journal of Physical Chemistry C 118 (2014) 16842-16850.
[22] S.-B. Wang, Y.-L. Min, S.-H. Yu, The Journal of Physical Chemistry C 111 (2007) 3551-3554.
[23] J. Velev, A. Bandyopadhyay, W. Butler, S. Sarker, Physical Review B 71 (2005) 205208.

[24] T.P. Raming, A.J.A. Winnubst, C.M. van Kats, A.P. Philipse, Journal of Colloid and Interface Science 249 (2002) 346-350.
[25] R. Ramesh, S. Sohila, C. Muthamizhchelvan, M. Rajalakshmi, S. Ramya, S. Ponnusamy, J Mater Sci: Mater Electron 22 (2011) 1357-1360.
[26] E. Darezereshki, Materials Letters 65 (2011) 642-645.
[27] I. Chernyshova, M. Hochella Jr, A. Madden, Physical Chemistry Chemical Physics 9 (2007) 1736-1750.
[28] Y. Xu, G. Zhang, G. Du, Y. Sun, D. Gao, Materials Letters 92 (2013) 321-324.
[29] G. Picasso Escobar, A. Quintilla Beroy, M.P. Pina Iritia, J. Herguido Huerta, Chemical Engineering Journal 102 (2004) 107-117.
[30] F. Herrera, A. Lopez, G. Mascolo, P. Albers, J. Kiwi, Applied Catalysis B: Environmental 29 (2001) 147-162.
[31] D. Walter, Thermochimica Acta 445 (2006) 195-199.
[32] S.R. Prim, M.V. Folgueras, M.A. de Lima, D. Hotza, Journal of Hazardous Materials 192 (2011) 1307-1313.
[33] K. Sivula, R. Zboril, F. Le Formal, R. Robert, A. Weidenkaff, J. Tucek, J. Frydrych, M. Grätzel, Journal of the American Chemical Society 132 (2010) 7436-7444.
[34] Y. Ling, G. Wang, D.A. Wheeler, J.Z. Zhang, Y. Li, Nano Letters 11 (2011) 2119-2125.
[35] Y. Lin, G. Yuan, S. Sheehan, S. Zhou, D. Wang, Energy & Environmental Science 4 (2011) 4862-4869.
[36] X. Gou, G. Wang, J. Park, H. Liu, J. Yang, Nanotechnology 19 (2008) 125606.
[37] J.A. Glasscock, P.R.F. Barnes, I.C. Plumb, A. Bendavid, P.J. Martin, Thin Solid Films 516 (2008) 1716-1724.
[38] R. Al-Gaashani, S. Radiman, N. Tabet, A.R. Daud, Journal of Alloys and Compounds 550 (2013) 395-401.
[39] J. Singh, M. Srivastava, J. Dutta, P.K. Dutta, International Journal of Biological Macromolecules 48 (2011) 170-176.
[40] A. Kumar, A. Verma, S. Bhardwaj, Open Applied Physics Journal 1 (2008) 11-19.
[41] T. Droubay, K.M. Rosso, S.M. Heald, D.E. Mccready, C.M. Wang, S.A. Chambers, Physical Review B 75 (2007) 104412-104422.
[42] L. Wang, D. Wang, H. Huang, Z. Han, Q. Cao, B. Gu, Y. Du, Journal of Alloys and Compounds 469 (2009) 1-3.
[43] G. Rojas-George, J. Silva, R. Castañeda, D. Lardizábal, O.A. Graeve, L. Fuentes, A. Reyes-Rojas, Materials Chemistry and Physics 146 (2014) 73-81.
[44] V. Khomchenko, D. Kiselev, J. Vieira, L. Jian, A. Kholkin, A. Lopes, Y. Pogorelov, J. Araujo, M. Maglione, Journal of Applied Physics 103 (2008) 024105-024110.
[45] P. Godara, A. Agarwal, N. Ahlawat, S. Sanghi, R. Dahiya, Journal of Alloys and Compounds 594 (2014) 175-181.
[46] X. Li, Z.-Q. Duan, Materials Letters 89 (2012) 262-265.
[47] W. Koehler, E. Wollan, M. Wilkinson, Physical Review 118 (1960) 58.
[48] F.J. Kahn, P. Pershan, J. Remeika, Physical Review Letters 21 (1968) 804.
[49] E. Balykina, E. Gan'shina, G. Krinchik, Zh. Éksp. Teor. Fiz 93 (1987) 1879-1887.

[50] J. Van Den Brink, D.I. Khomskii, Journal of Physics: Condensed Matter 20 (2008) 434217.
[51] D.I. Khomskii, Journal of Magnetism and Magnetic Materials 306 (2006) 1-8.
[52] J.W. Liu, G. Chen, Z.H. Li, Z.G. Zhang, International Journal of Hydrogen Energy 32 (2007) 2269-2272.
[53] R. Konta, T. Ishii, H. Kato, A. Kudo, The Journal of Physical Chemistry B 108 (2004) 8992-8995.
[54] H. Kato, A. Kudo, Catalysis Letters 58 (1999) 153-155.
[55] H. Kato, K. Asakura, A. Kudo, Journal of the American Chemical Society 125 (2003) 3082-3089.
[56] K. Iwashina, A. Kudo, Journal of the American Chemical Society 133 (2011) 13272-13275.
[57] H. Yang, J.X. Zhang, G.J. Lin, T. Xian, J.L. Jiang, Advanced Powder Technology 24 (2013) 242-245.
[58] L. Li, X. Wang, Y. Zhang, Materials Research Bulletin 50 (2014) 18-22.
[59] L. Li, X. Wang, Y. Lan, W. Gu, S. Zhang, Industrial & Engineering Chemistry Research 52 (2013) 9130-9136.

Chapter 2

Literature Review

This chapter contextualises the background to the theme which is covered in this thesis. It discusses the most relevant aspects which have been explored in this work namely; advanced organic processes and their mechanisms, nanomaterials, synthesis route for these materials, characterisation and application.

2.1 Advanced oxidation process

Advanced organic processes (AOP) involve the use of a light source and powerful oxidising reagents, such as H_2O_2 or O_3, to generate highly reactive radical species such as the hydroxyl radical ($OH^{\bullet}$), which attack and initiate the process of degrading molecules of organic pollutants. The AOP setup may use various types of combinations to generate these radicals. Table 2.1 provides some examples of typical AOP systems and their mechanisms for generating radical species [1, 2].

Table 2.1: Some AOP systems and their mechanism for generating a radical species.

Oxidation reagents	**Activation mechanism**
O_3/H_2O	$O_3 + H_2O \rightarrow 2HO^{\bullet} + O_2$
H_2O_2/Fe^{2+} (Fenton reagent)	$H_2O_2 + Fe^{2+} \rightarrow Fe^{3+} + 2HO^{\bullet}$
H_2O_2/Fe^{3+} (Fenton-like reaction)	$H_2O_2 + Fe^{3+} \rightarrow FeOOH^{2+} + H^+$ $FeOOH^{2+} \rightarrow Fe^{2+} + HO_2^{\bullet}$ $H_2O_2 + Fe^{2+} \rightarrow Fe^{3+} + 2HO^{\bullet}$
O_3/H_2O_2	$2O_3 + H_2O_2 \rightarrow 2HO^{\bullet} + 3O_2$
UV/H_2O_2 (high energy wavelengths)	$H_2O_2 \xrightarrow{h\nu} 2HO^{\bullet}$
O_3/Fe^{2+}	$O_3 + Fe^{2+} \rightarrow FeO^{2+} + O_2$ $H_2O + FeO^{2+} \rightarrow Fe^{3+} + HO^+ + HO^-$
Photocatalysis	$PC + h\nu \rightarrow PC + e^- + h^+$ $O_2 + e^- \rightarrow {}^{\bullet}O_2^-$

2.2 Photoinduced processes

The last twenty years have seen an increased interest in studying photoinduced processes with a view to understanding and harnessing their potential in chemical, environmental and industrial applications [3]. Most photoinduced processes exploit the ability of some materials to absorb light and excite electrons from a valence band (VB) to a conduction band (CB), creating in the process an energetic electron-hole (e^-- h^+) pair capable of initiating processes for destroying pollutants, chemical conversions and other useful processes, such as biomass conversion and environmental detoxification on recombination of the e^-- h^+ pair [3]. When a catalyst is involved in a photoinduced process, the reaction is referred to as photocatalysis and the catalyst as a photocatalyst. When the photocatalyst is not in the same phase as the pollutants the process is referred to as heterogeneous photocatalysis.

Semiconductors and other metal oxides have become the materials of interest in studies of photocatalysis for environmental remediation and wastewater purification [3]. Materials such as ZnO (E_g = 3.2 eV), WO_3 (E_g = 2.8 eV), TiO_2 (anatase, E_g = 3.2 eV), TiO_2 (rutile, = 3.0 eV), α-Fe_2O_3 (E_g = 2.2 eV) and $SrTiO_3$ (E_g = 3.4 eV) have all been studied with a view to maximize the efficiency of photocatalytic reactions. A photocatalytic process is generally composed of the following steps: (i) adsorption of the pollutant molecules on the surface of the photocatalyst, (ii) absorption of light by the photocatalyst, (iii) excitation of an electron, creating the e^- - h^+ pair which initiates the redox reaction, (iv) de-excitation of the e^-, and (iv) desorption of the product molecules [3]. Equations 2.1 to 2.6 below show a representative mechanism for a photocatalytic reaction.

$$PC + h\nu \rightarrow PC + e^- + h^+ \quad (2.1)$$

$$H_2O + h^+ \rightarrow H^+ + {}^{\cdot}OH \quad (2.2)$$

$$O_2 + e^- \rightarrow {}^{\cdot}O_2^- \quad (2.3)$$

$${}^{\cdot}O_2^- + H^+ \rightarrow HOO^{\bullet} \quad (2.4)$$

$$2HOO^{\bullet} \rightarrow H_2O_2 + O_2 \quad (2.5)$$

$$H_2O_2 + e^- \rightarrow OH^- + {}^{\cdot}OH \quad (2.6)$$

Equations 2.1-2.6: Representative mechanism for generating free radical in a photocatalytic reaction. *hc* is light energy, h^+ is the positive hole and e^- is the negative electron

The most widely used photocatalyst, TiO_2, has a bandgap of about 3.2 eV for the anatase phase and 3.0 eV for the rutile phase. Both phases require high energy wavelengths within the ultraviolet UV region of the electromagnetic spectrum for excitation. More effective use of solar radiation could be made by producing photocatalysts that have smaller bandgaps (about 2.1 eV), and therefore lower energy wavelengths ($\lambda \geq 380$ nm) can be utilised by these materials. These wavelengths correspond to the visible region of the electromagnetic spectrum and since it constitutes about 43% of the solar radiation reaching the earth [3], this is more desirable. As stated earlier, hematite and some perovskite oxides nanomaterials have bandgaps that fall within the visible region of the solar spectrum and as such can utilize sunlight effectively for decomposition of organic pollutants. It is therefore important to investigate these materials further.

2.3 Synthesis of functional nanomaterials

The synthesis of functional nanomaterials can be achieved through various chemical methods. The synthesis methods are usually tailored to suit the size and morphology of the intended materials. Some simple methods that have been used for synthesis of functional nanomaterials include those that will be described further in the subsequent sections.

2.3.1 Coprecipitation

The coprecipitation method is a simple method for the synthesis of functional nanomaterials. It involves the precipitation of soluble ions of the target materials by the action of an alkali (e.g. NaOH, KOH). This is followed by washing, drying and annealing at suitable temperatures to obtain the desired materials [4-6]. Surfactants are sometimes added to try and control the size of the product [7] but size control is generally poor for this method**.**

2.3.2 Hydrothermal/Solvothermal method

In this method, the chemical precursors are dissolved in a solvent (e.g. water or other organic solvents) or a mineralizer (e.g. KOH) and then subjected to heat at temperatures of around 200 °C in a Teflon-lined autoclave or a Parr bomb reactor at high pressure. The materials formed are then washed and dried [8-12]. The crystal structure and growth can be controlled by the use of structure directing agents or templating and addition of surfactants [13].

2.3.3 Microemulsion method

In the microemulsion method, a dispersion of immiscible liquids (oil/water) is stabilized by using surfactants and co-surfactants. The tiny droplets of either oil or water act as nanoreactors within which the materials are produced. Three types of microemulsion systems have been widely used for synthesis of nanoparticles, these are: (i) the oil-in-water (O/W) systems: These are systems in which spherical droplets of oil are dispersed in water, the oil droplets act as the nanoreactors in this system, (ii) the water-in-oil (W/O) systems; here, spherical droplets of water are dispersed in oil and the water droplets act as the nanoreactors and (iii) the water-in-supercritical carbon dioxide (W/sc-CO_2) in which water is dispersed in supercritical carbon dioxide and the water droplets act as the nanoreactors. Barring the cost of the reagents employed in this method, the size control is very good (a very narrow size range is possible) and materials with particle sizes range 5-25 nm are easily produced. Some chemicals that have been used as surfactants, co-surfactants and stabilizers in microemulsion synthesis include sodium bis(2-ethylhexyl) sulfosuccinate (often referred to as Aerosol OT (AOT)), cetyl trimethylammonium bromide (CTAB), perfluoropolyethercarboxylic (PFPE) acid, Triton X, Igepal, sodium lauryl sulfate (SLS), tween 80, polyethylene glycol, dodecanthiol, trioctyl phosphine (TOPO) and bis(2-ethyl-hexyl) amine [14-16].

2.3.4 Sol-gel method

The sol-gel route for the synthesis of nanomaterials is a very handy and versatile route for making functional nanomaterials. It involves the addition of a complexing agent (e.g. a polymer, citric acid or other suitable organic entities) to a solution of a colloidal dispersion of the metal ions of the target material, these complexing agents serve as cross-linkers between the ionic entities in solution [17, 18]. This is followed by a

gradual removal of the solvent molecules from the mixture to form a thick gel. The gel is dried and then calcined to produce the required precursor [19, 20]. In the Pechini method, a stoichiometric amount of citric acid and ethylene glycol is mixed with a solution of the metal nitrates of the target material. The temperature of the mixture is maintained at about 90 °C with continuous stirring to form a thick gel. The gel is then dried and precalcined to obtain the as-prepared powder. The as-prepared powders are then annealed at higher temperatures to obtain the finished product. Metal oxides can also be used as starting materials in this method [21, 22].

2.3.5 Combustion synthesis

This are a very widely used technique in the synthesis of ceramic, structural and functional materials. The technique has been used for the synthesis of a variety of functional materials such as ceramics, zeolites, mixed oxides and polymers. Different variants of this procedure can be described depending on either the medium in which the reaction occurs or the temperature at which they occur. A few examples of these processes include: (i) solid-state combustion method, (ii) low- or high-temperature combustion synthesis (LCS or HCS), (iii) solution combustion synthesis (SCS), and (iv) gel- and sol-gel combustion [23, 24]. Self-combustion processes exploit the fast, self-sustaining exothermic reaction that occurs between metal salts and organic fuels to bring about the production of functional materials [25]. Nitrates of metals in the target materials are mixed with chemical fuels (e.g. glycine, hydrazine or urea) and then heated to certain temperatures to ignite the mixture. The combustion is usually quick and no further calcinations are required [26-28].

2.3.6 Mechanochemical method

The mechanochemical method of synthesis is very commonly used in ceramic fabrication. It involves the mixing of stoichiometric quantities of the starting chemicals (mostly metal oxides) and milling them for a long period of time to produce very fine powder of the target materials. As solid-state reactions are very slow, the long milling period is necessary in order to increase the reacting surfaces of the ions thereby creating more efficient interaction between the ions. The energy requirement of this process is very high [29-31].

2.4 Characterisation of photocatalytic materials

The synthesis of materials is normally followed by other procedures aimed at characterizing and elucidating the structure and properties of the materials. These procedures normally require the use of some sophisticated instrumental equipment. The following are some of the procedures used in material characterisation.

2.4.1 Powder X-ray diffraction

X-rays are produced when high energy electrons emitted from a hot filament are made to collide with K-shell electrons in a target metal (Cu, Mo or Co). The K-shell electron is ejected and a vacancy is created in the K-shell. Electrons drop from the L- or M-shell to fill this vacancy and emit X-rays. A crystal lattice is composed of unit cells built from atoms anchored between arrays of atomic planes separated by a distance of d. For incident X-rays to be diffracted, the angle of diffraction must satisfy Bragg's law of diffraction which is given by $n\lambda = 2d\sin\theta$ (where n is an integer, λ is the wavelength of the incident X-ray, d is the space between atoms in adjacent planes and θ is the angle of incidence with respect to a particular lattice plane).

Powder X-ray diffraction (PXRD) is a versatile, non-destructive technique that can be used for phase identification and characterization of the structure of crystalline powdered materials. Its power lies in being able to generate unique fingerprints for different structures, the implication of which is that powders can be identified by matching the generated diffracted fingerprints with fingerprints from a database of known structures. Other information that can be obtained from X-ray diffraction include phase purity of crystalline materials, crystallinity, interatomic distance and the lattice parameters of the unit cell. Crystallite sizes of powder grains can also be estimated by using the Scherrer equation ($D = K\lambda/\beta\cos\theta$, where K is the Scherrer constant, λ is the wavelength of radiation and β is full width at half maximum).

The instrument for a PXRD consists of three basic components. These are: (i) the cathode ray tube which generates the electrons, (ii) the sample holder and (iii) the X-ray detector. The goniometer rotates the sample in the holder and maintains the angle of incident x-rays on the sample and detector. The instrument used in this work was a Bruker D8 Advance instrument with a Cu K_α radiation source (λ = 1.5406 Å) equipped with a DIFFRAC^{plus} BASIC evaluation package.

2.4.2 Electron microscopy

Electron microscopy is a powerful tool for analyzing the shape, size and surface morphology of powdered nanomaterials. Enlarged images of particles (of up to several thousands) obtained from scanning electron microscopy (SEM) allows for the analysis of the morphology, crystal structure, crystal surface and chemical composition at the surface of the powdered particles. SEM is composed of five fundamental parts namely; the gun, which is the source of the electron beam, electron lenses, the sample

compartment, the signal detectors, and data readout. The high energy electrons produced from the gun are used to scan the sample. The images are produced through a variety of signals collected from the surface of the samples by the detector, processed, and are collected at the data interface. The sample is normally spread on a small piece of black tape stuck to the flat head of the pin shaped sample holder. The samples can be observed directly if it is conducting, or gold or carbon coated if they are non-conducting [32, 33].

The Transmission electron microscopy (TEM) and high resolution transmission electron microscopy (HRTEM), being more powerful, allow for a closer look at individual crystallites in the powder. HRTEM can provide information on the lattice fringes of the crystallites. The instrumental set-up of the TEM is similar to that of the SEM. The basic components of the instrument includes, the gun, which is the source of the electron beam, the electromagnetic lense, the sample stage which allows for rotation of the sample, the recording device, and the data output device. Only a thin film of the sample can be analysed on the TEM as the electrons need to be transmitted through the material before the materials can be analysed. The samples are prepared by first dispersing a very little amount of the sample in ethanol by sonication. A thin film of the sample is then spread on a carbon grid by dipping the grid into the ethanol dispersion. The grid is left to dry before images are collected [32]. The TEM instrument used in this work was a JEOL JEM-1010, operating at an acceleration voltage of 120 V and the HRTEM instrument was a JEOL-JEM 2100 LAB6, equipped with a lanthanum hexaborite emission source and operated at an acceleration voltage of 200 V.

2.4.3 Mössbauer spectroscopy

^{57}Fe Mössbauer spectroscopy is a powerful non-destructive analytical method used for material characterization. Its power lies in its ability to detect iron in its environment and give a very precise insight into its electromagnetic properties. The Mössbauer effect arises due to the recoilless emission and absorbance of 14.4 keV γ-rays by nuclei within the crystal lattice of materials. Mössbauer spectroscopy is a unique technique which is very effective in the study of hyperfine interactions emanating from the way the electromagnetic moment of the nucleus interacts with the electromagnetic field of the electrons in its environments. This allows for the monitoring of the electron density around the nucleus.

The hyperfine parameters from which useful Mössbauer information are derived include the chemical isomer shift (IS), which gives information regarding the spin and oxidation state of the iron ion, as well as the interaction between the nuclear charge and the electronic density around the nucleus, quadrupole splitting (Δ_{EQ}) provides information about the symmetry of the charges around the nucleus and the hyperfine magnetic field (B_{hf}) which provides information regarding the magnetic properties of the iron ion [34]. The instrument used in this work was a conventional spectrometer using a 25 mCi ^{57}Co source sealed in a rhodium matrix and vibrated at constant acceleration, and calibrated by using a natural α-iron foil.

2.4.4 Fourier transform infrared spectroscopy

Infrared spectroscopy is a very good technique for studying the nature of the covalent bonds that exist in synthesized materials. It utilizes the infrared region of the electromagnetic spectrum for this purpose. Various kinds of functional groups can be

identified by using this method from their vibrational modes which are normally of different types (e.g. scissoring, stretching and bending) and are said to be infrared-active. For iron and perovskite oxides, the most important peaks occur between 300 and 650 cm^{-1}. This region contains peaks which are due to infrared-active vibrational modes for Fe-O and other metal-O bonds as well [35-39]. The FTIR instrument is composed of five basic parts. These include the infrared radiation source, the interferometer, the sample compartment, the detector and finally the data output device. In FTIR-ATR (Attenuated total reflectance) systems, the infrared radiation only interacts with the surface of the sample through the ATR crystal which is made of either ZnSe or Ge. A very small amount of sample is required for FTIR–ATR measurements and no sample preparation is required. The instrument used in this work was a PerkinElmer Spectrum RX1 fitted with a Ge ATR crystal.

2.4.5 Photoluminescence spectroscopy

Photoluminescence (PL) spectroscopy is a versatile, sensitive and non-destructive method used in the analysis of surface properties of functional materials. PL spectra occur as a result of the excitation and recombination of the e^--h^+ pair when the e^- loses the energy it gained for excitation to occur. Room temperature PL has been shown to occur in materials due to surface defects or impurities in their crystal lattice which might lead to formation of several trap states between the valence and conduction bands. An increase in the density of these trap states has been shown to correspond to an increase in the intensity of the emission and decreases with increasing efficiency of the carrier transport [40, 41]. The optical, optoelectronic and photocatalytic properties of perovskites have been studied by using PL spectroscopy and it has been shown that their band-gap energies fall mostly within the visible region of the electromagnetic

spectrum [42-45]. The PL instruments also have three basic components. These are the light source (which is a xenon lamp in the PerkinElmer LS instruments), the sample holder (a solid probe specially designed for powdered samples) and a suitable detector. No sample preparation is required before these measurements are done. The instrument used in this work was a PerkinElmer LS 55 spectroflourimeter.

2.4.6 Vibrating sample magnetometer

A vibrating sample magnetometer (VSM) measures the magnetic properties of materials. In a VSM the sample is placed in between a uniform magnetic field, with sensing coils suitably placed to pick up the induced voltage as the sample is sinusoidally vibrated in the magnetic field the induced voltage is proportional to the magnetization of the sample. The result is presented in the form of a hysteresis loop which gives the relationship between the sample magnetization and the corresponding applied magnetic field (the $M - H$ loop). Very important information about the magnetic properties of magnetic materials can be determined from the $M - H$ loop and the magnetic properties of the material characterized. Soft and hard magnetic materials, ferromagnetic, antiferromagnetic, diamagnetic, paramagnetic, superparamagnetic and even the presence of more than one magnetic phase can all be determined from the hysteresis of an $M - H$ loop. A very little amount of sample is required for magnetic hysteresis measurements (about 0.02 g) and no sample preparation is required [46]. A Lakeshore 735 VSM instrument was used throughout this work.

2.4.7 Surface area measurements

The surface area of a material refers to the open surface on the material which is available for adsorption of gas molecules. The Brunauer Emett and Teller (BET)

equation is an extension of the Langmuir equation. It uses the physisorption of gases such as N_2, Ar and Kr on the surface of the material that have been degassed (removal of all sorts of physisorbed entities) at low temperature to determine the total surface area available for adsorption. Other information that can be determined from the BET measurement include average pore size and pore size distribution (PSD). Samples are weighed into the sample tube (about 0.25 g) and are degassed first by a steady stream of nitrogen gas into the tube in a degassing chamber set at a temperature of 90 °C for an hour, next the gas flow is turned off and switched to vacuum to remove all the adsorbed N_2 gas on the sample and the temperature ramped up to 200 °C and left to evacuate overnight. The sample is then reweighed before the sample tube is attached to the analysis port. The instrument used for BET surface analysis in this work was a Micromeritrics Tristar II 3020 with three analysis ports, this means that three samples can be run simultaneously.

2.5 Literature review

Here, we present a quick review of published work on synthesis routes, magnetic and photocatalytic properties of hematite (α-Fe_2O_3) and perovskite-like orthoferrites.

2.5.1 Synthesis

The synthesis of α-Fe_2O_3 have been extensively researched and various simple methods for the preparation of various particle sizes and shapes have been developed. α-Fe_2O_3 nanoparticle synthesis mostly involves the use of simple chemicals such as $FeCl_3.6H_2O$, $FeNO_3.9H_2O$, $Fe_2(SO_4)_3.H_2O$, $FeSO_4.7H_2O$, NaOH, KOH and HCl as starting materials.

Among the most widely used methods for the synthesis of α-Fe_2O_3 nanoparticle is the hydrolysis method. This involves the hydrolysis of soluble metal ions by either the use

of heat (thermolysis) or the use of alkali (forced hydrolysis) [47-51]. This method is very cost-effective, the starting materials being $FeCl_3.6H_2O$ and HCl. α-Fe_2O_3 nanoparticles with a size range between 75 and 200 nm can be obtained by using this method. Size control has been shown to be possible in this method by varying some experimental conditions like pH, addition of some tri- or tetravalent cations [52], addition of some anions (e.g. Cl^-, F^- and Br^-) and the addition of surfactants (e.g. polyethylene glycol) [49, 53-56].

The coprecipitation method has also been extensively used to prepare α-Fe_2O_3 nanoparticles. It is also a simple method in which soluble metals are precipitated by using an alkali. Aside its simplicity, coprecipitation also has the advantage of a high percentage yield but the control of size and morphology is difficult. Some workers have used surfactants, such as CTAB (cetyltrimethyl ammonium bromide), in the reaction mixtures to serve as size and shape control agents [57, 58]. It proceeds via the formation of ferrihydrites [59] or goethite [58, 60] with three distinct stages. These are the nucleation stage, the growth stage, which leads to the formation of the ferrihydrite or goethite normally at mild temperatures (between 60 and 80 °C), and then the dehydration stage (normally at elevated temperatures of 250 °C and above) which leads to the formation of the α-Fe_2O_3 nanoparticles [60-62]. This method has been used to successfully synthesize pure and doped α-Fe_2O_3 nanostructures with different shapes like nanorods [58], spherical [59], polycrystalline [63] and hierarchical nanostructures [64]. Numerous perovskite structures, on the other hand, have also been synthesized by using the coprecipitation method. The starting materials in this case are mostly metal nitrates which are dissolved in water to form the metal ion solutions while ammonia is used as the precipitating agent, precursors are then annealed at high temperatures (800

°C and above) to obtain the pure crystalline perovskite powder. Pure polycrystalline perovskites of size range 50-500 nm, which are suitable for advanced technological application have been obtained using this method [6, 65-70].

The hydrothermal method of synthesis is also well-established and has been used for the synthesis of various types of functional materials such as microporous ceramics, zeolites, molecular sieves, superionic conductors, electronically conducting, magnetic materials and a host of other important functional materials. It involves chemical reactions occurring at elevated temperature and pressure in a sealed autoclave. Feng and Xu [13, 62] showed that the method exploits the fact that the physical and chemical properties of substances change at elevated temperatures as reactants dissolve and become fluid. Techniques applied in order to control the size and morphology of the synthesized materials include templating, the use of surfactants as structure directing agents, growth through crystal seeds and complexing. Nanoparticles with various morphologies and sizes have been synthesized by using hydrothermal synthesis and by introducing a variety of structure-directing agents and synthesis conditions (i.e. temperature and duration of synthesis). Huang *et al.* [71] synthesized solid and hollow spindles of α-Fe_2O_3 by means of a hydrothermal route under similar conditions and found that addition of CTAB to the second synthesis gave rise to the hollow spindles. Gu *et al.* [72] described the synthesis of snowflakes, micro-pine and bundles, i.e. hierarchical hematite structures via a controllable hydrothermal process with two iron precursor systems ($K_4[Fe(CN)_6].3H_2O$ and $K_3[Fe(CN)_6]$). The various morphologies were obtained by varying the ratio of the two precursors in the synthesis of each of the materials. Ahmmad *et al.* [73] reported the synthesis of mesoporous α-Fe_2O_3 nanoparticles in green tea extract. Spherical mesoporous nanoparticles of size range

between 40 and 80 nm were obtained through this green procedure. Table 2.2 gives a range of additives and synthesis conditions used for making various morphologies of pure and doped hematite and perovskites.

Table 2.2: Some additives, synthesis condition and morphologies of hematite and perovskites prepared by using the sol-gel method. DI stands for deionized water.

Fe source used	Solvent/Additives	Temp./time	Morphology shape/size/product	Ref.
$FeCl_3$	Water, Carbamide, polyisobutylene bis-succinimide and SPAN80	150 ^oC/12-15hr	Nanorods, nanotubes/30-50 diameter, 500-1100nm length/α-Fe_2O_3	[74]
$FeCl_3$	1,2-propanediamine	180 ^oC/6hr	Nanorods/α-Fe_2O_3	[75]
$FeCl_3 \cdot 6H2O$	Sodium oleate, ethanol, oleic acid	180 ^oC/12hr	Nanocubes, broad size distribution/α-Fe_2O_3	[76]
$FeCl_3$	3,3-thiodipropionic acid (TPA)	110-200 ^oC/6hr	Nanorods, microcapsule/α-Fe_2O_3	[77]
$Fe(NO_3)_3 \cdot 9H2O$	Water, Sodium citrate, urea.	160 ^oC/10hr	Porous nanospheres/α-Fe_2O_3	[78]
$FeCl_3 \cdot 9H_2O$	Urea, Ethylene glycol (EG)	160 ^oC/15hr	Hollow core shell hierarchical nanostructures/α-Fe_2O_3	[79]
$FeCl_3 \cdot 9H_2O$	Urea, tetrabutylammonium bromide (TBAB), EG	195 ^oC/1/2hr	Flowerlike structure/α-Fe_2O_3	[80]
$FeCl_3 \cdot 6H_2O$	Sodium acetate, acetic acid, water	200 ^oC/12hr	Porous nanocubes/ 20-50nm/α-Fe_2O_3	[81]
$Fe(NO_3)_3 \cdot 9H_2O$	1:1 water/ethanol solution, oleic acid, NaOH	200 ^oC/1hr	Plate-like particles/200nm and above/α-Fe_2O_3	[82]
$FeCl_3$	Water, Na_2SO_4, $NaHSO_3$	220 ^oC/8hr	Nanospheres, nanoellipsoids, polyhedral/50 1000nm/α-Fe_2O_3	[83]
$FeCl_3 \cdot 6H_2O$	Water, ethanol, urea, carbon spheres	60 ^oC/48hr	Cage-like nanospheres/30-600 nm/α-Fe_2O_3	[84]
$FeCl_3 \cdot 6H_2O$	Water, NaAcetate, PVP	200 ^oC/18hr	Granules/50 nm above/α-Fe_2O_3	[85]
$FeCl_3 \cdot 6H_2O$	DI water, CH_3COOK, Ionic liquid [bmim][Cl] NaOH	150-250 °C/3 to 8h	Nanorods, nanocubes, nanospheres, hollow Microspheres/α-Fe_2O_3	[86]
$FeCl_3.6H_2O$	DI water tetramethyl	160 °C /2h	Monodisperced	[87]

$MnSO_4.H_2O$	ammonium hydroxide (TMAH)		acicular/α-FeOOH	
$Fe(NO_3)_3.9H_2O$	DI water/Sodium citrate, urea	160 °C /2h	Uniform porous nanosphere/180 nm/ α-Fe_2O_3	[88]
$FeCl_3$	DI water/Urea	120 °C/10h	Porous flute-like/100 nm/β-FeOOH	[78]
$FeCl_3.6H_2O$	DI water/sodium dodecylbenzen sulfonate (SDBS)	180 °C/2h	Uniform Nanoellipsoid/80-90 nm/ α-Fe_2O_3	[8]
$Bi(NO_3).5H_2O$, $Fe(NO_3)_3.9H_2O$	DI water/KOH	160-220 °C/2.5-21h	Polycrystaline/$BiFeO_3$	[12]
$Ba(OH)_2.8H_2O$, TiO_2, $([C_4H_9O]_4Ti)$, $Ti(OH)_4$	DI water/NaOH	75-400 °C/8h	Spheres, porous spheric, cubic/150-300 nm/$BaTiO_3$	[9]
$([C_4H_9O]_4Ti)$, $ZrOCl_2.8H_2O$, $Pb(NO_3)_2$	DI water/polyvinyl alcohol (PVA), polyacrylic acid (PAA)/KOH	200 °C/12h	Nanowires/40 nm/$Pb(Zr_{0.5}Ti_{0.5})O_3$	[89]
$Fe(NO_3)_3.9H_2O$, $La(NO_3).xH_2O$	DI water/NaOH, Na_2CO_3	240-260 °C/5-7days	Cubes/10-20 μm/$LaFeO_3$	[90]

As earlier stated, the microemulsion method of synthesis can produce very fine particles with a very narrow size range. Wongwailikhit and Horwongsakol [91] synthesized uniform hematite nanoparticles with narrow size distribution of about 50 nm in a W/O system made up of water, n-heptane and Aerosol OT (AOT) as surfactant. The precursors (NH_4OH and $FeCl_3$) were dropped into the emulsion and the Fe_2O_3 forms in the water droplets, the system was allowed to stay overnight with continuous stirring in order to achieve equilibrium and the emulsion was broken using distilled water. The study was able to relate increase in hematite particle size with corresponding increase in water. Varying the water : oil, surfactant : oil or water surfactant ratio can also influence the nanoparticle sizes of the product as has been described by Han and co-workers [92]. In a study of microemulsion systems containing water/n-octane/CTAB for hematite synthesis, Han and co-workers were able to show that increasing the molar

ratio of water to CTAB lead to an increase in particle size of the synthesized hematite, while increasing the weight ratio of CTAB to n-octane (the oil) lead to a decrease in the particle size. In the case of perovskites, several perovskite-like systems have been synthesized by using the microemulsion method. For rare earth containing orthoferrites, the precursors are usually soluble nitrates of the desired metals. $LaMnO_3$ and $LaFeO_3$ (prepared through reverse and bicontinuous phase) with good catalytic properties for the reaction between NO and CO have been described by Giannakas *et al.*[93]. A similar reverse microemulsion method has also been described for the preparation of $La_{1-x}M_xFeO_3$, (where M = Sr, Ce) for the catalytic reaction between NO and CO; the synthesized materials had a high BET SSA and a particle size range between 20-80 nm which is an added advantage for catalytic surfaces [94]. Li *et al.* [95] also described a water-in-oil reverse microemulsion synthesis of Ca-doped $LaFeO_3$ with good visible light photocatalytic activity for degradation of methylene blue dye starting with the nitrates of the metals. The disadvantages of this method include the high cost of oils and surfactants used, low yield of synthesized materials and the difficulty associated with product recovery.

In the sol-gel process of nanomaterials synthesis, the selection of a complexing/size and shape-directing agent are very crucial for a successful synthesis of materials of desired size and shape [17, 18]. In the synthesis of hematite nanoparticles, the process sometimes goes through the formation of a less stable iron oxide polymorph γ-Fe_2O_3 or both γ- and α-Fe_2O_3 form together and pure α-Fe_2O_3 only forms when calcined at higher temperatures [19, 96, 97]. Zhang *et al.* [19] dissolved $Fe(NO_3)_3.9H_2O$ and citric acid in deionized water in a 1:1.1 ratio, refluxed the mixture at 70 °C and removed the water by rotary evaporation, dried the product and calcined it at different temperatures. The

results show the formation of γ-Fe_2O_3 at lower calcination temperatures; α-Fe_2O_3 peaks only started appearing for powders calcined at temperatures above 250 °C. A similar procedure was employed by Pawar *et al.* [20] by using a 1:1 mixture of citric acid and oxalic acid as complexing agents. The synthesized powders were calcined at temperatures between 450 and 650 °C to obtain α-Fe_2O_3 nanoparticles. The α-Fe_2O_3 phase formation started at 550 °C and the average particle size was 12.7 nm, the highest BET SSA of 91.54 m^2 g^{-1} was obtained for powders calcined at 600 °C. Other organic solvents can be used in place of deionized water. Ramesh *et al.* [97] for example dissolved $Fe(NO_3)_3$ in ethylene glycol (EG) with vigorous stiring and continuous heating to form the gel. The gel was dried at 300 °C for 5 h in air to form the α-Fe_2O_3 nanoparticles. The sol-gel method is also very suitable for synthesizing thin films of hematite on glass. Thin films of undoped and doped α-Fe_2O_3 nanostructures were synthesized starting with the precursor $FeCl_3.6H_2O$ which was dissolved in 2-methoxyethanol ($C_3H_8O_2$) and ethanolamine (C_2H_7NO) [98]. Walker and Tannenbaum, [99] on the other hand, used $Fe(NO_3).9H_2O$ as precursor. The precursor was dissolved completely in ethanol by stirring vigorously on a magnetic stirrer and gelation chemicals (propylene oxide, THF or pyridine) were then added. In both cases, the film was made on the glass by dip coating. Sol-gel synthesis of perovskite-like materials usually starts with metal nitrates or oxides which are dissolved in deionized water or dilute nitric acid to form a clear solution, followed by the addition of solutions of the crosslinkers and dispersants. These are citric acid and ethylene glycol in the Pechini method but other chemicals can also be used. Yang *et al.* [22] synthesized a series of $La_{0.6}Sr_{0.4}FeO_{3-\delta}$ that were precalcined at 800 °C for 8 h, pressed into pellets and calcined at different temperatures between 1000 and 1200 °C for 24 h and obtained materials

whose X-ray diffractograms were fitted to the rhombohedral (space group *R3C*) symmetry. Li *et al.* [100] also synthesized similar perovskite-like structures ($La_{1-x}Sr_xFeO_{3-\delta}$; x = 0-0.3) and calcined at much lower temperatures (600-650 °C) and obtained particles with an average crystallite size of 20 nm. Magalhaes *et al.* [101] synthesized highly crystalline pseudo-cubic $LaMn_{1-x}Fe_xO_3$ and $LaMn_{0.1-x}Fe_{0.90}Mo_xO_3$ by using the Pechini sol-gel method. Also solid solutions like rhombohedral $BiFeO_3$ and Ba-doped $BiFeO_3$ [102], rhombohedral $La_{(1-x)}Sr_xCo_{(1-y)}Fe_yO_3$ (x = 0, 0.3 and y = 0, 0.2) [103], orthorhombic $La_{0.8}Sr_{0.2}$(Mn, Fe, Co)O_3 [104] and $La_{(1-x)}Sr_xGa_{(1-y)}Mg_yO_{3-(x+y)/2}$ for various values of x and y [105-107] have all been made by using the citric acid method. Vazquez-Vazquez *et al.* [108] synthesized Ca substituted $LaMnO_3$ ($La_{0.67}Ca_{0.33}MnO_{3\pm\delta}$) in a sol-gel method containing urea as the gelification agent. A self combustion sol-gel method has also been used to synthesize $REFeO_3$ materials where RE = Y, La and Gd [109].

Wang *et al.*, [26] described a simple self-combustion method for the synthesis of perovskite materials with general formula $REFeO_3$ (where RE = rare earth). It involved dissolving stoichiometric amounts of the precursors (metal nitrates) and glycine in distilled water and stirring with a magnetic stirrer, and by eliminating the water content at a temperature of about 70 °C, the solution ignited to form the perovskite. A similar method has also been used by Bellakki *et al.* to synthesize (La, Ag)FeO_3 [38] and Cd substituted $LaFeO_3$ [110]. Li *et al.* [27] also described another combustion method by using ionic liquids. The precursors, as in the previous case, are metal nitrates $Fe(NO_3)_3.9H_2O$ and $La(NO_3)_3.6H_2O$, mixed with triethylamine hydrochloride $(C_2H_5)_3N.HCl$ (which serves as both the source of the cations in the ionic liquid and the fuel) and heated to a temperature of about 80 °C in air until they self-combust. In the

case of α-Fe_2O_3 nanoparticles, Deraz and Alarifi [111] have reported combusting a mixture of $Fe(NO_3)_3.9H_2O$ and glycine to obtain α-Fe_2O_3 nanoparticles.

The solid-state method for the synthesis of α-Fe_2O_3 nanoparticles via the combustion oxinates was described by Barrero *et al.* [112]. They synthesized Zn- and Ni-doped α-Fe_2O_3 nanoparticles in mixed form with ferrites ($NiFe_2O_4$ and $ZnFe_2O_4$) by combusting the mixed oxinates at 700 °C. Solid-state synthesis for perovskites involves mixing of stoichiometric amounts of the precursors followed by annealing at high temperature [113-119]. In the mechanochemical synthesis, however, longer milling time replaces calcinations at high temperatures [120, 121].

2.5.2 Magnetic and Photocatalytic properties

The magnetic and photocatalytic properties of materials is affected not only by the composition of the materials, but also by their shapes, sizes and morphology which are all dependent on the synthesis route which was used in the synthesis of the nanomaterials. The following presents summaries of published work that shows the effect of synthesis route on the magnetic and photocatalytic properties of hematite and some perovskites.

2.5.2.1 Hematite

The physical properties of functional materials vary with the method of synthesis. These include shape, size and even crystal defects in the lattice of the nanomaterials. Kamali *et al.* reported substantially different magnetic properties for two different α-Fe_2O_3 nanoparticles that were synthesized by the same method of sol-gel but with different tools for stirring [122]. Tadic *et al.* [82] synthesized plate-like α-Fe_2O_3

nanostructures and showed that changes in the shape and microstructure of the material could lead to an increase in the coercivity of the material after comparing the results with those of materials with different morphologies. Guo *et al.* [77] used the hydrothermal route to synthesize α-Fe_2O_3 nanoparticles with different sizes and morphology. Samples with different shapes showed slightly different magnetic behaviour, the trend for the coercive fields, however, was as expected: an increase with increase in crystallite sizes. Lian *et al.* [86] investigated the effect of the ionic liquid 1-n-butyl-3-methylimidazolium chloride ([bmim]Cl) on the morphology and magnetic properties of synthesized α-Fe_2O_3 nanoparticles and reported a variation in magnetization (all below 1.0 emu g^{-1}) and coercive field with change in the morphology of the materials. The Uv-visible measurements on the materials also indicated that their optical activities are also morphology dependent. Liu *et al.* [74] used a surfactant assisted hydrothermal route to synthesize α-Fe_2O_3 nanorods and nanotubes and showed that the magnetic properties of the particles were shape-dependent as both samples showed a difference in the Morin temperature T_m. Zysler *et al.* [123] had earlier shown the dependence of the magnetic properties of α-Fe_2O_3 nanopaticles on the crystallite sizes. The room temperature magnetization of pure α-Fe_2O_3 is usually low and its coercivity is dominantly controlled by its magnetoelastic anisotropy (which depends on the crystallite size) [124, 125]. Jacob and Abdu Khadar [126] also synthesized α-Fe_2O_3 nanoparticles of various sizes (12, 18 32 and 53 nm) via the coprecipitation route and showed that the coercivity of the samples increased with increase in particle size, as superparamagnetic properties increase as crystallite size decreased, and that T_m was absent in samples with particle size below 20 nm. Ramming *et al.* [47] were able to synthesize pure spherical α-Fe_2O_3 nanoparticles through the hydrolysis of ferric chloride

solution with an average crystallite size of 41 nm which showed superparamagnetic properties. Although the maximum magnetization of α-Fe_2O_3 is generally low (below 1.0 emu g^{-1}), some reports have indicated the possibility of obtaining higher values of magnetization for pure α-Fe_2O_3 nanoparticles. Tadic *et al.* [127] have reported a magnetization of 3.98 emu g^{-1} for pure α-Fe_2O_3 nanoparticles. As stated earlier, synthesized α-Fe_2O_3 sometimes comes with γ-Fe_2O_3 impurities. such impurities can be detected in the PXRD [128]. Although α-Fe_2O_3 and γ-Fe_2O_3 have similar values for H_{hf} (hyperfine field) and δ (isomer shift) and cannot be differentiated by using Mössbauer spectroscopy, the value of the saturation magnetization in the M-H loop can be an indicator of the presence of γ-Fe_2O_3 impurities in α-Fe_2O_3. Gnanaprakash *et al.* showed the enhancement of the maximum magnetization of α-Fe_2O_3 in the presence of γ-Fe_2O_3 impurities [129]. Also Akbar *et al.* [130] synthesized α-Fe_2O_3 via a citric acid sol-gel method and showed that a very small amount of γ-Fe_2O_3 impurity in the α-Fe_2O_3 can lead to a very significant increase in the value of saturation magnetization.

α-Fe_2O_3 nanoparticles have been shown to have good catalytic and photocatalytic properties and like other physical properties, it has been shown that these properties may also depend on the size and morphology of the particles. Lian *et al.* [11] synthesized hollow and broken peanut-shaped α-Fe_2O_3 nanostructures via the hydrothermal route and tested the photocatalytic properties of the materials on the photodegradation of diethyl phthalate DEP under irradiation from a 125 W UV lamp and in the presence of 0.02% H_2O_2, they reported an increase in efficiency from 88.5% for the hollow peanuts to 96.8% for the broken peanuts. The difference in the morphology of the materials was obtained by adding the surfactant CTAB in the synthesis procedure for the materials with broken peanuts shape. Xu *et al.* [131] also

reported the visible light photodegradation of rhodamine b (RhB) dye by α-Fe_2O_3 with various sizes and morphology in the presence of H_2O_2. The materials had been synthesized via a solvothermal process in a mixture of glycol and distilled water. Zhou *et al.* reported the synthesis of hierarchical mesoporous α-Fe_2O_3 structures with high SSA (116 m^2 g^{-1}) via the α-FeOOH coprecipitation method. The α-Fe_2O_3 powder showed very good photocatalytic properties for the degradation of RhB dye under UV irradiation, and electrochemical properties for use in Li-ion batteries [57]. Tong *et al.* [64] also degraded RhB by using α-Fe_2O_3 hierachical nanostructures with crystallite sizes in the range 14-41 nm and high SSA 19.4-151.2 m^2 g^{-1} that were synthesized via a coprecipitation route in D-(+)-glucose. A mass of 0.10 g of the powder was employed to degrade 20 ml of 1 x 10^{-5} mol dm^{-3} solution of RhB. The trend in the photodegradation showed that the photoactivity increased with decrease in crystallite sizes of the materials (which also corresponds to an increase in SSA). The photocatalytic activity of α-Fe_2O_3 on methyl orange under UV irradiation has also been reported [132, 133]. Gu *et al.* [72] used hydrothermally synthesized hierarchical α-Fe_2O_3 structures for the degradation of salicylic acid under UV irradiation. Cao *et al.* [134] reported the photodegradation of methylene blue (MB) dye by α-Fe_2O_3 nanoparticles with average crystallite sizes of 20 nm and SSA of 103 m^2 g^{-1} under visible light, MB absorption was monitored at 664 nm.

2.5.2.2 Perovskites

Rajendran and Bhattacharya studied a series of orthoferites, L_nFeO_3 (where L_n = La, Sm, Gd, Dy, Er, Yb, and Y) synthesized via the sol-gel route and reported that these orthoferrites all showed a weak ferromagnetic property at room temperature which does not saturate even in applied fields of 60 kOe for powders with average crystallite sizes of 25 nm [135]. Shen *et al.* also synthesized orthoferrites via the nitrate-citrate

combustion route and reported a weak ferromagnetic behavior for the orthoferrites, $YFeO_3$ and $LaFeO_3$, and "paraferromagnetic" for $GeFeO_3$. $LaFeO_3$ formed directly after combustion while $YFeO_3$ and $GdFeO_3$ only formed after annealing at 800 °C. The magnetization was higher in the as-burnt $LaFeO_3$, while the coercive field increased when calcined at 700 °C [109]. Paramagnetism was also reported for hydrothermally synthesized $GdFeO_3$ in an applied magnetic field of 20 kOe [35]. Thuy and Mihn [136] demonstrated the dependence of magnetic properties on particle sizes by synthesizing $LaFeO_3$ via two different methods namely sol-gel and mechanical milling to obtain materials with different particle sizes. The powder with the smaller particle size (sol-gel synthesized, size = 30 nm) had the higher value of magnetization while the powder with the larger crystallite size (mechanical milling) had the higher coercive field value. Among other factors that affect magnetic properties of orthoferrites, lattice defects also play a prominent role in influencing the maximum magnetization. Cristóbal *et al.* [121] demonstrated the effect of thermal treatment on the lattice defects in two different powders of $LaFeO_3$ that had been synthesized via the mechanochemical route. The as-milled powders were shown to have the highest M_S values while the M_S values of the thermally-treated powders decreased as annealing temperature increased. Doping or partial replacement of the ions in an ABO_3 system has been shown to improve the magnetic as well as multiferroic, properties of these materials. Consequently, the effect of several types of dopants on magnetic properties of pure orthoferrites have been studied. Hu *et al.* [137] reported an improvement in the magnetic response of $BiFeO_3$ when doped with increasing amount of Eu^{3+} ($Bi_{1-x}Eu_xFeO_3$ x = 0, 0.05, 0.1, 0.15, 0.2 and 0.3) and reaching a maximum at x = 0.1, the magnetization dropped for subsequent increase in x values and these they ascribed to a change from the rhombohedral *R3c*

lattice to the the orthorhombic *Pbmn* lattice. Du *et al.* [138] also reported an increase in magnetization for $Bi_{1-x}La_xFeO_3$ (where $0.0 \leq x \leq 0.2$) at room temperature and increased from 0.264 to 0.658 emu g^{-1} in an applied field of 30 kOe at 77 K for $BiFeO_3$ and $Bi_{0.9}La_{0.1}FeO_3$. A similar result was also reported by Yan *et al.* [139] for hydrothermally synthesized $Bi_{1-x}La_xFeO_3$ ($0.0 \leq x \leq 0.1$). Transition metals have also been used as dopants for orthoferrites. Yu and An [140] reported a big improvement in ferromagnetic properties of Sr and Mn doped $BiFeO_3$ compared to the pure material. First the effect of reduced crystallite sizes was monitored and it was observed that smaller particle sizes (30 nm of pure $BiFeO_3$) showed better responses to magnetization than the larger crystallite sizes (100 nm). The magnetic properties were further enhanced by the addition of the dopants. Work has also been done on the following bismuth ferrites and orthoferrites to determine the effect of the dopants on the magnetic properties of the pure materials: $La_{1-x}Ca_xFeO_3$ [141], $Bi_{1-x}Ca_xFeO_3$ [119], $La_{1-x}Sr_xFeO_3$ [22, 100], $Bi_{1-x}Sr_xFeO_3$ [120], $Bi_{1-x}Ba_xFeO_3$ [102], $La_{1-x}Cd_xFeO_3$ [110], $La_{1-x}Ag_xFeO_3$ [38], $BiFe_{1-x}Mn_xO_3$ [142, 143], $PrFe_{1-x}Ni_xO_3$ [144], $BiFe_{1-x}Co_xO_3$ [145] and $Bi_{1-x}Gd_xFeO_3$ [115, 146]. $Bi_{1-x}R_xFeO_3$ (where x = 0 – 1, and R = La, Nd, Sm, Eu and Tb) [147]. Sometimes a selection of more than one dopant with the properties of interest is used to partially substitute on both the A- and the B-sites. Yan *et al.* [148] synthesized $BiFeO_3$ and $Bi_{1-x}La_xFe_{1-y}Ru_yO_3$ and observed good improvements in the ferroelectric and ferromagnetic properties from $BiFeO_3$ to $Bi_{1-x}La_xFe_{1-y}Ru_yO_3$. Godara *et al.* [117] reported very large coercive field values for $Bi_{0.8}Ba_{0.2}Fe_{1-y}Co_yO_3$ ($x = 0.0 \leq y \leq 0.05$) of up to 4.47 kOe for y = 0. The increase in magnetization corresponded to the increase in the value of x.

Visible light photodegradation requires materials with low bandgap energies for efficient utilization of visible light, Perovskite-like ferrites with suitable bandgaps have been synthesized and demonstrated to effectively degrade organic dyes under visible light irradiation. Jiang *et al.* [149] synthesized wafer-like $BiFeO_3$ with a bandgap of 2.05 eV via a hydrothermal route and showed that the material could effectively degrade RhB dye under visible light irradiation in the presence H_2O_2. $BiFeO_3$ has also been shown to be able to undergo a Fenton-like catalytic degradation of RhB dye at an initial pH of 5.0 [150]. Gao *et al.* [151] reported the synthesis of $BiFeO_3$ via a citric acid sol-gel route and demonstrated the crystallite size dependence on the photocatalytic activity for the degradation of methyl orange. The results showed that the nanoparticulate powders were much more effective in the photocatalytic degradation of the dye than in the bulk. Li *et al.* [152] synthesized various uniform sizes of $BiFeO_3$ microcrystals via a controlled hydrothermal method and demonstrated the size dependence of the photocatalytic activity of the materials on the degradation of Congo red, again the smaller particles were shown to outperform the bigger ones. Gd-doping on $BiFeO_3$ has also been demonstrated to enhance the photocatalytic properties of $BiFeO_3$ in the visible light decomposition of RhB dye; a 10 % Gd doping showed the highest rate in the experiment [153]. Yang *et al.* [154] synthesized $TbFeO_3$ nanoparticles via a polyacrylamide gel route with an average particle size of 50 nm and an energy bandgap of 1.98 eV. The material exhibited pronounced photocatalytic activity towards the degradation of five organic dyes. The activity of the material with respect to dye type was observed to follow the order Congo red > acid fuchsine > methylene blue > rhodamine B > methyl orange. The kinetics of the reaction could be fitted to first order kinetics. Li *et al.* [155] reported the synthesis of $LnFeO_3$ (Ln = La, Sm) via a sol-gel

route. The particle sizes and optical band gaps were 29.04 nm and 2.2 eV for $LaFeO_3$ and 35.08 nm and 2.4 eV for $SmFeO_3$, respectively. Both materials were very effective in the degradation of RhB under visible light irradiation but the rate of decomposition was higher for $LaFeO_3$. Tang *et al.* [156] used a microwave-assisted sol-gel route to synthesize uniform spherical nanoparticles (average crystallite size = 80 nm) of $GdFeO_3$ and then annealed different portions at 300, 500, 700 and 900 °C. The photocatalytic activities of the powders were tested for the decomposition of methyl orange and the as-prepared was most effective. Li *et al.* [157] also synthesized $GdFeO_3$ nanoparticles (average crystallite sizes of 82 nm) via a glycol-assisted sol-gel method and used the material for the degradation of RhB. The nano-sized particles worked better than the larger particle sizes and the photocatalytic activities were enhanced by the addition of H_2O_2. The photocatalytic activities of $YFeO_3$ nanoparticles have also been reported on methyl orange by Zhang *et al.* [158, 159], in which he showed the importance of crystal size control in photocatalytic materials on one hand, and also that the photocatalytic activity in perovskite-like ferrites could be enhanced by the lattice structure of the materials. Here the hexagonal lattice was reported to have a narrower optical bandgap than the orthorhombic lattice and hence had a better photocatalytic property than the orthorhombic one. Ju *et al.* [160] reported a photo-Fenton-like catalytic avtivity for the degradation of RhB under visible light irradiation by using $EuFeO_3$ nanoparticles (crystallite size range 18.6 – 25.2 nm), the powders were synthesized via a sol-gel route and calcined at 700, 750 and 800 °C. The highest efficiency was recorded for powders that had been calcined at 750 °C. The generation of hydrogen by visible light in an ethanol-water system has also been reported for $PrFeO_3$ nanoparticles [161].

In the current research work both hematite and perovskite materials were synthesized and their magnetic and photocatalytic properties were evaluated.

References

[1] S. Esplugas, J. Giménez, S. Contreras, E. Pascual, M. Rodríguez, Water Research 36 (2002) 1034-1042.
[2] R. Andreozzi, V. Caprio, A. Insola, R. Marotta, Catalysis Today 53 (1999) 51-59.
[3] H. Riahi, W. Ouerghui, L. Thevenard, C. Gourdon, M.A. Maaref, A. Lemaître, O. Mauguin, C. Testelin, Journal of Magnetism and Magnetic Materials 342 (2013) 149-151.
[4] Y. Zeng, Y.S. Lin, S.L. Swartz, Journal of Membrane Science 150 (1998) 87-98.
[5] M. Vasquez-Mansilla, R.D. Zysler, C. Arciprete, M.I. Dimitrijewits, C. Saragovi, J.M. Greneche, Journal of Magnetism and Magnetic Materials 204 (1999) 7.
[6] M. Mori, N.M. Sammes, G.A. Tompsett, Journal of Power Sources 86 (2000) 395-400.
[7] J. Yue, X. Jiang, Q. Zeng, A. Yu, Solid State Sciences 12 (2010) 1152-1159.
[8] Y. Xu, S. Yang, G. Zhang, Y. Sun, D. Gao, Y. Sun, Materials Letters 65 (2011) 1911-1914.
[9] C.-T. Xia, E.-W. Shi, W.-Z. Zhong, J.-K. Guo, Journal of Crystal Growth 166 (1996) 961-966.
[10] C.-T. Xia, E.-W. Shi, W.-Z. Zhong, J.-K. Guo, Journal of the European Ceramic Society 15 (1995) 1171-1176.
[11] S. Lian, E. Wang, L. Gao, D. Wu, Y. Song, L. Xu, Materials Research Bulletin 41 (2006) 1192-1198.
[12] C. Chen, J. Cheng, S. Yu, L. Che, Z. Meng, Journal of Crystal Growth 291 (2006) 135-139.
[13] S. Feng, R. Xu, Accounts of Chemical Research 34 (2000) 239-247.
[14] M.A. López-Quintela, C. Tojo, M.C. Blanco, L. García Rio, J.R. Leis, Current Opinion in Colloid, Interface Science 9 (2004) 264-278.
[15] A.K. Gupta, M. Gupta, Biomaterials 26 (2005) 3995-4021.
[16] X. Dong, D. Potter, C. Erkey, Industrial & Engineering Chemistry Research 41 (2002) 4489-4493.
[17] A. Pomogailo, Colloid Journal 67 (2005) 658-677.
[18] S. Pandey, S. Mishra, Journal of Sol-Gel Science and Technology 59 (2011) 73-94.
[19] J. Zhang, L.X. Rong, Y. Liu, B.Z. Dong, Materials Science and Engineering: A 351 (2003) 224-227.
[20] M.J. Pawar, A.D. Khajone, M.D. Gaoner, P.S. Chandel, International Journal of Advanced Scientific Research and Technology 2 (2012) 471-476.
[21] H. Zhang, X. Fu, S. Niu, Q. Xin, Journal of Alloys and Compounds 459 (2008) 103-106.
[22] J. Yang, W. Yelon, W. James, Z. Chu, M. Kornecki, Y. Xie, X. Zhou, H. Anderson, A.G. Joshi, S. Malik, Physical Review B 66 (2002) 184415.
[23] K.C. Patil, S.T. Aruna, T. Mimani, Current Opinion in Solid State and Materials Science 6 (2002) 507-512.
[24] A.S. Mukasyan, P. Dinka, International Journal of Self-Propagating High-Temperature Synthesis 16 (2007) 23-35.

[25] A. Civera, M. Pavese, G. Saracco, V. Specchia, Catalysis Today 83 (2003) 199-211.
[26] Y. Wang, J. Zhu, L. Zhang, X. Yang, L. Lu, X. Wang, Materials Letters 60 (2006) 1767-1770.
[27] F.-t. Li, Y. Liu, Z.-m. Sun, R.-h. Liu, C.-g. Kou, Y. Zhao, D.-s. Zhao, Materials Letters 65 (2011) 406-408.
[28] F. Deganello, G. Marcì, G. Deganello, Journal of the European Ceramic Society 29 (2009) 439-450.
[29] Q. Zhang, F. Saito, Journal of Alloys and Compounds 297 (2000) 99-103.
[30] Q. Zhang, T. Nakagawa, F. Saito, Journal of Alloys and Compounds 308 (2000) 121-125.
[31] B.D. Stojanovic, Journal of Materials Processing Technology 143–144 (2003) 78-81.
[32] L.E. Murr, Materials Characterization 60 (2009) 397-414.
[33] J. Liu, Materials Characterization 44 (2000) 353-363.
[34] R. Zboril, M. Mashlan, D. Petridis, Chemistry of Materials 14 (2002) 969-982.
[35] Y. Zhang, A. Zheng, X. Yang, H. He, Y. Fan, C. Yao, CrystEngComm 14 (2012) 8432-8439.
[36] Z. Jing, S. Wu, Materials Letters 58 (2004) 3637-3640.
[37] E. Darezereshki, Materials Letters 65 (2011) 642-645.
[38] M.B. Bellakki, B.J. Kelly, V. Manivannan, Journal of Alloys and Compounds 489 (2010) 64-71.
[39] B.P. Barbero, J.A. Gamboa, L.E. Cadús, Applied Catalysis B: Environmental 65 (2006) 21-30.
[40] C.C. Mercado, F.J. Knorr, J.L. McHale, S.M. Usmani, A.S. Ichimura, L.V. Saraf, The Journal of Physical Chemistry C 116 (2012) 10796-10804.
[41] C.C. Mercado, F.J. Knorr, J.L. McHale, ACS Nano 6 (2012) 7270-7280.
[42] W.F. Zhang, Z. Yin, M.S. Zhang, Applied Physics A 70 (2000) 93-96.
[43] W.F. Zhang, J. Tang, J. Ye, Chemical Physics Letters 418 (2006) 174-178.
[44] J. Milanez, A.T. de Figueiredo, S. de Lazaro, V.M. Longo, R. Erlo, V.R. Mastelaro, R.W. Franco, E. Longo, J.A. Varela, Journal of Applied Physics 106 (2009) 043526-043524.
[45] A. Giri, N. Goswami, M.S. Bootharaju, P.L. Xavier, R. John, N.T.K. Thanh, T. Pradeep, B. Ghosh, A.K. Raychaudhuri, S.K. Pal, The Journal of Physical Chemistry C 116 (2012) 25623-25629.
[46] B. Dodrill, Lake Shore Cryotronics, Inc 575, 1-10.
[47] T.P. Raming, A.J.A. Winnubst, C.M. van Kats, A.P. Philipse, Journal of Colloid and Interface Science 249 (2002) 346-350.
[48] K. Kandori, Y. Nakamoto, A. Yasukawa, T. Ishikawa, Journal of Colloid and Interface Science 202 (1998) 499-506.
[49] K. Kandori, Y. Aoki, A. Yasukawa, T. Ishikawa, Journal of Materials Chemistry 8 (1998) 2287-2292.
[50] D. Fu, P.G. Keech, X. Sun, J.C. Wren, Physical Chemistry Chemical Physics 13 (2011) 18523-18529.
[51] Y.-H. Chen, F.-A. Li, Journal of Colloid and Interface Science 347 (2010) 277-281.
[52] J.-P. Jolivet, S. Cassaignon, C. Chanéac, D. Chiche, E. Tronc, Journal of Sol-Gel Science and Technology 46 (2008) 299-305.

[53] K. Kazuhiko, W. Mai, Colloid and Polymer Science 289 (2011) 981-991.
[54] K. Kandori, J. Sakai, T. Ishikawa, Physical Chemistry Chemical Physics 2 (2000) 3293-3299.
[55] K. Kandori, N. Okamoto, T. Ishikawa, Langmuir 18 (2002) 2895-2900.
[56] K. Kandori, S. Ohnishi, M. Fukusumi, Y. Morisada, Colloids and Surfaces A: Physicochemical and Engineering Aspects 331 (2008) 232-238.
[57] W. Zhou, L. Lin, W. Wang, L. Zhang, Q. Wu, J. Li, L. Guo, The Journal of Physical Chemistry C 115 (2011) 7126-7133.
[58] J. Yue, X. Jiang, A. Yu, Solid State Sciences 13 (2011) 263-270.
[59] H. Liu, Y. Wei, P. Li, Y. Zhang, Y. Sun, Materials Chemistry and Physics 102 (2007) 1-6.
[60] L.C. Varanda, M.P. Morales, M.J. Jafelicci, C.J. Serna, Journal of Materials Chemistry 12 (2002) 188-193.
[61] M. Mohapatra, S. Anand, International journal of Engineering, Science and Technology 2 (2010) 127-146.

[62] I. Abdulkadir, A.B. Aliyu, African Journal of Pure and Applied Chemistry 7 (2013) 114-121.
[63] M. Hosseini-Zori, F. Bondioli, T. Manfredini, E. Taheri-Nassaj, Dyes and Pigments 77 (2008) 53-58.
[64] G. Tong, J. Guan, Q. Zhang, Materials Chemistry and Physics 127 (2011) 371-378.
[65] F. Zhang, T. Karaki, M. Adachi, Powder Technology 159 (2005) 13-16.
[66] J. Tang, M. Zhu, T. Zhong, Y. Hou, H. Wang, H. Yan, Materials Chemistry and Physics 101 (2007) 475-479.
[67] S. Nakayama, Journal of Materials Science 36 (2001) 5643-5648.
[68] M. Kumar, S. Srikanth, B. Ravikumar, T.C.Alex, S.K. Das, Materials Chemistry and Physics 113 (2009) 803-815.
[69] P.V. Gosavi, R.B. Biniwale, Materials Chemistry and Physics 119 (2010) 324-329.
[70] M. De Guire, S. Dorris, R. Poeppel, S. Morissette, U. Balachandran, Journal of Materials Research 8 (1993) 2327-2335.
[71] J. Huang, M. Yang, C. Gu, M. Zhai, Y. Sun, J. Liu, Materials Research Bulletin 46 (2011) 1211-1218.
[72] J. Gu, S. Li, E. Wang, Q. Li, G. Sun, R. Xu, H. Zhang, Journal of Solid State Chemistry 182 (2009) 1265-1272.
[73] B. Ahmmad, K. Leonard, M. Shariful Islam, J. Kurawaki, M. Muruganandham, T. Ohkubo, Y. Kuroda, Advanced Powder Technology 24 (2013) 160-167.
[74] L. Liu, H.-Z. Kou, W. Mo, H. Liu, Y. Wang, The Journal of Physical Chemistry B 110 (2006) 15218-15223.
[75] Z. Li, X. Lai, H. Wang, D. Mao, C. Xing, D. Wang, Nanotechnology 20 (2009).
[76] S.-B. Wang, Y.-L. Min, S.-H. Yu, The Journal of Physical Chemistry C 111 (2007) 3551-3554.
[77] P. Guo, Z. Wei, B. Wang, Y. Ding, H. Li, G. Zhang, X.S. Zhao, Colloids and Surfaces A: Physicochemical and Engineering Aspects 380 (2011) 234-240.
[78] X. Gou, G. Wang, X. Kong, D. Wexler, J. Horvat, J. Yang, J. Park, Chemistry – A European Journal 14 (2008) 5996-6002.

[79] S.-W. Cao, Y.-J. Zhu, G.-F. Cheng, Y.-H. Huang, Journal of Physics and Chemistry of Solids 71 (2010) 1680-1683.
[80] L.S. Zhong, J.S. Hu, H.P. Liang, A.M. Cao, W.G. Song, L.J. Wan, Advanced Materials 18 (2006) 2426-2431.
[81] J. Hua, J. Gengsheng, Materials Letters 63 (2009) 2725-2727.
[82] M. Tadić, N. Čitaković, M. Panjan, Z. Stojanović, D. Marković, V. Spasojević, Journal of Alloys and Compounds 509 (2011) 7639-7644.
[83] Q.-j. Sun, X.-g. Lu, G.-y. Liang, Materials Letters 64 (2010) 2006-2008.
[84] J. Yu, X. Yu, B. Huang, X. Zhang, Y. Dai, Crystal Growth & Design 9 (2009) 1474-1480.
[85] M. Zhu, Y. Wang, D. Meng, X. Qin, G. Diao, The Journal of Physical Chemistry C 116 (2012) 16276-16285.
[86] J. Lian, X. Duan, J. Ma, P. Peng, T. Kim, W. Zheng, ACS Nano 3 (2009) 3749-3761.
[87] S. Krehula, S. Musić, Journal of Alloys and Compounds 426 (2006) 327-334.
[88] X. Gou, G. Wang, J. Park, H. Liu, J. Yang, Nanotechnology 19 (2008) 125606.
[89] J.Y. Choi, C.H. Kim, D.K. Kim, Journal of the American Ceramic Society 81 (1998) 1353-1356.
[90] W. Zheng, R. Liu, D. Peng, G. Meng, Materials Letters 43 (2000) 19-22.
[91] K. Wongwailikhit, S. Horwongsakul, Materials Letters 65 (2011) 2820-2822.
[92] L.-H. Han, H. Liu, Y. Wei, Powder Technology 207 (2011) 42-46.
[93] A.E. Giannakas, A.K. Ladavos, P.J. Pomonis, Applied Catalysis B: Environmental 49 (2004) 147-158.
[94] A.E. Giannakas, A.A. Leontiou, A.K. Ladavos, P.J. Pomonis, Applied Catalysis A: General 309 (2006) 254-262.
[95] F.-t. Li, Y. Liu, R.-h. Liu, Z.-m. Sun, D.-s. Zhao, C.-g. Kou, Materials Letters 64 (2010) 223-225.
[96] K. Woo, H.J. Lee, J.P. Ahn, Y.S. Park, Advanced Materials 15 (2003) 1761-1764.
[97] R. Ramesh, S. Sohila, C. Muthamizhchelvan, M. Rajalakshmi, S. Ramya, S. Ponnusamy, J Mater Sci: Mater Electron 22 (2011) 1357-1360.
[98] C. Aydın, S.A. Mansour, Z.A. Alahmed, F. Yakuphanoglu, J Sol-Gel Sci Technol 62 (2012) 397-403.
[99] J.D. Walker, R. Tannenbaum, Chemistry of Materials 18 (2006) 4793-4801.
[100] J. Li, X. Kou, Y. Qin, H. He, physica status solidi (a) 191 (2002) 255-259.
[101] F. Magalhães, F.C.C. Moura, J.D. Ardisson, R.M. Lago, Materials Research 11 (2008) 307-312.
[102] G. Rojas-George, J. Silva, R. Castañeda, D. Lardizábal, O.A. Graeve, L. Fuentes, A. Reyes-Rojas, Materials Chemistry and Physics 146 (2014) 73-81.
[103] S. Rousseau, S. Loridant, P. Delichere, A. Boreave, J.P. Deloume, P. Vernoux, Applied Catalysis B: Environmental 88 (2009) 438-447.
[104] K.L. da Silva, A. Börger, K.D. Becker, F. Tietz, D. Stöver, Solid State Ionics 192 (2011) 552-556.
[105] R. Polini, A. Pamio, E. Traversa, Journal of the European Ceramic Society 24 (2004) 1365-1370.
[106] R. Polini, A. Falsetti, E. Traversa, O. Schäf, P. Knauth, Journal of the European Ceramic Society 27 (2007) 4291-4296.

[107] R. Polini, A. Falsetti, E. Traversa, Journal of the European Ceramic Society 25 (2005) 2593-2598.
[108] C. Vazquez-Vazquez, M.C. Blanco, M.A. López-Quintela, R.D. Sánchez, J. Rivas, S.B. Oseroff, Journal of Materials Chemistry 8 (1998) 991-1000.
[109] H. Shen, J. Xu, A. Wu, Journal of Rare Earths 28 (2010) 416-419.
[110] M.B. Bellakki, V. Manivannan, J. Das, Materials Research Bulletin 44 (2009) 1522-1527.
[111] N.M. Deraz, A. Alarifi, Ceramics International 38 (2012) 4049-4055.
[112] C.A. Barrero, J. Arpe, E. Sileo, L.C. Sánchez, R. Zysler, C. Saragovi, Physica B: Condensed Matter 354 (2004) 27-34.
[113] S.K. Pradhan, J. Das, P.P. Rout, V.R. Mohanta, S.K. Das, S. Samantray, D.R. Sahu, J.L. Huang, S. Verma, B.K. Roul, Journal of Physics and Chemistry of Solids 71 (2010) 1557-1564.
[114] D. Li, J. Zheng, Z. Zou, Journal of Physics and Chemistry of Solids 67 (2006) 801-806.
[115] V.A. Khomchenko, V.V. Shvartsman, P. Borisov, W. Kleemann, D.A. Kiselev, I.K. Bdikin, J.M. Vieira, A.L. Kholkin, Acta Materialia 57 (2009) 5137-5145.
[116] V. Khomchenko, D. Kiselev, J. Vieira, L. Jian, A. Kholkin, A. Lopes, Y. Pogorelov, J. Araujo, M. Maglione, Journal of Applied Physics 103 (2008) 024105-024110.
[117] P. Godara, A. Agarwal, N. Ahlawat, S. Sanghi, R. Dahiya, Journal of Alloys and Compounds 594 (2014) 175-181.
[118] E. Folcke, J.M. Le Breton, Y. Bréard, A. Maignan, Solid State Sciences 12 (2010) 1387-1392.
[119] W.-t. Chen, A.J. Williams, L. Ortega-San-Martin, M. Li, D.C. Sinclair, W. Zhou, J.P. Attfield, Chemistry of Materials 21 (2009) 2085-2093.
[120] L. Wang, D. Wang, H. Huang, Z. Han, Q. Cao, B. Gu, Y. Du, Journal of Alloys and Compounds 469 (2009) 1-3.
[121] A.A. Cristóbal, P.M. Botta, P.G. Bercoff, J.M. Porto López, Materials Research Bulletin 44 (2009) 1036-1040.
[122] S. Kamali, N. Shahmiri, J.S. Garitaonandia, J. Ångström, M. Sahlberg, T. Ericsson, L. Häggström, Thin Solid Films 534 (2013) 260-264.
[123] R. Zysler, D. Fiorani, A. Testa, L. Suber, E. Agostinelli, M. Godinho, Physical Review B 68 (2003) 212408-212411.
[124] Y. Zhao, C.W. Dunnill, Y. Zhu, D.H. Gregory, W. Kockenberger, Y. Li, W. Hu, I. Ahmad, D.G. McCartney, Chemistry of Materials 19 (2007) 916-921.
[125] Q. Liu, V. Barrón, J. Torrent, H. Qin, Y. Yu, Physics of the Earth and Planetary Interiors 183 (2010) 387-397.
[126] J. Jacob, M. Abdul Khadar, Journal of Magnetism and Magnetic Materials 322 (2010) 614-621.
[127] M. Tadic, M. Panjan, V. Damnjanovic, I. Milosevic, Applied Surface Science 320 (2014) 183-187.
[128] N. Harshada, N.V. Kulkarni, S. Karmakar, B. Sahoo, I. Banerjee, P.S. Chaudhari, R. Pasricha, A.K. Das, S.V. Bhoraskar, S.K. Date, W. Keune, Materials Characterization 59 (2008) 1215-1220.
[129] G. Gnanaprakash, S. Ayyappan, T. Jayakumar, J. Philip, B. Raj, Nanotechnology 17 (2006) 5851-5857.

[130] S. Akbar, S.K. Hasanain, N. Azmat, M. Nadeem, Condensed matter 480 (2004) 19.
[131] Y. Xu, G. Zhang, G. Du, Y. Sun, D. Gao, Materials Letters 92 (2013) 321-324.
[132] Q. Zhang, X. Lu, L. Chen, Y. Shi, T. Xu, M. Liu, Materials Letters 106 (2013) 447-451.
[133] Y. Min, F. Zheng, Y. Zhao, Y. Chen, Solid State Sciences 13 (2011) 976-980.
[134] Z. Cao, M. Qin, B. Jia, Y. Gu, P. Chen, A.A. Volinsky, X. Qu, Ceramics International.
[135] M. Rajendran, A.K. Bhattacharya, Journal of the European Ceramic Society 26 (2006) 3675-3679.
[136] N.T. Thuy, D.L. Minh, Advances in Materials Science and Engineering 2012 (2012) 1-6.
[137] Z. Hu, M. Li, J. Liu, L. Pei, J. Wang, B. Yu, X. Zhao, Journal of the American Ceramic Society 93 (2010) 2743-2747.
[138] Y. Du, Z.X. Cheng, M. Shahbazi, E.W. Collings, S.X. Dou, X.L. Wang, Journal of Alloys and Compounds 490 (2010) 637-641.
[139] X. Yan, J. Chen, Y. Qi, J. Cheng, Z. Meng, Journal of the European Ceramic Society 30 (2010) 265-269.
[140] X. Yu, X. An, Solid State Communications 149 (2009) 711-714.
[141] E.K. Abdel-Khalek, H. Mohamed, Hyperfine Interactions 222 (2013) 57-67.
[142] K. Takahashi, M. Tonouchi, Journal of Magnetism and Magnetic Materials 310 (2007) 1174-1176.
[143] M. Azuma, H. Kanda, A.A. Belik, Y. Shimakawa, M. Takano, Journal of Magnetism and Magnetic Materials 310 (2007) 1177-1179.
[144] A.B. Makhdoomi, M. Ikram, R. Kumar, Journal of Magnetism and Magnetic Materials 322 (2010) 2581-2584.
[145] I. Coondoo, N. Panwar, A. Tomar, I. Bdikin, A.L. Kholkin, V.S. Puli, R.S. Katiyar, Thin Solid Films 520 (2012) 6493-6498.
[146] J.B. Li, G.H. Rao, Y. Xiao, J.K. Liang, J. Luo, G.Y. Liu, J.R. Chen, Acta Materialia 58 (2010) 3701-3708.
[147] Y.-j. Zhang, H.-g. Zhang, J.-h. Yin, H.-w. Zhang, J.-l. Chen, W.-q. Wang, G.-h. Wu, Journal of Magnetism and Magnetic Materials 322 (2010) 2251-2255.
[148] F. Yan, T.-J. Zhu, M.-O. Lai, L. Lu, Applied Physics Express 4 (2011) 111502.
[149] J. Jiang, J. Zou, M.N. Anjum, J. Yan, L. Huang, Y. Zhang, J. Chen, Solid State Sciences 13 (2011) 1779-1785.
[150] W. Luo, L. Zhu, N. Wang, H. Tang, M. Cao, Y. She, Environmental Science & Technology 44 (2010) 1786-1791.
[151] F. Gao, X.Y. Chen, K.B. Yin, S. Dong, Z.F. Ren, F. Yuan, T. Yu, Z.G. Zou, J.M. Liu, Advanced Materials 19 (2007) 2889-2892.
[152] S. Li, Y.-H. Lin, B.-P. Zhang, Y. Wang, C.-W. Nan, The Journal of Physical Chemistry C 114 (2010) 2903-2908.
[153] R. Guo, L. Fang, W. Dong, F. Zheng, M. Shen, The Journal of Physical Chemistry C 114 (2010) 21390-21396.
[154] H. Yang, J.X. Zhang, G.J. Lin, T. Xian, J.L. Jiang, Advanced Powder Technology 24 (2013) 242-245.
[155] L. Li, X. Wang, Y. Zhang, Materials Research Bulletin 50 (2014) 18-22.
[156] P. Tang, Y. Hu, T. Lin, Z. Jiang, C. Tang, Integrated Ferroelectrics 153 (2014) 73-78.

[157] L. Li, X. Wang, Y. Lan, W. Gu, S. Zhang, Industrial & Engineering Chemistry Research 52 (2013) 9130-9136.
[158] Y. Zhang, J. Yang, J. Xu, Q. Gao, Z. Hong, Materials Letters 81 (2012) 1-4.
[159] Y. Zhang, J. Feng, J. Xu, G. Chen, Z. Hong, Integrated Ferroelectrics 151 (2014) 108-115.
[160] L. Ju, Z. Chen, L. Fang, W. Dong, F. Zheng, M. Shen, Journal of the American Ceramic Society 94 (2011) 3418-3424.
[161] S.N. Tijare, S. Bakardjieva, J. Subrt, M.V. Joshi, S.S. Rayalu, S. Hishita, N. Labhsetwar, J Chem Sci 126 (2014) 517-525.

Chapter 3

The effect of synthesis method on the structure and magnetic and photocatalytic properties of α-Fe_2O_3

Ibrahim Abdulkadir, Hafiz M.I. Abdallah, Sreekantha B. Jonnalagadda and Bice S. Martincigh*

School of Chemistry and Physics, University of KwaZulu-Natal, Westville Campus, Private Bag X54001, Durban 4000, South Africa

*****Corresponding author: Tel: +27 31 2601394; Fax: +27 31 2603091; E-mail: martinci@ukzn.ac.za.

Abstract

Samples of α-Fe_2O_3 nanoparticles have been synthesized through the co-precipitation route in cetyltrimethylammonium bromide (Hem_PR), via a citric acid sol-gel method (Hem_SG) and a modified sol-gel method in Tween 20 (Hem_TW), and each were annealed at three different temperatures (400, 500 and 600 °C). The samples were characterized by X-ray diffraction (XRD), Fourier transform infrared spectroscopy (FTIR), transmission and high-resolution electron microscopy (TEM and HRTEM), Mössbauer spectroscopy and by means of a vibrating sample magnetometer (VSM). In addition, the photocatalytic behaviour of each sample was tested on the degradation of rhodamine B (RhB) in solution. All the characterization techniques showed the formation of phases of pure hematite nanoparticles with improved crystallinity after higher temperature annealing. However, the nanoparticles synthesized in Tween 20 showed the smallest particle size and highest BET surface area, saturation magnetization and photocatalytic activity. Of particular note was the ability of Tween 20 to control the growth of the particles so that grain sizes well below 10 nm were obtained. Thus, Tween 20, when used as a surfactant in the sol-gel route, can serve to improve the physical properties of synthesized hematite nanoparticles.

Keywords: *hematite; nanoparticles; Mössbauer spectroscopy; magnetic properties; Tween 20; photocatalysis*

3.1 Introduction

Hematite, α-Fe_2O_3, is the most thermodynamically stable of all the known iron oxides. It exhibits n-type semiconducting properties at ambient conditions and has a band gap energy of 2.1 eV which falls within the visible region of the electromagnetic spectrum. When the oxide is prepared in nano-dimensions it exhibits novel physical and chemical properties. Lately, α-Fe_2O_3 nanoparticles have received increased interest due to some of their fascinating properties which stand out from those of the bulk material. Their low cost and non-toxicity, coupled with their wide range of applications, for example, they have found use in pigments [1, 2], lithium ion batteries and gas sensors [3, 4], catalysis [5, 6], optical and biomedical devices [7, 8], water purification [9], solar energy conversion and magnetic materials [3, 10], have made α-Fe_2O_3 nanoparticles the most investigated of all the oxides.

Nanoparticles of different shapes and sizes can form and these include nanorods [11-13], nanofibres [14, 15], nanowires [16, 17] and nanocubes [18] among others. Various techniques have been used to synthesize α-Fe_2O_3. These include hydrothermal approaches, sol-gel processes, combustion, microemulsion techniques, pyrolysis and ultrasonic-assisted methods. The sol-gel and co-precipitation methods stand out as methods capable of producing high yields of α-Fe_2O_3 nanoparticles, with sol-gel being more hands-on in terms of morphology control [19]. It is known that the synthesis conditions strongly affect the physicochemical properties of the product. Consequently, it is expected that by using a different reaction medium or adding a surfactant in the preparation process might influence some of the physical properties (e.g. size, porosity, surface area [20, 21]) of the nanoparticles.

In this paper, hematite nanoparticles were prepared by means of three different routes, namely, (i) chemical precipitation in a cetyltrimethylammonium bromide (CTAB) solution, (ii) a sol-gel method in citric acid solution, and (iii) a sol-gel type method in the presence of the surfactant Tween 20, with a view to study and compare the structure, and magnetic, as well as photocatalytic, properties of the products.

3.2 Experimental

3.2.1 Materials

All reagents were used as received. These were $Fe(NO_3)_3.9H_2O$ (98% Saarchem), NaOH (98% Saarchem), citric acid (99.7% BDH Laboratories), Tween 20 (Prosynth grade Riedel-de Haën) and CTAB (95% Aldrich Chemicals). The deionized water used was from a Millipore Elix 5 UV Milli-Q apparatus.

3.2.2 Synthesis

3.2.2.1 Co-precipitation

$Fe(NO_3)_3.9H_2O$ (0.02 moles) was dissolved in deionized water containing CTAB (0.03 moles) and made up to 100 cm^3 to form a solution. NaOH (10 M) was then added to the solution while stirring to form a reddish-brown precipitate and the pH was adjusted to between 11 and 12. The resulting mixture was poured into a polyethylene bottle, sealed and placed in an oven which had been preheated to 80 °C. The mixture was kept at this temperature for 24 hours. The precipitate (now yellow) was washed several times with deionized water, filtered and dried in the oven at 100 °C for 2 hours. The dried powder was then placed in the furnace and heated at 400 °C for 2 hours. Two other separate portions were also annealed at 500 and 600 °C for 2 hours each. Hematite prepared by

this method will be referred to as Hem_PR followed by a number indicating the annealing temperature, that is, Hem_PR400, Hem_PR500 or Hem_PR600.

3.2.2.2 Sol-gel – Method 1

Citric acid (0.17 mol) was dissolved in deionized water (800 cm^3); $Fe(NO_3)_3.9H_2O$ (0.03 mol) was also dissolved in deionized water (200 cm^3). The ferric nitrate solution was added dropwise to the citric acid solution while vigorously stirring to obtain a clear solution. The solution was then heated at about 90 °C on a hot plate with continuous stirring until a gel formed. The gel was dried in the oven at 100 °C for 24 hours. The dry gel was then annealed in a furnace at 400 °C for 2 hours and then crushed to obtain the powder. Two other separate portions were also calcined at 500 and 600 °C for 2 hours each. Hematite prepared by this method will be referred to as Hem_SG followed by a number indicating the annealing temperature, that is, Hem_SG400, Hem_SG500 or Hem_SG600.

3.2.2.3 Sol-gel – Method 2

Tween 20 (200 cm^3) was made up to 800 cm^3 with deionized water; $Fe(NO_3)_3.9H_2O$ (0.03 mol) was also dissolved in deionized water (200 cm^3) and subsequently added dropwise to the Tween 20 solution while vigorously stirring. The clear yellow solution was then heated (with stirring) at 90 °C on a hot plate to form a black gel. The gel was dried in an oven at 100 °C for 24 hours and subsequently annealed in a furnace at 400 °C for 2 hours and then crushed to obtain the powder. Two other separate portions were also annealed at 500 and 600 °C for 2 hours each. Hematite prepared by this method will be referred to as Hem_TW followed by a number indicating the annealing temperature, that is, Hem_TW400, Hem_TW500 or Hem_TW600.

3.2.3 Characterization

High and low magnification images of the samples were collected with a JEOL-JEM 2100 LAB6 high resolution transmission electron microscope (HRTEM), with a lanthanum hexaborite emission source and operated at an acceleration voltage of 200 V, and a transmission electron microscope (JEOL JEM-1010, Tokyo Japan) respectively. Each sample was dispersed in ethanol in a small centrifuge tube and sonicated before being dispersed on a carbon grid and the images collected. The crystal structures of the synthesized products were determined by powder X-ray diffraction (PXRD) on a Bruker D8 Advance instrument with a Cu K_α radiation source (λ = 1.5406 Å). Diffractograms were recorded between a 2θ range of 15 and 90° and the results were analyzed with the DIFFRACT^{plus} basic evaluation package (2007). The Scherrer equation, $G = K\lambda/\beta\cos\theta$ (where K is the Scherrer constant of 0.89, λ is the wavelength of radiation and β is the full width at half maximum intensity), was used to calculate the grain size, G, of the particles. The attenuated total reflectance-Fourier transform infrared (ATR-FTIR) spectra of samples annealed at 400 °C were collected with a PerkinElmer Spectrum 100 instrument. Surface area analysis was performed on a Micromeritics Tristar II 3020 fully automated three-station surface area and porosity analyzer by using nitrogen at 77 K. The magnetic properties were determined with a LakeShore 735 vibrating sample magnetometer (VSM) which had been calibrated with a standard Ni sphere of saturation magnetization 54.7 emu g^{-1}. The magnetization curve was obtain at a maximum magnetic field of 14 kOe at room temperature. The zero-field ^{57}Fe Mössbauer spectra were obtained in transmission mode by a conventional spectrometer using a 25 mCi ^{57}Co source sealed in a rhodium matrix and vibrated at constant acceleration. The spectrometer was calibrated with a natural α-iron foil and all measurements were made

at room temperature. The spectra were then fitted with the aid of Recoil Mössbauer analysis software. Photocatalytic properties of the powders were screened in visible light by using a simple setup consisting of a 26 W fluorescent lamp (Osram Dulux D, 26 W, 1800 lm) held in a quartz glass jacket at about 7 cm above the rhodamine B (RhB) solution (100 cm^3 in volume with an initial absorbance of approximately 0.8) containing 0.1 g of synthesized powder at room temperature, which was being stirred continuously by a magnetic stirrer. The mixture was allowed to equilibrate for 30 minutes in the dark before the light was turned on. Samples were taken from the solution at regular intervals, centrifuged and filtered through a 0.45 μm syringe filter. Absorbance measurements of these samples were recorded with a Biochrome Libra S6 UV spectrophotometer at a λ_{max} of 556 nm to monitor the degradation process.

3.3 Results and discussion

In this work hematite was synthesized by using three different routes, namely: the goethite route in CTAB, the sol-gel route in citric acid, and the sol-gel route in Tween 20. The expectation was that the medium (i.e. citric acid or the CTAB and Tween 20 surfactants with their long hydrocarbon chains) would help in limiting the growth of the crystals and thereby effect a size control process on the crystals. It was also envisaged that some carbon atoms would be embedded into the core of the materials, which would then result in pores once the carbon was burnt off. In this manner it was hoped to produce highly porous nanoparticles of hematite that would possess a large surface area and serve as a good photocatalyst.

3.3.1 Phase purity and crystallinity

The powders all formed with a reddish brown colour. Hem_PR400 and Hem_SG400 appeared to be lighter in colour while Hem_TW400 was darker and finer. The X-ray diffractograms for the three samples annealed at 400 °C are shown in Fig. 1. The XRD patterns are similar and all display peaks typical for hematite which are in agreement with reported α-Fe_2O_3 peak positions (JCPDS No. 33-0664) [22]. Smaller peaks which occur at 2θ values between 29.330 and 33.159° are due to impurities and can be seen in the diffractograms of Hem_PR400 and Hem_TW400. Likely impurities that could be generated alongside α-Fe_2O_3 are Fe_3O_4, γ-Fe_2O_3 and oxyhydrites (i.e. α-, γ-, or amorphous FeOOH) [23-25]. The peak at a 2θ value of 29.32° corresponds to the position of the (220) peak for Fe_3O_4 and γ-Fe_2O_3 which are both spinels. Also the (110) α-Fe_2O_3 peak intensities for both Hem_PR400 and Hem_TW400 are abnormally high relative to their corresponding (104) planes. This could be attributed to the fact that the (110) α-Fe_2O_3 peak position corresponds to the spinel (311) peak for Fe_3O_4 and γ-Fe_2O_3 [26, 27]. This larger than expected intensity may be due to contributions from both sources thus confirming the presence of either α-Fe_2O_3 or γ-Fe_2O_3 phases in both samples [23]. The Hem_SG400 sample, however, shows normal α-Fe_2O_3 peak ratios. The peak intensities are generally low; this indicates poor crystallization for all powders annealed at 400 °C. XRD peaks for powders annealed at higher temperatures (500 and 600 °C), however, show a significant increase in peak intensity and adjustment of the peaks to normal α-Fe_2O_3 peak ratios (see Fig. 2). Thus, the crystallinity improves with an increase in annealing temperature. The spinel (220) peak (d = 29.00 ±1 nm), however, is still slightly visible for Hem_TW500 and even with increased intensity for Hem_PR500, but eventually disappears for Hem_TW600 and Hem_PR600 (Fig. 2).

This is an indication that the spinel impurity responsible for this peak is γ-Fe_2O_3, and not Fe_3O_4, since γ-Fe_2O_3 is known to convert to α-Fe_2O_3 at temperatures greater than 400 °C.

The values of the grain sizes for each of the powders synthesized were calculated from the Scherrer equation and are listed in Table 1. As can be seen the medium did effect size control of the particles as expected and the particle widths of all samples fall within the range of 26 to 33 nm.

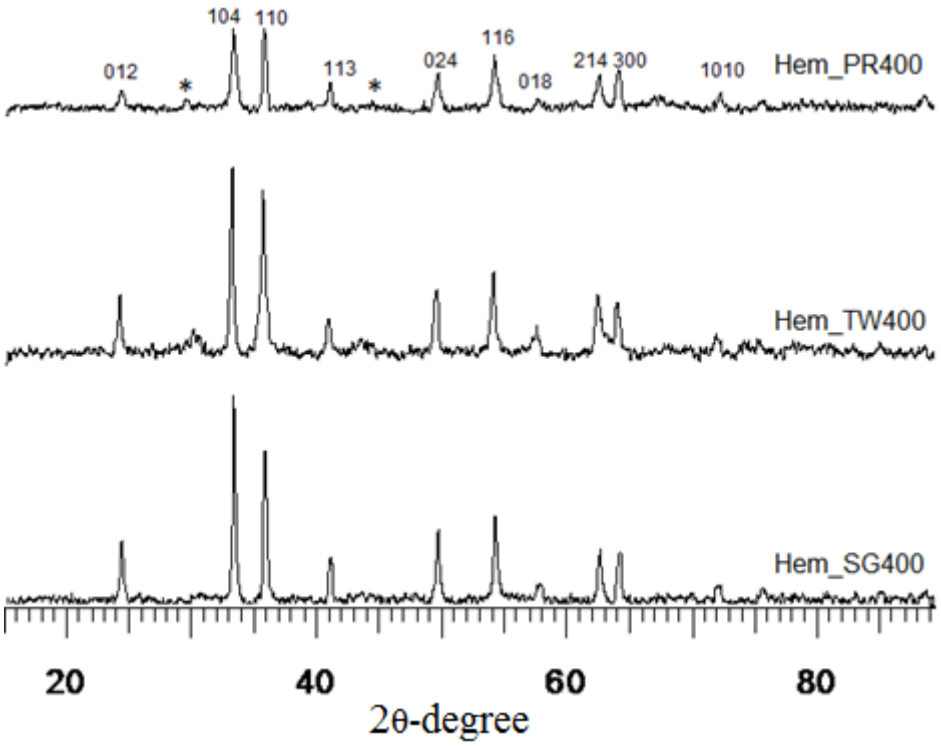

Figure 3.1. Powder X-ray diffractograms for hematite samples (Hem_TW400, Hem_SG400 and Hem_PR400) annealed at 400 °C. The * indicates the position of impurity peaks due to γ-Fe_2O_3.

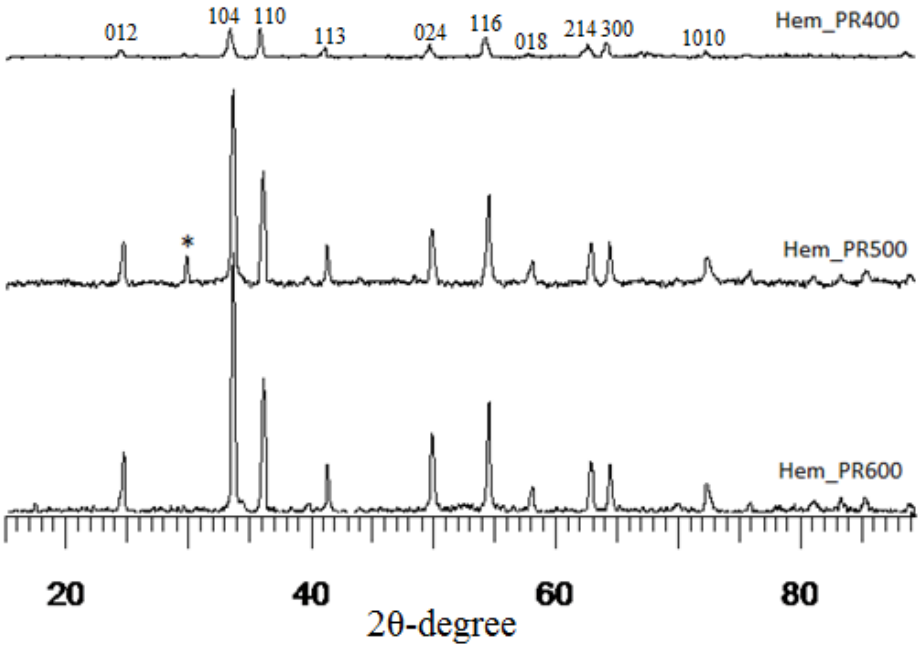

Figure 3.2. Powder X-ray diffractograms for hematite samples prepared by the co-precipitation route and annealed at three different temperatures, i.e. 400, 500 and 600 °C (Hem_PR400, Hem_PR500 and Hem_PR600). A more intense γ-Fe_2O_3 peak is observed for Hem_PR500 (indicated by *) which disappears completely in Hem_PR600.

3.3.2 Structural Characteristics

The expected IR absorption bands for hematite occur at around 540, 470 and 325 cm^{-1} and depending on the physical properties (i.e. size and morphology) of the crystals, the infrared bands can either move to higher or lower wavelengths [22, 28-30].

The ATR-FTIR spectra of samples annealed at 400 °C were collected with a PerkinElmer Spectrum 100 instrument which is capable of collecting signals between 380 and 4000 cm^{-1}. Consequently, the band expected at 325 cm^{-1} is not observed here. Two major peaks, which occur in the region between 389 and 600 cm^{-1}, are common to all three samples as can be seen in Fig. 3. In addition, the spectra for Hem_TW400 and Hem_PR400 also exhibit peaks between 640 and 1060 cm^{-1}. These are the regions of

interest for iron oxides/hydroxides; higher wavenumbers are mostly due to -OH stretching which could be as a result of adsorbed water molecules [29].

The two absorption bands that appear at approximately 520 and 430 cm^{-1} can be assigned to the hematite Fe-O stretching and O-Fe-O bending modes. The similar additional absorption bands observed between 640 and 1060 cm^{-1} in the spectra for Hem_PR400 and Hem_TW400 may well be due to the observation that both may contain small amounts of γ-Fe_2O_3 impurity. Namduri and Nasrazadani [29] observed the occurrence of γ-Fe_2O_3 Fe-O absorption bands between 630-660 cm^{-1}. Thus, the absorption peak observed at 641.94 cm^{-1} for Hem_PR400 may be as a result of the Fe-O stretching absorption for γ-Fe_2O_3. However, this might be misleading since it could also be attributed to an out-of-plane bending mode for –OH [31].

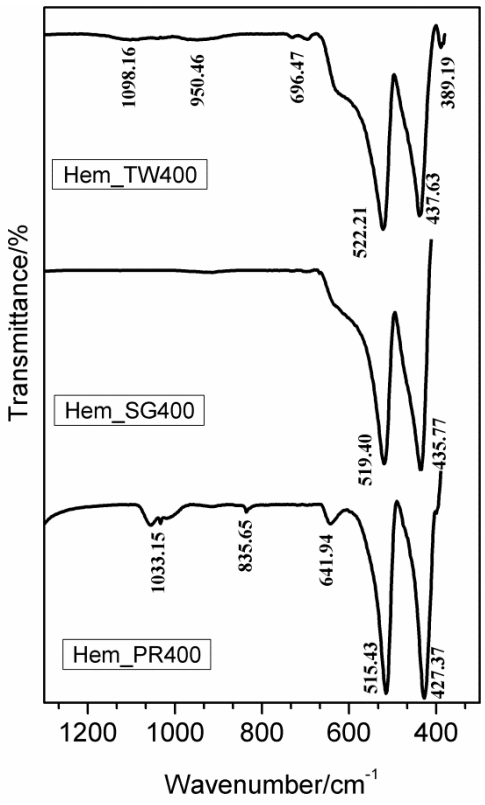

Figure 3.3. The ATR-FTIR spectra of the hematite samples annealed at 400 °C.

3.3.3 Morphology

The low magnification TEM images for powders annealed at 400 °C are presented in Fig. 4. The micrographs show nanorod clusters for the Hem_PR400 powder (Fig. 4a). These nanorods have average diameters of about 30 ± 6 nm and lengths of about 250 ± 50 nm. Fig. 4b is a HRTEM image for Hem_PR400 that shows its d spacing. Hem_SG400 and Hem_TW400, however, consist of nanoparticles of varying sizes ranging from below 10 nm to about 30 nm. The crystals for Hem_SG400 are more irregular in shape while those of Hem_TW400 showed a more regular spherical pattern. Average grain sizes calculated for both samples from the powder-XRD peaks by means of the Scherrer equation give mean values of 33 ± 11 nm for Hem_SG400 and 27 ± 9 nm for Hem_TW400. The TEM images, however, show a much smaller grain size especially for Hem_TW400. This could be an indication of a wide range in the distribution of grain sizes. This shows that Tween 20 was able to control the growth of the particles so that grain sizes well below 10 nm were obtained. This is a noteworthy result since solution-based syntheses of hematite typically produce much larger particle sizes. The inset in Fig. 4c shows the porous nature of the larger grains of Hem_SG400. Note the coalescence of tiny grains to form bigger grains in Hem_TW500 (Fig. 4g). The HRTEM images show the lattice fringes of the crystals. Improvement in crystallinity can be seen for powders annealed at higher temperatures in agreement with the PXRD results, suggesting that crystallinity increases with the annealing temperature.

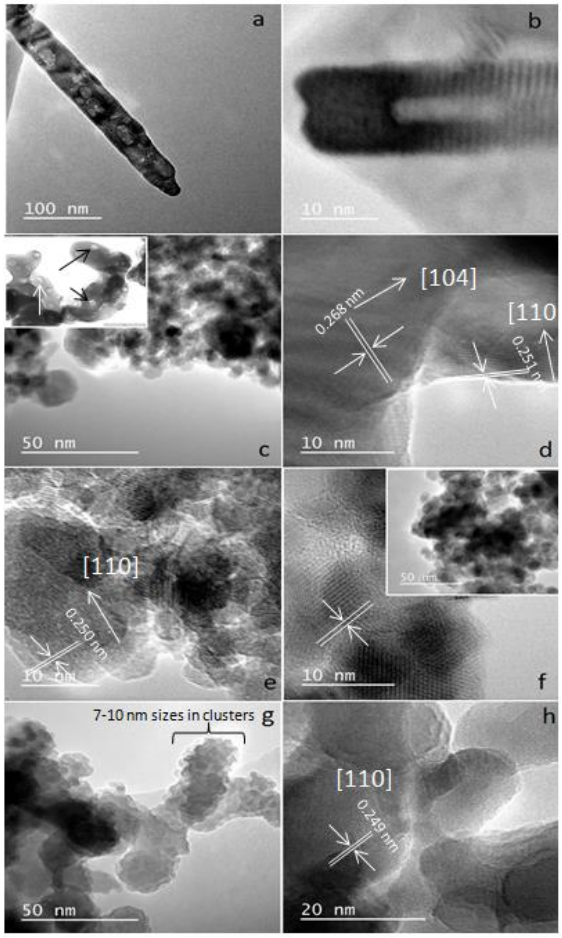

Figure 3.4. TEM and HRTEM images indicating pores, lattice fringes and growth direction for powders. (a and b) Hem_PR400, (c and d) Hem_SG400, (e) Hem_SG500, (f) Hem_TW400 and (g and h) Hem_TW500.

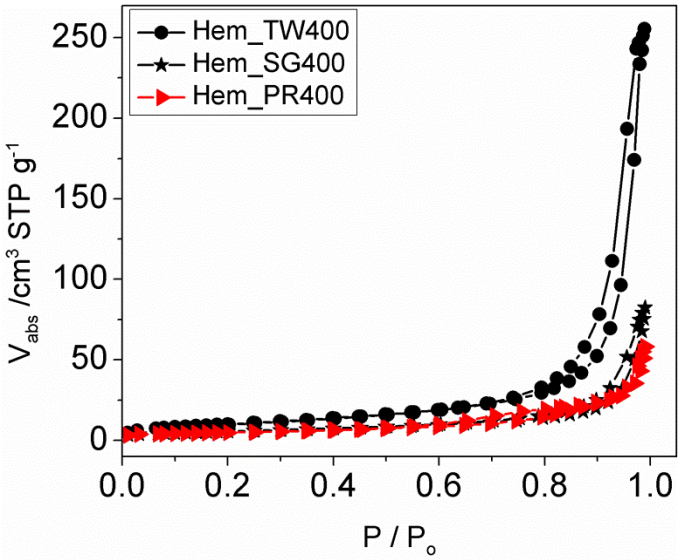

Figure 3.5: Adsorption-desorption isotherms in nitrogen at 77 K for Hem_PR400, Hem_SG400 and Hem_TW400.

3.3.4 Surface area and porosity

The surface areas and porosities of the hematite samples were determined from nitrogen adsorption/desorption isotherms at liquid nitrogen temperature (77 K). The specific surface area was calculated with the BET model and the pore size distribution by the BJH method. The N_2 adsorption/desorption isotherms at 77 K (Fig. 5) for these materials conform to the type II isotherm as classified by IUPAC [32]. The specific surface areas for Hem_PR400, Hem_SG400 and Hem_TW400 are 16.819, 20.271 and 37.149 m^2 g^{-1} respectively (Table 1). The surface area was highest for the particles synthesized in Tween 20. Again, this value is higher than those reported in most cases for sol-gel and some other solution-based synthetic routes and also for commercial α-Fe_2O_3 [33]. The hysteresis loops seen in the isotherms indicate that all samples contain porous particles with pore sizes ranging from meso- to macroporous. The BJH average pore size for Hem_PR400, Hem_SG400 and Hem_TW400 were 88.62, 20.71 and 38.92 nm respectively. The average pore sizes for the three hematite samples are shown in Table 1. The pore sizes are distributed between meso-pores (between 2 – 50 nm pore diameter) and macro-pores (pore diameter above 50 nm). These pore sizes are quite unusual for these samples, considering the mean grain sizes calculated for each sample by using the Scherrer equation. The implication is that some of the pores are actually bigger than the grains on which they are supposed to be found. These pore sizes, therefore, are due to spaces created between tiny particles within large clusters of particles (see Fig. 4(c-h)).

Table 3.1 Grain size, surface area and pore sizes for powders calcined at 400 °C.

Sample name	Grain size/nm	Surface area $m^2 g^{-1}$ ± 0.15	Average pore size/nm
Hem_PR400	26.34	16.82	88.62
Hem_SG400	32.86	20.27	20.71
Hem_TW400	27.39	37.15	38.92

3.3.5 Magnetic properties

Figure 3.6 shows the room temperature magnetization curves for all the samples annealed at 400 °C measured with a vibrating sample magnetometer in an applied field of 14 kOe. The magnetization curves for Hem_PR400 and Hem_TW400 show higher magnetization than is normally reported for pure hematite (normally below 1 emu g^{-1}) [34-36], which is normally due to the spin canting in α-Fe_2O_3 above its Morin temperature (T_M), creating weak ferromagnetism (WF) in the sublattice [37, 38]. Table 2 shows some magnetic parameters of the samples. The saturation magnetization M_S values range between 1.53 to 19.99 emu g^{-1}. Hem_TW400 shows superparamagnetic properties with a very low coercivity value H_C of 10 Oe. H_C values also increase as the crystal size G increases (see Table 2). The high M_S value for Hem_TW400 is a confirmation of the PXRD results which show the presence of small amounts of γ-Fe_2O_3 in the sample; small amounts of γ-Fe_2O_3 in α-Fe_2O_3 powder can drastically increase the M_S values [39, 40]. However, Hem_PR400 shows an M_S value which is higher than that reported for hematite but not as high as for Hem_TW400. This can be attributed to the shape and/or the large size of its particles which are nanorods with dimensions as stated earlier (i.e. diameters of 30 ± 6 nm and lengths of 250 ± 50 nm). The magnetization curves for Hem_TW500 and Hem_TW600 are presented in Fig. 7. The magnetization curves are observed to reduce with increasing annealing temperature indicating that γ-Fe_2O_3 converts to hematite at a temperature between 400 and 600 °C [22, 41].

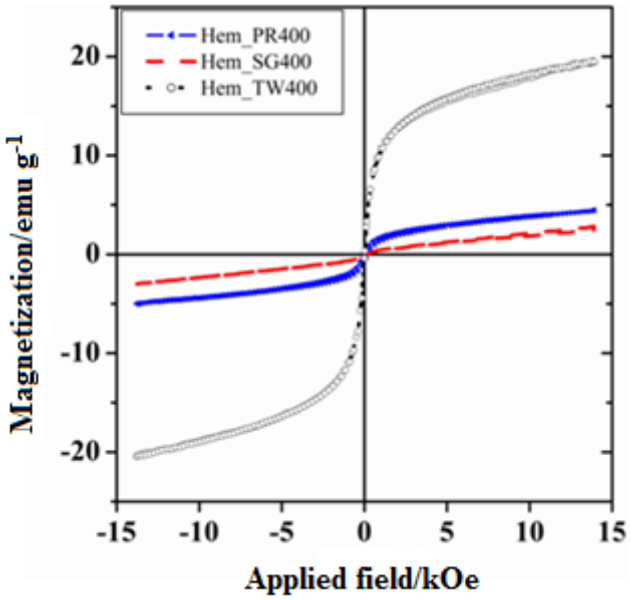

Figure 3.6. Room temperature magnetization curves for hematite samples annealed at 400 °C.

Table 3.2. Magnetic properties for hematite samples annealed at 400, 500 and 600 °C measured at room temperature.

Sample	G/nm	H_C/Oe	M_S/emu g^{-1}	M_R/emu g^{-1}	M_R/M_S
Hem-PR400	26.34	125.55	4.73	0.44	0.094
Hem_PR500	32.69	329.12	1.57	0.17	0.059
Hem_PR600	38.39	242.25	2.78	0.07	0.040
Hem-SG400	32.86	38.35	2.91	0.18	0.062
Hem_SG500	33.86	363.50	2.63	0.30	0.114
Hem_SG600	36.24	518.61	1.531	0.12	0.078
Hem-TW400	27.39	10.03	19.99	0.47	0.014
Hem_TW500	30.31	20.06	6.84	0.26	0.023
Hem_TW600	35.02	301.01	1.60	0.14	0.096

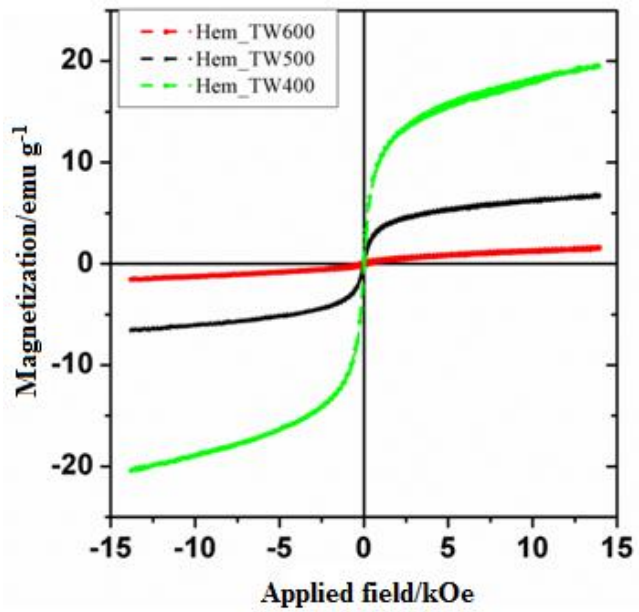

Figure 3.7. Hysteresis loops for Hem_TW400, 500 and 600 showing the reduction in magnetization with increase in annealing temperature.

Figure 3.8(a) shows the relationship between annealing temperature and grain size. As expected, grain sizes increased with increase in annealing temperature. M_R/M_S (refered to as the squareness of the hysteresis loop) and coercivity values (H_C) could be useful in describing the magnetic hardness/softness of magnetic materials; an increase in the values of these parameters would imply a tendency towards hardness and higher ferromagnetic properties [34]. Coercivity values for Hem_SG and Hem_TW powders increase with increase in grain size and with calcination temperature indicating an increase in hardness and ferromagnetic character. However, the M_R/M_S values are irregular and show different trends for different sets of samples (Fig. 8b). The trends in the M_R/M_S and coercivity values for Hem_PR powders could be due to the morphology and the large sizes of its particles, which are above the critical particle sizes reported for hematite [34, 35]

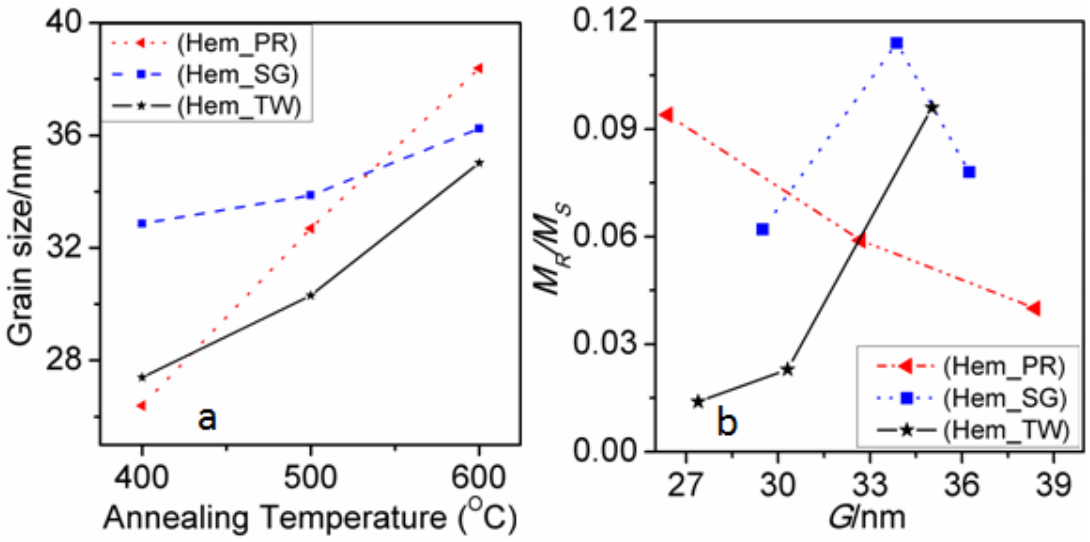

Figure 3.8. Plots of (a) grain size versus annealing temperature, and (b) M_R/M_S versus grain size.

3.3.6 Mössbauer spectroscopy analysis

Figure 3.9 shows selected fitted Mössbauer spectra for hematite samples annealed at 400, 500 and 600 °C. The results of the spectral fittings are shown in Table 3.3. The Mössbauer parameters obtained for samples annealed at 400 °C indicate that the samples, with the exception of Hem_SG400, do not contain pure hematite but rather they contain a mixture of hematite and some other iron oxide impurity. This impurity, as observed from the PXRD results, may either be Fe_3O_4 or γ-Fe_2O_3 and, perhaps, a small amount of ferrihydrites. The distribution of cations in spinel Fe_3O_4 and γ-Fe_2O_3 can be represented as follows $Fe^{3+}[Fe^{2+}\ Fe^{3+}]O_4$ and $Fe^{3+}[\square\ Fe^{3+}]O_3$ respectively, where □ represents a vacant octahedral (B-) site. This implies that Fe_3O_4 and γ-Fe_2O_3 have two crystallographic sites designated A and B; the ions outside the parentheses are on the A- or tetrahedral site while those within the parentheses are on the B- or octahedral site. This implies that Mössbauer spectra for pure Fe_3O_4 can be fitted with two sextet subspectra with the octahedral site having twice the area of the tetrahedral site and thus its presence is easy to detect if it occurs as an impurity in α-Fe_2O_3. On the other hand,

γ-Fe_2O_3 is difficult to detect in a mixture with α-Fe_2O_3 because both sites are equivalent and therefore are not distinguishable from α-Fe_2O_3. Although some reports have shown that the isomer shift (δ) and magnetic hyperfine field (B_{hf}) for γ-Fe_2O_3 are lower than those for α-Fe_2O_3, the line between the two is very blurred and complementary PXRD data is required [24, 42-44].

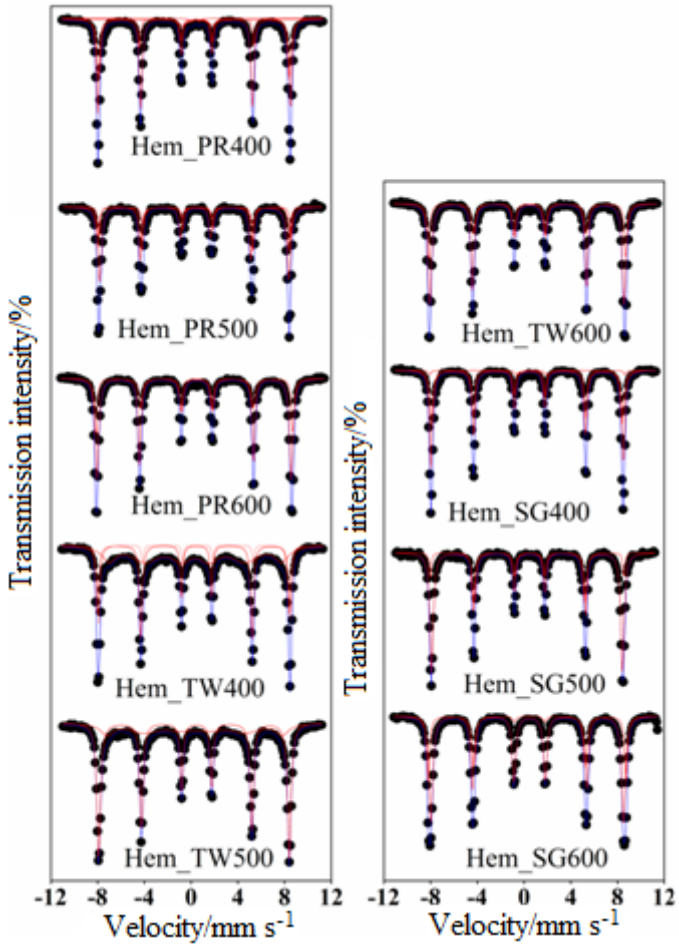

Figure 3.9. Mössbauer spectra for hematite samples annealed at different temperatures, namely, 400, 500 and 600 °C.

Table 3.3. The Mössbauer hyperfine parameters for the hematite samples prepared by different synthetic methods and annealed at 400, 500 and 600 °C. *H – hematite, MH – maghemite, δ – isomer shift, Δ_{EQ} – quadrupole shift, B_{hf} – hyperfine magnetic field and *f* – fraction population of Fe^{3+} ions at H and MH sites.

(a) Samples annealed at 400 °C.

Sample	Sublattice*	δ/mm s^{-1}	Δ_{EQ}/mm s^{-1}	B_{hf}/kOe	*f*/%
HemPR400	Fe^{3+}	0.36	0.64	_	0.77
	H	0.40	-0.066	522.52	22.75
	H	0.36	-0.105	512.02	48.42
	MH	0.42	-0.169	505.59	28.06
HemSG400	H	0.35	-0.095	503.90	48.00
	H	0.35	-0.045	511.60	18.00
	H	0.36	-0.146	511.76	34.00
HemTW400	H	0.36	-0.108	513.28	23.00
	H	0.37	-0.113	505.50	32.20
	MH	0.34	0.029	448.30	44.80

(b) Samples annealed at 500 °C.

HemPR500	MH	0.32	-0.081	508.23	41.00
	H	0.42	-0.162	504.89	59.00
HemSG500	H	0.36	-0.106	507.00	67.00
	H	0.36	-0.108	514.20	33.00
HemTW500	MH	0.35	-0.002	454.60	17.10
	H	0.36	-0.11	503.52	60.00
	H	0.36	-0.10	511.87	23.00

(c) Samples annealed at 600 °C.

HemPR600	H	0.36	-0.10	523.35	45.00
	H	0.37	-0.12	515.53	55.00
HemSG600	H	0.37	-0.11	524.71	52.30
	H	0.37	-0.10	511.31	47.70
HemTW600	H	0.36	-0.21	514.16	52.00
	H	0.37	0.001	515.40	48.00

The Mössbauer spectrum for Hem_PR400 (Figure 3.9) has been fitted with 4 subspectra, namely, 3 sextets and 1 doublet (Table 3.3a). The B_{hf} values for the three sextets fall within the range of B_{hf} values for α-Fe_2O_3 and γ-Fe_2O_3 (450 to a little above 500 kOe). The δ values are a little higher than usual (0.404 and 0.421 mm s^{-1}) for crystalline Fe^{3+}. These higher δ values are as a result of defects in the crystal lattice of the crystallites which can be seen from Table 3.3 to fall back to values within the normal range with increased crystallinity (i.e. for the samples annealed at higher temperature) [45, 46]. The same applies to other subspectra with δ values of 0.4 mms^{-1} and above. This explains the general increase in the intensity of the peaks as we go from lower to higher annealing temperatures for all the samples, which also results in higher B_{hf} values. This is in agreement with the PXRD results from which it was possible to show that the powders not only contained impurities but that the crystals are defective with crystallinity increasing for powders annealed at higher temperatures. The presence of Fe_3O_4 was excluded in Hem_PR400 because the B_{hf} values displayed by all subspectra are much higher than the B_{hf} value for Fe_3O_4. Moreover, the colour of the sample, which is reddish, does seem to suggest the absence of Fe_3O_4 which is black in colour. The quadrupole doublet in the spectrum indicates a paramagnetic contribution (0.77% paramagnetic properties) which might be due to the presence of a very small amount of surface ferrihydrite in the sample [25]. The Mössbauer parameters (δ and Δ_{EQ} with values of 0.356 and 0.64 mm s^{-1} respectively) indicate that the doublet could be as a result of an Fe^{3+} located on the surface of the iron oxide core [47].

Samples with two or more hematite subspectra are as a result of variation in the grain sizes of the nanoparticles with larger particles having a larger B_{hf} value [48, 49]. This is

expected and it agrees with the results obtained from TEM which shows that the powders contain various size ranges of nanoparticles.

The results obtained in this work show that both Hem_PR400 and Hem_TW400 contain a mixture of poorly crystalline α- and γ-Fe_2O_3 with the well crystalline α-Fe_2O_3 phase favored at higher annealing temperatures. The implication of this is that both α- and γ-oxyhydroxides (FeOOH) may have been produced at the point of nucleation in the co-precipitation method, which then begins to convert to the corresponding Fe_2O_3 when it is annealed at 400 °C and ultimately changes into pure α-Fe_2O_3 which is the most stable iron oxide polymorph according to the following reactions.

$$Fe^{3+} + 3OH^- \longrightarrow (\alpha+\gamma) - FeOOH + H_2O \quad (3.1)$$

$$2(\alpha+\gamma) - FeOOH \longrightarrow (\alpha+\gamma) - Fe_2O_3 + H_2O \xrightarrow{heat(>400\,^\circ C)} \alpha - Fe_2O_3 \quad (3.2)$$

Another scenario would be the formation of γ-FeOOH alone at the point of nucleation which then converts to the corresponding γ-Fe_2O_3 at temperatures above 300 ^oC. γ-Fe_2O_3 is known to begin to convert to α-Fe_2O_3 at about 400 °C. However, the sol-gel methods, would most likely have started from γ-Fe_2O_3, as has been reported, and slowly convert to α-Fe_2O_3 at higher annealing temperatures [50]. The PXRD, VSM and Mössbauer spectroscopy results are all in agreement in this regard.

3.3.7 Photocatalytic activities

The photocatalytic activity of the hematite samples was investigated by monitoring the photodegradation of the dye, rhodamine B, under visible light illumination. Figure 3.10 shows the photodegradation curves obtained. From -30 to 0 min represents the adsorption-desorption equilibrium before the samples were illuminated. All powders were able to adsorb between 10-20% of the dye molecules thereby lowering the

absorbance considerably from the initial value. Photodegradation began at 0 minutes and as can be seen from the plots only Hem_TW400 was able to appreciably degrade RhB dye both without and in the presence of H_2O_2. Powders annealed at higher temperatures, however, only mostly adsorbed the dye molecules and tended to desorb the dye rather than photodegrade it once the illumination began. The reduced photocatalytic rate (Figure 3.11) could either be as a result of the increase in the particle grain size at higher annealing temperatures (Table 3.1), which might not favour a slower electron-hole recombination (this trend can also be noticed in samples calcined at 400 °C as the least active in this series is Hem_PR400 which has the largest average particle size as determined from the Scherrer equation) or as a result of the conversion of the γ-Fe_2O_3 nanoparticles present in the powder to α-Fe_2O_3 as observed in the data obtained in sample characterization, or a combination of both reasons. The implication of the second suggestion would be that the α-Fe_2O_3 and γ-Fe_2O_3 composite has a better photocatalytic ability than pure α-Fe_2O_3.

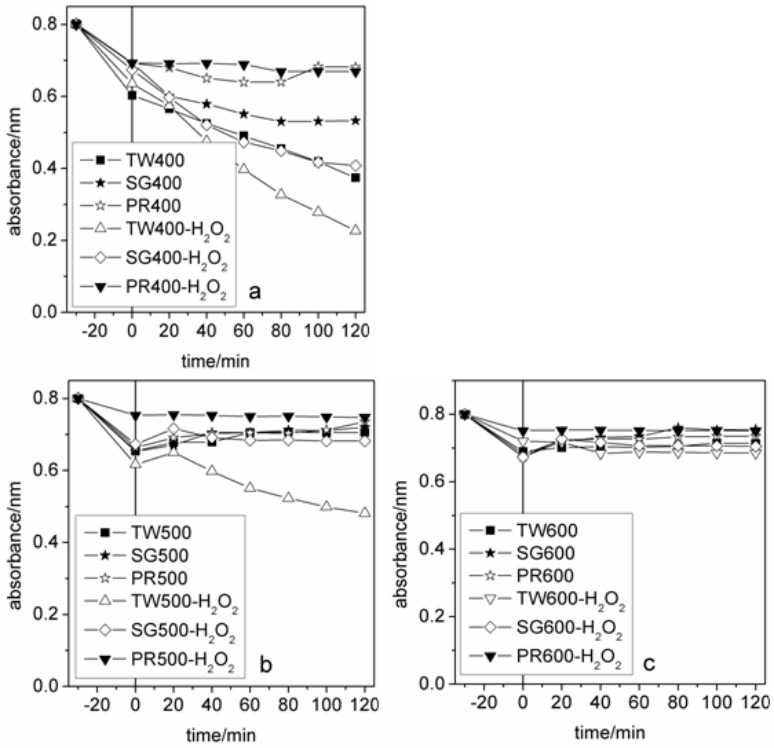

Figure 3.10. Photocatalytic activities of hematite powders annealed at different temperatures tested on the photodegradation of the dye, rhodamine B. (a), (b) and (c) are plots for 400, 500 and 600 °C respectively. TW, SG and PR represent Hem_TW, Hem_SG and Hem_PR respectively.

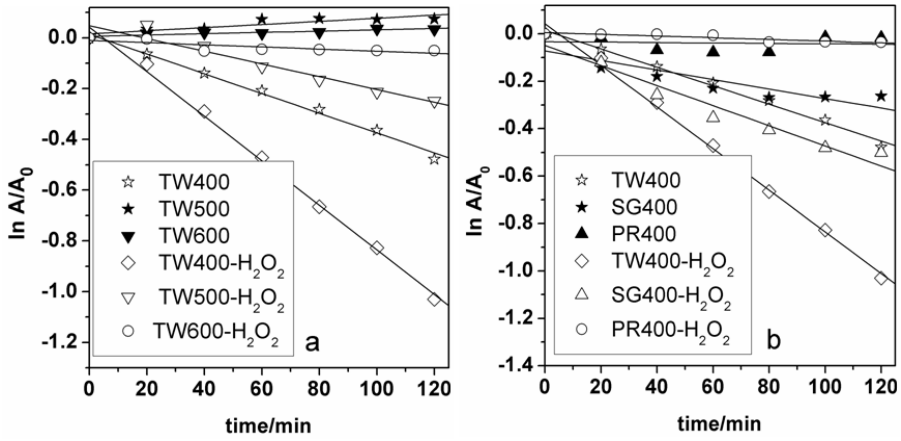

Figure 3.11. Linear plots of the pseudo-first-order photodegradation reaction. (a) is linear plots for Hem_TW powders with and without H_2O_2, (b) is linear plots for all powders calcinned at 400 °C. Again TW, SG and PR represent Hem_TW, Hem_SG and Hem_PR respectively.

3.3.7.1 Mechanism of photodegradation

A possible mechanism for the photodegradation of RhB dye is shown in Scheme 1. As shown earlier, Hem_TW400 has particles with the smallest grain sizes (often below 10 nm). This is good for reducing the speed of the (e^-, h) recombination [51-53]. Consequently, there would be enough time for h^+ to interact with H_2O in the presence of light [54] to generate $^{\bullet}OH$ (eqn. 4) and for e^- to interact with dissolved oxygen to generate a superoxide ion (eqn. 5). For the Hem_TW400-H_2O_2 system, however, more $^{\bullet}OH$ can be generated according to equation 8 at the beginning of the reaction. These radicals then react with the dye and the photocatalytic degradation proceeds faster [55, 56].

A possible reaction pathway for the generation of e^-, h^+ pair and free radicals required for the photodegradation of RhB dye by active samples is illustrated in scheme 3.1.

$$Fe(III) + h\nu \rightarrow Fe(II) + e^- + h^+ \quad (3.3)$$

$$H_2O + h^+ \rightarrow H^+ + {}^{\cdot}OH \quad (3.4)$$

$$O_2 + e^- \rightarrow {}^{\cdot}O_2^- \quad (3.5)$$

$$^{\cdot}O_2^- + H^+ \rightarrow HOO^{\bullet} \quad (3.6)$$

$$2HOO^{\cdot} \rightarrow H_2O_2 \quad (3.7)$$

$$H_2O_2 + e^- \rightarrow OH^- + {}^{\cdot}OH \quad (3.8)$$

$$Rhb + {}^{\cdot}OH \rightarrow \text{degraded product} \quad (3.9)$$

Scheme 3.1. A possible reaction scheme for the photodegradation of RhB dye by active samples.

3.4 Conclusions

Physical and magnetic properties of α-Fe_2O_3 nanoparticles depend on the method as well as the medium in which the nanoparticles are synthesized. The synthetic routes studied in this work produced a mixture of γ- and α-Fe_2O_3 nanoparticles at an annealing temperature of 400 °C. Formation of pure crystalline α-Fe_2O_3 was favoured with increasing annealing temperature (500 and 600 °C). This was also accompanied by an increase in particle size. The PXRD, VSM and Mössbauer results are all concordant on the composition of the samples at each annealing temperature. α-Fe_2O_3 nanoparticles synthesized in Tween 20 have the smallest particle size and highest BET surface area, saturation magnetization and photocatalytic activity. This implies that the synthetic medium (Tween 20, a polysorbate surfactant), can be a very good additive to the precursor solution in a Pechini type sol-gel synthesis of α-Fe_2O_3 in order to effectively impact on the properties of the synthesized powders.

Acknowledgements

IA is grateful to the College of Agriculture, Engineering and Science at the University of KwaZulu-Natal for the award of a Ph.D. bursary and a Doctoral Scholarship. The authors thank Dr VO Nyamori for his helpful suggestions to improve the manuscript. The vibrating sample magnetometer used in this work was provided by the National Research Foundation of South Africa.

References

[1] D. Walter, Thermochimica Acta 445 (2006) 195-199.
[2] S.R. Prim, M.V. Folgueras, M.A. de Lima, D. Hotza, Journal of Hazardous Materials 192 (2011) 1307-1313.
[3] C. Wu, P. Yin, X. Zhu, C. OuYang, Y. Xie, The Journal of Physical Chemistry B 110 (2006) 17806-17812.
[4] X. Gou, G. Wang, J. Park, H. Liu, J. Yang, Nanotechnology 19 (2008) 125606.
[5] S.D. Tilley, M. Cornuz, K. Sivula, M. Grätzel, Angewandte Chemie 122 (2010) 6549-6552.
[6] F. Herrera, A. Lopez, G. Mascolo, P. Albers, J. Kiwi, Applied Catalysis B: Environmental 29 (2001) 147-162.
[7] Y. Xu, G. Zhang, G. Du, Y. Sun, D. Gao, Materials Letters 92 (2013) 321-324.
[8] P. Tartaj, M.P. Morales, T. Gonzalez-Carreño, S. Veintemillas-Verdaguer, C.J. Serna, Advanced Materials 23 (2011) 5243-5249.
[9] S. Zeng, K. Tang, T. Li, Z. Liang, D. Wang, Y. Wang, W. Zhou, The Journal of Physical Chemistry C 111 (2007) 10217-10225.
[10] I. Thomann, B.A. Pinaud, Z. Chen, B.M. Clemens, T.F. Jaramillo, M.L. Brongersma, Nano Letters 11 (2011) 3440-3446.
[11] R. Ramesh, K. Ashok, G.M. Bhalero, S. Ponnusamy, C. Muthamizhchelvan, Crystal Research and Technology 45 (2010) 965-968.
[12] X. Gou, G. Wang, X. Kong, D. Wexler, J. Horvat, J. Yang, J. Park, Chemistry – A European Journal 14 (2008) 5996-6002.
[13] T.P. Almeida, M. Fay, Y. Zhu, P.D. Brown, The Journal of Physical Chemistry C 113 (2009) 18689-18698.
[14] Y. Zhu, J.C. Zhang, J. Zhai, L. Jiang, Thin Solid Films 510 (2006) 271-274.
[15] W. Zheng, Z. Li, H. Zhang, W. Wang, Y. Wang, C. Wang, Materials Research Bulletin 44 (2009) 1432-1436.
[16] X. Wen, S. Wang, Y. Ding, Z.L. Wang, S. Yang, The Journal of Physical Chemistry B 109 (2004) 215-220.
[17] R. Wang, Y. Chen, Y. Fu, H. Zhang, C. Kisielowski, The Journal of Physical Chemistry B 109 (2005) 12245-12249.
[18] S.-B. Wang, Y.-L. Min, S.-H. Yu, The Journal of Physical Chemistry C 111 (2007) 3551-3554.
[19] A.-H. Lu, E.L. Salabas, F. Schüth, Angewandte Chemie International Edition 46 (2007) 1222-1244.
[20] L. Liu, H.-Z. Kou, W. Mo, H. Liu, Y. Wang, The Journal of Physical Chemistry B 110 (2006) 15218-15223.
[21] M.R. Housaindokht, A. Nakhaei Pour, Solid State Sciences 14 (2012) 622-625.
[22] E. Darezereshki, Materials Letters 65 (2011) 642-645.
[23] N.M. Deraz, A. Alarifi, Ceramics International 38 (2012) 4049-4055.
[24] J. Jacob, M. Abdul Khadar, Journal of Magnetism and Magnetic Materials 322 (2010) 614-621.
[25] M. Žic, M. Ristić, S. Musić, Journal of Molecular Structure 834–836 (2007) 141-149.
[26] J.P. Gaviría, A. Bohé, A. Pasquevich, D.M. Pasquevich, Physica B: Condensed Matter 389 (2007) 198-201.

[27] A.T. Goulart, M.F.J. Filho, J.D. Fabris, J.M.D. Coey, Physics and Chemistry of Minerals 25 (1997) 63-69.
[28] W.R. Fischer, U. Schwertmann, Clays and Clay Minerals 23 (1975) 33-34,.
[29] H. Namduri, S. Nasrazadani, Corrosion Science 50 (2008) 2493-2497.
[30] C.J. Serna, M. Ocana, J.E. Iglesias, Journal of Physics C: Solid State Physics 20 (1987) 473.
[31] P.S.R. Prasad, K. Shiva Prasad, V. Krishna Chaitanya, E.V.S.S.K. Babu, B. Sreedhar, S. Ramana Murthy, Journal of Asian Earth Sciences 27 (2006) 503-511.
[32] K. Sing, D. Everett, R. Haul, L. Moscou, R. Pierotti, J. Rouquerol, T. Siemieniewska, Pure Appl. Chem 54 (1982) 17.
[33] S. Akbar, S.K. Hasanain, N. Azmat, M. Nadeem, Condensed matter 480 (2004) 19.
[34] T.P. Raming, A.J.A. Winnubst, C.M. van Kats, A.P. Philipse, Journal of Colloid and Interface Science 249 (2002) 346-350.
[35] Q. Liu, V. Barrón, J. Torrent, H. Qin, Y. Yu, Physics of the Earth and Planetary Interiors 183 (2010) 387-397.
[36] J. Lian, X. Duan, J. Ma, P. Peng, T. Kim, W. Zheng, ACS Nano 3 (2009) 3749-3761.
[37] Ö. Özdemir, D.J. Dunlop, Journal of Geophysical Research: Solid Earth (2014).
[38] Ö. Özdemir, D.J. Dunlop, Journal of Geophysical Research: Solid Earth 110 (2005) B09104.
[39] R. Ramesh, S. Sohila, C. Muthamizhchelvan, M. Rajalakshmi, S. Ramya, S. Ponnusamy, J Mater Sci: Mater Electron 22 (2011) 1357-1360.
[40] G. Gnanaprakash, S. Ayyappan, T. Jayakumar, J. Philip, B. Raj, Nanotechnology 17 (2006) 5851.
[41] Y. El Mendili, J.-F. Bardeau, N. Randrianantoandro, F. Grasset, J.-M. Greneche, The Journal of Physical Chemistry C 116 (2012) 23785-23792.
[42] N. Harshada, N.V. Kulkarni, S. Karmakar, B. Sahoo, I. Banerjee, P.S. Chaudhari, R. Pasricha, A.K. Das, S.V. Bhoraskar, S.K. Date, W. Keune, Materials Characterization 59 (2008) 1215-1220.
[43] E. Schmidbauer, M. Keller, Journal of Magnetism and Magnetic Materials 297 (2006) 107-117.
[44] R. Zboril, M. Mashlan, D. Petridis, Chemistry of Materials 14 (2002) 969-982.
[45] P.G. Bercoff, H.R. Bertorello, M.I. Oliva, Physica B: Condensed Matter 398 (2007) 204-207.
[46] S.J. Stewart, R.A. Borzi, E.D. Cabanillas, G. Punte, R.C. Mercader, Journal of Magnetism and Magnetic Materials 260 (2003) 447-454.
[47] S. Kamali-M, T. Ericsson, R. Wäppling, Thin Solid Films 515 (2006) 721-723.
[48] O.M. Lemine, M. Sajieddine, M. Bououdina, R. Msalam, S. Mufti, A. Alyamani, Journal of Alloys and Compounds 502 (2010) 279-282.
[49] N.H. Gangs, A. Simopoulos, A. Kostikas, N.J. Yassoglou, S. Filippakis, Clays and Clay Minerals 21 (1973) 151-160.
[50] J. Zhang, L.X. Rong, Y. Liu, B.Z. Dong, Materials Science and Engineering: A 351 (2003) 224-227.
[51] Z. Zhang, C.-C. Wang, R. Zakaria, J.Y. Ying, The Journal of Physical Chemistry B 102 (1998) 10871-10878.
[52] N. Xu, Z. Shi, Y. Fan, J. Dong, J. Shi, M.Z.C. Hu, Industrial & Engineering Chemistry Research 38 (1999) 373-379.

[53] M. Anpo, T. Shima, S. Kodama, Y. Kubokawa, The Journal of Physical Chemistry 91 (1987) 4305-4310.
[54] V.A. Khomchenko, V.V. Shvartsman, P. Borisov, W. Kleemann, D.A. Kiselev, I.K. Bdikin, J.M. Vieira, A.L. Kholkin, Acta Materialia 57 (2009) 5137-5145.
[55] B. Ohtani, Chemistry Letters 37 (2008) 216-229.
[56] G. Liu, S. Liao, D. Zhu, L. Liu, D. Cheng, H. Zhou, Materials Research Bulletin 46 (2011) 1290-1295.

Chapter 4

Synthesis, characterization and photocatalytic activities of perovskite-like $Nd_{0.5}(Bi_{0.2}X_{0.2}Mn_{0.1})\ FeO_{3-\delta}$ (X = Ca, Sr and Ba)

Ibrahim Abdulkadir, Bice S. Martincigh* and Sreekantha B. Jonnalagadda

School of Chemistry and Physics, University of KwaZulu-Natal, Westville Campus, Private Bag X54001, Durban, 4000, South Africa

*Corresponding author: Tel: +27 31 2601394; Fax: +27 31 2603091; E-mail: martinci@ukzn.ac.za

Abstract

Novel nanomaterials, with the formula $Nd_{0.5}(Bi_{0.2}X_{0.2}Mn_{0.1})FeO_{3-\delta}$ (where X = Ca, Sr and Ba), were synthesized by using a modified citric acid sol-gel approach and were fully characterised using instrumental methods of analysis. Scanning electron microscopy, high resolution transmission electron microscopy and powder X-ray diffraction analysis of the powders showed that the prepared materials contain highly crystalline perovskite-type nanoparticles. The lattice parameters, after refinements showed that the particles have either an orthorhombic or rhombohedral structure. Brunauer Emett and Teller specific surface areas ranged between 3-14 $m^2 g^{-1}$ with the Ba-substituted powders having the highest surface area. The hysteresis loop obtained by vibrating sample magnetometer analysis of the samples provided an insight into the interesting magnetic properties of the materials. Mössbauer spectroscopy analysis showed that the magnetic properties of the materials were due to canted antiferromagnetism related to the size of the alkaline earth metal substituent. The magnetic hyperfine fields of the sub-spectra were also analysed. The samples were screened for photocatalytic activity in the visible region of the solar spectrum against the depletion of the organic dye, Rhodamine B. The samples exhibited good photocataltic activity over a wide pH range of 3 to 8, and the Ca and Sr substituted materials were found to be the better photocatalyts.

Keywords: *Multiferroics; Perovskites; Mössbauer spectroscopy; magnetic properties; photocatalytic activity.*

4.1 Introduction

Perovskites are known to exhibit a wide variety of interesting properties due to their structural flexibility and the fact that they can accommodate most of the elements in the periodic table to give rise to a large variety of polar solid solutions with fascinating properties known as multiferroics [1]. The chemistry of the $A^{3+}B^{3+}O_3$ (A = rare earth and B = transition metal) perovskites imparts intriguing ferromagnetic, ferroelectric, magnetoresistant, optical, catalytic, as well as photocatalytic properties, which find use in a number of emerging fields drawing considerable attention towards the study of the properties of this family of compounds [2-6]. Perovskites are also known to stabilize higher oxidation states and substitution of some of the A^{3+} or B^{3+} sites with a transition metal M^{2+} can introduce new electronic arrangements, oxygen vacancies, and variation in bond lengths and valence of cationic species into the lattice. As a result, materials with an entirely new set of properties are born [7-9]. The introduction of M^{2+} (where M^{2+} = Ca, Sr, Ba) has been shown to drastically change the properties of perovskites by either introducing defects into the material lattice or by creating a deficiency in the oxygen content. Alteration of bond lengths due to size and charge of these ions is possible [10-12]. In this work, we substituted some of the Nd^{3+} in orthorhombic $Nd_{0.8}Bi_{0.2}FeO_3$ with $M^{2+}{}_{0.2}$ (where M = Ca, Sr, Ba) and $(Mn^{2+}/Mn^{3+}/Mn^{4+})_{0.1}$. As stated earlier Ca, Sr and Ba have been shown to introduce defects in such structures [13]. Mn, on the other hand, can act as a Jahn-Teller ion, especially in the +3 state [14]. In this communication we report the synthesis and characterization of the new materials by determining their specific surface area, and magnetic and photocatalytic properties.

4.2 Experimental

4.2.1 Materials

Nd_2O_3 (99.8%), citric acid (99.7%) (BDH Chemicals), $Fe(NO_3)_3.9H_2O$ (98%), $Bi(NO_3)_3.5H_2O$ (97%), $Sr(NO_3)_2$ (99%), $Ba(NO_3)_2.5H_2O$ (99%), $Ca(NO_3)_2$ (99%) $Mn(CH_3OO)_2$ (99 %) $K_2Cr_2O_7$ (99%), Ag_2SO_4 (99%) (Saarchem), concentrated HNO_3 (55%), ethylene glycol (99%) (Promark Reagents), concentrated H_2SO_4 (98%), $HgSO_4$, ferrous ammonium sulfate (Merck), rhodamine B (The Coleman and Bell Co., U.S.A.) and H_2O_2 30% vol. (100 vol) (Minema Chemicals) were used as received. Deionised water from a Millipore Milli-Q Elix 5 UV system was used throughout and is hereafter referred to as Milli-Q water.

4.2.2 Synthesis of $(Nd_{0.5}Bi_{0.2}X_{0.2}Mn_{0.1})FeO_{(3-\delta)}$

$(Nd_{0.5}Bi_{0.2}X_{0.2}Mn_{0.1})FeO_{(3-\delta)}$ (X = Ca, Ba and Sr) powders were prepared by a modified sol-gel process. $Fe(NO_3)_3.9H_2O$ (0.03 mol) and $Mn(CH_3OO)_2$ (0.003 mol) were dissolved in Milli-Q water (about 20 cm^3) in a beaker (A). Nd_2O_3 (0.0075 mol) and $Bi(NO_3)_3.5H_2O$ (0.006 mol) were dissolved in dilute nitric acid (about 15 cm^3, 6 mol dm^{-3}) and added to the solution in beaker (A) with continuous stirring. Then, 0.006 mol $Ca(NO_3)_2$ was dissolved in about 10 cm^3 of Milli-Q water and also added to beaker (A) to give the amount of metals required to form the perovskites. The solution was mixed thoroughly, made up to 200 cm^3 with Milli-Q water and then gradually poured into a burette. The solution was then added (drop-wise) to a citric acid solution (400 cm^3, 0.15 mol) in a separate beaker (B) which was continuously being stirred by a magnetic stirrer at room temperature. The solution was clear without any precipitate. Once the addition was completed and with the solution still being stirred, the temperature of the mixture

was raised to 90 ^{o}C and the water evaporated until the volume of the solution reduced to about 50 cm^3, ethylene glycol (100 cm^3) was added and the heating and stirring continued until a thick gel formed in beaker (B). The gel was removed from the beaker and placed in a crucible in an oven at 120 ^{o}C for 24 h to dry. The dry gel was subsequently pre-calcined at 400 ^{o}C for 4 hrs to remove all organic components. Separate portions of the precalcined powder were then annealed separately, one at 750 ^{o}C and the other at 900 ^{o}C, in a muffle furnace for 4 h each. The same procedure was repeated with $Sr(NO_3)_2$ and $Ba(NO_3)_2.5H_2O$.

4.2.3 Characterisation

Scanning electron microscopy (SEM) data were collected with a ZEISS Ultra plus field emission gun scanning electron microscope. A JEOL-JEM 2100 LAB6 high resolution transmission electron microscope (HRTEM) with a lanthanum hexaborite emission source and operated at an acceleration voltage of 200 V was used to observe the lattice fringes and examine the crystallinity of the crystals. Transmission electron microscopy (TEM) (JEOL JEM-1010) was used to analyse the morphology of the crystals. For the TEM and HRTEM analyses, each sample was dispersed in ethanol in a small centrifuge tube and sonicated before being dispersed on a carbon grid and the images collected. The crystal structure and crystallite size where determined by powder X-ray diffraction (PXRD) analysis with a Bruker D8 advance instrument with a Cu K_α radiation source (λ = 1.5406 Å). The diffractograms were fitted and analysed by using the DIFFRACT^{plus} basic evaluation package (2007). Equation 4.1 (Scherrer eauation) was used to determine the average crystallite sizes of particles.

$$D = \frac{K\lambda}{\beta\cos\theta} \qquad (4.1)$$

where K is the Scherrer constant with a value of 0.9, λ is the wavelength of radiation and β is the full width at half maximum of the most prominent peak.

Surface areas were determined by nitrogen adsorption at 77 K and the BET equation method with a Micromeritrics Tristar II 3020 fully automated three-station surface area and porosity analyzer. The attenuated total reflectance-Fourier transform infrared (ATR-FTIR) spectra of the samples were collected with a PerkinElmer FTIR Spectrum 100 ATR instrument.

The magnetic properties were determined with a LakeShore model 735 vibrating sample magnetometer (VSM) which had been calibrated with a standard Ni sphere of saturation magnetization 54.7 emu g^{-1}. The maximum applied magnetic field was 14 kOe and analyses were performed at room temperature. The distribution of the Fe species and the source of the magnetism were determined by means of Mössbauer spectroscopy measurements on samples annealed at 900 °C. The room temperature ^{57}Fe Mössbauer spectra were obtained in transmission mode with a conventional spectrometer using a 25 mCi ^{57}Co source sealed in a rhodium matrix and vibrated at constant acceleration. The spectrometer was calibrated by a natural α-iron foil. Photoluminescence (PL) spectra were obtained for all the samples with a PerkinElmer LS 55 spectrofluorimeter equipped with a high energy pulsed xenon source for excitation. Samples were excited at energies between 375 to 410 nm and the emission was monitored from 430 nm to 700 nm.

4.2.4 Photocatalytic activity

The photocatalytic activity of each sample was tested on Rhodamine B (RhB) dye in the presence of H_2O_2 at room temperature. Irradiation was performed with a 26 W

fluorescent lamp (Osram Dulux D, 26 W, 1800 lm) placed in a quartz jacket and held at about 7 cm above the RhB dye solution (which was continuously stirred with a magnetic stirrer) containing various amounts of synthesized materials and H_2O_2. A period of 30 min was allowed for equilibration in the dark before the lamp was turned on. Aliquots of the dye solution were withdrawn at regular intervals of 20 min, centrifuged and filtered through a 0.45 μm syringe filter (Millipore). The photodegradation was monitored by measuring the absorbance of the samples with a Biochrom Libra S6 UV spectrophotometer at the wavelength of maximum absorption (λ_{max}) for RhB of 556 nm. The effect of initial dye concentration, amount of photocatalytic material used and solution pH were investigated. Chemical oxygen demand (COD) measurements were also done on the dye solution after 180 min of photodegradation for each powder by using the standard procedure described in the literature [15].

4.3 Results and discussion

The sol-gel synthesis method was used to obtain dry brown powders of $(Nd_{0.5}Bi_{0.2}Ba_{0.2}Mn_{0.1})FeO_{(3-\delta)}$ (NdBa400), $(Nd_{0.5}Bi_{0.2}Sr_{0.2}Mn_{0.1})FeO_{(3-\delta)}$ (NdSr400) and $(Nd_{0.5}Bi_{0.2}Ca_{0.2}Mn_{0.1})FeO_{(3-\delta)}$ (NdCa400) after the calcinations at 400 °C to burn off the organic carbon content of the powders. Powders annealed at 750 and 900 °C are indicated by replacing 400 in the naming system above with the temperature at which the powder was annealed (e.g. NdBa750 and NdBa900 for NdBa powders annealed at 750 and 900 °C respectively). The NdBa750, NdBa900, NdSr750 and NdSr900 powders were fine and black in colour while that of NdCa750 and NdCa900 were blackish brown. The Goldschmidt tolerance factor (t) for perovskites in this case is given by:

$$t = \frac{((0.5r_{Nd}+0.2r_{Bi}+0.2r_X+0.1r_{Mn})+r_O)}{\sqrt{2}(r_{Fe}+r_O)} \quad (4.2)$$

where r represents the ionic radius of the subscripted atom (r_{Nd} = 0.983 Å, r_{Bi} = 0.96 Å, r_X = (r_{Ca} = 1.34 Å, r_{Sr} = 1.44 Å or r_{Ba} = 1.61 Å), r_{Mn} = 0.58 Å, r_{Fe} = 0.78 Å, r_O = 1.4 Å) [16]. The tolerance factor for the Ca, Sr, and Ba substituted materials are t_{Ca} = 0.7815, t_{Sr} = 0.7880 and t_{Ba} = 0.7991 respectively. The values of the tolerance factors predicts that the materials will crystallize in distorted orthorhombic lattices.

4.3.1 Morphology

SEM images of the three powders are presented in Figure 4.1. Visual inspection of the images reveals nanoparticle sizes in the range between 30-50 nm. Figure 4.1b shows the agglomeration of the NdBa900 nanoparticles into giant porous wafer-like structures. The particles are well crystallized as can be seen from the lattice fringes displayed in the HRTEM micrographs (Figure 4.2). The spherical shape of some of the crystals can be seen in Figure 4.3, which shows crystals of NdSr900 with an average crystallite size between 25-30 nm.

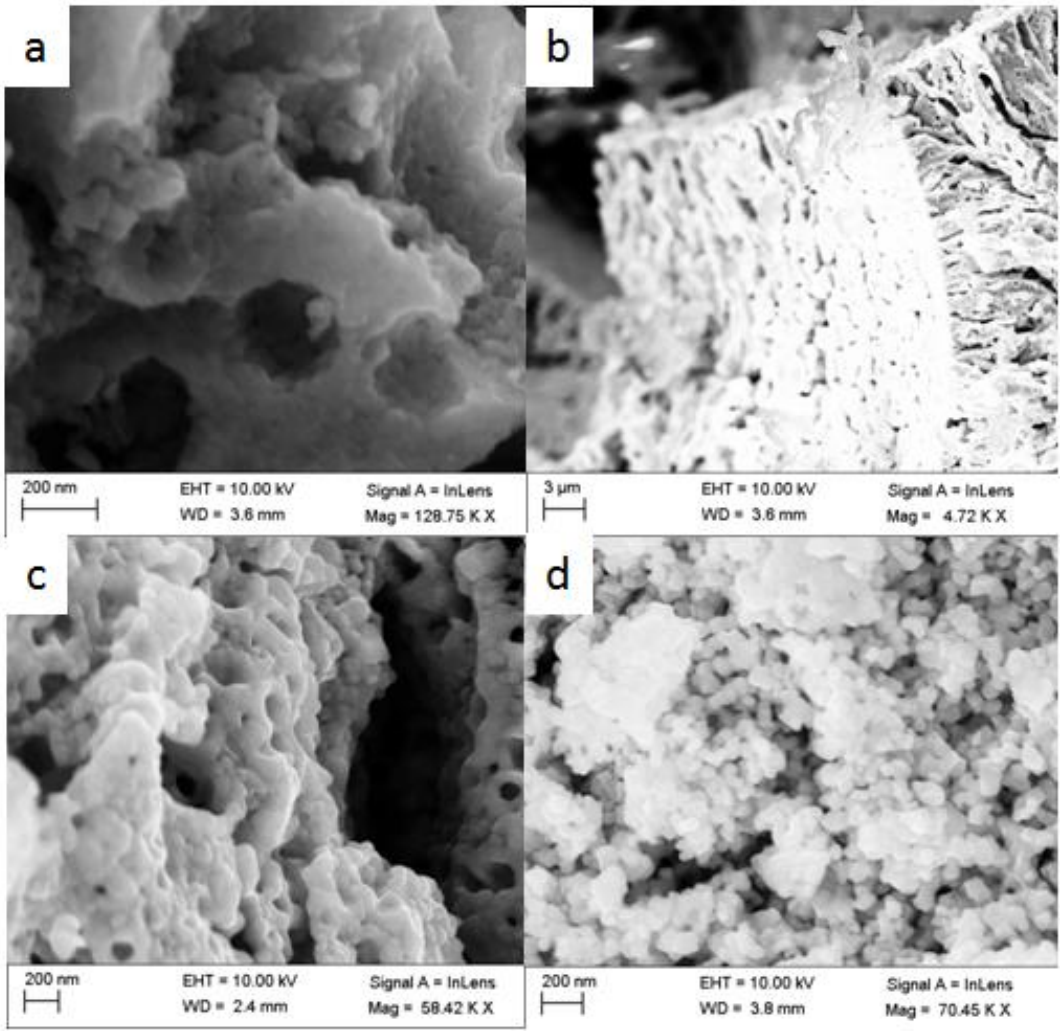

Figure 4.1: SEM images of a) and b) NdBa900, c) NdCa900 and d) NdSr900.

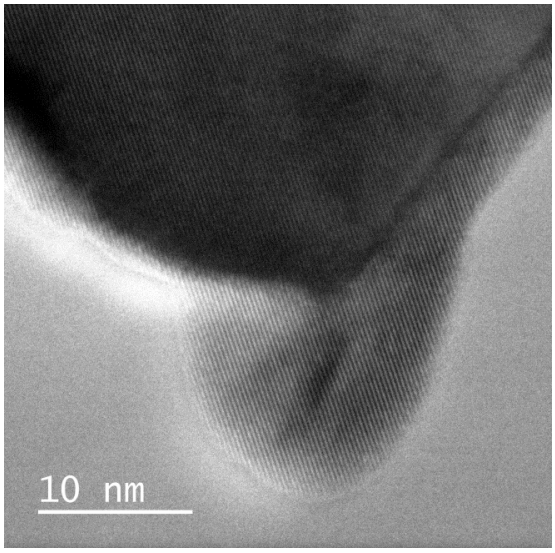

Figure 4.2: HRTEM image for NdBa900 which is representative for all the powders.

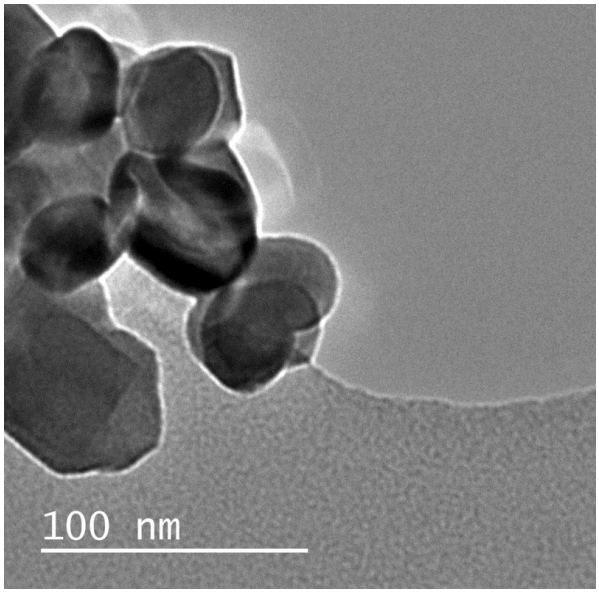

Figure 4.3: TEM micrograph for NdSr900 showing average crystallite sizes of between 25-30 nm.

4.3.2 Crystal phase characterisation

Figure 4.4 shows the PXRD patterns for the three powders. All the diffractograms show the presence of single phase perovskite-like patterns. The powders were all crystallized in an orthorhombic lattice of space group *Pnma,* which is as a result of a distortion of

the cubic arrangement in the lattices. These are in agreement with the value of the tolerance factor *t* (Table 4.1), calculated from Goldschmidt equation where values between 0.7 and 0.9 are expected for samples to crystallize in the orthorhombic lattice. The perovskite peaks begin to emerge at a calcination temperature of 400 °C but the powders are still largely amorphous or contain mixed oxides. As the annealing temperature is increased, the atoms were re-oriented into the lattice and the perovskite patterns were fully formed at an annealing temperature of 750 °C with broad peaks. The broadness of the peaks are due to the small sizes of the particles which are within the nano range. For powders annealed at 900 °C, the widths of the peaks were reduced due to the corresponding increase in crystallite sizes of the powders. The clear and distinct peaks indicate that the particles are highly crystalline. The lattice parameters obtained by refinement using the DIFFRAC^{plus} software are also shown in Table 4.1. A careful observation of the peaks (Figure 4.4) also shows that there is a general shift of the peaks towards a lower 2θ value as we move from the Ca substituted powder through to Sr to the Ba substituted sample and this can be attributed to the strain in the lattice, which is caused by the increase in atomic size of the substituent atoms [3, 6]. The Scherrer equation gives grain sizes of between 18 to 27 nm with a size increase in all sample particles at a higher annealing temperature as earlier observed from the PXRD peak widths. The estimated grain sizes obtained also conform with the observations from SEM and TEM (Table 4.1).

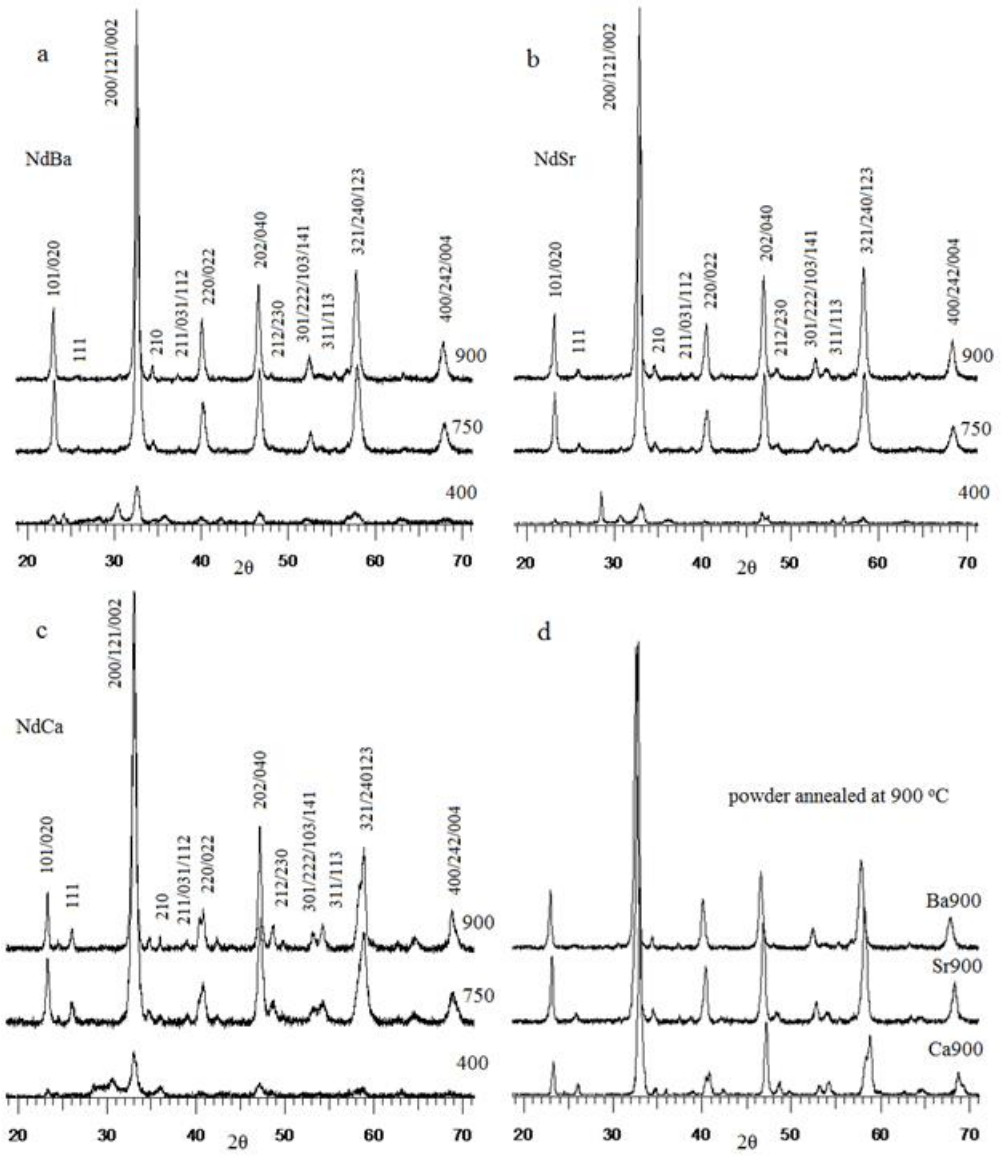

Figure 4.4: Powder X-ray diffraction peaks for (a) NdBa 400-900 °C, (b) NdSr 400-900 °C, (c) NdCa 400-900 °C and (d) for NdCa, NdSr and NdBa all annealed at 900 °C.

Table 4.1: Unit cell dimensions, alkaline-earth (AE) ionic radii and crystallite sizes (D) obtained from the Scherrer equation for the synthesized powders. *crystallite sizes calculated from Scherrer equation.

Sample	Cell parameters			System	Space group	Tolerance factor/*t*	AE Ionic radius/Å	*D/nm ± 1
	a/Å	b/Å	c/Å					
NdBa750	5.5451	7.7550	5.4748	Ortho.	Pnma	0.80	1.61	22.58
NdBa900	5.5457	7.7658	5.4858	Ortho.	Pnma	0.80	1.61	26.17
NdSr750	5.5155	7.7141	5.4440	Ortho.	Pnma	0.79	1.44	22.89
NdSr900	5.5254	7.7331	5.4617	Ortho.	Pnma	0.79	1.44	27.08
NdCa750	5.5099	7.6925	5.4206	Ortho.	Pnma	0.78	1.34	18.25
NdCa900	5.4977	7.6975	5.4238	Ortho.	Pnma	0.78	1.34	25.74

4.3.3 Surface characterisation

The FTIR-ATR spectra obtained for the powders are shown in Figure 4.5. The peaks at around 380 and 550 cm^{-1} are characteristic of the metal-oxygen stretching and oxygen-Fe-oxygen bending modes confirming the formation of the octahedradral FeO_6 of perovskites [17-19]. The increase in size of the metal-oxygen peak and a corresponding decrease in size of the peak at 1500 cm^{-1} indicates progress in the formation of the MO_6 perovskite lattice and the removal of surface –OH (Figure 4.5a-c). This is also an indication of a reduction in the surface area of the materials. The only other peaks observed are those at around 3500 to 3000 cm^{-1} and around 1460 cm^{-1} that arise due to the stretching and bending modes of water molecules and other OH^- groups adsorbed on the surface of the particles. No carbonyl peaks were observed in any of the spectra.

The spectra thus suggest that ABO_3 perovskite-like structures had been produced in all cases (Figure 4.5d-f).

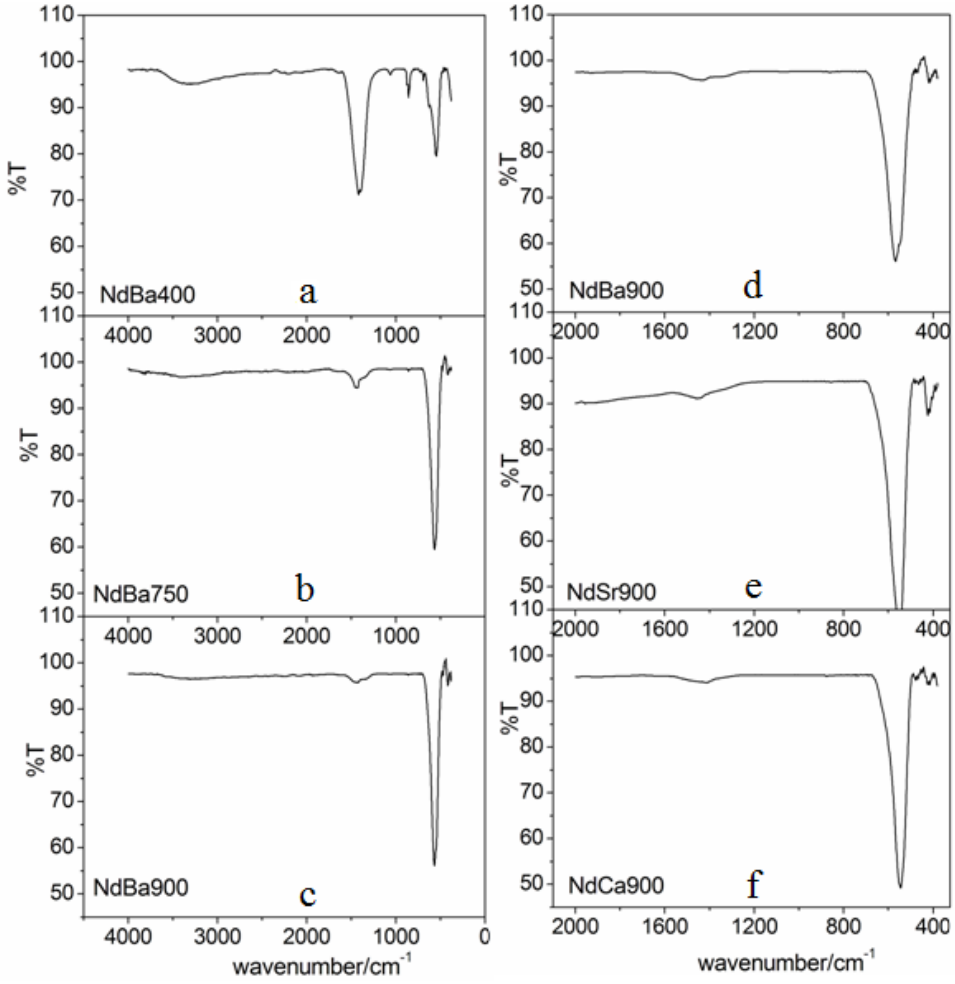

Figure 4.5: Room temperature ATR-FTIR spectra for NdBa powders annealed at different temperatures (a-c) and for NdBa, NdSr and NdCa annealed at 900 °C (d-f).

4.3.4 Surface areas and pore sizes

The BET specific surface areas (SSA) for NdCa900, NdSr900, and NdBa900 are 3.32, 4.31 and 5.28 $m^2\ g^{-1}$ respectively. Powders annealed at 750 °C have higher SSAs (i.e. NdCa750, NdSr750 and NdBa750 have SSAs of 14.09, 8.77 and 10.92 $m^2\ g^{-1}$ respectively). The N_2 adsorption-desorption isotherms at 77 K for some of these materials are shown in Figure 4.6. The isotherms conform to the type II isotherm

according to the IUPAC classification [20]. The hysteresis loops in the isotherm indicate that all the powders contain some porous particles. The pore size distribution plots for the pores show a unimodal curve for the powders annealed at 750 °C, which is spread between meso- and macroporosity. The modes reduce and tilt towards the macroporous range (Figure 4.6 insets) for both NdBa900 and NdSr900 powders and disappear in the case of NdCa900 showing a strong dependence of the pore sizes on annealing temperature, which also results in a decrease in surface area.

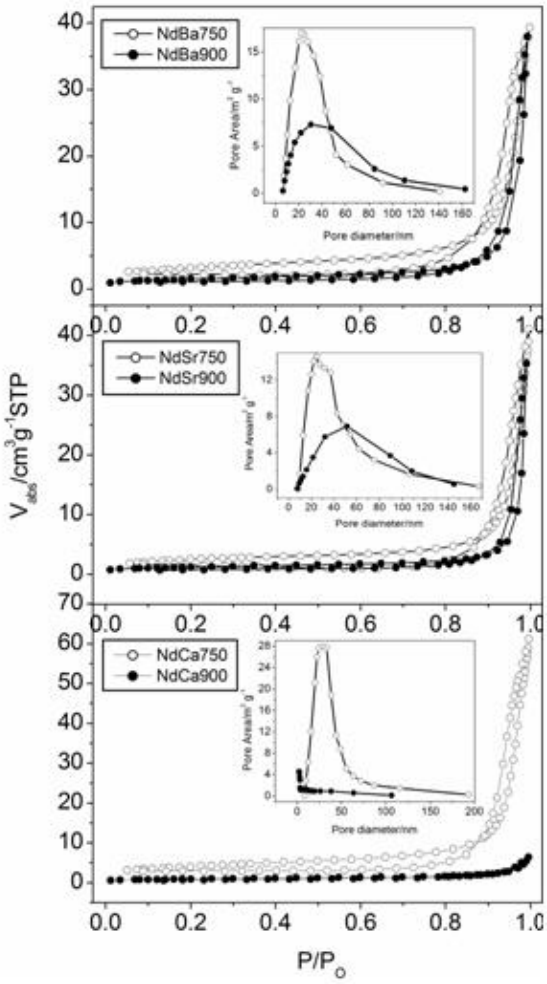

Figure 4.6 Adsorption-desorption isotherms for nitrogen at 77 K for powders annealed at 900 °C.

4.3.5 Magnetic properties

The room temperature magnetization curves for the powders are shown in Figure 4.7. The hysteresis loops for the Ba and Sr containing powders show characteristics which indicate the presence of both ferromagnetic (FM) and anti-ferromagnetic (AFM) arrangements of magnetic moments. The magnetization curves show a higher saturation magnetization for the Sr substituted powder while the Ba substituted powder shows the largest coercivity (H_C). Table 4.2 displays data obtained for each hysteresis loop. The shape of the hysteresis loops for the Ba and Sr substituted powders suggests the presence of a secondary magnetic phase as earlier stated. Note the 'constriction' on both sides of the loops, this is as a result of interaction between the soft and hard magnetic components of the powders [21]. The large coercivities are as a result of a combination of magnetic anisotropy and coupling between the FM and AFM ordering in both powders [22]. The hysteresis loops for all the powders calcined at 400 °C show properties of soft magnets with very small coercivities and high saturation magnetization (Figure 4.7a-c). However, at higher annealing temperatures, the ions are re-oriented into the larger perovskite lattice and the coercivities for the Ba and Sr substituted powders become very large with lower saturation magnetization while the saturation magnetization collapses almost completely to a paramagnetic (PM) or anti-ferromagnetic (AFM) behaviour in the Ca substituted sample [23]. An increase in the M_R/M_S value indicates an increase in the hardness of a magnetic material. The powders therefore become harder and more ferromagnetic at higher annealing temperatures due to an increase in both the values of the M_R/M_S and coercivity [24]. The hysteresis loops for both the Ba and Sr substituted materials also appear to be symmetric around $H = 0$ (zero magnetic field) with no obvious exchange bias (EB) effect. EB causes the loop to

shift along the field axis and its value is given by $[H_{C+}(T) + H_{C-}(T)]/2$ where ($H_{C+}(T)$ and $H_{C-}(T)$ are the absolute values in the positive and negative coercive fields) and is a result of the exchange coupling effect between the ferromagnetic (FM) and anti-ferromagnetic (AFM) components of a given material [25, 26]. In the next section we find that the Mössbauer spectroscopy of the powders did not reveal any paramagnetic contributions implying that the Néel temperature (T_N) for the powders might be well above room temperature. T_N normally reported for some materials with similar compositions is normally very much higher than room temperature. Temperature ranges of between 400 and 700 K have been reported for the T_N and FM and AFM materials only become paramagnetic above their T_N [27-32].

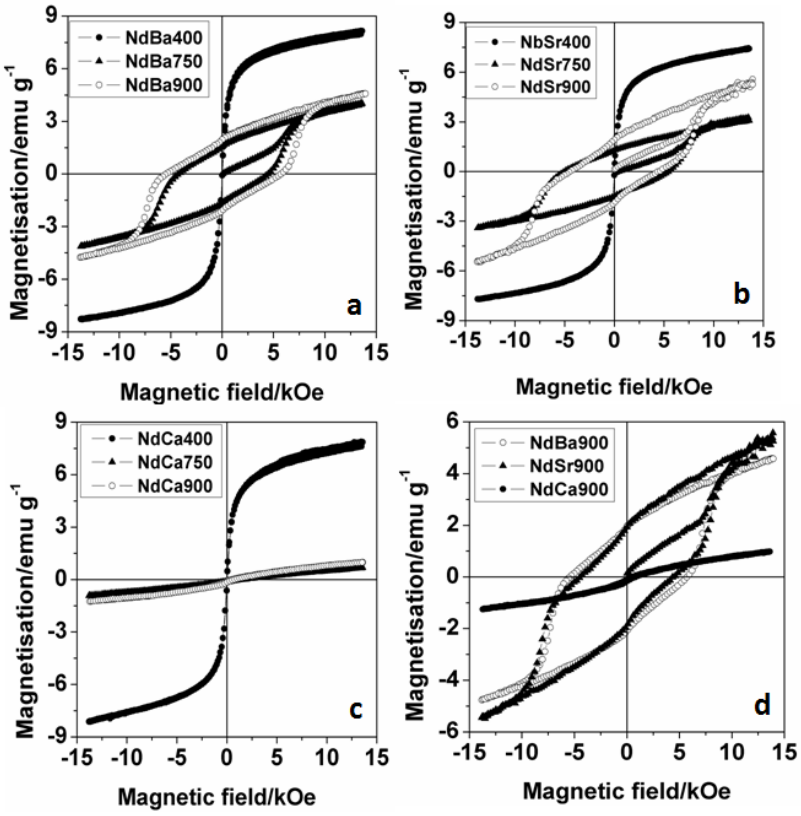

Figure 4.7: *M-H* loops for powders annealed at different temperatures. The last three digits indicate the annealing temperature. (a) NdBa, (b) NdSr, (c) NdCa, and (d) NdBa, NdSr, and NdCa annealed at 900 °C.

Table 4.2: Magnetic properties of powders annealed at different temperatures. Coercivity - H_C, saturation magnetisation - M_S, remanant magnetisation - M_R, squarness - M_R/M_S, crystallite sizes as obtained from the Scherrer equation - D

Sample	D/nm ± 1	H_C/Oe	M_S/emu g^{-1} ± 0.4	M_R/emu g^{-1} ± 0.4	M_R/M_S
NdBa750	22.58	4355.1	4.0	1.6	0.398
NdSr750	22.89	5239.1	3.2	1.3	0.415
NdCa750	18.25	174.00	0.7	0.1	0.025
NdBa900	26.17	5583.0	4.6	1.9	0.432
NdSr900	27.08	4435.5	5.6	1.9	0.344
NdCa900	25.74	164.92	1.0	0.1	0.027

4.3.6 Mössbauer spectroscopic analysis

In order to investigate the Fe ion distribution and the source of the magnetism, the room temperature Mössbauer spectra for the powders annealed at 900 °C were measured and fitted by using the Recoil software. The fitted spectra are shown in Figure 4.8. All spectra were fitted with two magnetic hyperfine sub-spectra. The Mössbauer hyperfine parameters obtained from a Lorentzian fitting of these spectra are shown in Table 4.3. Here we are only interested in the composition and valence of the Fe ions in the lattice of the materials. As stated earlier (section *4.3.5*), the Mössbauer spectrum for the NdCa900 powder represents the anti-ferromagnetic (AFM) ordering of the components below the T_N [33]. Hyperfine contributions for the two sub-spectra represent the presence of different Fe environments. The sub-spectrum ($\delta = 0.097$ *mm* s^{-1} B_{hf} = 479.5 kOe, $f = 26\%$) is unusual. The δ value corresponds to an Fe^{4+} but the B_{hf} is much higher than expected for a normal Fe^{4+} field. This, coupled with its f (low percentage) and Δ_{EQ} (= -0.45 which points to some degree of distortion) values, indicates that the

contribution could be attributed to a high spin (*HS*) Fe^{4+} on an oxygen deficient component, perhaps a $CaFeO_{3-\delta}$ with a high T_N value. Despite the presence of the Fe^{4+}, magnetic measurements on the sample show it to be antiferromagnetic. The two hyperfine sub-spectra for NdSr900 fit an Fe^{3+} ions contribution with one of the sub-spectra also showing heavy distortion ($\Delta_{EQ} = 0.436$) in its lattice. These Δ_{EQ} values also indicate the presence of distortion in the Fe^{3+} environment for this sub-spectrum. The two NdBa900 contributions have been attributed to HS Fe^{3+} in different electronic environments. The introduction of M^{2+} is supposed to force a valency change from Fe^{3+} to Fe^{4+} which would result in the formation of a magnetic superstructure Fe^{4+}-O-Fe^{3+}. The predominance of Fe^{3+} in NdSr900 and NdBa900, however, points to an oxygen vacancy in the crystals [7]. This also implies that the source of the magnetism in both materials is the canted antiferromagnetism due to the size difference of the substituent [34]. This can also be seen in the difference in M_R values of the material (Table 4.1). This is further supported by the fact that no paramagnetic features were detected in the spectra which indicates that all the components are below their T_N at room temperature. Components like $SrFeO_3$ with $T_N = 138$ K would be paramagnetic at room temperature, while oxygen deficient $SrFeO_{2.5}$ (T_N = 700 K) would not be [35-37].

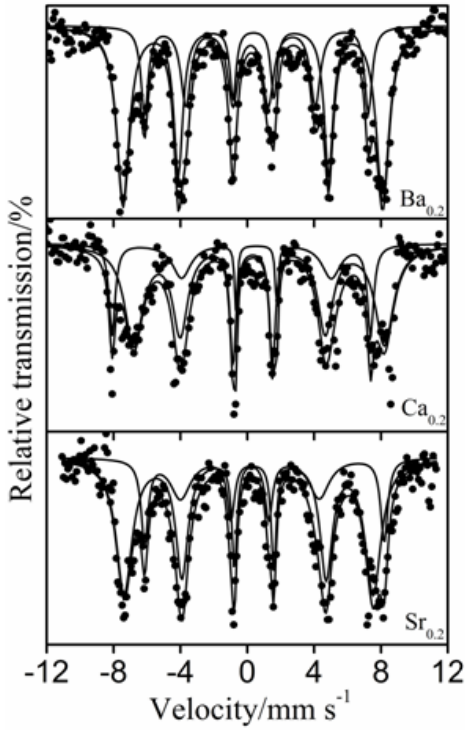

Figure 4.8: Mössbauer spectra of powders. $Ba_{0.2}$ = NdBa900, $Ca_{0.2}$ = NdCa900 and $Sr_{0.2}$ = NdSr900.

Table 4.3: Parameters obtained from the Lorentzian fitting of the Mössbauer spectra of the powders. Isomer shift is $\delta/mm\ s^{-1}$, electronic splitting is $\Delta_{EQ}/mm\ s^{-1}$, hyperfine field is B_{hf}, linewidth is $\tau/mm\ s^{-1}$ and site population is *f*.

Sample	$\delta/mm\ s^{-1}$	$\Delta_{EQ}/mm\ s^{-1}$	B_{hf}/kOe	$\tau/mm\ s^{-1}$	*F*	*Valence*
NdCa900	0.097	-0.451	479.5	0.098	26.0	Fe^{4+}
	0.519	0.189	465.0	0.210	74.0	Fe^{3+}
NdSr900	0.245	-0.163	462.0	0.180	69.0	Fe^{3+}
	0.591	0.436	444.4	0.270	31.0	Fe^{3+}
NdBa900	0.375	0.175	415.0	0.390	35.9	Fe^{3+}
	0.354	-0.018	481.0	0.220	64.1	Fe^{3+}

4.3.7 Photoluminescence measurements

The photoluminescence (PL) emission spectra for the NdSr samples annealed at 750 and 900 °C monitored at room temperature are shown in Figure 4.9. PL emission spectra

occur as a result of the recombination of the e^-/h^+ pair when the electron loses the energy it gained for excitation to occur. The samples show a series of emission spectra corresponding to a series of excitation wavelengths between 370 and 410 nm. The emission peaks (monitored between 570-603 nm) move to lower energies correspondingly as the excitation wavelength is moved to a lower excitation energy line similar to what has been previously reported [38, 39]. The emission peak intensity increases relative to its excitation energy and reaches a maximum at 395 nm excitation energy and then begins to drop with subsequent increase in excitation wavelength (Figure 4.9). PL has been shown to occur in crystalline perovskites at room temperature due to the so-called intrinsic luminescence. This could either arise due to the presence of defects in the lattice (interstitial atoms, dislocation or vacancies), or the presence of an oxygen vacancy (due to variation in bond length due to ionic size/charge difference), or due to the presence multiple trap states created by the interactions of the various energy states of the atoms between their valence band (VB) and their conduction band (CB). The excitation energies fall within the visible region and so the powders can utilize visible light to bring about photocatalytic degradation of organic materials.

The reduction of the intensity of the emission peaks for NdSr900 indicates that the time used for recombination has increased and this is good for photocatalysis [40]. Similar PL results were obtained for all the powders. Table 4.4 shows the excitation energies and the corresponding emission energies which resulted in PL in these samples.

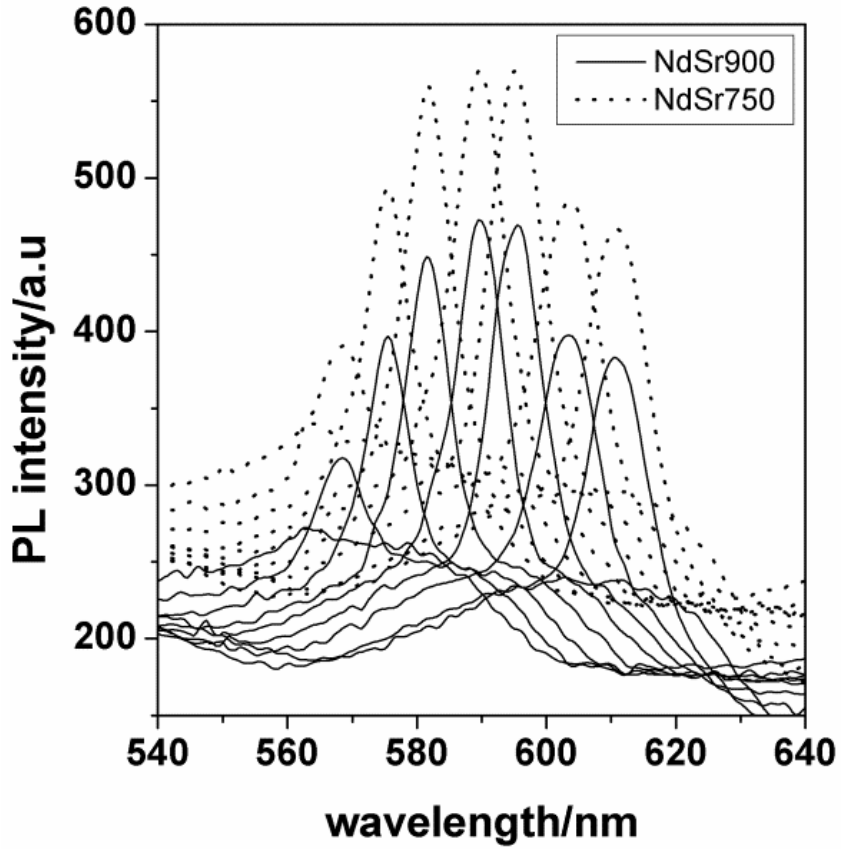

Figure 4.9: Photoluminescence spectra for NdSr750 and NdSr900.

Table 4.4: Shift in excitation energies E_{ex} with a corresponding shift in emission energies E_{em} for the powders calcined at 750 and 900 °C.

E_{ex}/eV	3.31	3.26	3.22	3.18	3.14	3.10	3.06
E_{em}/eV	2.18	2.16	2.13	2.11	2.08	2.06	2.03

4.3.8. Photocatalytic screening

The results of the photocatalytic screening of the synthesized materials annealed at different temperatures on rhodamine B (RhB) in the presence of H_2O_2 is shown in Figure 4.10. The photocatalytic activity of the materials can be seen to increase with increase in the annealing temperature. Samples calcined at 400 and 750 °C basically

showed no or little activity for photocatalysed decolourisation of the dye. However, the powders annealed at 900 °C exhibited enhanced activity for all the sets of powders.

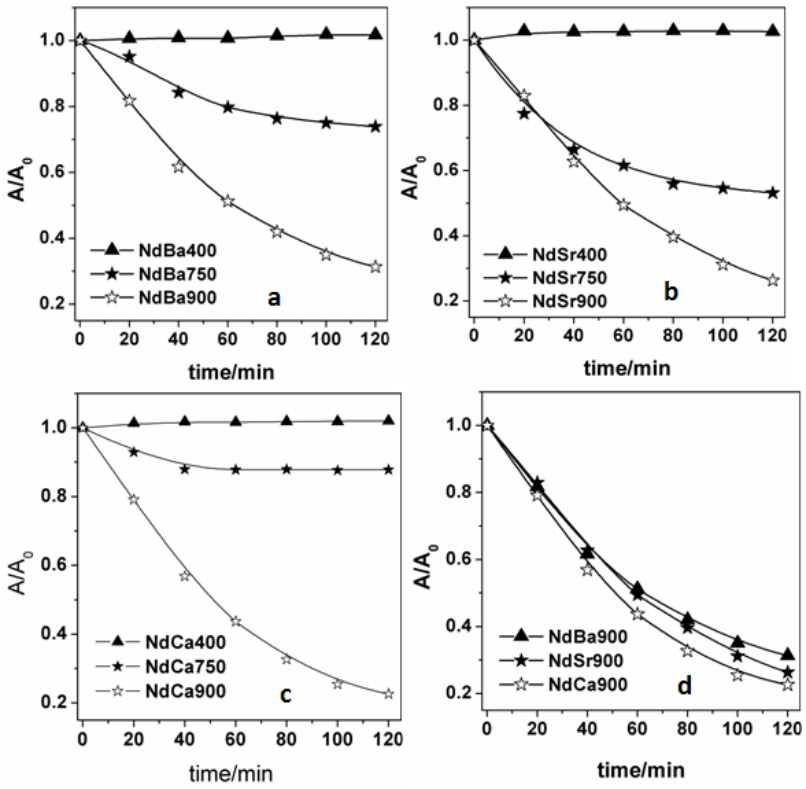

Figure 4.10: Photodegradation of RhB when irradiated with visible light in the presence of H_2O_2 (3×10^{-5} mol dm^{-3} and 1.5 g dm^{-3} of catalyst). (a) NdCa400, 750 and 900, (b) NdSr400, 750 and 900, (c) NdBa400, 750 and 900, and (d) NdBa900, NdSr900 and NdCa900.

Across the series, however, the activity is observed to decrease as the atomic number of the alkaline-earth group metal increases (i.e. with increase in the radius of the alkaline-earth metal) (Figure 4.10d). The activity also depends on the amount of photocatalyst used in the reaction. Results show an increase in activity with increase in the initial amount of catalyst material and reaching an optimum mass of 1.5 g dm^{-1}. The photocatalytic degradation of RhB dye on these powders can be described by a pseudo-first-order kinetic equation which is given by.

$$ln\frac{C}{C_0} = k_{obs}t, \quad (4.3)$$

where C_0 and C are the initial concentration and concentration of the dye at time t, and k_{obs} is the observed rate constant.

The reactions all followed pseudo-first-order kinetics as can be seen from the plots of log A/A_0 versus time (Figure 4.11). In the absence of a catalyst, the rate of degradation of the dye was almost zero even in the presence of H_2O_2, implying that the photocatalyst was essential for the degradation reaction. A fast reaction was observed with H_2O_2 in presence of NdCa900 (Table 4.5), with a rate constant of 0.013 min^{-1}, followed closely by NdSr900/H_2O_2 with a rate constant of 0.0114 min^{-1}.

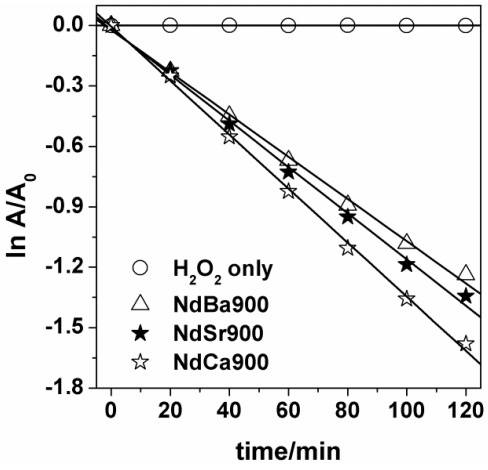

Figure 4.11: Effect of materials annealed at 900 °C on the photodegradation of RhB from which it can be observed that the NdCa900 (1.5g dm^{-3})/H_2O_2 (3×10^{-5} mol dm^{-3}) system has the highest rate constant while peroxides alone did not degrade the dye.

Table 4.5: Rate constants for the photocatalyst (1.5 g dm^{-3})/H_2O_2 (3×10^{-5} mol dm^{-3}) systems at the natural pH of the dye.

Photocatalyst/H_2O_2	k_{obs}/min^{-1}
H_2O_2 only	3.7×10^{-5}
NdBa900/H_2O_2	0.0099
NdSr900/H_2O_2	0.0115
NdCa900/H_2O_2	0.0130

4.3.8.1 Effect of amount of photocatalyst

The effect of the amount of photocatalyst on RhB photodegradation was also studied at its natural pH. The amount of powder loaded was varied between 0.5 g and 2.0 g dm^{-3} of RhB solution. Figure 4.12a shows the photodegradation profile of the dye with varied amounts of added catalyst. The rate of dye depletion (Figure 4.12b) increased with the amount of catalyst reaching a maximum value at 1.5 g L^{-1} and a further increase to 2 g L^{-1} lowered the rate of decolourisation. This decrease could be attributed to light scattering or a screening effect caused by the powder particles from photodegradation sites as the particles prevent light from penetrating the dye solution. It could also be due to agglomeration of powder particles on the surface of the solution which would not only prevent light from reaching the active sites, but it would also reduce the surface area available for adsorption [41]. Figure 4.13 shows a plot of the rate constants against amount of powders loaded, and maximum rates were attained at 1.5 g L^{-1} loading. The percent efficiency (E%) of the photocatalysed degradation of Rhb as given by

$$E(\%) = \frac{A_0 - A}{A_0} \times 100 \qquad 4.4$$

(where A_0 is the initial absorbance, and A is the absorbance at a time t (of 2 hours in these experiments) was calculated and the values are presented in Table 4.6.

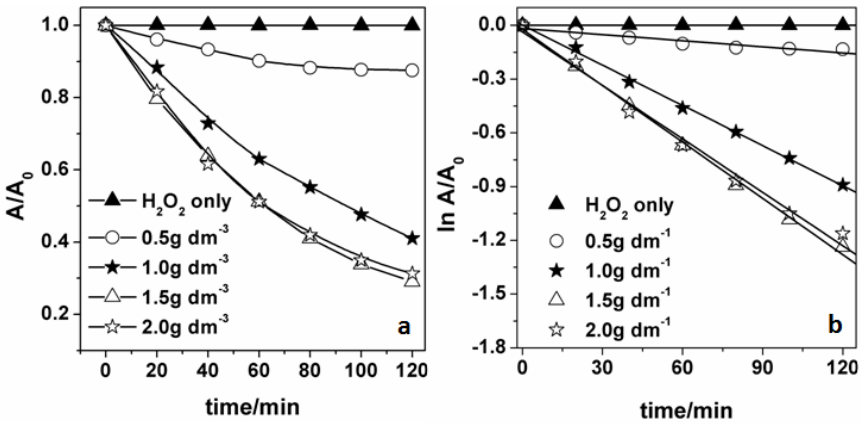

Figure 4.12: a) Degradation profile for RhB dye in the presence of varying amounts of catalyst NdBa900 and a constant peroxide concentration ($3x10^{-5}$ mol dm^{-3}). b) Pseudo-first-order rates for the degradation of RhB by NdBa900. Similar trends were obtained for NdCa900 and NdSr900.

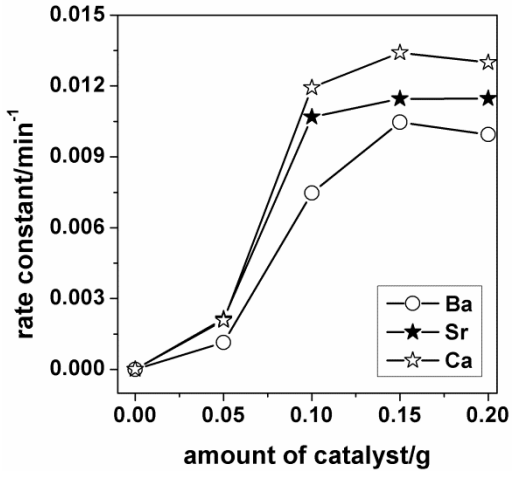

Figure 4.13: Rates of photodegradation of RhB increased with the mass of catalyst added, maximum rates are observed at 1.5 g L^{-1} for all powders (Ca, Ba and Sr = NdCa900, NdBa900 and NdSr900 respectively).

Table 4.6: Efficiency of the photocatalytic degradation of RhB at constant pH and H_2O_2 concentration (3×10^{-5} mol dm^{-3}).

Amount of powder/g dm^{-1}	Efficiency/%		
	NdCa900	NdSr900	NdBa900
0.00	0.00	0.00	0.00
0.5	22.20	22.08	12.44
1.0	74.87	70.97	66.47
1.5	79.41	73.94	70.96
2.0	77.39	73.68	68.71

4.3.8.2 Effect of pH

The pH of the solution is an important parameter and it plays a significant role in varying the properties and activity of the photocatalyst surface. The pH of the solution determines the surface charge of the powder particles and also the charge of the dye and its ability to adsorb to the catalyst surface. UV-absorbance measurements for RhB monitored at a pH range between 3 and 8 indicated that RhB is stable and does not degrade upon illumination in the absence of H_2O_2 and photocatalyst. The presence of every catalyst, however, showed photocatalysed degradation and an increase in the rate of decolourisation of the dye with decrease in pH (Figure 4.14a), which suggests that the catalyst materials are active over a wide range of pH and acidic pH better facilitates the degradation of the dye.

The rate of decolourisation of the dye by NdSr900 and NdCa900 varied to some extent. While NdSr900 showed a higher rate at higher pH conditions, NdCa900 displayed better activity at pH 3 (Table 4.7).

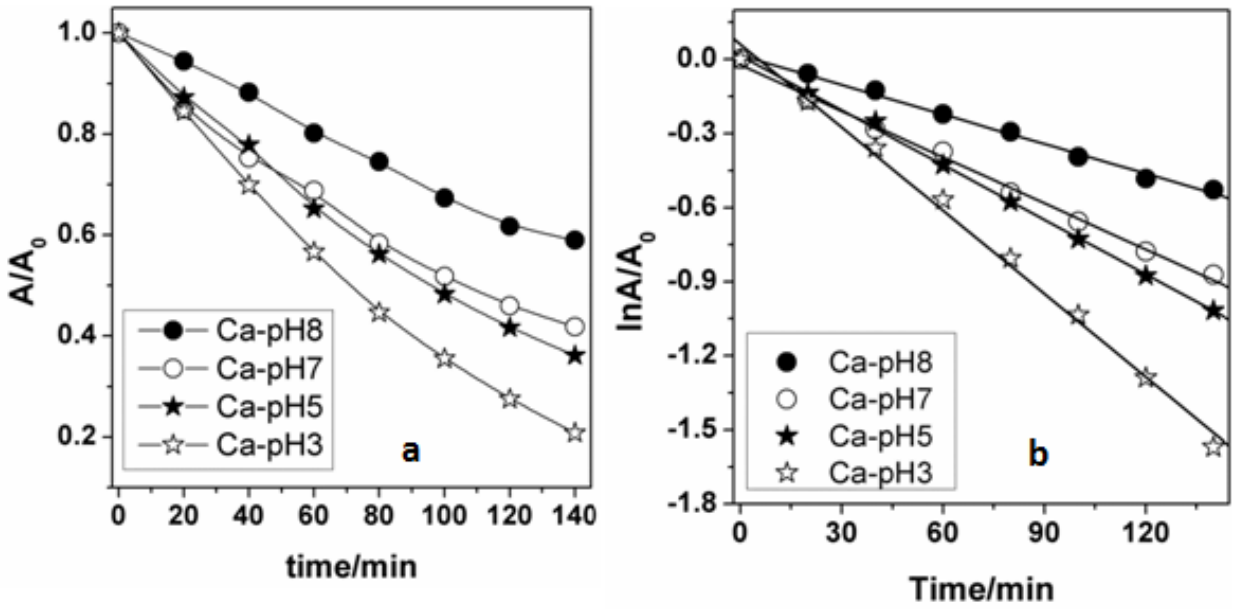

Figure 4.14: Rate of decolourisation of RhB with change in pH for the NdCa900 photocatalyst: (a) normalized absorbance versus time plots and (b) pseudo-first-order plots for the same reactions. (Mass of catalyst = 1.5 g dm^{-3} and $[H_2O_2]$ = 3 × 10^{-5} mol dm^{-3}).

Table 4.7: Variation of rate of RhB decolourisation with change in pH for different photocatalyst (conditions: amount of catalyst (1.5 g dm^{-3}) and peroxide added (3 × 10^{-5} mol dm^{-3}) remain constant).

Solution pH	Pseudo first-order constant /min		
	NdCa900	NdSr900	NdBa900
8.0	0.00399	0.00644	0.00162
7.0	0.00622	0.00651	0.00645
5.0	0.00738	0.00796	0.00697
3.0	0.01122	0.00915	0.00888

4.3.8.3 Effect of peroxide concentration

Decolourisation of RhB dye in this process is initiated by the generation of hydroxyl radicals ($^{\bullet}OH$) via H_2O_2 splitting by the photocatalyst powder as neither the photocatalyst nor the peroxide alone was able to degrade the dye. The effect of H_2O_2 concentration on the decolourisation process at the natural pH of the dye shows a steady

increase in rate with increase in H_2O_2 concentration for all the powders, as expected, reaching a maximum at 3×10^{-5} mol dm^{-3} of H_2O_2 (Figure 4.15). A further increase in the amount of H_2O_2, however, does not lead to a further increase in rates but rather a stagnation or reduction of rates is observed. An explanation for this could be that at lower concentration of H_2O_2, $^{\bullet}OH$ are produced which aid to increase the rate of decolourisation of the dye until the optimum concentration is reached (3×10^{-5} mol dm^{-3}). When the concentration of H_2O_2 is increased beyond this optimum concentration, the $^{\bullet}OH$ radicals produced either recombine to form H_2O_2 or probably become scavengers of valence bond holes rather than facilitating the decolourisation process of the dye, and hence the rates are either stagnated or reduced. The trend was the same for all the catalyst materials used (Table 4.8).

Table 4.8: Effect of H_2O_2 concentration on the rate of decolourisation of RhB at its natural pH and in the presence of 1.5 g dm^{-3} of photocatalyst.

$[H_2O_2]$/mol dm^{-3}	Pseudo first-order rate constant/min		
	NdCa900	NdSr900	NdBa900
$1x10^{-5}$	0.00792	0.00289	0.00188
$2x10^{-5}$	0.01019	0.00493	0.00540
$3x10^{-5}$	0.01300	0.01147	0.00718
$3.5x10^{-5}$	0.01160	0.01006	0.00667

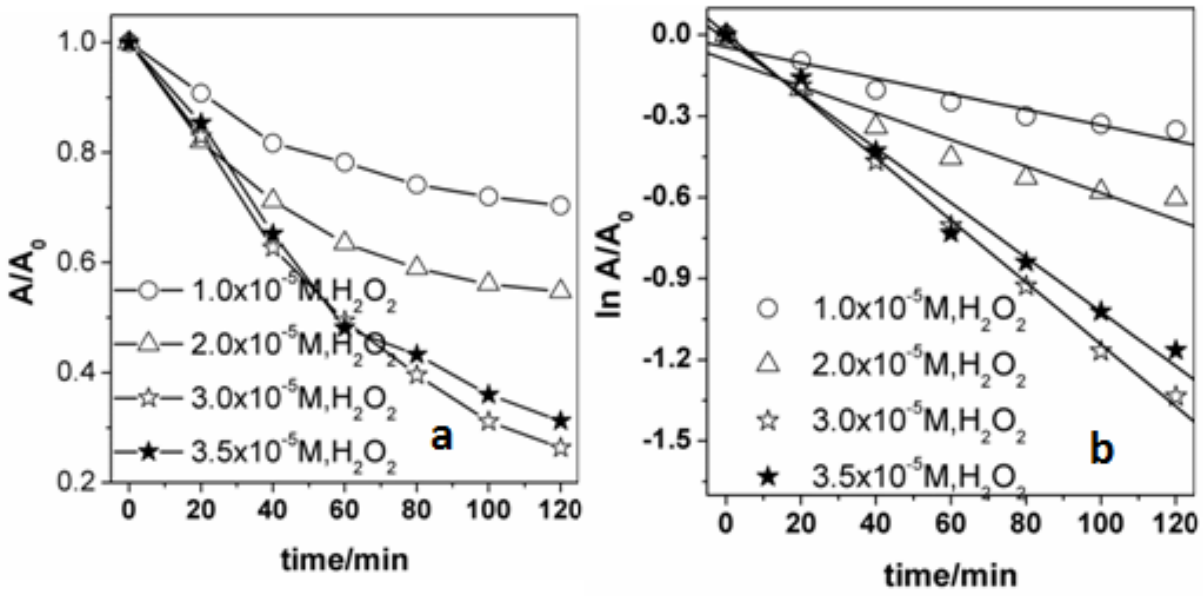

Figure 4.15: (a) The Effect of H_2O_2 concentration on the rate of photodegradation of RhB dye solution in the presence of NdSr900 (1.5 g dm^{-3}) and at the natural pH of of RhB. (b) The pseudo-first-order plots for the same reactions.

4.3.8.4 Effect of dye concentration

To study the effect of initial dye concentration on the photodegradation rates the amount of catalyst and H_2O_2 were kept constant (1.5 g and 3×10^{-5} mol dm^{-3} respectively) while the amount of dye was varied between 1.5 to 5 mg dm^{-3}. A representative normalized and natural log plot of the absorbance versus time for photodegradation is shown in Figure 4.16. Although the value for the rates of the photodegradation are close, there appears to be a marginal decrease in pseudo-first-order rate constant with a decrease in the initial dye concentration. An explanation for this could be that the degradation of the dye depends on the presence of $^{\bullet}OH$ radicals and the rate of generation of the hydroxyl radical could to some extent be impacted by the initial concentration of the dye [42]. Similar trends were observed with the other catalyst materials.

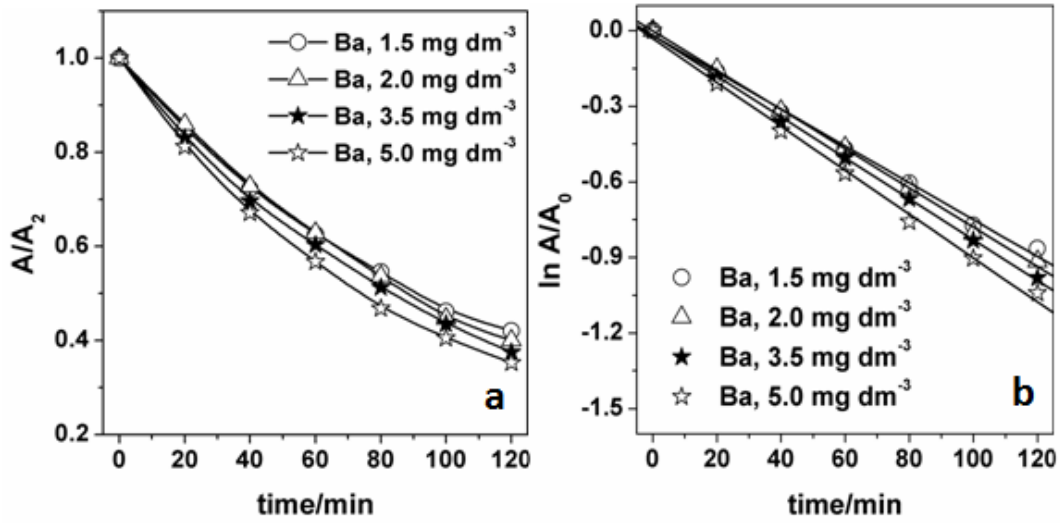

Figure 4.16: Effect of initial concentration of dye on reaction rate at the natural pH of dye for the catalyst Ba = NdBa900.

4.3.8.5 Chemical Oxygen Demand (COD)

The results of the COD analysis of the degraded dye solution after three hours of photodegradation activity is presented in Figure 4.17. The result shows that mineralization is least in the dye solution that has been photodegraded with NdBa900; the solution has the highest COD value, implying that the dye may have been broken down into smaller units of colourless organic compounds but not much mineralization has occurred. NdCa900, however, has the lowest COD value, which implies that the degree of mineralization is highest in this case and, therefore, NdCa900 is the most efficient in mineralization of the dye. The photodegradation of the dye can be represented generally by

$$\mathrm{RhB} + \mathrm{H_2O_2} + \mathrm{h\nu} + \mathrm{PC} \rightarrow \text{organic intermediates} + \mathrm{CO_2} + \mathrm{H_2} \qquad (5).$$

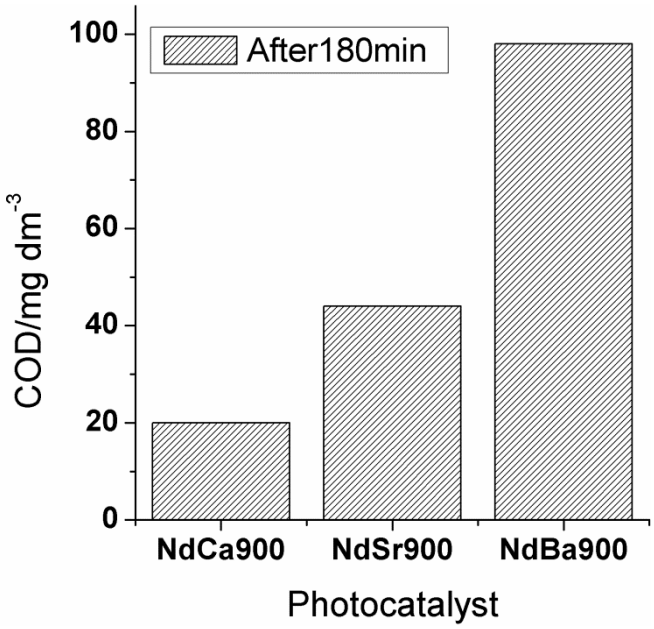

Figure 4.17: COD (mg dm^{-3}) values for the photocatalysts after degrading the RhB dye for three hours.

4.3.8.6 Mechanism

The following reactions could be responsible for the generation of the active $^{\bullet}OH$ radicals required to initiate the degradation process of the RhB dye in these photocatalytic systems. The first is the photogeneration of an electron-hole pair in the photocatalysts. The generated electrons in the conduction band of the catalyst can then be trapped in the H_2O_2 to cause the production of the radicals according to the following mechanism where hc is energy of light:

$$PC + h\nu \rightarrow e^- + h^+ \quad (4.6)$$

$$H_2O_2 + e^- \rightarrow {}^{\cdot}OH + OH^- \quad (4.7)$$

The h^+ can also react with water to generate more radicals as follows:

$$H_2O + h^+ \rightarrow H^+ + {}^{\cdot}OH \quad (4.8)$$

The hydroxyl radicals can also be produced via a photo-Fenton or a Fenton-like mechanism involving the Fe^{3+} ions in the B-site and H_2O_2 according to the following reactions:

$$H_2O_2 + Fe^{3+} \rightarrow Fe - OOH^{2+} + H^+ \quad (4.9)$$

$$Fe - OOH^{2+} \rightarrow Fe^{2+} + HO_2^{\bullet} \quad (4.10)$$

$$H_2O_2 + Fe^{2+} \rightarrow Fe^{3+} + 2HO^{\bullet} \quad (4.11)$$

A direct $h\nu/H_2O_2$ interaction to produce hydroxyl radicals have been ruled out since the dye did not degrade under this condition.

4.4 Conclusions

Novel $Nd_{0.5}(Bi_{0.2}X_{0.2}Mn_{0.1})FeO_{3-\delta}$ perovskite-type powders (where X = Ca, Sr and Ba) were successfully synthesized by using a simple sol-gel method and annealed at both 750 and 900 ^oC. The materials were characterized by means of BET, XRD, HRTEM, SEM, VSM, Mössbauer spectroscopy and PL spectroscopy. The powders were crystalline and crystallinity increased with increase in annealing temperature. PXRD refinement shows that powders annealed at 900 °C all crystallized in a single phase perovskite-like orthorhombic lattice in agreement with the tolerance factor values calculated from the Goldschmidt equation. The different Fe environments and the high coercive field values deduced from the Mössbauer spectroscopy and VSM respectively, however, show that the powders may contain a secondary magnetic phase. The room temperature magnetization analysis showed significant maximum magnetization with a large coercive field for NdSr900 and NdBa900. This high coercive field make these materials candidates for application in memory devices. The PL spectra show a series

of emission peaks arising from the so-called intrinsic luminescence which shifts correspondingly as the excitation energy is varied. The photocatalytic activities of the powders in the presence of H_2O_2 show that the powders function as good photocatalysts for the degradation of dyes in the visible light range over a wide range of pH conditions. The Ca and Sr substituted powders exhibited very good catalytic activity towards photodegradation and mineralisation of the model dye, rhodamine B. The improved magnetic properties of the materials will allow for easy catalyst recovery from dye solutions.

Acknowledgements

IA is grateful to the College of Agriculture, Engineering and Science at the University of KwaZulu-Natal for the award of a Ph.D. bursary and a Doctoral Scholarship. The Vibrating Sample Magnetometer used in this work was provided by the National Research Foundation of South Africa.

References

[1] M. Johnsson, P. Lemmens, Handbook of Magnetism and Advanced Magnetic Materials (2007) 1-11.
[2] Y. Zhang, A. Zheng, X. Yang, H. He, Y. Fan, C. Yao, CrystEngComm 14 (2012) 8432-8439.
[3] S. Rousseau, S. Loridant, P. Delichere, A. Boreave, J.P. Deloume, P. Vernoux, Applied Catalysis B: Environmental 88 (2009) 438-447.
[4] C.-C. Hu, Y.-L. Lee, H. Teng, Journal of Materials Chemistry 21 (2011) 3824-3830.
[5] I. Grinberg, D.V. West, M. Torres, G. Gou, D.M. Stein, L. Wu, G. Chen, E.M. Gallo, A.R. Akbashev, P.K. Davies, J.E. Spanier, A.M. Rappe, Nature 503 (2013) 509-512.
[6] B.P. Barbero, J.A. Gamboa, L.E. Cadús, Applied Catalysis B: Environmental 65 (2006) 21-30.
[7] V.I. Torgashev, A.A. Volkov, A.A. Bush, E.S. Zhukova, S.N. Migunov, A.N. Lobanov, B.P. Gorshunov, Phys. Solid State 49 (2007) 1652-1657.
[8] J. Li, Y. Duan, H. He, D. Song, Journal of Alloys and Compounds 315 (2001) 259-264.
[9] T.C. Gibb, Journal of Materials Chemistry 1 (1991) 23-28.
[10] L. Li, Q. Wei, X. Ren, W. Su, Physica B: Condensed Matter 205 (1995) 81-86.
[11] Y.-H. Lee, J.-M. Wu, Y.-C. Chen, Y.-H. Lu, H.-N. Lin, Electrochemical and Solid-State Letters 8 (2005) F43-F46.
[12] N. Kallel, S.B. Abdelkhalek, S. Kallel, O. Peña, M. Oumezzine, Journal of Alloys and Compounds 501 (2010) 30-36.
[13] V. Mathe, K. Patankar, R. Patil, C. Lokhande, Journal of Magnetism and Magnetic Materials 270 (2004) 380-388.
[14] M.W. Lufaso, P.M. Woodward, Acta Crystallographica Section B: Structural Science 60 (2004) 10-20.
[15] I. Williams, Environmental Chemistry: A Modular Approach, Wiley (2001),pp. 276-280.
[16] R.t. Shannon, Acta Crystallographica Section A: Crystal Physics, Diffraction, Theoretical and General Crystallography 32 (1976) 751-767.
[17] I. Parkin, A. Komarov, Q. Fang, Polyhedron 15 (1996) 3117-3121.
[18] P. Junploy, S. Thongtem, T. Thongtem, Superlattices and Microstructures 57 (2013) 1-10.
[19] J. Jiang, J. Zou, M.N. Anjum, J. Yan, L. Huang, Y. Zhang, J. Chen, Solid State Sciences 13 (2011) 1779-1785.
[20] K. Sing, D. Everett, R. Haul, L. Moscou, R. Pierotti, J. Rouquerol, T. Siemieniewska, Pure and Applied Chemistry 54 (1982) 603-619.
[21] Z. Shan, J. Liu, V.M. Chakka, H. Zeng, J. Jiang, Magnetics, IEEE Transactions on 38 (2002) 2907-2909.
[22] S. Chatterjee, S. Giri, S. De, S. Majumdar, Ferromagnetic/antiferromagnetic exchange coupling in Ni_2MnSn-derived magnetic shape memory alloys, Journal of Physics: Conference Series, IOP Publishing, 2010, pp. 032011-032014.
[23] C. Paduani, J.A. Valcanover, J.D. Ardisson, C.A. Samudio Pérez, M.I. Yoshida, Brazilian Journal of Physics 37 (2007) 1111-1114.

[24] T.P. Raming, A.J.A. Winnubst, C.M. van Kats, A.P. Philipse, Journal of Colloid and Interface Science 249 (2002) 346-350.
[25] S. Madeswaran, S. Tamano, S. Goto, K. Tokiwa, A study on the magnetic behavior of Nd-Fe-B/α-Fe nanocomposite films, Journal of Physics: Conference Series, IOP Publishing, 2010, p. 012014.
[26] S. Darling, S. Bader, Journal of Materials Chemistry 15 (2005) 4189-4195.
[27] V. Markovich, R. Puzniak, D. Mogilyansky, X. Wu, K. Suzuki, I. Fita, A. Wisniewski, S. Chen, G. Gorodetsky, The Journal of Physical Chemistry C 115 (2010) 1582-1591.
[28] J. Mao, Y. Sui, X. Zhang, X. Wang, Y. Su, Z. Liu, Y. Wang, R. Zhu, Y. Wang, W. Liu, X. Liu, Solid State Communications 151 (2011) 1982-1985.
[29] J. Lindén, A. Kjekshus, P. Karen, J. Miettinen, M. Karppinen, Journal of Solid State Chemistry 139 (1998) 168-175.
[30] D. Kim, C. Kim, C.-O. Kim, S.S. Yoon, M. Naka, M. Tsunoda, M. Takahashi, Journal of Magnetism and Magnetic Materials 304 (2006) e356-e358.
[31] W.-t. Chen, A.J. Williams, L. Ortega-San-Martin, M. Li, D.C. Sinclair, W. Zhou, J.P. Attfield, Chemistry of Materials 21 (2009) 2085-2093.
[32] F.J. Berry, F.C. Coomer, C. Hancock, Ö. Helgason, E.A. Moore, P.R. Slater, A.J. Wright, M.F. Thomas, Journal of Solid State Chemistry 184 (2011) 1361-1366.
[33] S. Layek, H. Verma, Advanced Materials Letters 3 (2012).
[34] L. Wang, D. Wang, H. Huang, Z. Han, Q. Cao, B. Gu, Y. Du, Journal of Alloys and Compounds 469 (2009) 1-3.
[35] E. Folcke, J.M. Le Breton, Y. Bréard, A. Maignan, Solid State Sciences 12 (2010) 1387-1392.
[36] T.C. Gibb, Journal of the Chemical Society, Dalton Transactions (1985) 1455-1470.
[37] C.S. Kim, Y.R. UHM, J.C. Sur, Journal of the Korean Physical Society 37 (2000) 4.
[38] W.F. Zhang, Z. Yin, M.S. Zhang, Applied Physics A 70 (2000) 93-96.
[39] D. Li, J. Zheng, Z. Zou, Journal of Physics and Chemistry of Solids 67 (2006) 801-806.
[40] X.Z. Li, F.B. Li, C.L. Yang, W.K. Ge, Journal of Photochemistry and Photobiology A: Chemistry 141 (2001) 209-217.
[41] S. Ahmed, M. Rasul, R. Brown, M. Hashib, Journal of Environmental Management 92 (2011) 311-330.
[42] I.K. Konstantinou, T.A. Albanis, Applied Catalysis B: Environmental 49 (2004) 1-14.

Chapter 5

Synthesis, characterization and photocatalytic activities of substituted REBFO perovskite-like materials

Ibrahim Abdulkadir, Bice S. Martincigh* and Sreekantha B. Jonnalagadda

School of Chemistry and Physics, University of KwaZulu-Natal, Westville Campus, Private Bag X54001, Durban, 4000, South Africa

*Corresponding author: Tel: +27 31 2601394; Fax: +27 31 2603091; E-mail: martinci@ukzn.ac.za

Abstract

Nanomaterials, with the formula $Eu_{0.5}(Bi_{0.2}X_{0.2}Mn_{0.1})FeO_{3-\delta}$ (where X = Ca, Sr and Ba), were synthesized by using the citric acid sol-gel route and separate portions were annealed at either 600, 700, 800 or 900 °C. Scanning electron microscopy, high resolution transmission electron microscopy and powder X-ray diffraction analysis of the powders showed that they contain crystalline perovskite-type nanoparticles. Crystallinity increased with higher annealing temperature. The lattice parameters after refinement showed that the particles have either an orthorhombic or rhombohedral structure. BET specific surface areas ranged between 7 to 18 m^2 g^{-1} with the Ba-substituted powders having the highest surface area. Vibrating sample magnetometer analysis of the hysteresis loop provided an insight into the interesting magnetic properties of the powders and also the variation in coercivity with annealing temperature. Photoluminescence emission spectra were observed for all the powders in the visible region at room temperature indicating potential for photoactivity. The powders were all screened for photocatalytic activity against an organic dye (rhodamine B) in the visible region of the solar spectrum and the results were all positive with Ca containing powders having the highest photocatalytic efficiency.

Keywords**:** *Multiferroics; magnetic properties; photoluminescence; photocatalytic properties*

5.1 Introduction

Rare earth perovskite-like oxides with the general formula ABO_3 (where A is a large rare earth metal and B is a smaller transition metal) have very good potential for use in advanced technologies. They exhibit a wide variety of characteristics due to the flexibility of their structure, and the fact that they can accommodate a wide range of elements. Some of the properties exhibited include ferromagnetism, ferroelectricity, ferroelasticity [1, 2], piezo and pyroelectric [3, 4], as well as catalytic and photocatalytic properties [5-7]. Some perovskites, like $BiFeO_3$ exhibit multiferroic properties, a situation where coupling of electric (lone pair of electrons on Bi^{3+}), magnetic (a transition metal Fe^{3+}) and structural geometry (due to FeO_6 octahedra) result in multiferroicity [8, 9]. The potential of the perovskite-like oxides have attracted a lot of interest and have lead to the fabrication and characterization of novel members of the family with a view to exploiting their properties in emerging technological fields. The most widely used methods for influencing the properties of perovskite-like materials is by partial substitution of the metals on either the A- or the B-site with other metals (smaller or divalent metals) to create oxygen vacancies and limited distortion to the crystal lattice. Divalent metals such as Ca^{2+}, Sr^{2+}, Ba^{2+} and Pb^{2+} have been shown to be very good dopants in this regard [10, 11]. Introducing small divalent alkaline earth-metals into an $A^{3+}B^{3+}O_3$ system can create bond length variation and oxygen vacancies that can serve to introduce the needed structural change in the crystal that would impact on new properties to the materials. In this work, we studied a rare earth RE substituted $BiFeO_{(3-\delta)}$ (REBFO, where RE = Eu^{3+}) with a general formula $((RE_{0.5}Bi_{0.2}M_{0.2}Mn_{0.1})FeO_{(3-\delta)}$ system into which have been introduced alkaline-earth metals (M = Ca^{2+}, Sr^{2+} and Ba^{2+}) and a Jahn-Teller metal Mn^{3+}/Mn^{4+} with a view to determine its structural, magnetic, optical and photocatalytic properties.

5.2 Experimental

5.2.1 Materials

Eu_2O_3 (99.9%), citric acid (99.7%) (BDH Chemicals), $Fe(NO_3)_3.9H_2O$ (98%), $Bi(NO_3)_3.5H_2O$ (97%), $Sr(NO_3)_2$ (99%) $Ba(NO_3)_2.5H_2O$ (99%), $Ca(NO_3)_2$ (99%) $Mn(CH_3OO)_2$ (99%), $K_2Cr_2O_7$ (99%), (Saarchem), ferrous ammonium sulfate, concentrated H_2SO_4 (98 %) and $HgSO_4$ (Merck), chemically pure concentrated HNO_3, ethylene glycol (99%) (Promark Reagents), rhodamine B dye (the coleman and bell Co.), H_2O_2 30% vol. (100 vol) (Minema Chemicals) were used as received. Deionised water from a Millipore Milli-Q Elix 5UV water purification unit was used throughout and is hereafter referred to as Milli-Q water.

5.2.2 Synthesis of $(Eu_{0.5}Bi_{0.2}X_{0.2}Mn_{0.1})FeO_{(3-\delta)}$

$(Eu_{0.5}Bi_{0.2}X_{0.2}Mn_{0.1})Fe\ O_{(3-\delta)}$ (X = Ca, Ba and Sr) powders were all prepared by the Pechini-type sol-gel method in citric acid. The precursors ($Fe(NO_3)_3.9H_2O$, Eu_2O_3, $Sr(NO_3)_2$, $Mn(CH_3OO)_2$, and $Bi(NO_3)_3.5H_2O$), in the correct mole ratio, were all dissolved in dilute nitric acid (15 cm^3, 6 mol dm^{-3}). The solution was mixed thoroughly, made up to 200 cm^3 with Milli-Q water and then gradually poured into a burette. This solution was then added (drop-wise) to a citric acid solution (400 cm^3, 0.15 mol) in a beaker which was continuously stirred by a magnetic stirrer at room temperature. Once the addition was completed, and with the solution still being stirred, the temperature of the mixture was raised to 90 ^oC and allowed to stand until the volume of the solution reduced to about 50 cm^3, ethylene glycol (100 cm^3) was then added and the heating and stirring continued until a thick gel formed. The gel was then dried in an oven at 120 ^oC for 24 hrs, pre-calcined at 400 ^oC for 4 hrs to remove all organic components, and then separate portions were annealed at different temperatures (600, 700, 800 and 900 ^oC) in a muffle furnace for 4 hrs. Small portions of the Sr and Ba substituted powders were annealed at 1000 °C for 4 hrs to investigate the effect of a higher annealing temperature on the crystallinity of their perovskite lattice. These portions were not used in the photocatalytic test.

5.2.3 Characterisation

The surface morphology and microstructure of the materials was studied by using a JOEL JEM 2100 LAB6 high resolution transmission electron microscope (HRTEM) equipped with a lanthanum hexaborite emission source and operated at an acceleration voltage of 200 V. Each sample was dispersed in ethanol in a small centrifuge tube and sonicated before being dispersed on a carbon grid and the images collected. Powder X-ray diffraction (PXRD) analysis was performed with a Bruker D8 Advance instrument with a Cu K_α radiation source (λ = 1.5406 Å). The Scherrer equation

$$D = \frac{k\lambda}{\beta\cos\theta} \qquad (5.1)$$

was used to determine the average crystallite sizes of the particles.

where *k* is the Scherrer constant with a value of (0.89), λ is the wavelength of radiation and β is full width at half maximum.

Surface areas were determined by nitrogen adsorption at 77 K and the BET equation method by using a Micromeritrics Tristar II 3020 fully automated three-station surface area and porosity analyzer. Fourier transform infrared-attenuated total reflectance spectra (FTIR-ATR) were recorded on a PerkinElmer Spectrum RX1 instrument fitted with an ATR accessory. The magnetic properties were analysed with a LakeShore model 735 vibrating sample magnetometer (VSM) which had been calibrated by using a standard Ni sphere of saturation magnetization 54.7 emu g^{-1}. The maximum applied magnetic field was 14 kOe and measurements were performed at room temperature (RT). Photoluminescence spectra of the materials was studied by using a PerkinElmer LS 55 spectrofluorimeter equipped with a high energy pulsed xenon source for excitation. The samples were excited at wavelengths between 375 to 405 nm and the emission was monitored between 430 nm to 700 nm.

5.2.4 Photocatalytic screening

Photocatalytic activity of each sample was tested on rhodamine B (RhB) dye solution (that have been prepared by dissolving the dye powder in Milli-Q water) in the presence of H_2O_2 at room temperature. Samples were irradiated with a 26 W fluorescent lamp (Osram Dulux D, 26 W, 1800 lm) placed in a quartz jacket and held at about 7 cm above the RhB dye solution (which was continuously stirred with a magnetic stirrer) containing various amounts of the synthesized materials and H_2O_2. A 30 min. period was allowed for equilibration in the dark before the lamp was turned on. Aliquots of the dye solution were withdrawn at regular intervals of 20 min, centrifuged and filtered through a 0.45 μm syringe filter (Millipore). Photodegradation of the dye was monitored by measuring the absorbance of each aliquot with a Biochrom Libra S6 UV spectrophotometer at a wavelength of maximum absorption (λ_{max}) for RhB of 556 nm. The chemical oxygen demand (COD) analysis of the irradiated dye solution was done by oxidizing the organic carbon with potassium dichromate and then back-titrating the excess dichromate with ferrous ammonium sulfate [12].

5.3 Results and discussion

Dry powders of perovskites $(Eu_{0.5}Bi_{0.2}Ba_{0.2}Mn_{0.1})FeO_{(3-\delta)}$ (EuBa), $(Eu_{0.5}Bi_{0.2}Sr_{0.2}Mn_{0.1})Fe\ O_{(3-\delta)}$ (EuSr) and $(Eu_{0.5}Bi_{0.2}Ca_{0.2}Mn_{0.1})Fe\ O_{(3-\delta)}$ (EuCa) were obtained after calcination and annealing at 600, 700, 800 and 900 °C with colours ranging from dark brown to black. The Goldschmidts tolerance factor (assuming that all substitutions occur on the A-site) is given by

$$t_X = \frac{((0.5r_{\mathrm{Eu}}+0.2r_{\mathrm{Bi}}+0.2r_X+0.1r_{\mathrm{Mn}})+r_{\mathrm{O}})}{\sqrt{2}(r_{\mathrm{Fe}}+r_{\mathrm{O}})} \quad (5.2)$$

where t_X is Goldschmidts tolerance factor for the material in which X has been substituted and r is the radius of the ions of the subscripted atoms. (r_{Eu} = 0.947 Å, r_{Bi} = 0.96 Å, r_X = (r_{Ca} = 1.34 Å, r_{Sr} = 1.44 Å or r_{Ba} = 1.61 Å, r_{Mn} = 0.58 Å, r_{Fe} = 0.78 Å, r_O = 1.4 Å) [13]. The equation predicts

an orthorhombic lattice for all the materials with the following t values:- t_{Ca} = 0.7757, t_{Sr} = 0.7821 and t_{Ba} = 0.7932.

5.3.1 Phase purity and crystallinity

The crystalline phases, degree of crystallinity and particle sizes of the powders were determined by using powder X-ray diffraction. Figure 5.1 shows the diffractograms obtained for the calcium substituted powders. The results show that the powders all formed crystalline orthorhombic perovskite-type lattices with space group Pbnm. Since the diffractograms fit the diffraction pattern of $Gd_{0.5}Ca_{0.5}FeO_{2.5}$ (ICCD 00-052-0152), this indicates that all the ions have been incorporated into the perovskite lattice as no impurity peaks are present. The cell parameters for all the powders are shown in Table 5.1. The orthorhombic cell volume appears to decrease as the annealing temperature increases, since the cell volumes are determined by the ionic sizes of atoms present within the lattice, this implies that the higher oxidation states of the ions with smaller ionic sizes are stabilised at higher annealing temperatures thereby leading to a decrease in the cell volumes. The general trend for the cell volumes for powders substituted with different X^{2+} ions is $Ca^{2+} < Sr^{2+} < Ba^{2+}$ in accordance to the size of the cation. The formation of the perovskite phase begins at an annealing temperature of 600 °C since the 112, 220 and 024 planes are clearly visible. The broad peaks are due to the nanocrystalline nature of the powder particles. The decrease in the broadness of the peaks at higher annealing temperatures coupled with an increase in intensity and sharpness indicates an increase in the sizes and crystallinity of the powder particles. The crystal sizes calculated from the Scherrer equation by using the 112 peaks are presented in Table 5.1 and the results show the average crystallite sizes increasing with an increase in annealing temperature for all the powders. Peak intensities are higher for the Ca-containing powders at each annealing temperature (Figure 5.2), while the peaks for the Sr- and Ba- containing materials are mostly broad with low intensities. This is related to a combination of microstrain and crystallite size broadening coupled with some lattice defect [14, 15] in the material which is related to the size of the alkaline-earth metal

substituted as follows; Ba > Sr > Ca. The powders annealed at higher temperature (1000 °C) show better diffraction peaks for both the Sr- and Ba- substituted powders (Figure 5.3). The better resolved peaks are as a result of the higher temperature treatment of the lattice defect.

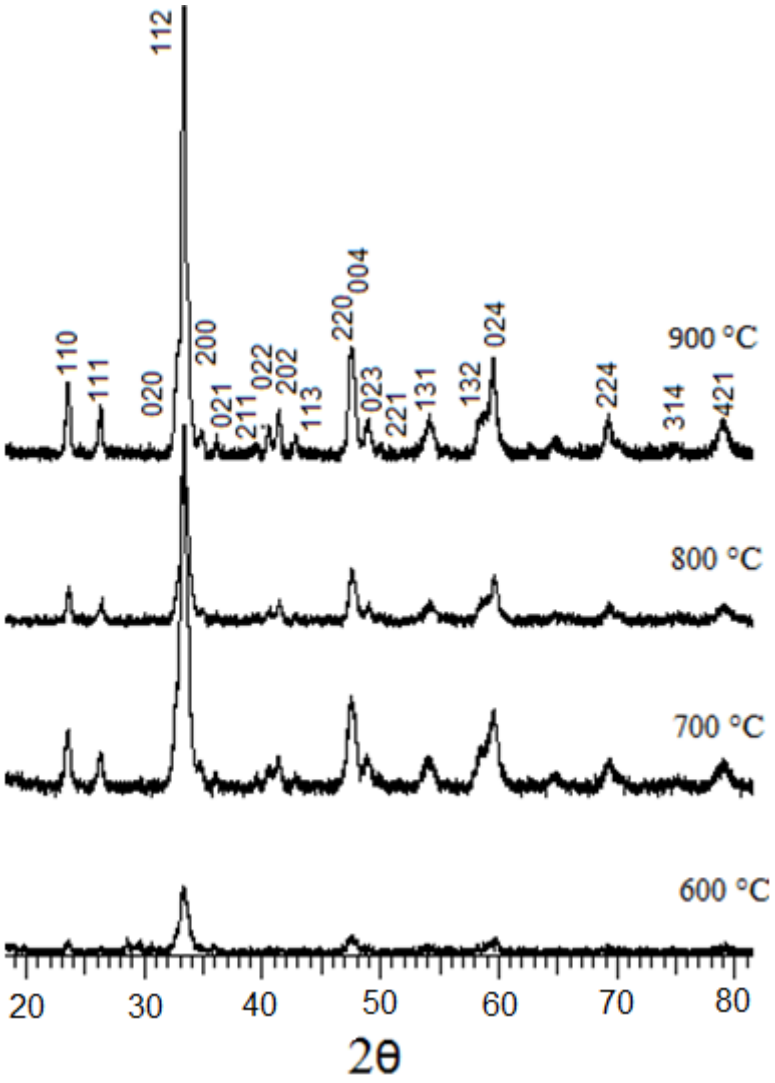

Figure 5.1: Powder X-ray diffractograms for orthorhombic EuCa600-900.

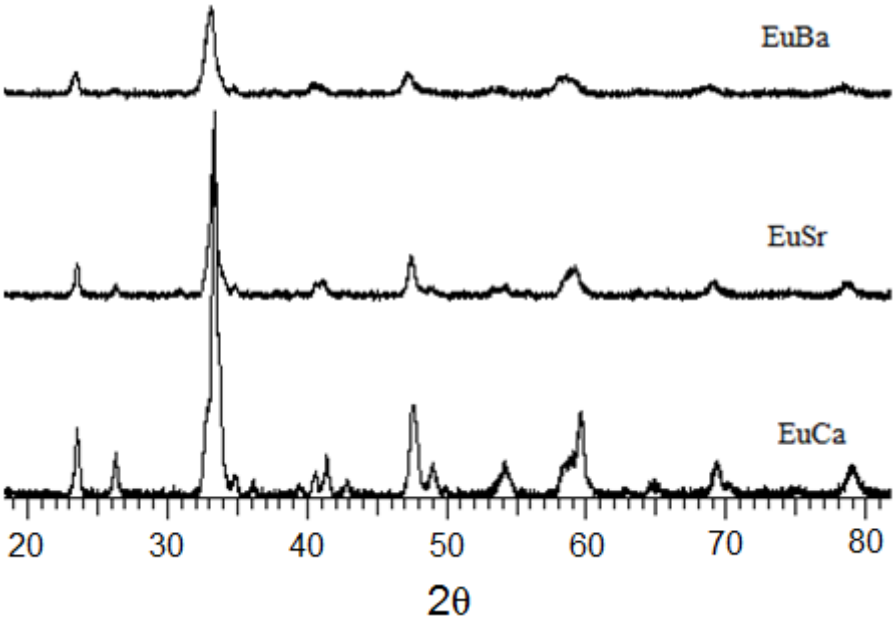

Figure 5.2: Powder x-ray diffractograms for powders annealed at 900 °C.

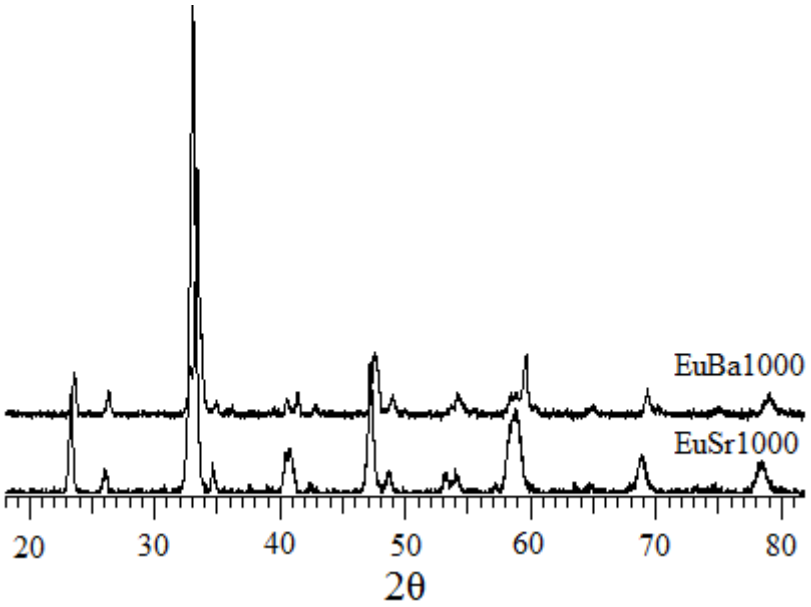

Figure 5.3: Diffractograms are more resolved and with higher intensity due to the high temperature treatment of EuBa1000 and EuSr1000.

Table 5.1: cell parameters, crystallite sizes and BET surface areas for the powders annealed at 700, 800 and 900 °C.

Samples	Cell parameters				Crystallite size, *D*/nm (± 1.5)	BET SSA/m^2 g^{-1} (± 0.01)
	a/Å	b/Å	c/Å	V/$Å^3$		
EuCa700	5.395	5.525	7.647	227.939	16.34	18.65
EuCa800	5.362	5.514	7.631	225.576	20.93	11.72
EuCa900	5.357	5.513	7.649	225.927	25.96	7.477
EuSr700	5.424	5.535	7.699	231.147	17.52	17.70
EuSr800	5.382	5.525	7.646	227.392	18.49	14.91
EuSr900	5.401	5.518	7.679	228.870	23.01	11.30
EuBa700	5.482	5.591	7.799	239.075	14.18	16.09
EuBa800	5.476	5.585	7.799	238.525	18.09	14.80
EuBa900	5.407	5.566	7.761	233.576	22.02	11.62

5.3.2 Microstructural characterization

The low magnification HRTEM images of the crystals show particles with a size range between 13-20 nm in agreement with the calculated sizes from the Scherrer equation (Table 5.1). The EuBa material formed some nanocubes as well as spherical nanoparticles, while the EuSr and EuCa powders contained largely spherical nanoparticles (Figures 5.4 and 5.5).

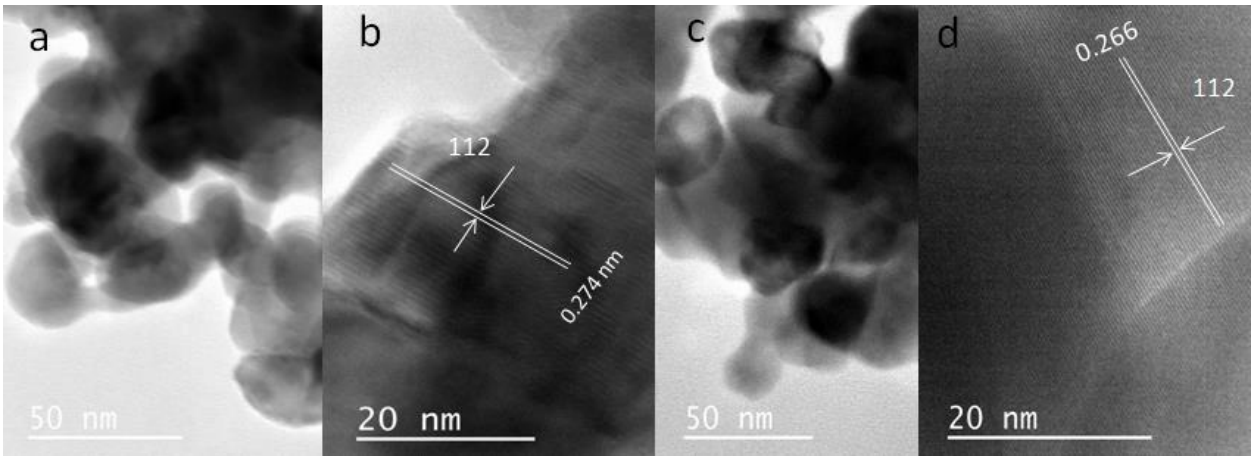

Figure 5.4: Crystal morphology (a) spherical shape of EuBa900 particles, (b) 112 lattice for EuBa900, (c) crystals of EuSr900, and (d) 112 lattice of EuCa900.

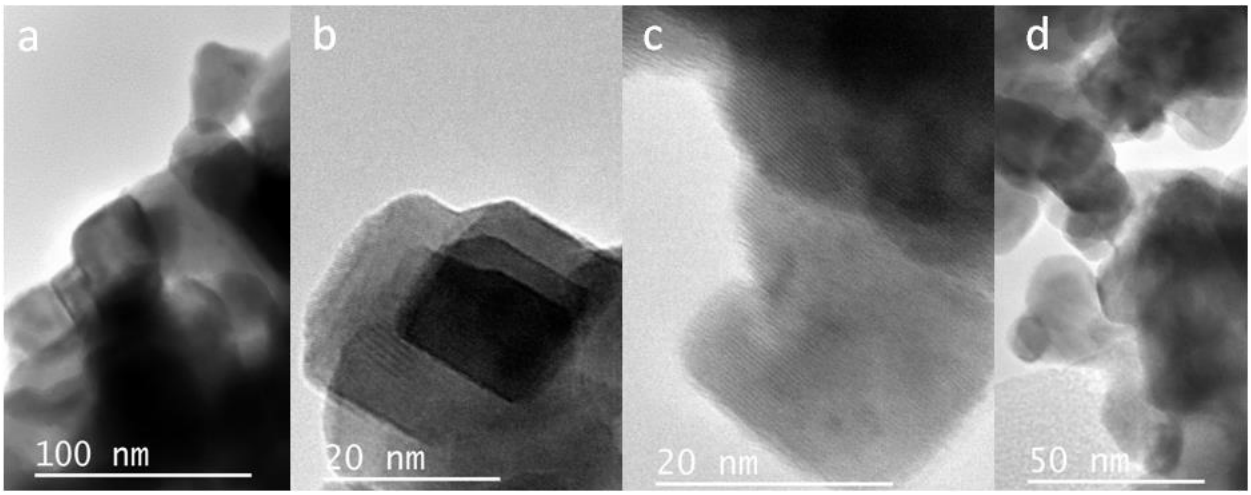

Figure 5.5: Cubic crystals of (a) EuBa900, (b) EuBa800, (c) and (d) lattice fringes and nanocubes for EuBa700 respectively.

5.3.3 Surface characterisation

The ATR-FTIR spectra for some of the substituted powders (600-900 °C) are shown in Figure 5.6. The peaks are observed at two important regions, namely, 600-380 cm^{-1} and between 1500-1300 cm^{-1}. The peak at around 1450 cm^{-1} has been assigned to different types of bending and stretching modes for –O-H of water molecules adsorbed at the surface of the particles. This peak gradually diminished with higher annealing temperatures as can be observed for the Ba substituted powders (Figure 5.6a) [16]. This reduction in OH peak size is an indication of the removal of surface adsorbed H_2O at higher annealing temperature. It could also be an indication of the diminishing BET specific surface area (SSA) of the materials. A similar pattern was observed for other samples. The peaks that occur between 600 and 380 cm^{-1}, however, represent the cumulative absorption of various Fe – O and O – Fe – O bending and vibration modes for octahedral FeO_6 and these peaks can be seen to increase in size at higher annealing temperatures [6, 16-18]. Figure 5.6b shows FTIR spectra for samples annealed at 900 °C. They all exhibit similar peak positions, thereby indicating the formation of perovskite lattice octahedra in the powders.

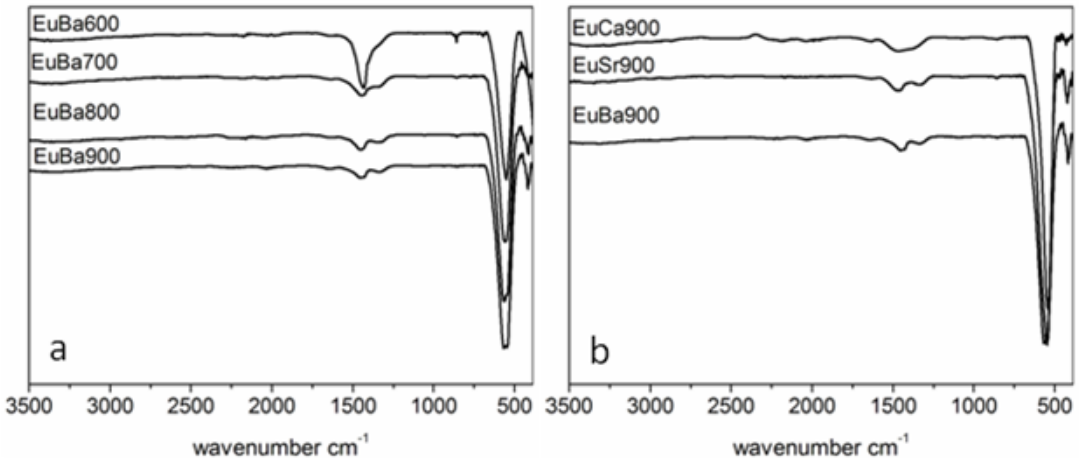

Figure 5.6: (a) FTIR peaks for Ba-substituted powders annealed at temperatures from 600 to 900 °C, and (b) powders annealed at 900 °C.

5.3.4 Surface area and porosity

The BET surface areas for the powders are presented in Table 5.1. The surface areas obtained ranged between 7.28 and 18.65 m^2 g^{-1}. Lower surface areas were obtained for powders annealed at higher temperatures. The N_2 adsorption-desorption (A-D) isotherms at 77 K for these materials conform to the type II isotherm according to the IUPAC classification [19]. The hysteresis loops indicate that all powders contain porous particles with pore sizes ranging from meso- to macroporous, Figure 5.7 shows the A-D isotherm for NdBa700 and similar plots were obtained for all other samples. Figure 5.7 (insets) are modal plots of pore size distribution (PSD). The curves show that the pore sizes are distributed between meso- and macroporous with the pore area for the mesopores dropping continuously as annealing temperature is increased. This contributes to the drop observed in the specific surface area of the materials.

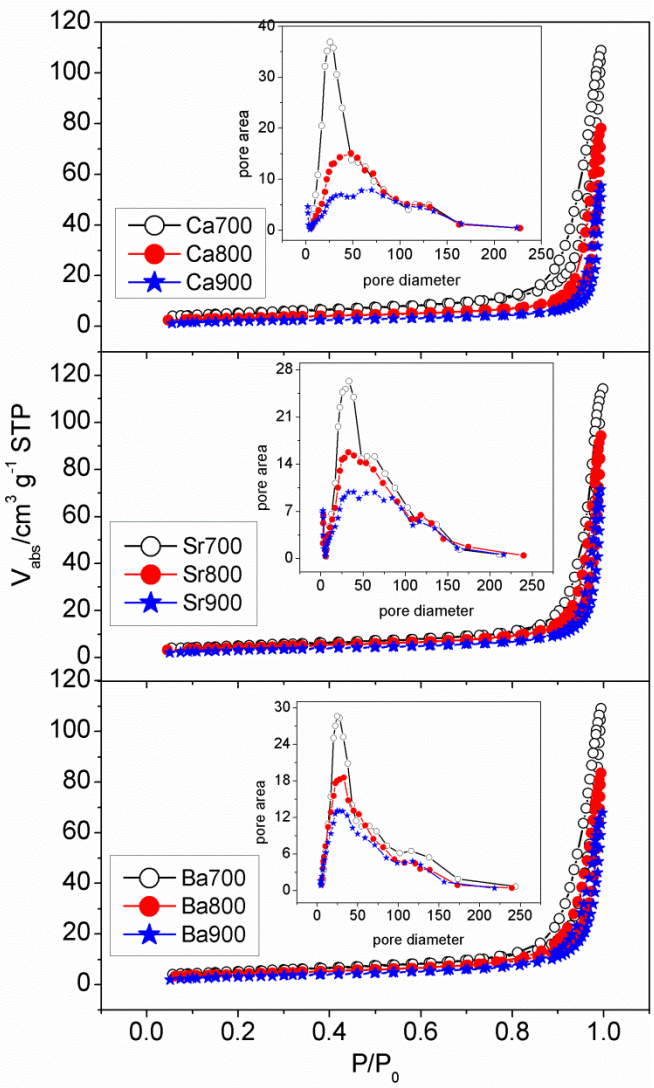

Figure 5.7: Adsorption-desorption isotherms showing features corresponding to a type II IUPAC classification, the insets show the variation of the pore size distribution as anneling temperature increased.

5.3.5 Magnetic properties

The hysteresis loops for the room temperature magnetization of EuBa600-900 are shown in Figure 5.8a. A large and steady increase in the value of the coercive field is observed between EuBa600 and EuBa800, however, a slight increase in the coercivity is observed between EuBa800 and EuBa900 as the critical domain size (a size limit after which further increase in size does not lead to a further increase in the coercivity) is approached [20]. The large coercive field in the magnetic material is a measure of the hardness of the magnetic material which

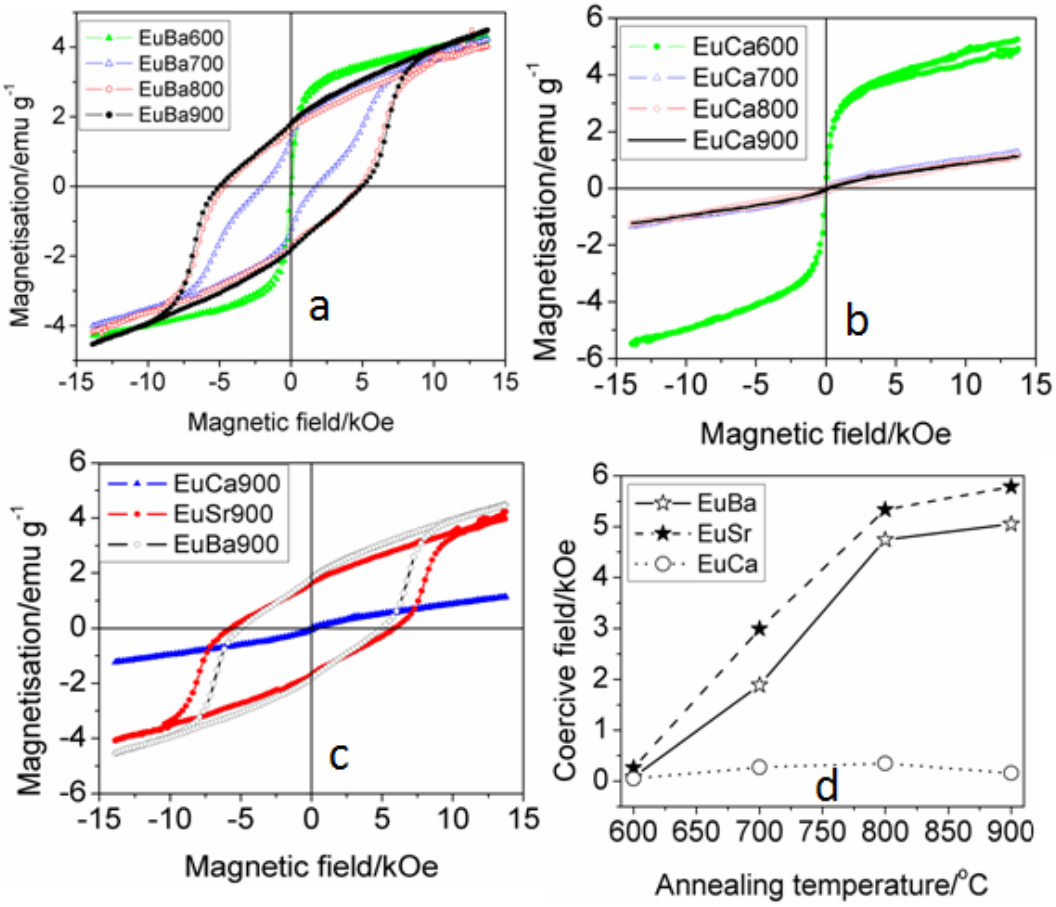

Figure 5.8: (a) Hysteresis loops for EuBa annealed from 600 to 900 °C, (b) hysteresis loops for EuCa annealed from 600 to 900 °C, (c) hysteresis loops for all the powders annealed at 900 °C and (d) a plot of relationship between coercive field and annealing temperature for all the powders.

increases with increase in annealing temperature and gives rise to the corresponding increase in the values for remanent magnetization M_R [21] and (M_R/M_S). The slight constriction at the middle of the loop indicates the presence of the remnants of materials with soft magnetic properties and the constriction is as a result of interaction between these two phases [22]. Similar results were obtained for the EuSr series and the magnetisation parameters are presented in Table 5.2. The trend is, however, different in the case of the EuCa series (Figure 5.8b). The magnetisation collapses completely for the powders annealed at 700 °C and above as can be seen from the plot, indicating that these powders might have either a predominantly paramagnetic (PM) or anti-ferromagnetic (AFM) property. The AFM contribution in all the

powders could originate from the Fe–O or Fe–O–Fe interactions when there is an angular deviation from 180° which could be caused by the introduction of the divalent alkaline-earth metal (i.e. Sr^{2+} and Ba^{2+}) [23]. Figure 5.8c shows the hysteresis loops for the powders annealed at 900 °C. Large coercive fields can be seen for EuBa and EuSr annealed at 800 and 900 °C. Such large coercivities (above 4 kOe at room temperature) can be attributed to the result of both the magnetic anisotropy and the spin coupling between the FM and the AFM components of the material [23, 24]. Figure 5.8d shows the increase in coercivity with increasing annealing temperature between 600 and 800 °C. The magnetization parameters are presented in Table 5.2.

Table 5.2: Magnetization parameters obtained from M-H hysteresis loops of samples annealed from 600 to 900 °C. M_S = saturation magnetisation, M_R = remanent magnetisation, M_R/M_S = squareness, H_C = coercive field.

Samples	M_S/emu g^{-1}	M_R/emu g^{-1}	M_R/M_S	H_C/Oe
EuCa600	5.25	0.300	0.055	44.315
EuCa700	1.26	0.020	0.051	269.19
EuCa800	1.13	0.010	0.052	354.51
EuCa900	1.13	0.002	0.037	155.45
EuSr600	4.09	0.840	0.215	256.79
EuSr700	4.94	1.059	0.367	2990.7
EuSr800	4.23	1.703	0.415	5335.9
EuSr900	4.22	1.624	0.399	5784.0
EuBa600	4.27	0.389	0.101	73.981
EuBa700	4.22	1.381	0.323	1882.0
EuBa800	4.47	1.623	0.386	4740.7
EuBa900	4.68	1.8003	0.402	5051.2

5.3.6 Photoluminescence

Figure 5.9 shows the emission peaks for excitations at different energies between 380 and 405 nm. A series of narrow emission peaks which shifts according to the shift in excitation energy were observed. The emission peaks extend over wavelengths corresponding to various colours (green to red) in the visible region [25]. PL has been shown to occur in perovskites either due to the presence of impurities within the crystal lattice of the material, the presence of defects/oxygen vacancies within the lattice, or the formation of multiple trap states between the valence band (VB) and the conduction band (CB) levels of the material [26-28]. These peaks occur in the visible region of the electromagnetic spectrum indicating that these materials can function as photocatalysts utilising visible light to bring about the degradation of organic pollutants.

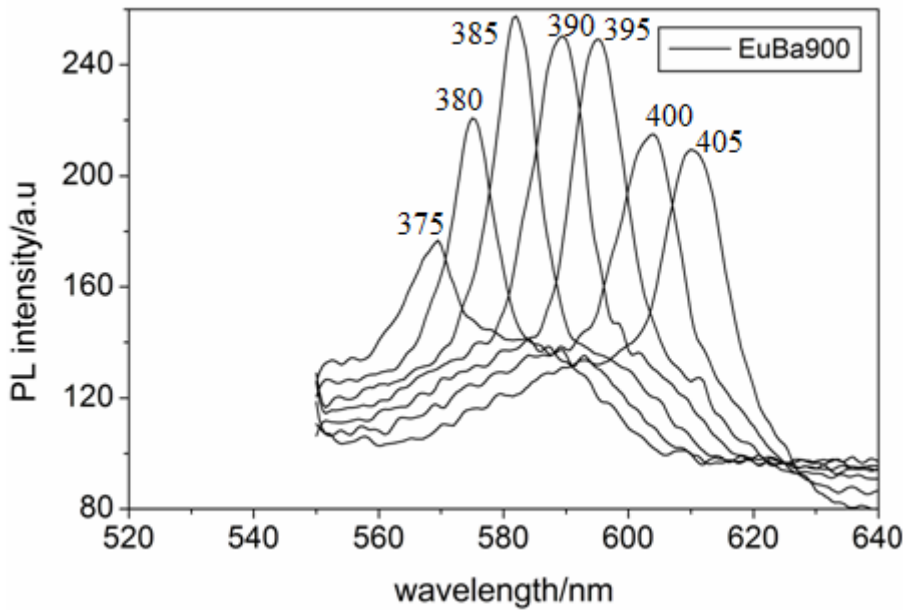

Figure 5.9: A series of photoluminescence emission spectra for EuBa900. The corresponding excitation wavelengths are indicated above the peaks

5.3.7 Photocatalytic screening

In the photocatalytic degradation of organic dyes, the nature of the photocatalyst and the conditions under which the reactions occur are vital in determining the efficiency of the photocatalytic reaction. The following is the investigation of the effect of varying some of the parameters in the photocatalytic degradation of RhB.

5.3.7.1 Effect of annealing temperature on efficiency

The RhB solution only photodegrades in the presence of a combination of the photocatalytic material and H_2O_2 for all the powders. Figure 5.10a shows the result of the photocatalytic screening of the powders prepared at annealing temperatures of 700, 800 and 900 °C for the EuSr series of powders. The powders all show good photocatalytic activities with respect to RhB photodegradation with the activity increasing for powders annealed at higher temperatures. This implies that the powder annealed at 900 °C has the highest photocatalytic activity. Similar results were obtained for all the other powders. Figure 5.10b shows the photodegradation activity for all the powders annealed at 900 °C. All the powders showed a good ability to decompose RhB. The decomposition, however, was slightly higher for the EuCa900 powder. The pseudo-first-order rate constant for the photodegradation of RhB in the presence of these powders and H_2O_2 are shown in Table 5.3.

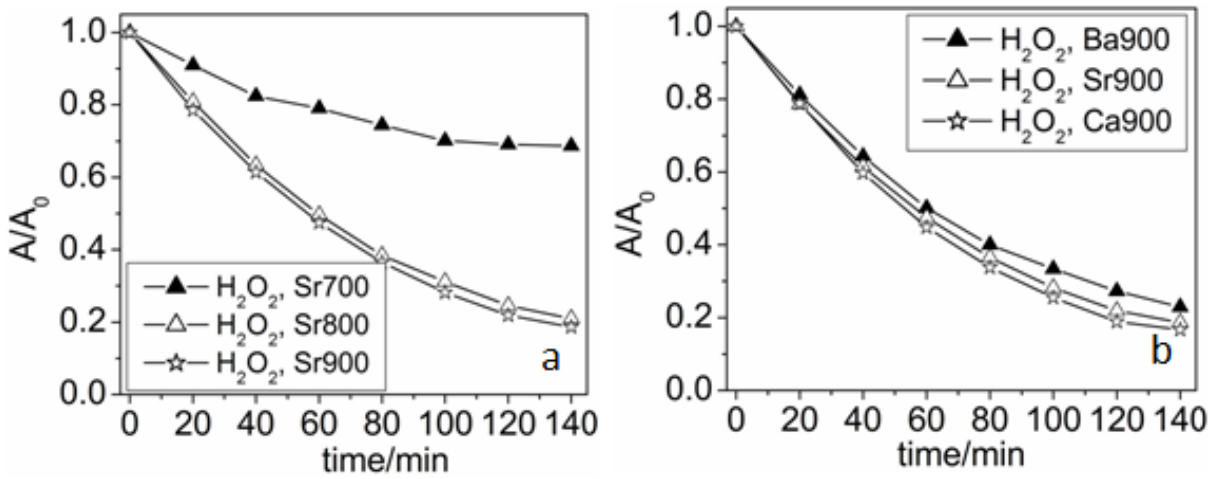

Figure 5.10: (a) Time dependence of the photodegradation of RhB for 1.5 g dm^{-3} EuSr700 to 900, and (b) time dependence of the photodegradation of RhB for the powders annealed at 900 °C.

Table 5.3: Rates of RhB photodegradation for the powders ((1.5 g dm^{-3}, 3.0 × 10^{-5} mol dm^{-3} H_2O_2). annealed at 900 °C.

Sample	k_{obs}/min^{-1}	R^2
EuCa900	1.34 x 10^{-2}	0.998
EuSr900	1.23 x 10^{-2}	0.999
EuBa900	1.07 x 10^{-2}	0.999

The photodegradation of RhB by these photocatalysts follows pseudo-first-order reaction kinetics and can be represented by

$$ln\frac{A}{A_0} = k_{obs}t. \quad (5.3)$$

Where A_0 and A are the initial absorbance and the absorbance of the dye solution at time t (min) respectively, and k_{obs} (min^{-1}) is the observed rate constant. The linear regression coefficients

(R^2) for the materials annealed at 900 °C as shown in Table 5.3 and all show a good fit to pseudo-first-order kinetics.

5.3.7.2 Effect of photocatalyst loading

The effect of photocatalyst loading of EuBa900 on the photodegradation of RhB dye is presented in Figure 5.11. Generally, there is an increase in the decolourisation of the RhB dye solution as the amount of the photocatalyst powder is increased. An optimum amount (of 1.5 g L^{-1} of photocatalytic material) is reached, above which the rate of photodegradation of the dye is decreased. The initial increase in the rate of decomposition of the dye as the amount of the photocatalyst is increased could be attributed to a consequent increase in surface area. The latter decrease, however, could be due to (a) the presence of excess photocatalyst materials which rather than act to enhance the photodegradation, block the light from reaching the photodegradation sites and hence reduce the rate of decomposition of the dye, or (b) aggregation of the photocatalyst particles leading to a decrease in surface area available for photodegradation [29-31].

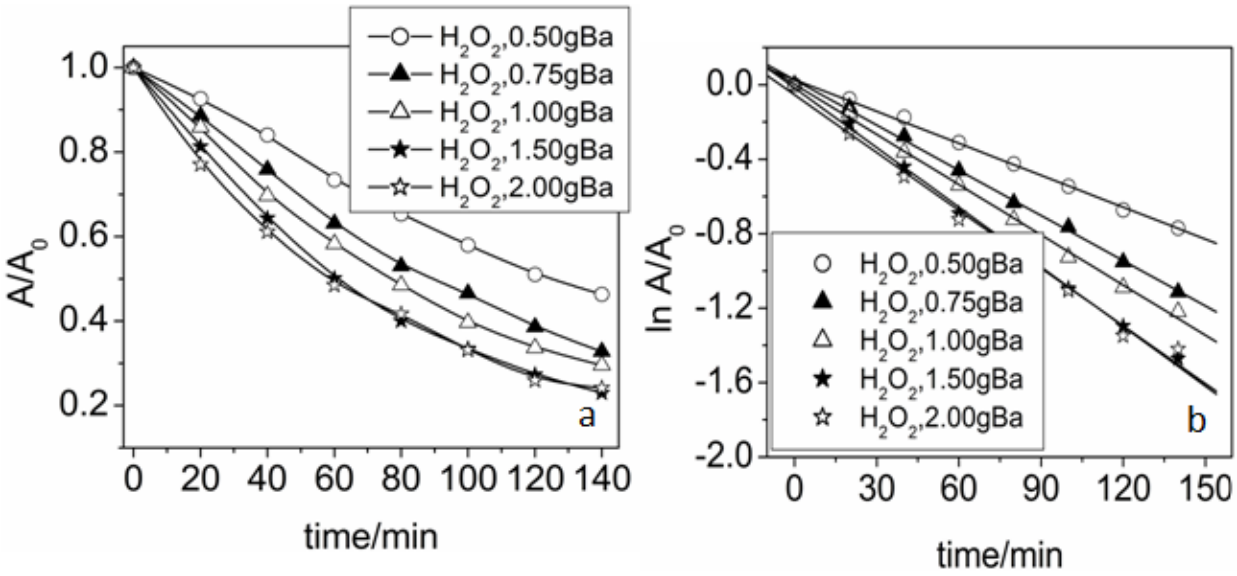

Figure 5.11: (a) Degradation time dependence of RhB for different amounts of EuBa900 powders, (b) plot pseudo-first-order kinetics plots for the same reactions.

Similar results were obtained for the other powders. Figure 5.12 shows the relationship between the rate constants of the photodegradation reactions against the photocatalyst loading for all the powders.

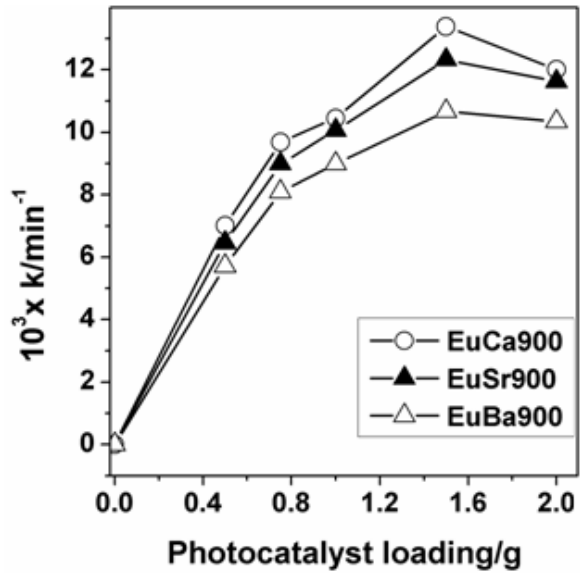

Figure 5.12: Increase in the rate of photodegradation with increase in amount of photocatalyst.

5.3.7.3 Effect of solution pH on the photodecomposition

The pH of a solution plays a significant role in the determination of the properties and activities of the photocatalyst. The pH of the solution determines the surface charge of the powder particles and the charge of the dye, the adsorption of the dye at the photocatalyst surface and the oxidation potential of the valence band [32] of the photocatalyst. The photocatalytic degradation of the dye was monitored at various pH values between 8 and 3 and the results show that the powders are active within a wide range of pH. Figure 5.13 shows the time-dependent plots of the normalised absorbance values for RhB for the EuSr900 photocatalysed decomposition, with the rate of the reaction increasing for the lower pH values (decomposition rates highest for pH 3). Similar results were obtained for the other powders. Table 5.4 presents the values of the

pseudo-first-order rate constants for all the other powders. As can be seen, the Ca-substituted material is the most photocatalytically active.

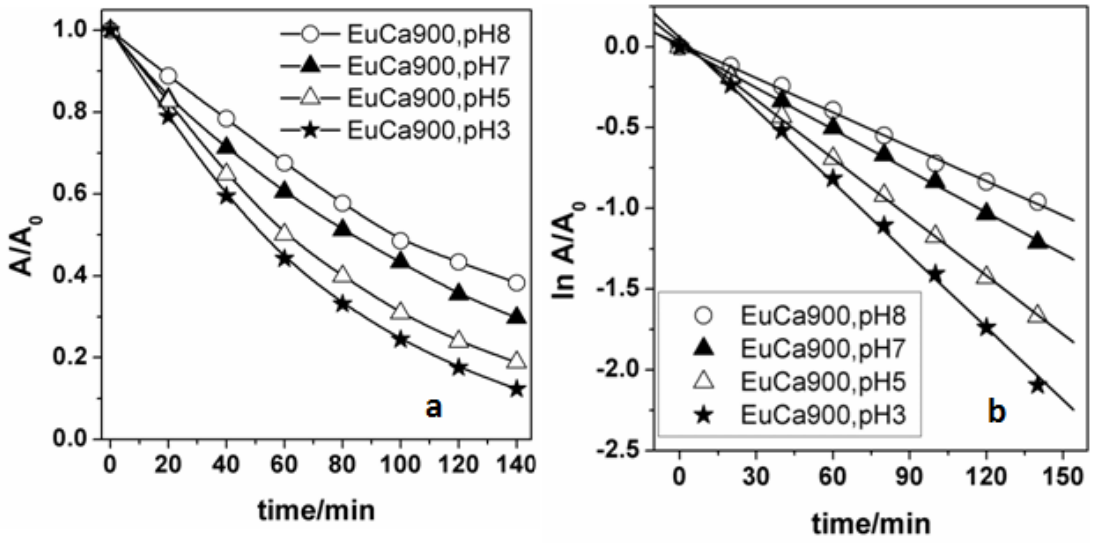

Figure 5.13: (a) Degradation time-dependence of RhB for EuCa900 powders, and (b) pseudo-first-order plots for the same reactions at different pH values.

Table 5.4: Pseudo-first-order rate constants for the photodegradation of RhB with different photocatalyst powders at different pH values.

pH	k_{obs}/min^{-1}		
	EuCa900	EuSr900	EuBa900
8	0.00709	0.00711	0.00795
7	0.00858	0.00801	0.0059
5	0.01209	0.00979	0.01031
3	0.01495	0.01164	0.01095

5.3.7.4 Effect of RhB concentration on rate of decomposition

The effect of the variation of the initial concentration of the RhB dye on the rate of photodegradation was studied by keeping the amount of photocatalyst and H_2O_2 constant. The results of these reactions with EuBa900 powders are presented in Figure 5.14. Little variation in the rates of photodegradation of the dye can be observed but, generally, when the reaction rates are very close and without a clear trend, it indicates that the rate of the reaction does not depend on the initial concentration of the dye. The rate constants for the reactions (Table 5.5) show that the difference in the observed rate constants of the photodegradation for each of the other powders is very similar. The Ca-substituted material is marginally more active.

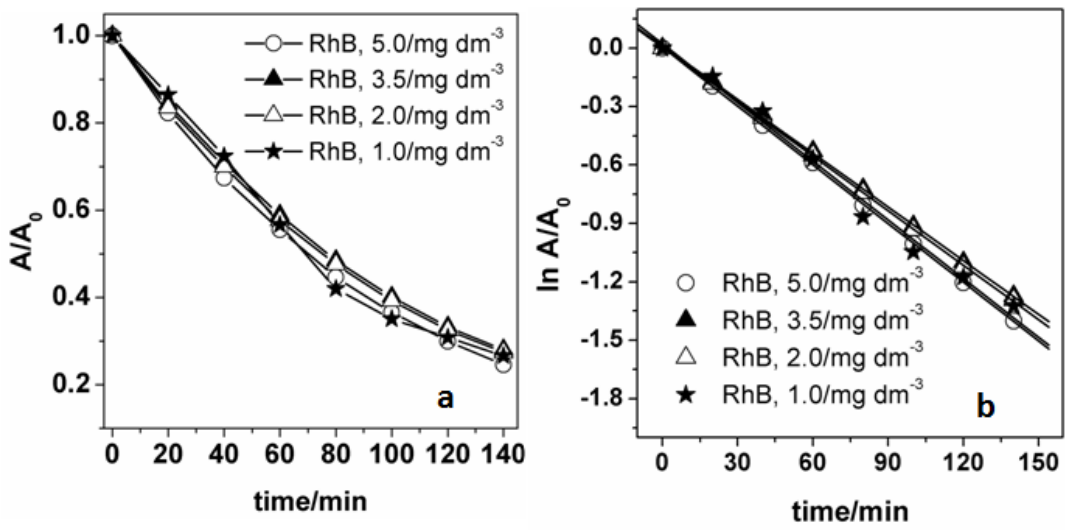

Figure 5.14: (a) Degradation time-dependence for varying initial concentrations of the RhB dye with EuBa900 (1.5 g dm^{-3} and 3.0×10^{-5} mol dm^{-3} H_2O_2) and (b) pseudo-first order plots for the same reactions.

Table 5.5: Pseudo-first-order rate constants for photocatalysts (1.5 g dm^{-3} of catalyst in the presence of 3.0×10^{-5} mol dm^{-3} H_2O_2) at different initial concentrations of the RhB dye.

Dye conc/mg dm^{-3}.	k_{obs}/min^{-1}		
	EuCa900	EuSr900	EuBa900
5.0	0.01233	0.01062	0.01006
3.5	0.01216	0.01157	0.00927
2.0	0.01312	0.01174	0.00934
1.0	0.01172	0.01058	0.01005

5.3.7.5 Mineralization

The chemical oxygen demand (COD) is a procedure that has been widely used to estimate the organic strength of wastewater. Here we have employed this process in order to determine the extent of mineralization of the RhB dye in the solution. The values for the COD of the samples obtained after 3 hrs of photodecomposition are presented in Figure 5.15. It is apparent that the extent of mineralization of the RhB dye molecules is greatest for the Ca substituted material.

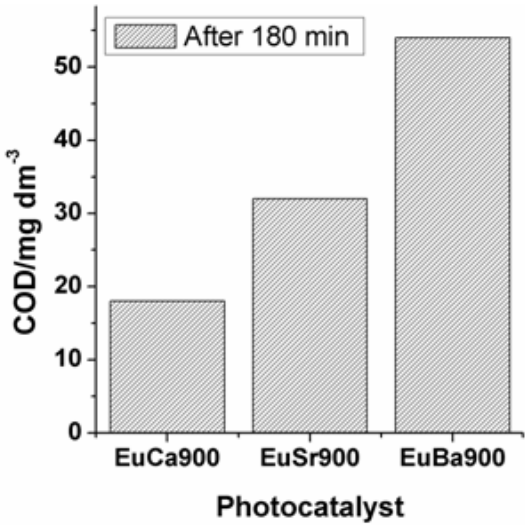

Figure 5.15: COD values for the degraded RhB dye solution after 3 hrs indicate that EuCa900 was most efficient in mineralizing RhB to CO_2 and H_2.

5.3.7.6 Mechanism

The following reactions could be responsible for generation of the active $^{\bullet}OH$ radicals required to initiate the degradation process of the RhB dye in these photocatalytic systems. The first is the photogeneration of an electron-hole pair in the photocatalysts. The generated electron in the conduction band of the catalyst can then be trapped in the H_2O_2 to cause the production of radicals according to the following mechanism:

$$PC + h\nu \rightarrow e^- + h^+ \quad (5.4)$$

$$H_2O_2 + e^- \rightarrow {}^{\bullet}OH + OH^- \quad (5.5)$$

The h^+ can also react with water to generate more radicals as follows:

$$H_2O + h^+ \rightarrow H^+ + {}^{\bullet}OH \quad (5.6)$$

The hydroxyl radicals can also be produced via a photo-Fenton or a Fenton-like mechanism involving the Fe^{3+} ions in the B-site and H_2O_2 according to the following reactions:

$$H_2O_2 + Fe^{3+} \rightarrow Fe - OOH^{2+} + H^+ \quad (5.7)$$

$$Fe - OOH^{2+} \rightarrow Fe^{2+} + HO_2^{\bullet} \quad (5.8)$$

$$H_2O_2 + Fe^{2+} \rightarrow Fe^{3+} + 2HO^{\bullet} \quad (5.9)$$

A direct $h\nu/H_2O_2$ interaction to produce hydroxyl radicals has been ruled out since the dye did not degrade under this condition.

5.4 Conclusions

We have successfully synthesized a perovskite-type material with the general formula $(Eu_{0.5}Bi_{0.2}X_{0.2}Mn_{0.1})FeO_{3-\delta}$ (X = Ca, Sr and Ba). PXRD characterisation shows that the powders annealed at 700, 800 and 900 °C all crystallized in the orthorhombic perovskite lattice with

crystallite sizes ranging between 14 and 26 nm and BET surface areas of 7 and 19 m^2 g^{-1}. VSM analysis shows interesting properties indicating the presence of both FM and AFM characteristics that result in very large coercive field for samples annealed at 800 and 900 °C. The materials also show a series of photoluminescence emission spectra corresponding to excitation energies in the visible region of the electromagnetic spectrum, indicating that they could function as photocatalysts utilising energy within the visible region. Photocatalytic screening of the powder for degradation of the RhB dye showed very good activities for the powders annealed at 900 °C with EuCa900 being the most efficient in mineralising the organic dye into CO_2/H_2. These materials are good candidates for use in the field of environmental chemistry for purification of water contaminated by organic dye. Their ability to degrade organic pollutants could be exploited also in cleaning wastewater from pharmaceutical industries which contain toxic pollutants that have been implicated in endocrine disruption. The improved ferromagnetism exhibited by the EuBa and the EuSr series means that they can be easily recovered by applying a magnetic field. The coercive field values obtained in these materials could also be exploited for possible application in memory devices.

Acknowledgements

IA is grateful to the College of Agriculture, Engineering and Science at the University of KwaZulu-Natal for the award of a Ph.D. bursary and a Doctoral Scholarship. The vibrating sample magnetometer used in this work was provided by the National Research Foundation of South Africa.

References

[1] N. Thongmee, A. Watcharapasorn, S. Jiansirisomboon, Current Applied Physics 8 (2008) 367-371.
[2] I. Grinberg, D.V. West, M. Torres, G. Gou, D.M. Stein, L. Wu, G. Chen, E.M. Gallo, A.R. Akbashev, P.K. Davies, J.E. Spanier, A.M. Rappe, Nature 503 (2013) 509-512.
[3] M.D. Peel, S.E. Ashbrook, P. Lightfoot, Inorganic Chemistry 52 (2013) 8872-8880.
[4] D.S. Paik, S.E. Park, T.R. Shrout, W. Hackenberger, Journal of Materials Science 34 (1999) 469-473.
[5] S. Rousseau, S. Loridant, P. Delichere, A. Boreave, J.P. Deloume, P. Vernoux, Applied Catalysis B: Environmental 88 (2009) 438-447.
[6] W. Luo, L. Zhu, N. Wang, H. Tang, M. Cao, Y. She, Environmental Science & Technology 44 (2010) 1786-1791.
[7] C.-C. Hu, Y.-L. Lee, H. Teng, Journal of Materials Chemistry 21 (2011) 3824-3830.
[8] J. Van Den Brink, D.I. Khomskii, Journal of Physics: Condensed Matter 20 (2008) 12.
[9] S. Kim, E. Choi, A. Bhalla, Ferroelectric Letters 34 (2007) 84-94.
[10] H. Zhang, X. Fu, S. Niu, Q. Xin, Journal of Alloys and Compounds 459 (2008) 103-106.
[11] Z. Lu, L. Chen, Y. Tang, Y. Li, Journal of Alloys and Compounds 387 (2005) L1-L4.
[12] M.W. Lufaso, P.M. Woodward, Acta Crystallographica Section B: Structural Science 60 (2004) 10-20.
[13] R.t. Shannon, Acta Crystallographica Section A: Crystal Physics, Diffraction, Theoretical and General Crystallography 32 (1976) 751-767.
[14] T. Ungár, L. Balogh, G. Ribárik, Metallurgical and Materials Transactions A 41 (2010) 1202-1209.
[15] O. Clemens, R. Kruk, E.A. Patterson, C. Loho, C. Reitz, A.J. Wright, K.S. Knight, H. Hahn, P.R. Slater, Inorganic Chemistry (2014).
[16] P. Junploy, S. Thongtem, T. Thongtem, Superlattices and Microstructures 57 (2013) 1-10.
[17] I. Parkin, A. Komarov, Q. Fang, Polyhedron 15 (1996) 3117-3121.
[18] J. Jiang, J. Zou, M.N. Anjum, J. Yan, L. Huang, Y. Zhang, J. Chen, Solid State Sciences 13 (2011) 1779-1785.
[19] K. Sing, D. Everett, R. Haul, L. Moscou, R. Pierotti, J. Rouquerol, T. Siemieniewska, Pure and Applied Chemistry 54 (1982) 603-619.
[20] G. Xiong, G. Wei, X. Yang, L. Lu, X. Wang, Journal of Materials Science 35 (2000) 931-936.
[21] M. De Guire, S. Dorris, R. Poeppel, S. Morissette, U. Balachandran, Journal of Materials Research 8 (1993) 2327-2335.
[22] Z. Shan, J. Liu, V.M. Chakka, H. Zeng, J. Jiang, IEEE Transactions on Magnetics 38 (2002) 2907-2909.
[23] P. Godara, A. Agarwal, N. Ahlawat, S. Sanghi, R. Dahiya, Journal of Alloys and Compounds 594 (2014) 175-181.

[24] S. Chatterjee, S. Giri, S. De, S. Majumdar, Ferromagnetic/antiferromagnetic exchange coupling in Ni_2MnSn-derived magnetic shape memory alloys, Journal of Physics: Conference Series, IOP Publishing, 2010, pp. 032011-032014.
[25] K.N. Shide, S.J. Dhoble, H.C. Swart, K. Park, Series in Materials Science 174 (2012) 41-60.
[26] W.F. Zhang, Z. Yin, M.S. Zhang, Applied Physics A 70 (2000) 93-96.
[27] W.F. Zhang, J. Tang, J. Ye, Chemical Physics Letters 418 (2006) 174-178.
[28] D. Li, J. Zheng, Z. Zou, Journal of Physics and Chemistry of Solids 67 (2006) 801-806.
[29] L. You-ji, C. Wei, Catalysis Science & Technology 1 (2011) 802-809.
[30] D. Chen, A.K. Ray, Water Research 32 (1998) 3223-3234.
[31] S. Ahmed, M. Rasul, R. Brown, M. Hashib, Journal of Environmental Management 92 (2011) 311-330.
[32] M. Aliabadi, T. Sagharigar, Journal of Applied Environmental Biological Sciences 1 (2011) 620-626.

Chapter 6

Synthesis and the effect of annealing temperature on the structural, magnetic and photocatalytic properties of $(La_{0.5}Bi_{0.2}Sr_{0.2}Mn_{0.1})FeO_{(3-\delta)}$

Ibrahim Abdulkadir, Bice S. Martincigh* and Sreekantha B. Jonnalagadda

School of Chemistry and Physics, University of KwaZulu-Natal, Westville Campus, Private Bag X54001, Durban 4000, South Africa

*Corresponding author: Tel: +27 31 2601394; Fax: +27 31 2603091; E-mail: martinci@ukzn.ac.za

Abstract

Novel perovskite-type nanomaterials with the composition $(La_{0.5}Bi_{0.2}Sr_{0.2}Mn_{0.1})FeO_{3-\delta}$, were synthesized by using the citric acid sol-gel route and annealed at temperatures from 400 to 900 °C. Scanning electron microscopy, and powder X-ray diffraction analysis of the powders showed that they contain crystalline perovskite-type nanoparticles. Crystallinity increased with annealing temperature. The lattice parameters after refinement showed that the particles crystallized in a rhombohedral structure. The Brunuar-Emmet-Teller (BET) specific surface areas ranged between 2 and 21 $m^2 g^{-1}$. Vibrating sample magnetometer analysis of the hysteresis loops showed an increase in coercivity with increasing annealing temperature. Very large coercive fields of about 54 kOe were obtained for samples annealed at 900 °C. Photoluminescence spectroscopy showed that the powders were all active in the visible region and could be useful for visible light photodegradation of organic dyes. The powders were all screened for photocatalytic activity against an organic dye (Rhodamine B) in the visible region of the solar spectrum and the photocatalytic activities were good for powders annealed at 700 °C and above.

Keywords: *multiferroics, coercive field, photoluminescence, photocatalytic activities*.

6.1 Introduction

Numerous studies have focussed on synthesizing and studying materials that can be used to advance technological fields. One outstanding family of materials that have received considerable attention is the perovskites and the perovskite-like materials. These are a group of materials that can generally be represented by the formula ABX_3 (where A^{3+} could be a large rare-earth metal, B^{3+} is a smaller transition metal and X^{2-} is a nonmetal, mostly, oxygen). They have a tendency for displaying an array of very interesting characteristics due to the flexibility of the structure of these compounds and their ability to accommodate almost all the elements on the periodic table in different types of combinations. The perovskite structure lends itself to manipulation by means of simple approaches, thereby creating novel materials with interesting properties suitable for application in advanced technologies. Multiferroic perovskite materials, having both ferromagnetic and ferroelectric properties (e.g. doped and undoped $BiFeO_3$), have been studied extensively due to their potential application in electric and magnetic devices [1-4]. Similarly, rare earth perovskite-like solid solutions have been subjected to intensive investigation due to their potential for use as cathodes in solid oxide fuel cells (SOFC) [5-7], acoustic transducers, piezo- and pyroelectric devices [8-10], sensors [11, 12], memory and capacitor devices [13], as well as environmental catalytic and photocatalytic materials [14-18]. In order to make multiferroic materials, several ions with varying physical properties can be introduced into the material of interest to make it more robust and suited for certain purposes. Introducing ferroelectricity into a given material, for example, can be achieved by either incorporating some d^0 configuration transition metal (TM) ions (e.g. Ti^{4+}) into the system, or by introducing a TM with a lone pair of electrons (e.g. Bi^{3+} and Pb^{2+}) in

which the lone pair is responsible for the ferroelectricity [19, 20]. Introducing some other smaller divalent ions can also create bond length variations and oxygen defects which might enhance the ferromagnetic (FM) properties of the material as well as its photocatalytic properties. Synthesis of these materials normally involves doping, or partially substituting the A^{3+} and/or B^{3+} ions with other metal ions capable of imparting those properties of interest. M^{2+} ions (e.g. Ca^{2+}, Sr^{2+}, Ba^{2+}, Cd^{2+} and Pb^{2+}) have been used to impart novel properties on rare earth perovskite-like solid solutions due to their ability to create bond length variations, oxygen vacancies and defects in the material lattice [21-25]. In this work, we used a Pichini-type sol-gel method to synthesize a novel perovskite-like solid solution, $La_{0.5}(Bi_{0.2}Sr_{0.2}Mn_{0.1})FeO_{3-\delta}$, and then investigated the effect of annealing temperature on the magnetic and photocatalytic properties of these materials at room temperature.

6.2 Experimental

6.2.1 Materials

$Fe(NO_3)_3.9H_2O$ (98%) (Saarchem), La_2O_3 (99.8%) (BDH Chemicals), $Bi(NO_3)_3.5H_2O$ (97%) (Saarchem), $Sr(NO_3)_2$ (99%) (Saarchem), $Mn(CH_3OO)_2$ (98%), $K_2Cr_2O_7$ (99%) Ag_2SO_4 (99%) (Saarchem), citric acid (99.7%) (BDH Chemicals), chemically pure concentrated H_2SO_4 (98%), $HgSO_4$ (99%) and $(NH_4)_2Fe(SO_4)_2.6H_2O$ (99%) (Merck), chemically pure concentrated HCl (37%) and HNO_3 (55%) (Promark Reagents), ethylene glycol (99%) (Promark Chemicals), rhodamine B (The Coleman and Bell Co), and H_2O_2 30% vol. (100 vol) (Minema Chemicals) were used as received. Deionised water from a Millipore Milli-Q Elix 5 UV water purification system was used throughout and hereafter referred to as Milli-Q water.

6.2.2 Synthesis of $(La_{0.5}Bi_{0.2}X_{0.2}Mn_{0.1})FeO_{(3-\delta)}$

$(La_{0.5}Bi_{0.2}Sr_{0.2}Mn_{0.1})FeO_{(3-\delta)}$ samples were prepared by a sol-gel process. $Fe(NO_3)_3.9H_2O$ was dissolved in Milli-Q water (30 cm^3). La_2O_3, $Sr(NO_3)_2$, $Mn(CH_3OO)_2$ and $Bi(NO_3)_3.5H_2O$ were dissolved in dilute nitric acid (about 15 cm^3, 6 mol dm^{-3}) solution to give the amount of metals required in the correct mole ratio. The solutions were mixed thoroughly, made up to 200 cm^3 with Milli-Q water and then gradually poured into a burette. The solution was then added (drop-wise) to a citric acid solution (400 cm^3, 0.15 mols) in a beaker which was continuously stirred by a magnetic stirrer at room temperature to form a single clear solution. Once the addition was completed, and with the solution still stirring, the temperature of the mixture was raised to 90 ^oC. The arrangement was left to evaporate until the volume of the solution was reduced to about 50 cm^3, ethylene glycol (100 cm^3) was added and the heating and stirring continued until a thick gel formed. The gel was then removed from the beaker and placed in a crucible in an oven at 120 ^oC for 24 hrs to dry. The dry gel was subsequently pre-calcined at 400 ^oC for 4 hrs to remove all the organic material. Separate sample portions of the powders were subsequently annealed in a muffle furnace for 4 hrs at annealing temperatures (T_A) of 500, 600, 700, 800 and 900 ^oC.

6.2.3 Characterization

The morphology and microstructure of the powders was analysed by means of a ZEISS Ultra plus field emission gun scanning electron microscope (FEGSEM). The crystal lattice and crystallite size were determined by powder X-ray diffraction (PXRD) analysis. The diffractograms were collected on a Bruker D8 Advance diffractometer equipped with a Cu K_α radiation source and the Scherrer equation $D = k\lambda/\beta\cos\theta$ (where D is the crystallite size, k is the Scherrer constant, λ is the wavelength of the radiation

and β is the full width at half maximum) was used to calculate the average crystallite sizes of the powder particles. Surface areas were determined by nitrogen adsorption and the BET equation method using a Micromeritrics Tristar II 3020 fully automated three station surface area and porosity measuring instrument. The magnetic properties were studied with a LakeShore model 735 vibrating sample magnetometer (VSM) which had been calibrated by using a standard Ni sphere of saturation magnetization 54.7 emu g^{-1}. The maximum applied magnetic field was 14 kOe and the measurements were performed at room temperature. Thermogravimetric analysis (TGA) and differential scanning calorimetry (DSC) measurements were obtained for each sample using a TG/DTA thermal analyzer (TA instruments SDT Q600 thermal analyzer) in air. The temperature range of the analysis was between 25 to 1000 °C. FTIR spectra for each sample was recorded on a PerkinElmer FTIR spectrum 100 fitted with an attenuated total reflectance (ATR) accessory. The photoluminescence spectra were monitored at three excitation wavelengths (380, 390 and 400 nm) by means of a PerkinElmer LS 55 spectrofluorimeter equipped with a high energy pulsed xenon source for excitation.

6.2.4 Photocatalytic screening

The photocatalytic activity of each sample was tested on rhodamine B (RhB) dye in the presence of H_2O_2 at room temperature. A 26 W fluorescent lamp (Osram Dulux D, 26 W, 1800 lm) placed in a quartz jacket at about 7 cm from the top of the dye solution was used as the source of white light. A mass of 1.5 g dm^{-3} of each of the powders was used for the test. Aliquots of the irradiated dye solution were withdrawn at regular intervals and analyzed by means of a Biochrom Libra S6 UV spectrophotometer and a Shimadzu UV-3600 UV-VIS-NIR spectrophotometer at the wavelength of maximum absorption (λ_{max}) for RhB (556 nm).

6.3 Results and discussion

A total of six powder samples were obtained after annealing at different temperatures. The sample calcined at 400 °C was labelled as LaSr400, other samples where similarly labelled with the last three digits representing the temperature at which the powder was annealed. The colour of the samples changed from dark brown for LaSr400 to black for LaSr700 to 900.

6.3.1 Phase purity and crystallinity

Figure 6.1a shows the powder X-ray diffractograms for the samples annealed at temperatures from 400 to 900 °C. The evolution of the perovskite peaks of 100, 110, 111, 200, 210 and 211 planes can be observed at T_A of 400 °C but the powder can be said to be composed of mixed oxides at this T_A. At 500 °C, the perovskite pattern has formed fully and the crystallinity and purity of the crystals increases with increasing T_A through 600 to 700 °C. This is evident in the increase in sharpness and intensity of the peaks and the disappearance of all impurity peaks on the diffractograms indicating the formation of a single phase perovskite-like crystal. All peaks were indexed to a rhombohedral perovskite pattern with space group R3C by using the Diffrac^{plus} software. The peak positions for the very small peaks from T_A = 800 to 900 °C indicated by (*) correspond to peak positions for an orthorhombic perovskite lattice and could be attributed to the onset of transformation of the crystals from the rhombohedral to the orthorhombic lattice, indicating the possibility of a full transformation of the lattice at higher T_A. another reason for these peaks could be phase separation, which would lead to the emergence of a secondary phase within the powder lattice. Table 6.1 shows the calculated lattice parameters and the crystal sizes obtained by using the Scherrer equation. The unit cell volume is observed to increase from T_A = 500 °C to T_A

700 °C, which also corresponds to the powders having the highest peak intensity. Figure 6.1b shows the peak intensities of the 211 plane for all the powders and the intensity for T_A 700 °C can be seen to be highest (the same scale for vertical axes is used for all diffractograms). The absence of impurity peaks at this T_A is also an indication that all the ions have been incorporated into the rhombohedral lattice. A little reduction in cell volume is also observed at T_A = 800 °C and T_A = 900 °C. This is attributed to the distortion in the rhombohedral lattice which, as stated earlier could indicate phase separation or the beginning of a transformation of the lattice to an orthorhombic lattice.

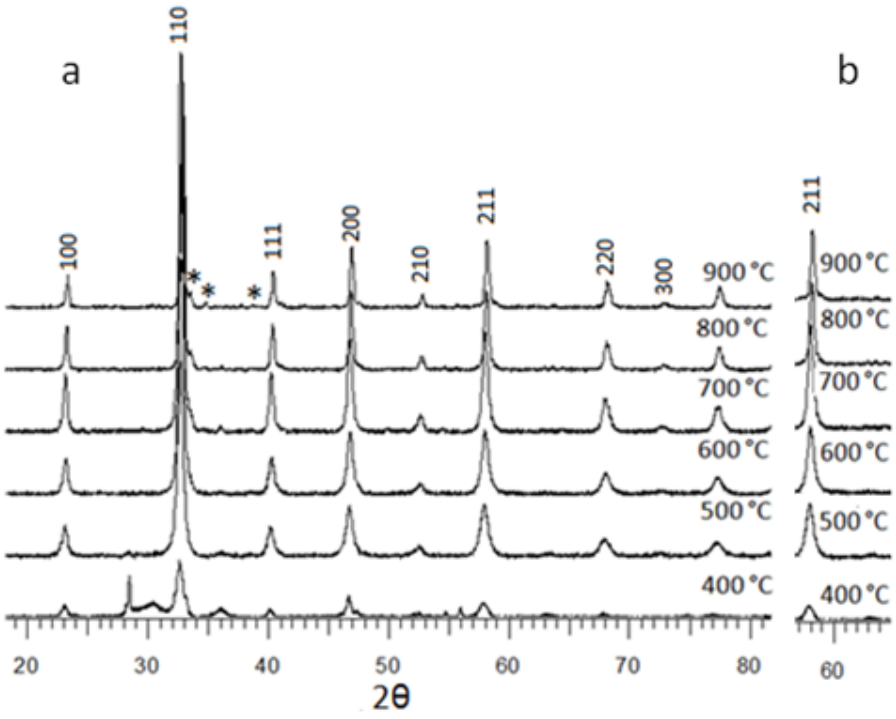

Figure 6.1: Powder X-ray diffraction peaks for $La_{0.5}(Bi0_{.2}Sr_{0.2}Mn_{0.1})FeO_{(3-\delta)}$ annealed at temperatures (T_A) from 400 to 900 °C, and (b) showing the evolution and slight shift in 211 plane towards smaller angle due to strain.

Table 6.1: Lattice parameters for $La_{0.5}(Bi0_{.2}Sr_{0.2}Mn_{0.1})FeO_{(3-\delta)}$ annealed at different temperatures.

Samples	Cell parameters				Space group	Lattice system	R/R_0	SSA/m^2 g^{-1} (± 0.01)
	a/Å	b/Å	c/Å	V/$Å^3$				
LaSr500	5.522	5.522	13.397	408.516	*R3C*	Rhomb.	8.41	20.57
LaSr600	5.517	5.517	13.390	407.626	*R3C*	Rhomb.	7.85	16.81
LaSr700	5.528	5.528	13.446	410.943	*R3C*	Rhomb.	8.51	8.68
LaSr800	5.511	5.511	13.407	407.156	*R3C*	Rhomb.	7.99	3.90
LaSr900	5.508	5.508	13.408	406.769	*R3C*	Rhomb.	7.18	2.26

6.3.2 BET specific surface area

The N_2 adsorption-desorption isotherms of the powders (Figure. 6.2) all display a type II pattern according to the IUPAC classification [26]. The specific surface areas (SSA) for the synthesized powders ranged from 2.26 to 22.34 m^2 g^{-1} with the SSA decreasing as the T_A increases (see Table 6.1). The relative pressure can be seen to push towards $P/P_0 = 1$ indicating the predominance of larger pores at higher calcination temperatures. Figure 6.2 (inset) shows the pore size distribution of the materials for T_A from 500-900 °C. The mesopores in the samples annealed at the lower T_A disappear rapidly at high T_A and flatten out completely at T_A of 900 °C. The cumulative effect of this is a steady decrease in the value of the SSA as the annealing temperature increases (Figure 6.3). The SSA values fall within the SSA values obtained for similar materials that have been prepared by using a similar procedure [27]. The activation energy for the reduction of the surface area can be calculated by using the Arrhenius plot of the natural log of the BET SSA against the reciprocal of the annealing temperature according to

$$ln\, S_{BET} = ln\, A - \frac{E_A}{R}(1|T) \qquad (6.1).$$

Where S_{BET} is BET surface area, E_A is the activation energy for surface reduction, R is the universal gas constant (value 8.314 J K^{-1} mol^{-1}), T is the annealing temperature , and A is a constant.

The activation energy for the reduction of the surface area calculated from Figure 6.4 is 43±7 kJ mol^{-1}.

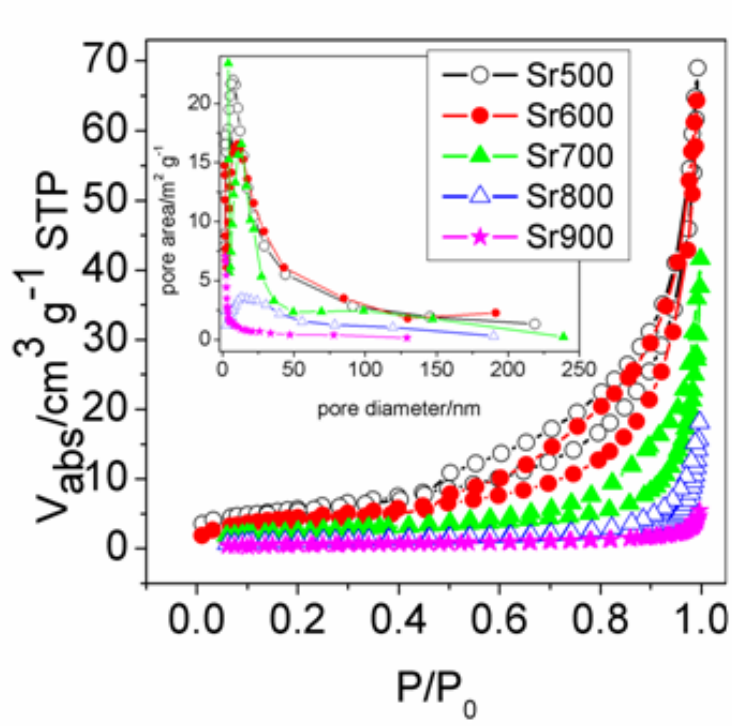

Figure 6.5: N_2 adsorption-desorption isotherms obtained at 77 K for LaSr500-900. Inset shows the pore size distribution for the corresponding isotherms.

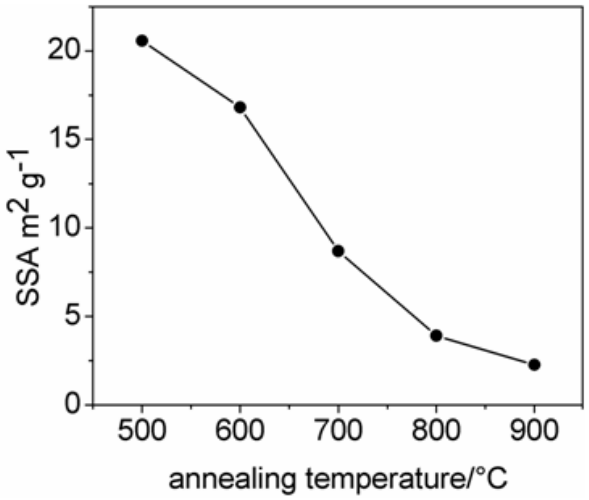

Figure 6.6: decrease in SSAs of the powders as annealing temperature increases.

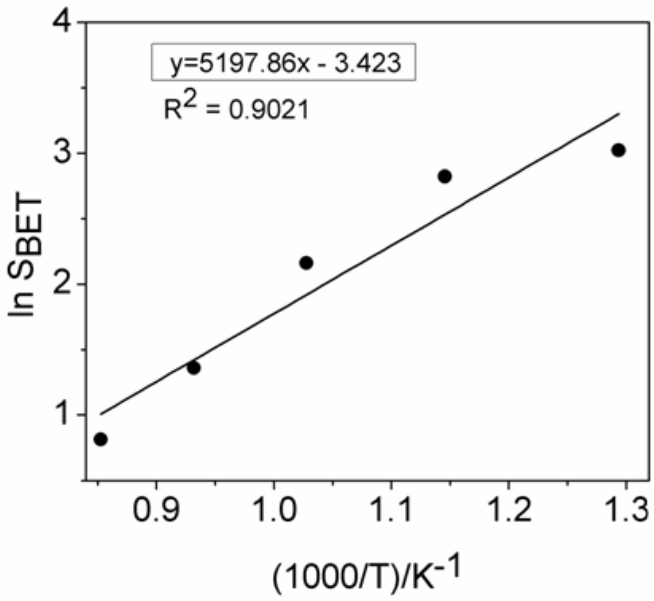

Figure 6.7: The Arrhenius plot drawn to obtain the activation energy for the reduction of the surface area with increasing annealing temperature.

6.3.3 Surface characterisation

The Fourier transform infrared spectra for the samples are presented in Figure 6.5. The spectra show peaks of interest at two distinct regions. The peaks that occur at about

1470 cm^{-1} have been assigned to symmetric and asymmetric ionized carboxyl group stretching vibrations from carbonates and adsorbed O-H and CO_2 groups that are present on the powder surface, while peaks that occur at around 570 cm^{-1} are due to the stretching and vibrating modes of metal-O bonds [28, 29]. The gradual disappearance of the carbonate peaks at higher T_A and the simultaneous increase of the metal-O peaks indicates the progress in the formation of the perovskite crystals in agreement with the PXRD results.

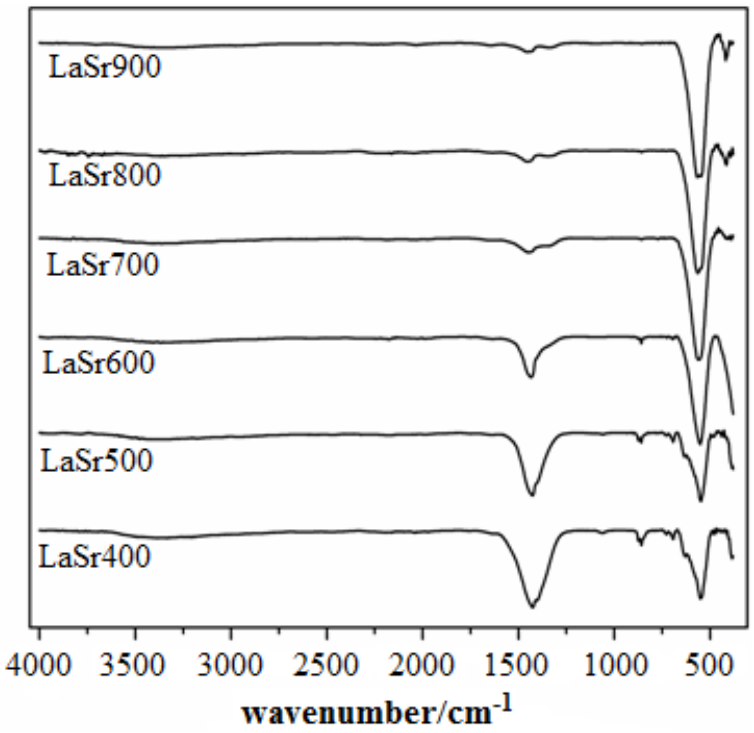

Figure 6.5: FTIR-ATR spectra of synthesizd powders.

6.3.4 Thermal stability

Thermogravimetric analysis (TGA) and differential scanning calorimetry (DSC) measurements were carried out on a small portion of the LaSr400 powder and the

thermal response was monitored between the temperature range of 25 and 1000 °C. As expected, a gradual drop in weight is observed between the temperature range of 25-475 °C representing the removal of surface water molecules and any other small molecules such as CO_2 present (Figure 6.6). The sharp drop in weight between 480-660 °C has been attributed to decomposition of all organic entities, such as oxalates and carbonates, accompanied by the release of a large amount of carbon dioxide further to a temperature of about 700 °C. Very small increases in weight can be observed from about 740 °C to about 880 °C and this has been attributed to oxygen uptake by the powder. There were no visible exotherms on the DSC curve representing the crystallization point of the powder. This is because, as can be seen from the PXRD plots (Figure 6.1), the perovskite phase appears to have crystallized during the pre-annealing treatment of the powders and all the peaks can be seen at T_A of 400 °C.

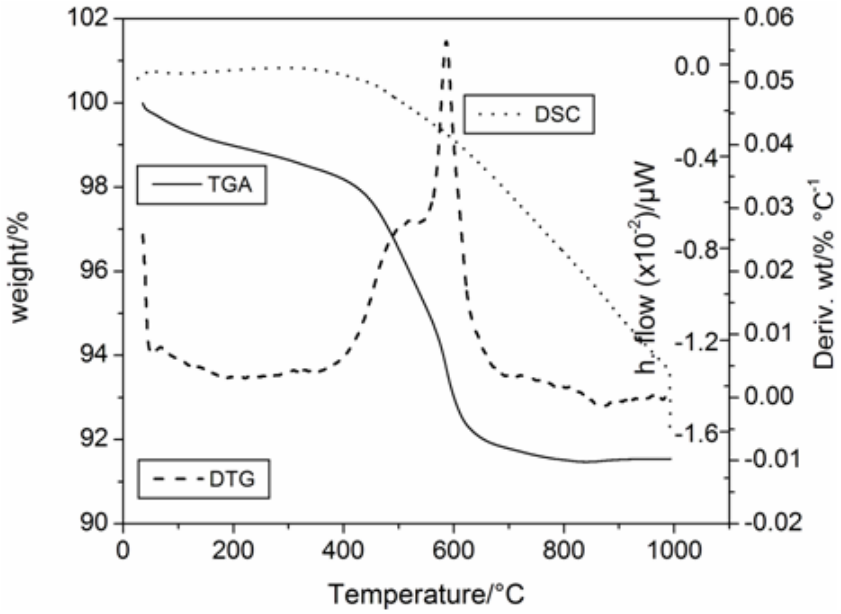

Figure 6.6: TGA-DSC plot showing the thermal proccesses occurring at various temperatures for LaSr400.

6.3.5 Magnetic properties

The magnetic properties of the samples were investigated by means of a vibrating sample magnetometer and the room temperature magnetization profiles are presented in Figure 6.7. The hysteresis loops all show largely ferromagnetic properties with varying degrees of maximum magnetization. The drop in maximum magnetization with increasing annealing temperature can be attributed to an increase in order in the magnetic sites [30]. This can also be seen from the PXRD peaks in Figure 6.1. At T_A 400 °C, the powder is mainly composed of mixed metallic oxides the result of which is that higher magnetization observed. With increasing T_A, however, more of the metal oxides are incorporated into the perovskite lattice which gives rise to an increase in order of the magnetic sites and hence a reduction in maximum magnetization [31, 32]. From the PXRD peaks of these powders, the perovskite lattice becomes fully formed at T_A 600-700 °C. This corresponds to powders with the lowest values for magnetization and also the point at which the rapid increase in coercivity begins (Figure 6.7a). The coercive field values for annealed powders increased with increase in T_A between 400-600 °C, from T_A of 700 °C. However, much larger increases in the coercive field of powders is observed through to T_A = 900 °C, which has the largest coercive field value of 5.50 kOe (Figure 6.7b). The large coercive fields observed can be attributed to one, or a combination of the following reasons: (i) an increase in coercive field can occur due to an increase in crystallite sizes of materials which is related to the multi-domain energy barrier due to magnetic anisotropy, and (ii) the effect of exchange coupling due to interactions between the ferromagnetic (FM) and the antiferromagnetic components/phases within the powder matrix [33-37]. We believe that the latter effect

plays a more prominent role in producing the coercive field values observed in our powders. The constriction on the loops is typical for powders containing a combination of hard and soft magnetic properties, which indicates that the powders contain a secondary magnetic phases [38]. The increase in magnetization observed from T_A = 700 °C through T_A = 900 °C is attributed to the increase in the crystallite size of the perovskite phase (see Table 6.2). The room temperature magnetization parameters for all the powders are presented in Table 6.2. A general description of the dependence of the room temperature saturation magnetisation M_S and coercive field H_C of the powders with the changes in T_A shows that the magnetic properties of the powders annealed at temperatures from 400 to 900 °C is marked by two distinct stages. The first is the T_A = 400 to 600 °C, which is marked by a rapid reduction in maximum magnetization, and the second is the T_A = 700 to 900 °C, which is marked by a rapid increase in the value of the coercive field, and these variations are shown in Figure 6.8. An increasing M_R/M_S ratio, which corresponds to an increase in M_R values, is an indication of the increase in the ferromagnetic properties of the material as well as its hardness.

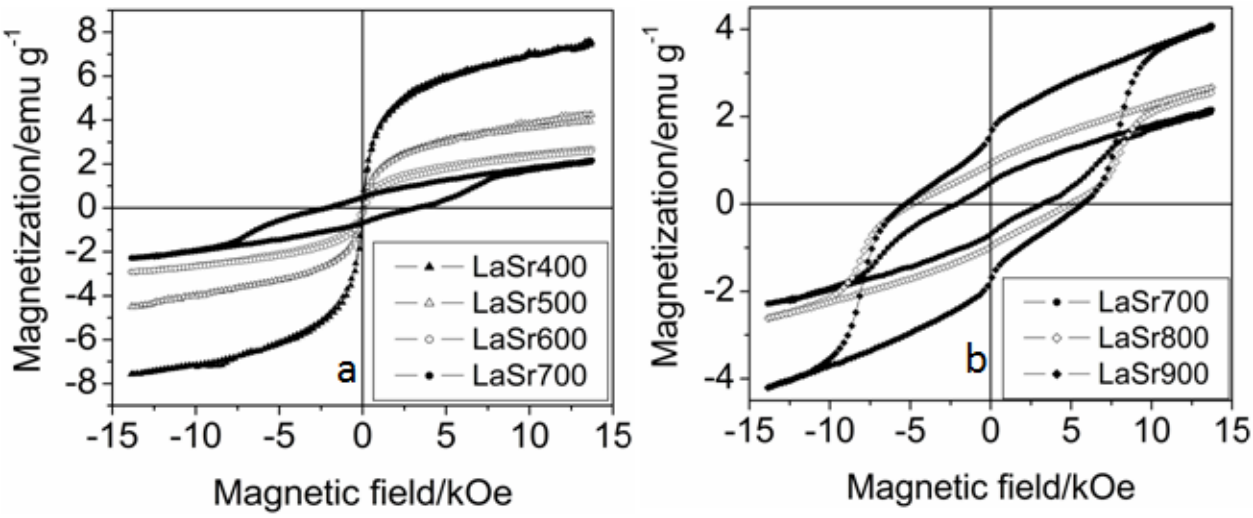

Figure 6.7: M-H loops for samples annealed at different T_A: (a) samples LaSr400-700, and (b) samples LaSr700-900.

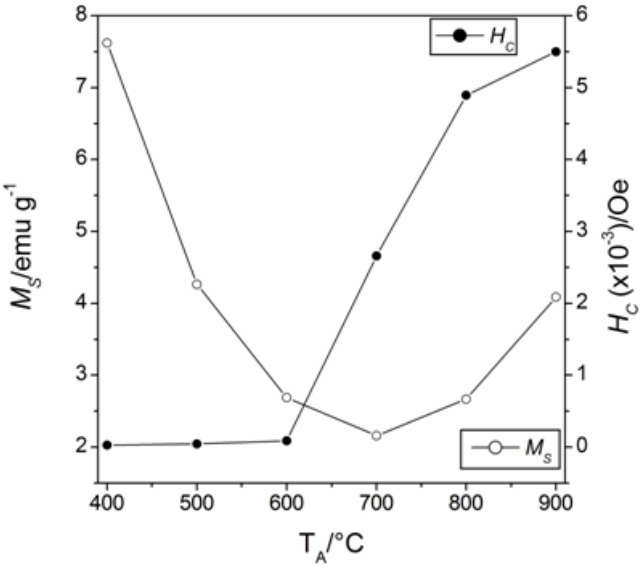

Figure 6.8: Variation of M_S and H_C with increasing T_A for LaSr400-900.

Table 6.2: VSM magnetization parameters for LaSr400-900 measured at room temperature. Crystallite sizes were obtained from PXRD by using the Scherrer equation.

Samples	M_S/emu g^{-1} (± 0.4)	M_R/emu g^{-1} (± 0.4)	H_C/Oe (± 1)	M_S/M_R	Crystallite sizes/nm (± 1.5)
LaSr400	7.62	0.12	29.19	0.031	19.62
LaSr500	4.26	0.02	46.72	0.036	20.68
LaSr600	2.68	0.03	87.88	0.059	21.68
LaSr700	2.16	0.49	2659.0	0.265	26.65
LaSr800	2.67	0.92	4892.7	0.360	34.71
LaSr900	4.09	1.61	5497.3	0.405	40.56

6.3.6 Microstructural characterisation

The SEM images for the samples annealed at (a) 400, (b) 700 and (c) 900 °C are shown in Figure 6.9. The micrographs shows tiny spherical crystals forming at T_A = 400 °C (Figure 6.9a) within the matrix. These spherical crystals constitute the initial stage of crystal growth right after the nucleation process. Annealing the powders at higher T_A leads to an increase in crystal size due to incorporation of more ions into the crystals in the growth stage (Figure 6.9b and 6.9c) of crystal formation as can be observed in the images and also corroborated by the PXRD and FTIR data. The crystal sizes as observed in the micrographs also agree with the values calculated by using the Scherrer equation, which are given in Table 6.2.

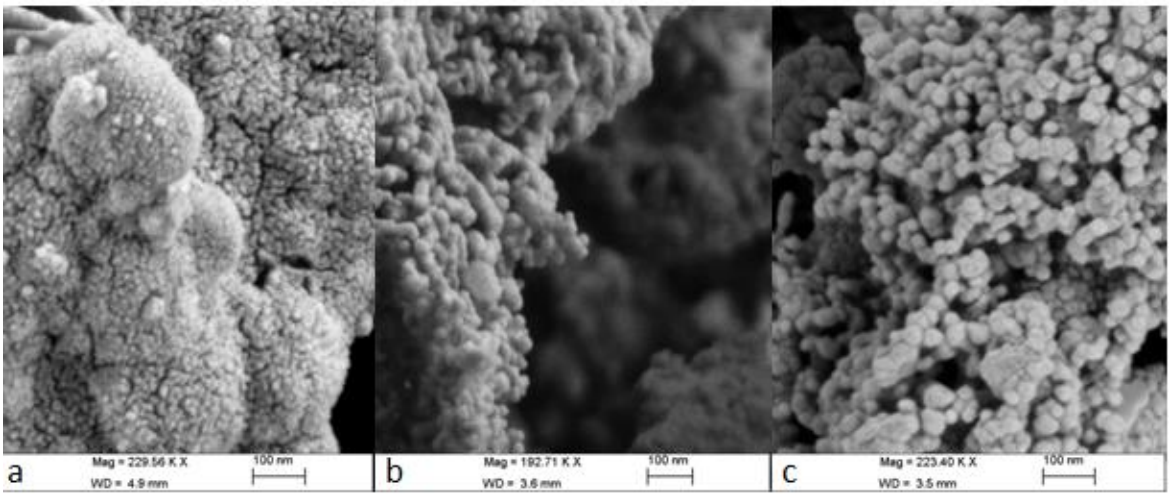

Figure 6.9: SEM images for (a) LaSr400, (b) LaSr700, and (c) LaSr900.

6.3.7 Photoluminescence

Figures 6.10 and 6.11 show the room temperature emission of these materials showing a T_A dependent photoluminescence (PL) spectral intensity. The spectra show an initial decrease in the PL intensity as T_A changes from 400 to 600 °C for an excitation wavelength of 380 nm (Figure 6.10), and subsequently, an increase in intensity is observed for increasing T_A values (Figure 6.11). Figure 6.11 shows the PL spectra for powders annealed at T_A values from 600 to 900 °C. The powders were excited at three different λ_{ex} values and the emission was monitored between 530 to 660 nm. Three emission peaks were observed with λ_{em} shifting correspondingly with the shift in λ_{ex}.

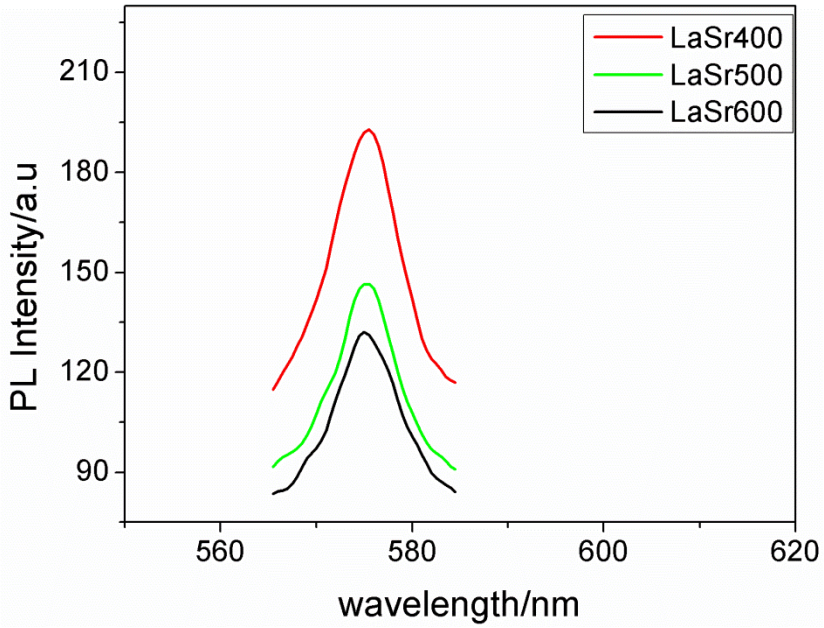

Figure 6.10: PL spectra showing the emission peak intensities for the samples indicated, the excitation wavelength was 380 nm.

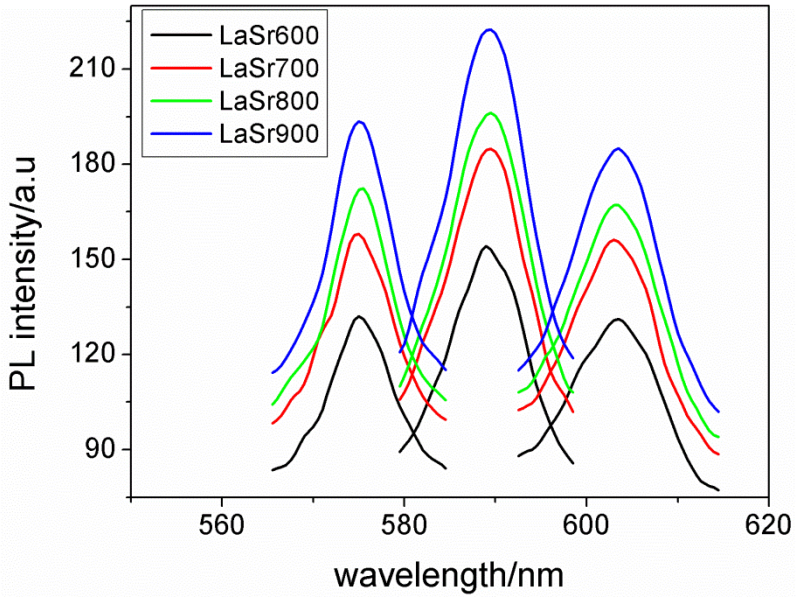

Figure 6.11: PL spectra showing shifts in the emission peak positions as excitation wavelength is varied. The excitation wavelengths are indicated along with the peaks (a) λ_{ex} = 380 nm, (b) λ_{ex} = 390 nm and (c) λ_{ex} = 400 nm.

Generally, however, the peak intensities for these peaks increased for powders annealed at higher T_A values as can be seen from Figure 6.11. The increase in peak intensity here appears to reflect the corresponding increase in crystallinity and crystal size [39]. The origin of the initial decrease in the PL intensity, therefore, would be as a result of the perovskite lattice evolution and the lattice structure order-disorder effect occurring at various stages of the T_A [40-42]. The excitation energies fall within the visible region which indicates that the powders can be used as photocatalysts for decomposition of organic materials.

6.3.8 Photocatalytic screening

The results of the photocatalytic screening of the powders on rhodamine B dye are presented in Figure 6.12. The results (Figure 6.12a) show an increasing but slow rate of photodegradation of the RhB dye by LaSr400, LaSr500 and LaSr600. According to the data obtained from FTIR and TGA analysis at these stages the powders still contain carbonates, which probably act to interfere with active photodegradation sites on the catalysts. As more of the obstructing carbonates are removed, the photocatalytic activity increased. A more rapid decolourization rate is observed for LaSr700, LaSr800 and LaSr900. The highest decolourization rate was recorded for LaSr700. This may be attributed to the fact that at T_A = 700 °C, all interfering carbonates have already been removed allowing for a maximally active surface for adsorption and decolourization. Also, LaSr700 has the highest surface area when compared to LaSr800 and LaSr900. The drop in absorption between -30 and 0 minutes is due to the molecules adsorbed on the surface of the photocatalysts; the photodegradation starts at 0 minute when the lamp is switched on. Figure 6.12b shows the results of the photodegradation of the dye when H_2O_2 (3.0×10^{-5} mol dm^{-3}) is added. H_2O_2 without light does not degrade the dye,

while the dye molecules desorb faster than degrade for LaSr400 and LaSr500. Much more rapid decolourization rates can be seen for LaSr700, LaSr800 and LaSr900. Figure 6.13 shows the reduction of the absorption intensity as the dye is degraded by LaSr700 at different contact time.

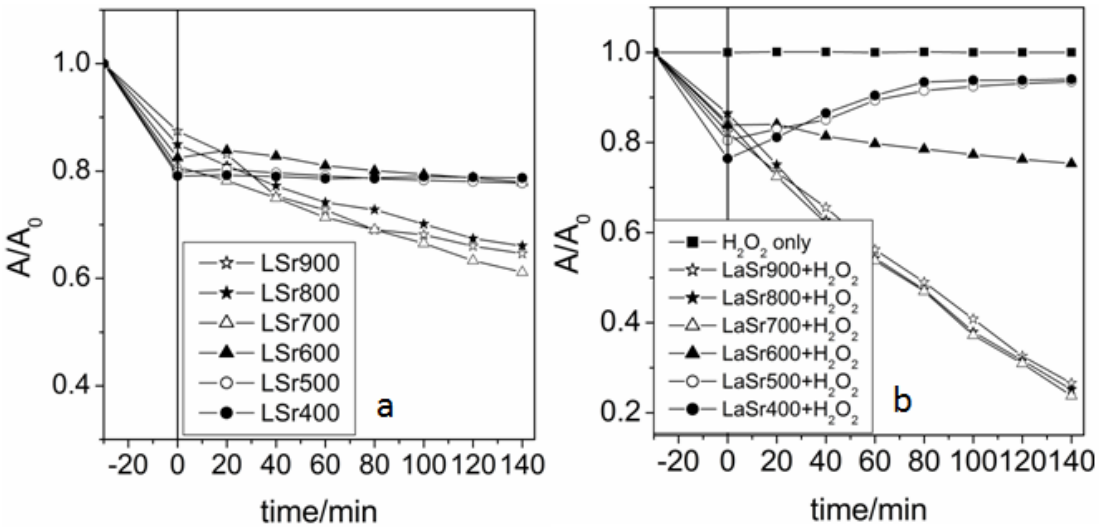

Figure 6.12: Photodegradation of RhB (a) in the presence of photocatalyst and irradiation, and (b) in the presence of photocatalyst, light and H_2O_2.

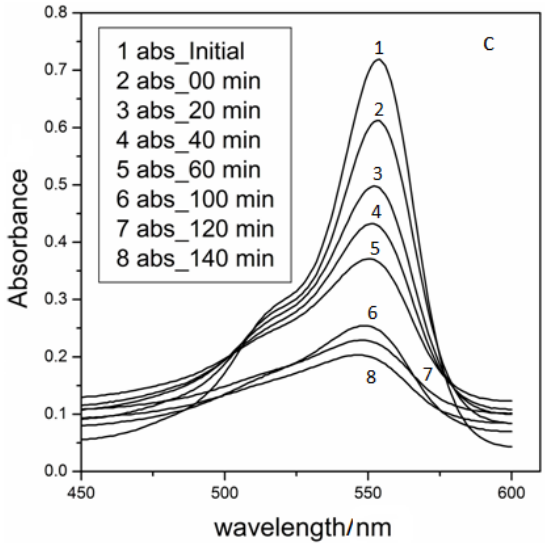

Figure 6.13: degradation profile of RhB dye under irradiation with visible light and in the presence of H_2O_2 (3.0×10^{-5} mol dm^{-3}).

The photocatalytic process follows a pseudo-first-order pattern and can be described by the first order kinetics equation $ln(C/C_0) = k_{abs}t$, where C_0 and C are the initial concentration and concentration of the dye at time t, and k_{obs} is the observed rate constant. Figure 6.14 shows the kinetics plots for the most active systems as observed in the photocatalytic screening. The rate constants are shown in Table 6.3.

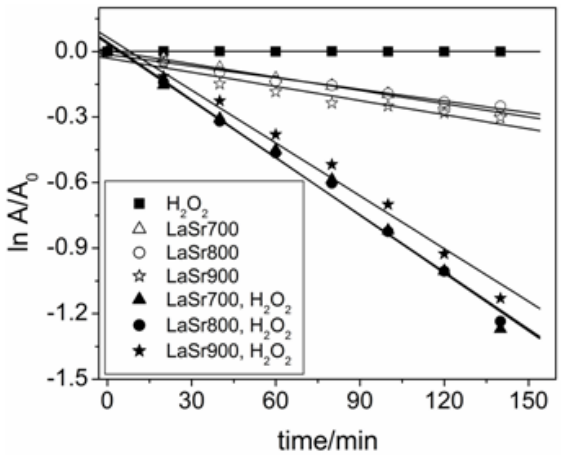

Figure 6.14: linear plots for LaSr700, LaSr800 and LaSr900 (1.5 g dm^{-3} of catalyst) in the presence and absence of H_2O_2 (3.0 x 10^{-5} mol dm^{-3}).

Table 6.3: Rate constants for the photocatalyst (1.5 g dm^{-3})/H_2O_2 (3 × 10^{-5} mol dm^{-3}) systems at the natural pH of the dye.

Reaction conditions	k_{obs}/min^{-1}
H_2O_2 only	3.7×10^{-5}
LaSr700	2.0×10^{-3}
LaSr800	1.8×10^{-3}
LaSr900	2.2×10^{-3}
LaSr700/H_2O_2	8.8×10^{-3}
LaSr800/H_2O_2	8.7×10^{-3}
LaSr900/H_2O_2	8.1×10^{-3}

6.3.8.1 Mineralization

The results of the carbon oxygen demand (COD) analysis of the degraded dye solution after 3 hours of photodegradation activity is presented in Figure 6.15. All the dye solutions became colourless after 180 min. of irradiation. It can be seen that mineralization is highest in the solution that has been photodegraded in the presence of LaSr700. The degree of mineralization in the presence of LaSr800 and LaSr900 are close, with COD values of 48 and 46 mg dm^{-3} respectively. The COD values are an indicator that some of the dye molecules have only been broken down to smaller colourless organic molecules and may require longer irradiation period for complete mineralization.

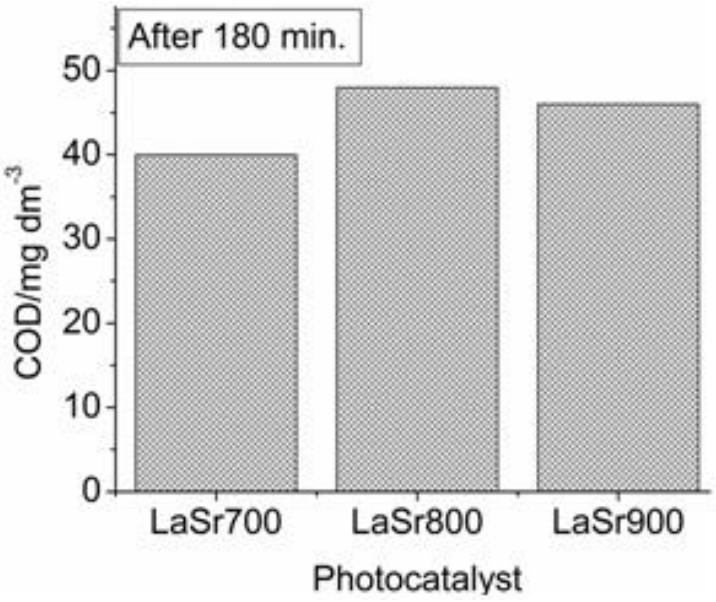

Figure 6.15: Extent of mineralization of RhB dye in the presence of photocatalyst, H_2O_2, and visible light after 3 hours.

6.4 Conclusions

A novel rare earth perovskite-type material $(La_{0.5}Bi_{0.2}Sr_{0.2}Mn_{0.1})FeO_{(3-\delta)}$ has been synthesized and its structure, and magnetic and photocatalytic properties investigated by powder X-ray diffraction, Fourier transform infrared spectroscopy, thermogravimetric analysis, vibrating sample magnetometer and photoluminescence spectroscopy. The results of the analysis show that the powders annealed at different temperatures crystallized in a rhomboheral lattice. The crystallization started right from the point of the precalcination (i.e. 400 °C) with crystallinity increasing for higher annealing temperatures (T_A). The BET surface areas for the powders was within the range 2.26-20.57 m^2g^{-1}. The VSM results show that the powders are weakly ferromagnetic with coercive fields increasing to above 5400 Oe for the powder annealed at T_A = 900 °C. Photoluminescence spectroscopy shows that the powders absorbed within the visible region indicating they might be useful for visible light photodegradation of pollutant organic molecules. The photocatalytic screening of the powders was tested on a rhodamine b dye solution. The powders annealed at T_A = 700, 800 and 900 °C were the most active in decolourizing the dye solution. The materials present an opportunity for the utilization of sunlight as a limitless source of energy. Its ferromagnetic properties mean that it can easily be recovered from the dye solution and reused. The synthesized materials are good candidates for photocatalytic degradation of organic dyes.

Acknowledgements

IA is grateful to the College of Agriculture, Engineering and Science at University of KwaZulu-Natal for the award of a PhD bursary and a Doctoral Scholarship. The

Vibrating Sample Magnetometer used in this work was provided by the National Research Foundation of South Africa.

References

[1] K. Sardar, J. Hong, G. Catalan, P.K. Biswas, M.R. Lees, R.I. Walton, J.F. Scott, S.A. Redfern, Journal of Physics: Condensed Matter 24 (2012) 045905-045912.
[2] H. Lahmar, S. Habouti, C.-H. Solterbeck, M. Dietze, M. Es-Souni, Journal of Applied Physics 107 (2010) 024104-024111.
[3] A. Lahmar, K. Zhao, S. Habouti, M. Dietze, C.-H. Solterbeck, M. Es-Souni, Solid State Ionics 202 (2011) 1-5.
[4] S. Kim, E. Choi, A. Bhalla, Ferroelectric Letters 34 (2007) 84-94.
[5] S.J. Skinner, Fuel Cells Bulletin 4 (2001) 6-12.
[6] S.J. Skinner, International Journal of Inorganic Materials 3 (2001) 113-121.
[7] E. Maguire, B. Gharbage, F. Marques, J. Labrincha, Solid State Ionics 127 (2000) 329-335.
[8] L. Ramajo, M. Castro, A. del Campo, J. Fernandez, F. Rubio-Marcos, Journal of the European Ceramic Society 34 (2014) 2249-2257.
[9] M.D. Peel, S.E. Ashbrook, P. Lightfoot, Inorganic Chemistry 52 (2013) 8872-8880.
[10] D.S. Paik, S.E. Park, T.R. Shrout, W. Hackenberger, Journal of Materials Science 34 (1999) 469-473.
[11] V. Lantto, S. Saukko, N. Toan, L. Reyes, C. Granqvist, Journal of Electroceramics 13 (2004) 721-726.
[12] M. Ghasdi, H. Alamdari, S. Royer, A. Adnot, Sensors and. Actuators B: Chemical 156 (2011) 147-155.
[13] C.-Y. Chung, Y.-S. Chang, G.-J. Chen, C.-C. Chung, T.-W. Huang, Solid State Communications 145 (2008) 212-217.
[14] J. Zhu, H. Li, L. Zhong, P. Xiao, X. Xu, X. Yang, Z. Zhao, J. Li, ACS Catalysis (2014) 2917-2940.
[15] K. Yu, S. Yang, C. Liu, H. Chen, H. Li, C. Sun, S.A. Boyd, Environmental Science & Technology 46 (2012) 7318-7326.
[16] J. Tang, Z. Zou, J. Ye, The Journal of Physical Chemistry C 111 (2007) 12779-12785.
[17] M. Machida, J.-i. Yabunaka, T. Kijima, Chemistry of Materials 12 (2000) 812-817.
[18] L. Fei, J. Yuan, Y. Hu, C. Wu, J. Wang, Y. Wang, Crystal Growth & Design 11 (2011) 1049-1053.
[19] J. Van Den Brink, D.I. Khomskii, Journal of Physics: Condensed Matter 20 (2008) 434217-434228.
[20] D.I. Khomskii, Journal of Magnetism and Magnetic Materials 306 (2006) 1-8.
[21] J. Yang, W. Yelon, W. James, Z. Chu, M. Kornecki, Y. Xie, X. Zhou, H. Anderson, A.G. Joshi, S. Malik, Physical Review B 66 (2002) 184415-184423.
[22] K. Takahashi, M. Tonouchi, Journal of Magnetism and Magnetic Materials 310 (2007) 1174-1176.
[23] J. Li, X. Kou, Y. Qin, H. He, Physica Status Solidi (a) 191 (2002) 255-259.
[24] M.B. Bellakki, V. Manivannan, J. Das, Materials Research Bulletin 44 (2009) 1522-1527.
[25] M. Azuma, H. Kanda, A.A. Belik, Y. Shimakawa, M. Takano, Journal of Magnetism and Magnetic Materials 310 (2007) 1177-1179.

[26] K. Sing, D. Everett, R. Haul, L. Moscou, R. Pierotti, J. Rouquerol, T. Siemieniewska, Pure Appl. Chem 54 (1982) 603-619.
[27] L. Bouyssieres, R. Schifferli, L. Urbina, P. Araya, J.M. Palacios, Journal of the Chilean Chemical Society 50 (2005) 407-412.
[28] G.R.O. Silva, J.C. Santos, D.M. Martinelli, A.M.G. Pedrosa, M.J.B. de Souza, D.M.A. Melo, Materials Sciences and Applications 1 (2010) 39-45.
[29] M. Lee, J. Jun, J. Jung, Y. Kim, S. Lee, Bullettin of the Korean Chemical Society 26 (2005) 1591-1596.
[30] A.A. Cristóbal, P.M. Botta, P.G. Bercoff, J.M. Porto López, Materials Research Bulletin 44 (2009) 1036-1040.
[31] X.-M. Liu, S.-Y. Fu, C.-J. Huang, Materials Science and Engineering: B 121 (2005) 255-260.
[32] P.E. Kazin, L.A. Trusov, S.E. Kushnir, N.V. Yaroshinskaya, N.A. Petrov, M. Jansen, Journal of Physics: Conference Series 200 (2010) 072048-072051.
[33] K. Sadhana, K. Praveena, S. Matteppanavar, B. Angadi, Applied Nanoscience 2 (2012) 247-252.
[34] K. Parekh, Indian Journal of Pure and Applied Physics 48 (2010) 581-585.
[35] S. Majumdar, H. Huhtinen, S. Granroth, P. Paturi, Journal of Physics: Condensed Matter 24 (2012) 206002-206009.
[36] P. Godara, A. Agarwal, N. Ahlawat, S. Sanghi, R. Dahiya, Journal of Alloys and Compounds 594 (2014) 175-181.
[37] S. Chatterjee, S. Giri, S. De, S. Majumdar, Ferromagnetic/antiferromagnetic exchange coupling in Ni_2MnSn-derived magnetic shape memory alloys, Journal of Physics: Conference Series (2010) 032011-032014.
[38] D. Schmool, N. Keller, M. Guyot, R. Krishnan, M. Tessier, Journal of Magnetism and Magnetic Materials 195 (1999) 291-298.
[39] Z. Lu, L. Chen, Y. Tang, Y. Li, Journal of Alloys and Compounds 387 (2005) L1-L4.
[40] J. Milanez, A.T. de Figueiredo, S. de Lazaro, V.M. Longo, R. Erlo, V.R. Mastelaro, R.W. Franco, E. Longo, J.A. Varela, Journal of Applied Physics 106 (2009) 043526-043526-043527.
[41] L. Cavalcante, A. Simoes, J. Espinosa, L. Santos, E. Longo, J. Varela, P. Pizani, Journal of Alloys and Compounds 464 (2008) 340-346.
[42] M. Anicete-Santos, E. Orhan, M. de Maurera, L. Simoes, A. Souza, P. Pizani, E. Leite, J. Varela, J. Andrés, A. Beltrán, Physical Review B 75 (2007) 165105-165115.

Chapter 7

Synthesis and the effect of annealing temperature on the structural, magnetic and photocatalytic properties of $(La_{0.5}Bi_{0.2}Ba_{0.2}Mn_{0.1})FeO_{(3-\delta)}$

Ibrahim Abdulkadir, Bice S. Martincigh* and Sreekantha B. Jonnalagadda

School of Chemistry and Physics, University of KwaZulu-Natal, Westville Campus, Private Bag X54001, Durban 4000, South Africa

*Corresponding author: Tel: +27 31 2601394; Fax: +27 31 2603091; E-mail: martinci@ukzn.ac.za

Abstract

Novel $La_{0.5}Bi_{0.2}Ba_{0.2}Mn_{0.1}FeO_{3-\delta}$, with a perovskite-like structure, was synthesized by using the citric acid sol-gel route. The powder was precalcined at 400 °C and then separate portions were annealed at temperatures of 500, 600, 700, 800 and 900 °C. Transmission electron microscopy and powder x-ray diffraction analysis of the powders showed that they contain crystalline rhombohedral perovskite-type nanoparticles. The BET specific surface areas ranged between 4.19 and 27.75 $m^2 g^{-1}$, decreasing with increasing annealing temperature. Vibrating sample magnetometer analysis of the hysteresis loops showed an increase in coercive field with increasing annealing temperature. Very large coercive fields of about 5.57 kOe were obtained for samples annealed at 900 °C. Photoluminescence spectroscopy showed that all the powders were active in the visible region and could be useful for visible light photodegradation of pollutants. The powders were all screened for photocatalytic activity against an organic dye (rhodamine B) in the visible region of the solar spectrum and the photocatalytic activities were good particularly for powders annealed at 900 °C.

Keywords: *perovskites, doping, Arrhenius equation, coercive field, photocatalytic properties.*

7.1 Introduction

Perovskite solid-solutions are a large family of multifunctional materials that exhibit fascinating properties which are of interest in emerging technologies. Solid solutions with multiferroic properties have received considerable attention in recent years due to their potential for application in various fields of advanced technologies. They have been found to exhibit intriguing magnetic and electric (ferromagnetic, ferroelectric and ferroelastic) properties [1-6], dielectric, piezo and pyroelectric properties [7-9], catalytic as well as photocatalytic properties [10-12]. Perovskite-like materials are built on a flexible structure which allows for easy substitution and replacement of the ions on either the A- or B-site, and by selecting atoms with the suitable properties, materials with novel properties can be produced [13, 14]. The multiferroic properties exhibited by $BiFeO_3$ are due to the coupling of the electric field due to the lone pair of electrons on the Bi^{3+}, the magnetic field due to the Fe^{3+}, and the structural geometry of the FeO_6 octahedra [13, 15]. The properties of perovskite-like materials can also be influenced by partial replacement (doping) of either sites of the material with smaller divalent ions (e.g. Ca, Sr, and Ba) [16]. This doping method has been used to synthesize materials with required properties for applications in areas of interest. Orthoferrites are perovskite-like systems in which a rare-earth (RE) metal occupies the A-site in the material lattice (i.e $REBO_3$) and have also been shown to display interesting characteristics [17-23]. In this work, we synthesize a novel orthoferrite solid solution with the general formula $(La_{0.5}Bi_{0.2}Ba_{0.2}Mn_{0.1})FeO_{(3-\delta)}$ via a solution route with a view to obtaining materials with good magnetic and photocatalytic properties, and analyze the effect of annealing temperature on their specific surface area, magnetic as well as photocatalytic properties.

7.2. Experimental

7.2.1 Materials

$Fe(NO_3)_3.9H_2O$ (98%) (Saarchem), La_2O_3 (99.9%) (BDH Chemicals), $Bi(NO_3)_3.5H_2O$ (97%) (Saarchem), $Ba(NO_3)_2$ (99%) (Saarchem), $Mn(CH_3OO)_2$ (99%), $K_2Cr_2O_7$ (99%), Ag_2SO_4 (99%) (Saarchem), citric acid (99.7) (BDH Chemicals), chemically pure concentrated H_2SO_4 (98%), $HgSO_4$ (99%) and $(NH_4)_2Fe(SO_4)_2.6H_2O$ (99%) (Merck), ethylene glycol (99%) (Promark Chemicals), chemically pure concentrated HCl (37%) and HNO_3 (55%) (Promark Reagents), rhodamine B (The Coleman and Bell Co), and H_2O_2 30% vol. (100 vol) (Minema Chemicals) were used as received. Deionized water from a Millipore Milli-Q Elix 5 UV water purification system was used throughout and is hereafter refered to as Milli-Q water.

7.2.2 Synthesis of $(La_{0.5}Bi_{0.2}Ba_{0.2}Mn_{0.1})FeO_{(3-\delta)}$

$(La_{0.5}Bi_{0.2}Ba_{0.2}Mn_{0.1})FeO_{(3-\delta)}$ powders were prepared by a Pechini-type sol-gel process. A solution of $Fe(NO_3)_3.9H_2O$ was prepared by dissolving 0.03 mol of the salt in Milli-Q water (20 cm^3). La_2O_3 (0.0075 mol), $Ba(NO_3)_2$ (0.006 mol), $Mn(CH_3OO)_2$ (0.003 mol) and $Bi(NO_3)_3.5H_2O$ (0.006 mol) were dissolved in dilute nitric acid (about 25 cm^3, 6 mol dm^{-3}) solution to give the amount of metals required for the stoichiometry of the material. The two solutions were mixed thoroughly, made up to 200 cm^3 by adding Milli-Q water and then gradually poured into a burette. The solution was then added (drop-wise) to a citric acid solution (400 cm^3, 0.15 mol) in a beaker which was continuously being stirred by a magnetic stirrer at room temperature to form a clear solution. Once the addition was completed and while still stirring, the temperature of the mixture was raised to 90 °C and the solution continuously evaporated until the volume of the solution was reduced to about 50 cm^3, ethylene glycol (100 cm^3) was added and

the heating and stirring continued until a thick gel formed. The gel was then removed from the beaker and placed in a crucible in an oven at 120 ^{o}C for 24 hrs to dry. The dry gel was subsequently pre-calcined at 400 ^{o}C for 4 hrs to remove all organic components present. Separate sample portions of the powders were subsequently annealed in a muffle furnace for 4 hrs at 500, 600, 700, 800 and 900 ^{o}C.

7.2.3 Characterization

Transmission electron microscopy (TEM) (JEOL JEM 1010) was used to analyse the morphology of the crystals. The crystal lattice structure was determined by powder X-ray diffraction (PXRD) analysis by using a Bruker D8 Advance diffractometer equipped with a Cu K_{α} radiation source. The crystallite sizes of the powder crystals were calculated by using the Scherrer equation $D = K\lambda/\beta\cos\theta$ (where D is the average crystallite size of the material K is the Scherrer constant, λ is the wavelength of the radiation and β is the full width at half maximum). The surface areas of the synthesized materials were determined by nitrogen adsorption and the BET equation method by using a Micromeritrics Tristar II 3020 fully automated three-station surface area and porosity analyzer. The magnetic properties of the powders at room temperature were analysed by using a Lakeshore 735 vibrating sample magnetometer (VSM) which had been calibrated with a standard Ni sphere for magnetization measurements. The maximum applied field was 14 kOe. Thermogravimetric analysis (TGA) and differential scanning calorimetry (DSC) measurement were obtained for each sample by using a TGA/DSC thermal analyzer (TA Instruments SDT-Q600 thermal analyzer) in air. The temperature range of the analysis was between 25 and 1000 °C. A PerkinElmer FTIR Spectrum 100 coupled to an attenuated total reflectance accessory was used to collect the FTIR spectra of the samples. The photoluminescence emission

spectra of the powders were monitored at 590 nm by carrying out the excitation at a wavelength of 390 nm by means of a PerkinElmer LS 55 spectrofluorimeter equipped with a high energy pulsed xenon source for excitation.

7.2.4 Photocatalytic screening

The photocatalytic activity of each sample was tested on rhodamine B dye in the presence of H_2O_2 at room temperature. The irradiation was from a 26 W fluorescent lamp (Osram Dulux D, 26 W, 1800 lm) placed in a quartz jacket at about 7 cm above the dye solution. A mass of 1.5 g dm^{-3} of the synthesized material was used first, in the absence of H_2O_2, and then in the presence of H_2O_2 (3.0×10^{-5} mol dm^{-3}). The degradation of the RhB dye solution was monitored by using a Biochrom Libra S6 UV spectrophotometer at a wavelength of maximum absorbance (λ_{max}) for RhB of 556 nm. A 30 min period was allowed for equilibration before the photodegradation process began. The chemical oxygen demand (COD) for the degraded solution was determined by using the procedure described in literature [24].

7.3 Results and discussion

Fine powdered samples were obtained with colour varying from brown for samples calcined at 400 °C, to black for samples annealed at 700 °C and above. The samples were labelled LaBa followed by the temperature at which the powder was annealed (e.g. LaBa500, LaBa600 and LaBa900 for samples annealed at 500, 600 and 900 °C respectively).

7.3.1 Phase characterisation

The powder X-ray diffraction (PXRD) conducted on the samples (Figure 7.1) show that the perovskite peaks begin to form very early at the pre-calcination stage (T_A = 400 °C). All the perovskite peaks can be seen in the diffractogram of the sample calcined at 400 °C with low intensities. The formation of these peaks indicates that the nucleation and growth of the crystals have already begun at this temperature. The presence of several other peaks, however, shows that the powder is composed mainly of mixed oxides at this stage. As the annealing temperature (T_A) increased, however, the intensity of the perovskite peaks also increased and the powder crystallizes in a single phase rhombohedral lattice with space group R3C at T_A of 600 °C. The absence of any impurity peaks at T_A = 600 °C is an indication that all the ions have been incoporated into the perovskite lattice. The broadness of the peaks is due to the nanosize nature of the crystallites. The broadness decreases as T_A increases, showing that the crystallite sizes increase with increase in T_A. At T_A of 700 °C and above, some tiny peaks (labelled *) begin to emerge on the diffractograms, suggesting that some form of distortion or phase separation may be occurring in the lattice of the powders. We attribute this, coupled with the reduction in the intensities of the rhombohedral perovskite peaks for T_A = 800 and 900 °C to phase separation occurring in the sample lattice and the emergence of a small amount of secondary phase in the powder lattice. The calculated cell parameters obtained by fitting the experimental peaks to the rhombohedral peaks of $(La_{0.4}Sr_{0.6})FeO_3$ (PDF 01-082-1963) using the Diffrac^{plus} software are presented in Table 7.1. The general trend observed from these parameters shows a reduction in the volume of the unit cell with increase in T_A. This could be as a result of stabilization of higher oxidation states for metals like iron. As more Fe^{2+} ions

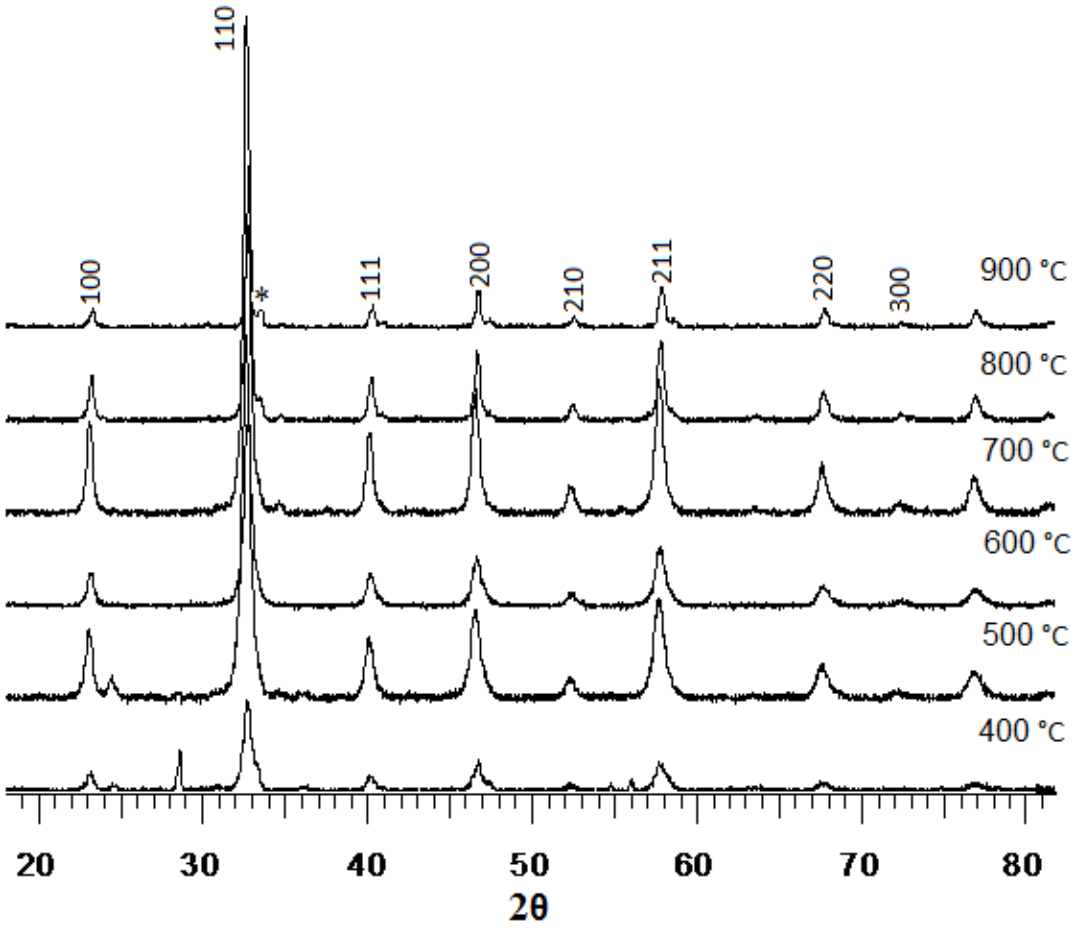

Figure 7.1: Powder X-ray diffraction peaks for $La_{0.5}(Bi_{0.2}Ba_{0.2}Mn_{0.1})FeO_{(3-\delta)}$ annealed at temperatures (T_A) from 400 to 900 °C.

Table 7.1: Lattice parameters for $La_{0.5}(Bi_{0.2}Ba_{0.2}Mn_{0.1})FeO_{(3-\delta)}$ annealed at different temperatures.

Samples	Cell parameters				Space group	Lattice system	R/R_0	SSA/ $m^2\ g^{-1}$
	a/Å	b/Å	c/Å	V/Å^3				
LaBa500	5.546	5.546	13.460	414.00	*R3C*	Rhomb.	8.41	27.75
LaBa600	5.492	5.492	13.232	395.99	*R3C*	Rhomb.	7.85	20.63
LaBa700	5.489	5.489	13.235	406.01	*R3C*	Rhomb.	8.51	12.46
LaBa800	5.492	5.492	13.250	399.70	*R3C*	Rhomb.	7.99	5.91
LaBa900	5.491	5.491	13.216	398.42	*R3C*	Rhomb.	7.18	4.19

are converted to Fe^{3+} or even Fe^{4+}, a reduction in the volume of the unit cell would be expected. The effect would be expected for Mn^{2+} to Mn^{4+} or Bi^{3+} to Bi^{5+} conversions as well.

7.3.2 Microstructural characterisation

The TEM images of samples annealed at 400, 700 and 900 °C are shown in Figure 7.2. The early stages of crystal formation can be seen in Figure 7.2(a) where small crystals coexist with largely undifferentiated amorphous structures. At an annealing temperature of 700 °C however, the crystals are fully formed and spherical shapes of diameter between 20 and 26 nm in agreement with the average crystallite size calculated from Scherrer equation can clearly be seen. At 900 °C, however, the crystals become larger and dense. This observation concurs with the decrease in the broadness of the peaks in PXRD with increase in temperature.

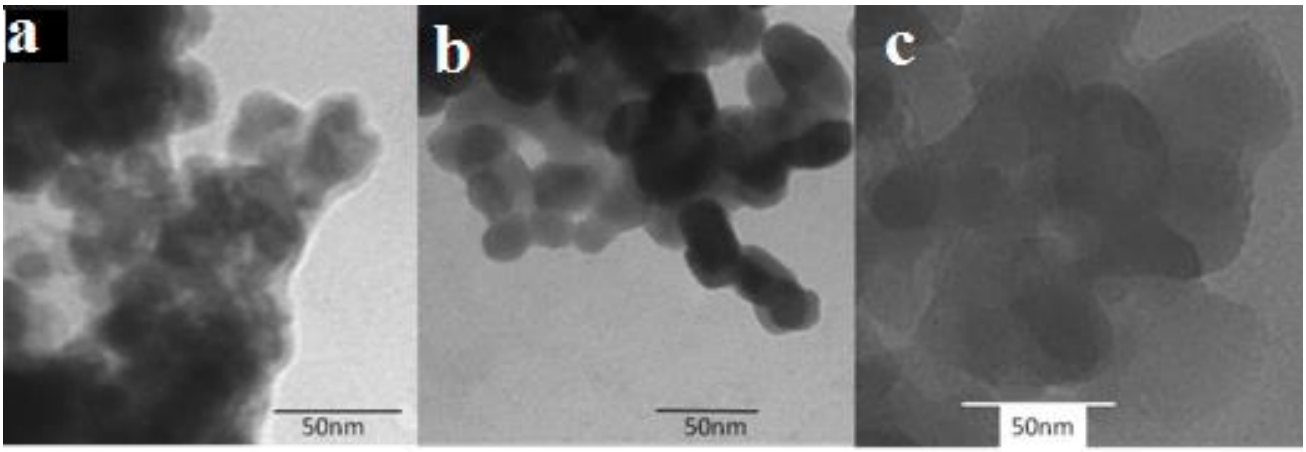

Figure 7.2: TEM migrographs for: (a) the beginning of crystal formation in LaBa400, (b) well formed spherical particles of LaBa700, and (c) the larger and dense particles of LaBa900.

7.3.3 BET surface areas

The BET specific surface area (SSA) for the samples is also displayed in Table 7.1. The SSA values for all the powders range between 4.19 and 27.75 m^2 g^{-1}, with LaBa500 having the highest SSA. The adsorption-desorption isotherms show hysteresis, which indicates that the materials are porous. Figure 7.3 shows the adsorption-desorption isotherms for the materials LaBa500-900. The isotherms correspond to the type II isotherm on the IUPAC scale [25]. The value of the relative pressure tending towards 1 with increasing T_A indicates the disappearance of smaller pores and the predominance of larger ones which eventually leads to a reduction in the value of the SSA of the materials. The inset in Figure 7.3 shows the reduction of the mesopores and a shift towards macropores and the eventual disappearance of the mesopore modal peak at a T_A of 900 °C. Figure 7.4 shows the relationship between the SSA of the materials and T_A. The activation energy for the reduction of the surface area can be worked out by plotting the natural log of the BET specific surface area (S_{BET}) against the inverse of the T_A in K and fitting the plot to the Arrhenius equation [20], which is given by

$$ln\, S_{BET} = ln\, A - \frac{E_A}{R}(1|T). \qquad (7.1)$$

where S_{BET} is the BET surface area, E_A is the activation energy for surface reduction, R is the universal gas constant (8.314 J K^{-1} mol^{-1}), T is the annealing temperature , and A is a constant.

Figure 7.5 shows this plot and the value of the E_A calculated from the slope of the graph is 37±5 kJ mol.$^{-1}$. This value is a little higher than values that have been reported for pure $LaFeO_3$ (20 kJ mol^{-1} [26] and 28 kJ mol^{-1} [20]). The difference in the values can

be accounted for by the doping that has been carried out on the A-site of the materials and the fact that a different synthesis route was used for the preparation of our materials.

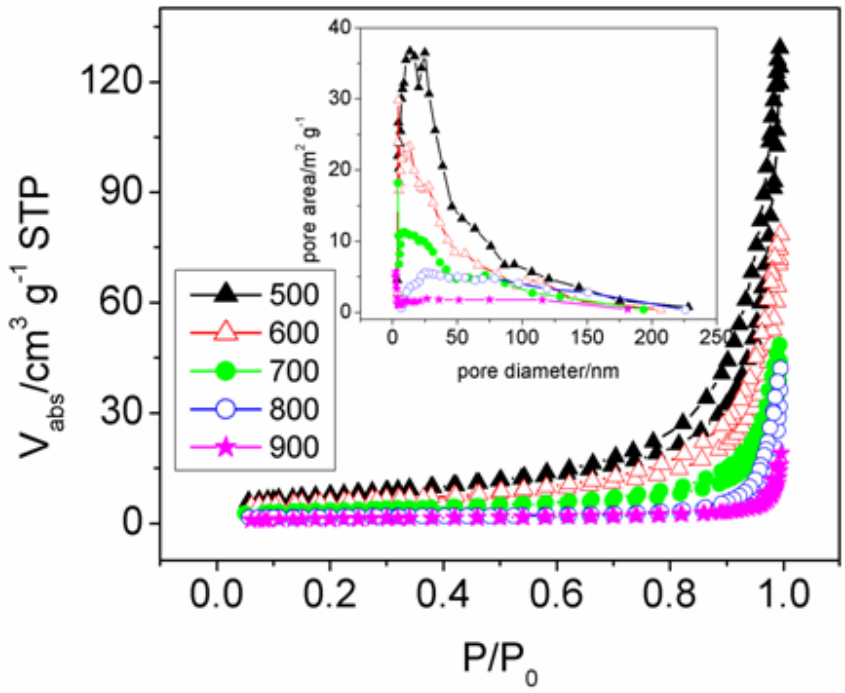

Figure 7.3: Adsorption-desorption isotherms for LaBa500-900. The inset shows the disappearance of the bi-modal mesopore peaks with increasing T_A.

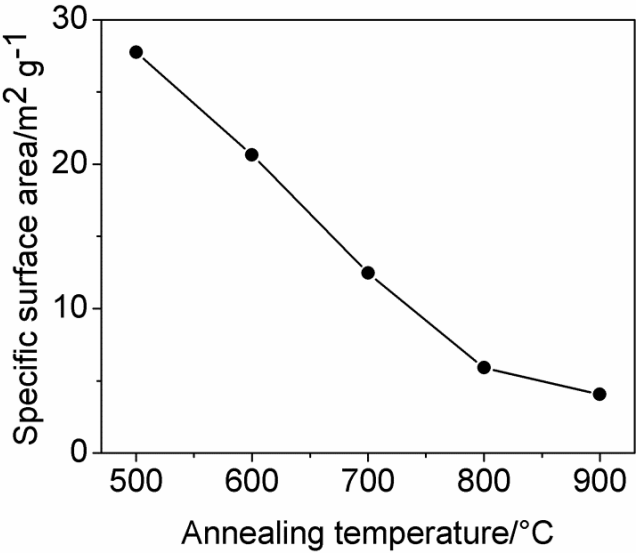

Figure 7.4: Decrease in SSA with increase in annealing temperature.

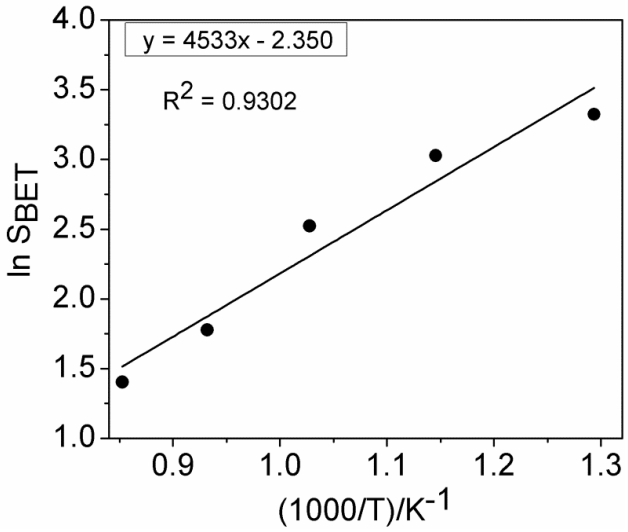

Figure 7.5: Arrhenius plot of specific surface area versus inverse of annealing temperature for LaBa500-900 from which the activation energy for surface reduction was obtained.

7.3.4 Thermal stability

The thermogravimetric analysis of the pre-calcined powder is shown in Figure 7.6. A total loss in weight of 5.8% was observed throughout the heating range (25-1000 °C). The bulk of this loss in weight is concentrated between 400 and 700 °C which can be attributed to the decomposition of oxalates to carbonates and the subsequent decomposition of the carbonates to release CO_2. The initial gradual drop in the weight of the powder from room temperature to about 200 °C can be attributed to the removal of small molecules such as H_2O and CO_2, and remnant organic molecules are burnt and vaporized between 200 and 390 °C. The crystallization events are, however, not captured on the DSC plot.

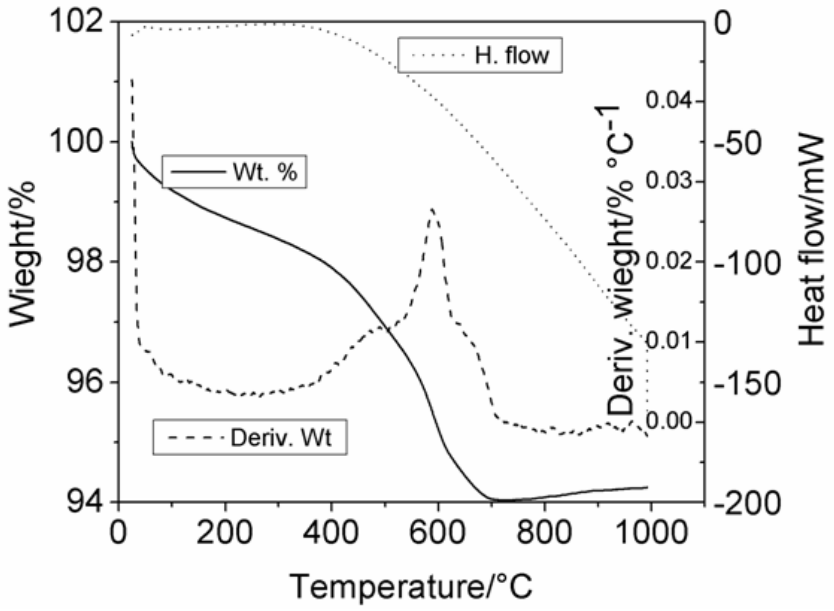

Figure 7.6: Thermal stability of the precalcined LaBa powder between 25 and 1000 °C obtained in an atmosphere of air.

7.3.5 Surface characterization

Figure 7.7 shows the FTIR-ATR spectra of the powders LaBa400-900 collected at room temperature. The broad peak centred at about 1400 cm^{-1} is assigned to the stretching and bending vibration modes from adsorbed H_2O molecules on the surface of the powder crystals [27]. The gradual decrease in the peak intensity of this peak with increasing T_A indicates removal of adsorbed water molecules. It can also be an indicator of a decrease in the surface area of the materials with increase in T_A as observed in the BET surface area analysis. The broad peaks between 500 to 600 cm^{-1} are due to the stretching vibration modes of the O–Fe–O and Fe–O bonds [28, 29]. This peak increases in intensity as the T_A increases and confirms the formation of the perovskite FeO_6 octahedra. The increase in the peak intensity also indicates that more

of the iron is incorporated into the perovskite octahedra at higher temperature, suggesting a gradual increase in ordering in the perovskite lattice as T_A increases.

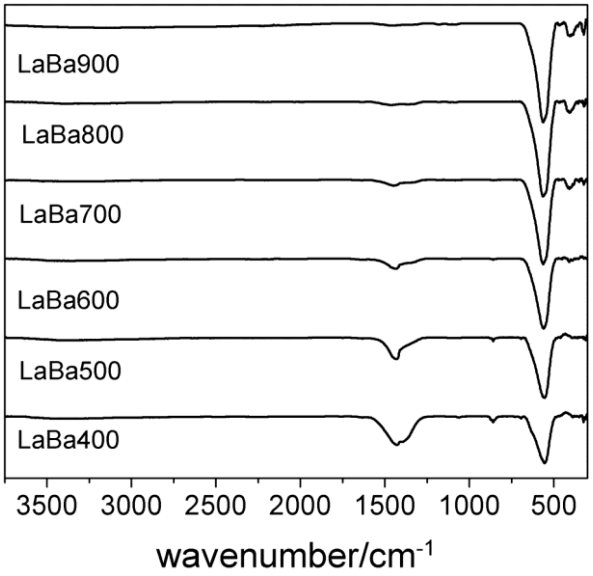

Figure 7.7: FTIR-ATR spectra of the synthesized materials LaBa400-900.

7.3.6 Magnetic properties

The room temperature magnetization curves (Figure 7.8) of the powders shows some weak ferromagnetic properties. The trend for the saturation magnetization (M_S) and coercive field (H_C) for powders annealed at different T_A values is characterized by two distinct stages. The first stage is characterized by a decrease in the magnetization for powders annealed between T_A = 400 and 700 °C, while the second is characterized by an increase in coercive field H_C for samples annealed between T_A = 700 and 900 °C. The first stage represents the magnetization of the powders at the point of nucleation and growth of the perovskite lattice. As more ions are incorporated into the perovskite lattice the M_S values for powders annealed at higher T_A decrease until a T_A = 600 °C, when all the ions have been incorporated into the lattice; this agrees with the

observation made from the PXRD results where peaks for a single phase rhombohedral structure can be seen. The decrease in the value of magnetization can be attributed to an increase in order in the perovskite lattice [30]. The gradual increase in coercive field at this stage, however, can be attributed to magnetic anisotropy due to the increase in the size of the crystals [31, 32]. The second stage consists of powders annealed at T_A = 700 to 900 °C, the M_S at this stage is relatively stable as only a slight increase is observed, however, a large increase in coercive field of up to 5.60 kOe is observed at this stage. The increase in coercive field at this stage can be attributed to a combination of magnetic anisotropy and exchange coupling between the ferromagnetic (FM) and the antiferromagnetic (AFM) phases within the powder lattice [33]. The introduction of Ba^{2+} into the perovskite lattice could lead to a variation in the bond lengths in the superlattice or the formation of oxygen vacancies. The former would lead to a change in the bond angle of the superlattice, while the latter would lead to a change in valency of the ions in the lattice (e.g., Fe^{3+}–O–Fe^{4+}). In both cases, an increase in the ferromagnetic character would be observed. The AFM superexchange interactions, however, arise from symmetric interactions such as Fe^{3+}–O–Fe^{3+} [34, 35]. The values of the coercive fields show that a secondary magnetic phase might exist in the lattice of the powder in agreement with a similar observation made of a likely phase separation event at higher T_A values from the PXRD results as explained earlier. Table 7.2 shows the magnetic parameters obtained from the room temperature magnetization of the powders, a general increase in the squareness M_S/M_R represents an increase in the ferromagnetic character of the powders at higher T_A. Figure 7.9 shows the variation of M_S and H_C as a function of T_A, the relative stabilization of the M_S values at T_A = 600 °C and the sudden jump of the H_C values from 264 Oe to 4.70 kOe at T_A = 700 °C also

corroborate the results obtained from PXRD that a pure perovskite phase was obtained at 600 °C.

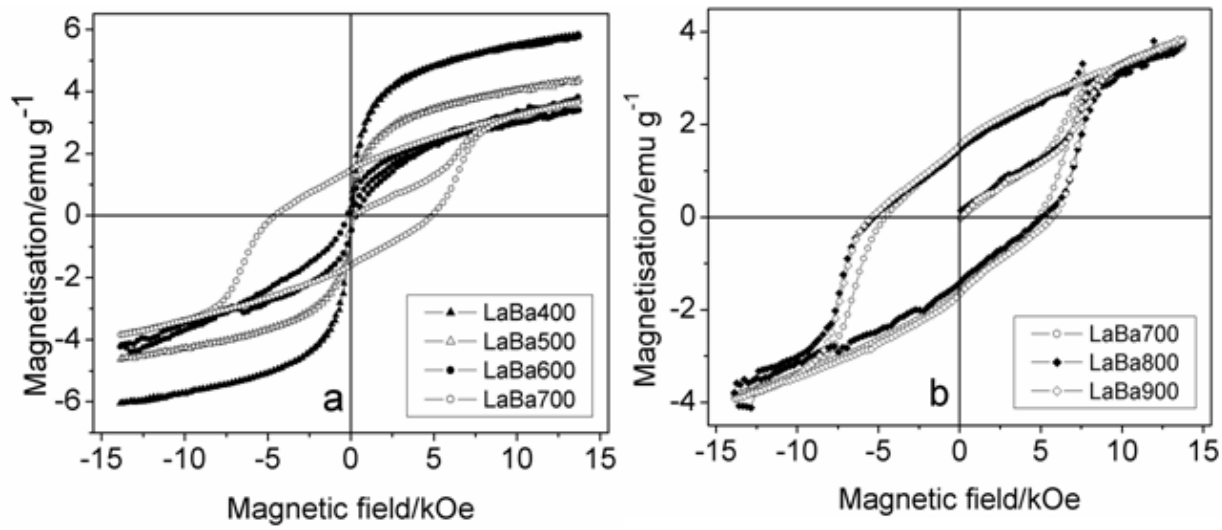

Figure 7.8: Room temperature hysteresis loops showing the magnetization profiles of the materials annealed at various T_A.

Table 7.2: Magnetization parameters showing the variation in saturation magnetization, remanent magnetization and coercive field for LaBa400-900. Crystallite sizes were obtained by applying the Scherrer equation to the PXRD data.

Samples	M_S/emu g^{-1} (±0.4)	M_R/emu g^{-1} (±0.04)	H_C/Oe (± 2)	M_S/M_R	Crystallite sizes/nm (± 2)
LaSr400	5.82	0.09	31	0.036	18.49
LaSr500	4.38	0.07	40	0.039	19.28
LaSr600	3.82	0.36	264	0.113	19.43
LaSr700	3.69	1.47	4712	0.408	24.21
LaSr800	3.80	1.45	5162	0.363	30.41
LaSr900	3.83	1.55	5597	0.414	32.42

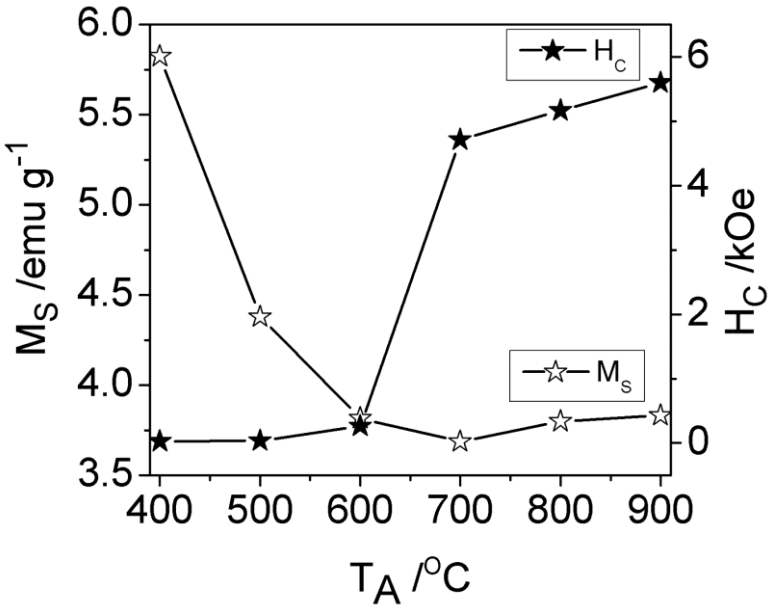

Figure 7.9: Variation of room temperature saturation magnetization and coercive field with increase in annealing temperature.

7.3.7 Photoluminescence

The photoluminescence (PL) of the samples excited at 390 nm and monitored at an emission wavelength of 590 nm is presented in Figure 7.10. In perovskite-like crystals, photoluminescence have been shown to occur at room temperature either due to the presence of intrinsic or extrinsic defects or the formation of trap states between the valence and conduction bands [36-38]. The peak intensities do not show a clear trend with the crystallinity of the synthesized materials as can be seen from other analytical methods (PXRD and FTIR). The excitation energies, however, fall within the visible region of the electromagnetic energy, implying that the materials could utilize visible light to bring about the photodegradation of organic molecules.

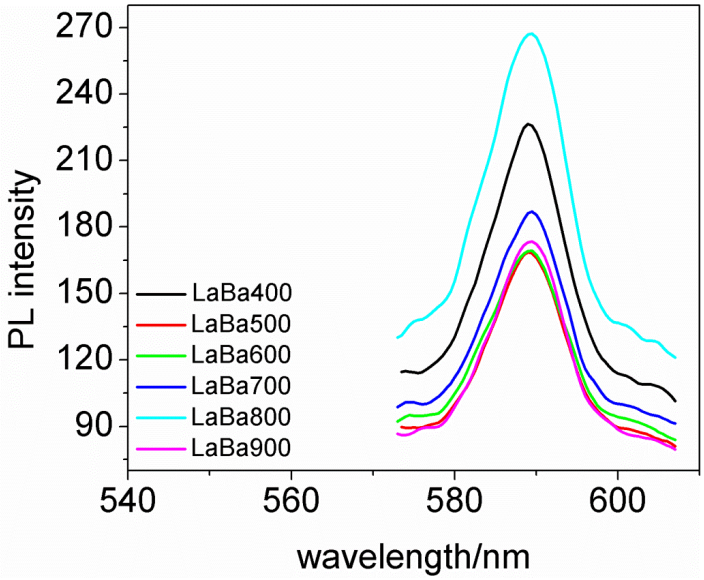

Figure 7.10: PL spectra showing the emission intensities of the LaBa powders at 590 nm (2.11 eV) when excited at 390 nm.

7.3.8 Photocatalytic screening

The results of the photocatalytic screening of the materials on the photodegradation of RhB dye at room temperature are presented in Figure 7.11. The photodegradation of the dye in the presence of the photocatalysts only showed small degradation rates for all the powders but the materials annealed at T_A of between 700 and 900 °C were more active (Figure 7.11a). The first 30 min. of the reactions involved the adsorption of the dye molecules onto the surface of the photocatalysts, most of these adsorbed molecules were released once the photocatalytic process began at 0 min for materials annealed at T_A of 400 to 600 °C and hence the increase in absorbance. In the presence of H_2O_2, however, the rates of photodegradation of the dye molecules increased (Figure 7.11b). The photodegradation reaction follows pseudo-first-order reaction kinetics represented by the equation $ln(A/A_0) = k_{obs}t$, where A_0 and A are the initial concentration and the concentration of the dye at time t respectively, and k_{obs} is the observed rate constant.

The rate constants for the powders LaBa700-900 are shown in Table 7.3. Figure 7.12 shows the photodegradation profile for the RhB dye solution in the presence of LaBa900 and H_2O_2.

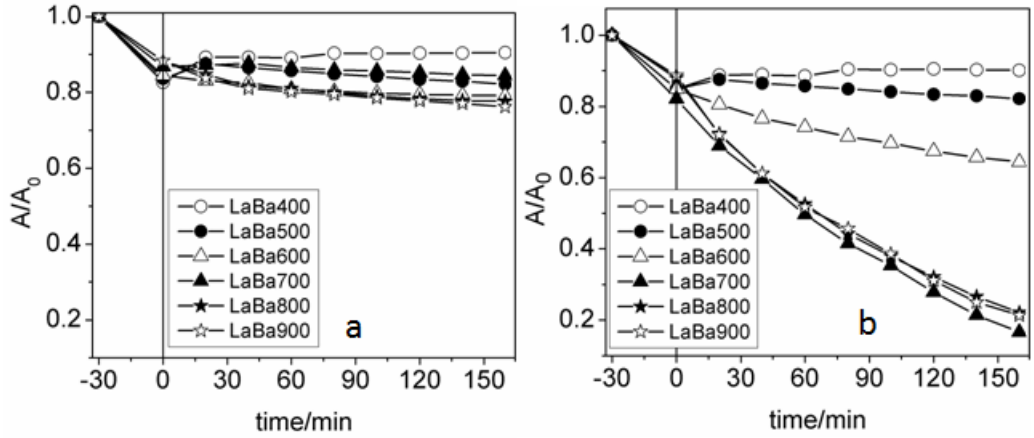

Figure 7.11: Photodegradation profile of RhB dye solution: (a) LaBa400-900 in the absence of H_2O_2, and (b) LaBa400-900 in the presence of H_2O_2.

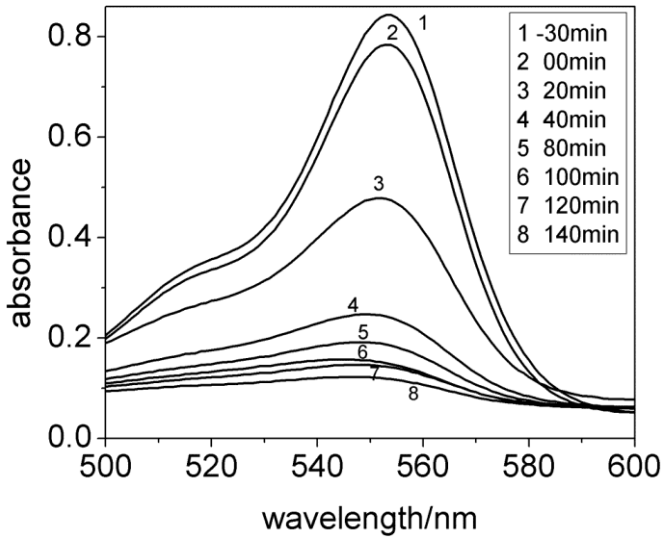

Figure 7.12: Photodegradation profile of RhB in the presence of LaBa900 and H_2O_2 showing the decrease in absorbance of the dye solution.

Table 7.3: Observed rate constants for the photodegradation of RhB in the presence of 1.5 g dm^{-3} of photocatalyst and 3.0 x 10^{-5} mol dm^{-3} H_2O_2 for samples annealed at 700-900 °C.

System	**k_{obs}/min^{-1}**
H_2O_2	4.4045×10^{-6}
LaBa700	7.833×10^{-4}
LaBa800	7.26×10^{-4}
LaBa900	2.207×10^{-4}
LaBa700 + H_2O_2	8.76×10^{-3}
LaBa800 + H_2O_2	8.45×10^{-3}
LaBa900 + H_2O_2	9.79×10^{-3}

7.3.8.1 Mineralisation of RhB dye solution

The result of the chemical oxygen demand (COD) analysis of the photodegraded dye solution in the presence of LaBa700 (1.5 g dm^{-3}) and H_2O_2 (3.0×10^{-5} mol dm^{-3}) for 3 hours is presented in Figure 7.13. The gradual decrease in the value of the COD indicates the continous mineralization of the dye molecules, converting them to CO_2 and H_2O. Figure 7.14 shows the COD results of the mineralization of the dye molecules for the most active powders namely; LaBa700-900, after three hours of photodegradation. The COD values appear to be very close, with the value for LaBa900 being slightly lower.

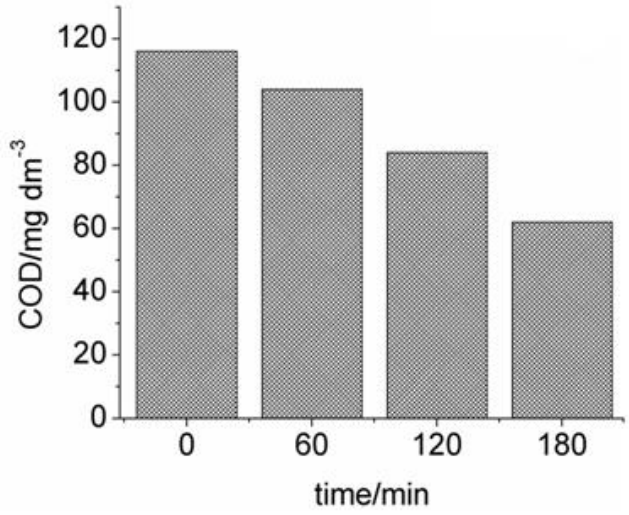

Figure 7.13: The decrease in the values of COD for the RhB dye solution photodegraded in the presence of 1.5 g dm^{-3} of LaBa700 and 3.0 x 10^{-5} mol dm^{-3} H_2O_2 monitored for a 3 hr period.

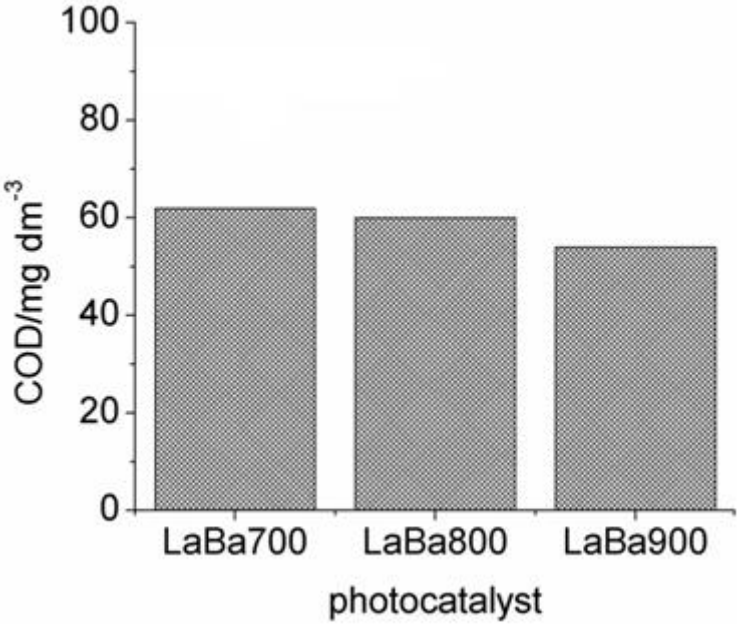

Figure 7.14: COD values for the RhB dye solution photodegraded in the presence of 1.5 g dm^{-3} of LaBa700, LaBa800 and LaBa900 and 3.0 × 10^{-5} mol dm^{-3} H_2O_2 after a period of 3 hrs.

7.3.8.2 Mechanism of RhB degradation

We propose the following reaction mechanism for the entire degradation process. The first is the photogenaration of an electron-hole pair in the photocatalysts (PC). The generated electron in the conduction band of the catalyst can then be trapped by H_2O_2 to cause the production of the radicals according to the following mechanism:

$$PC + h\nu \rightarrow e^- + h^+ \quad (7.2)$$

$$H_2O_2 + e^- \rightarrow {}^{\cdot}OH + OH^- \quad (7.3)$$

The h^+ can also react with adsorbed water to generate more radicals as follows:-

$$H_2O + h^+ \rightarrow H^+ + HO^{\bullet} \quad (7.4)$$

Hydroxyl radicals can also be produced via a photo-Fenton or a Fenton-like mechanism involving the Fe^{3+} ions in the B-site of the perovskite photocatalyst and H_2O_2 according to the following reaction:

$$H_2O_2 + Fe^{3+} \rightarrow Fe - OOH^{2+} + H^+ \quad (7.5)$$

$$Fe - OOH^{2+} \rightarrow Fe^{2+} + HO_2^{\bullet} \quad (7.6)$$

$$H_2O_2 + Fe^{2+} \rightarrow Fe^{3+} + 2HO^{\bullet} \quad (7.7)$$

A direct $h\nu/H_2O_2$ interaction to produce hydroxyl radicals has been ruled out since the dye did not degrade under this condition.

7.4 Conclusions

We used a citric acid sol-gel route to synthesize a novel perovskite-like material with general formula $(La_{0.5}Bi_{0.2}Ba_{0.2}Mn_{0.1})FeO_{(3-\delta)}$. PXRD characterization shows that the powders crystallized in a rhombohedral perovskite-like lattice. The surface areas of the powders decreased with increasing values of T_A. The activation energy for the

reduction of the surface area obtained from the Arrhenius plot is 37 kJ mol^{-1}. The coercive field increased with increase in annealing temperature and a very high coercive field of 5.60 kOe was recorded for LaBa900. The materials also show PL activities in the visible region of the electromagnetic spectrum, indicating that they can utilize visible light to function as photocatalysts. Very good activities were recorded for the photocatalytic degradation of RhB dye in the presence of H_2O_2. In conclusion, we propose this material as a suitable material for use in photodegradation of toxic organic molecules, which include dyes and other colourless organic molecules such as phenol and other pharmaceutical waste which have been implicated in endocrine disruption. The materials are simple to prepare. Their high coercive fields could be useful in making magnetic recording materials. Their improved magnetic properties means that they can easily be recovered from wastewater after use by applying an external magnetic field.

Acknowledgements

IA is grateful to the College of Agriculture, Engineering and Science at the University of KwaZulu-Natal for the award of a PhD bursary and a Doctoral Scholarship. The Vibrating Sample Magnetometer used in this work was provided by the National Research Foundation of South Africa.

References

[1] Z. Zhou, L. Guo, H. Yang, Q. Liu, F. Ye, Journal of Alloys and Compounds 583 (2014) 21-31.
[2] N. Thongmee, A. Watcharapasorn, S. Jiansirisomboon, Current Applied Physics 8 (2008) 367-371.
[3] K. Sardar, J. Hong, G. Catalan, P.K. Biswas, M.R. Lees, R.I. Walton, J.F. Scott, S.A. Redfern, Journal of Physics: Condensed Matter 24 (2012) 045905-045912.
[4] H. Lahmar, S. Habouti, C.-H. Solterbeck, M. Dietze, M. Es-Souni, Journal of Applied Physics 107 (2010) 024104-024111.
[5] A. Lahmar, K. Zhao, S. Habouti, M. Dietze, C.-H. Solterbeck, M. Es-Souni, Solid State Ionics 202 (2011) 1-5.
[6] I. Grinberg, D.V. West, M. Torres, G. Gou, D.M. Stein, L. Wu, G. Chen, E.M. Gallo, A.R. Akbashev, P.K. Davies, J.E. Spanier, A.M. Rappe, Nature 503 (2013) 509-512.
[7] M.D. Peel, S.E. Ashbrook, P. Lightfoot, Inorganic Chemistry 52 (2013) 8872-8880.
[8] D.S. Paik, S.E. Park, T.R. Shrout, W. Hackenberger, Journal of Materials Science 34 (1999) 469-473.
[9] V. Bedekar, O.D. Jayakumar, J. Manjanna, A.K. Tyagi, Materials Letters 62 (2008) 3793-3795.
[10] S. Rousseau, S. Loridant, P. Delichere, A. Boreave, J.P. Deloume, P. Vernoux, Applied Catalysis B: Environmental 88 (2009) 438-447.
[11] W. Luo, L. Zhu, N. Wang, H. Tang, M. Cao, Y. She, Environmental Science & Technology 44 (2010) 1786-1791.
[12] C.-C. Hu, Y.-L. Lee, H. Teng, Journal of Materials Chemistry 21 (2011) 3824-3830.
[13] J. Van Den Brink, D.I. Khomskii, Journal of Physics: Condensed Matter 20 (2008) 434217-434228.
[14] D.I. Khomskii, Journal of Magnetism and Magnetic Materials 306 (2006) 1-8.
[15] S. Kim, E. Choi, A. Bhalla, Ferroelectric Letters 34 (2007) 84-94.
[16] V. Khomchenko, D. Kiselev, J. Vieira, L. Jian, A. Kholkin, A. Lopes, Y. Pogorelov, J. Araujo, M. Maglione, Journal of Applied Physics 103 (2008) 024105-024110.
[17] X. Li, Z.-Q. Duan, Materials Letters 89 (2012) 262-265.
[18] L. Li, X. Wang, Y. Zhang, Materials Research Bulletin 50 (2014) 18-22.
[19] L. Li, X. Wang, Y. Lan, W. Gu, S. Zhang, Industrial & Engineering Chemistry Research 52 (2013) 9130-9136.
[20] R. Köferstein, L. Jäger, S.G. Ebbinghaus, Solid State Ionics 249–250 (2013) 1-5.
[21] L. Ju, Z. Chen, L. Fang, W. Dong, F. Zheng, M. Shen, Journal of the American Ceramic Society 94 (2011) 3418-3424.
[22] J. Jiang, J. Zou, M.N. Anjum, J. Yan, L. Huang, Y. Zhang, J. Chen, Solid State Sciences 13 (2011) 1779-1785.
[23] F. Gao, X.Y. Chen, K.B. Yin, S. Dong, Z.F. Ren, F. Yuan, T. Yu, Z.G. Zou, J.M. Liu, Advanced Materials 19 (2007) 2889-2892.
[24] I. Williams, Wiley (2001).

[25] K. Sing, D. Everett, R. Haul, L. Moscou, R. Pierotti, J. Rouquerol, T. Siemieniewska, Pure Appl. Chem 54 (1982) 603-619.
[26] R. Andoulsi, K. Horchani-Naifer, M. Férid, Cerâmica 58 (2012) 126-130.
[27] P. Junploy, S. Thongtem, T. Thongtem, Superlattices and Microstructures 57 (2013) 1-10.
[28] G.R.O. Silva, J.C. Santos, D.M. Martinelli, A.M.G. Pedrosa, M.J.B. de Souza, D.M.A. Melo, Materials Sciences and Applications 1 (2010) 39-45.
[29] M. Lee, J. Jun, J. Jung, Y. Kim, S. Lee, Bulletin-Korean Chemical Society 26 (2005) 1591-1596.
[30] A.A. Cristóbal, P.M. Botta, P.G. Bercoff, J.M. Porto López, Materials Research Bulletin 44 (2009) 1036-1040.
[31] K. Sadhana, K. Praveena, S. Matteppanavar, B. Angadi, Appl Nanosci 2 (2012) 247-252.
[32] K. Parekh, Indian Journal of Pure and Applied Physics 48 (2010) 581-585.
[33] P. Godara, A. Agarwal, N. Ahlawat, S. Sanghi, R. Dahiya, Journal of Alloys and Compounds 594 (2014) 175-181.
[34] S. Majumdar, H. Huhtinen, S. Granroth, P. Paturi, Journal of Physics: Condensed Matter 24 (2012) 206002-206009.
[35] S. Chatterjee, S. Giri, S. De, S. Majumdar, Ferromagnetic/antiferromagnetic exchange coupling in Ni2MnSn-derived magnetic shape memory alloys, Journal of Physics: Conference Series, IOP Publishing, 2010, pp. 032011-032014.
[36] W.F. Zhang, Z. Yin, M.S. Zhang, Applied Physics A 70 (2000) 93-96.
[37] W.F. Zhang, J. Tang, J. Ye, Chemical Physics Letters 418 (2006) 174-178.
[38] D. Li, J. Zheng, Z. Zou, Journal of Physics and Chemistry of Solids 67 (2006) 801-806.

Chapter 8

Synthesis and effect of annealing temperature on the structural, magnetic and photocatalytic properties of $(La_{0.5}Bi_{0.2}Ca_{0.2}Mn_{0.1})FeO_{(3-\delta)}$

Ibrahim Abdulkadir, Bice S. Martincigh* and Sreekantha B. Jonnalagadda

School of Chemistry and Physics, University of KwaZulu-Natal, Westville Campus, Private Bag X54001, Durban 4000, South Africa

*Corresponding author: Tel: +27 31 2601394; Fax: +27 31 2603091; E-mail: martinci@ukzn.ac.za

Abstract

Novel perovskite-type nanomaterials with the composition $La_{0.5}(Bi_{0.2}Ca_{0.2}Mn_{0.1})FeO_{3-\delta}$ were synthesized by using the citric acid sol-gel route and annealed at temperatures from 400 to 900 °C. Scanning electron microscopy and powder X-ray diffraction analysis of the powders showed that they contain crystalline perovskite-type nanoparticles. Crystallinity increased with higher annealing temperature. The lattice parameters, after refinement, showed that the particles crystallized in a rhombohedral structure. The BET specific surface areas ranged between 2.76-27.37 $m^2 g^{-1}$ with an activation energy for surface area reduction of 41 kJ mol^{-1}. Vibrating sample magnetometer analysis of the hysteresis loops showed a slight increase in coercive field with increasing annealing temperature. Photoluminescence spectroscopy showed that the powders were all active in the visible region and could be useful for visible light photodegradation of organic dyes. The powders were all screened for photocatalytic activity against an organic dye (Rhodamine B) in the visible region of the solar spectrum and the photocatalytic activities were good for powders annealed at 700 °C and above. In addition, a mineralization of up to 70% was achieved after 3 hrs of photodegradation. Therefore, these materials show good potential for the photocatalytic degradation of orgnic pollutants.

Keywords: *multiferroics, coercive field, photoluminescence, photocatalytic activities*.

8.1 Introduction

Perovskite-like materials have found use in several fields of advanced technologies such as gas sensors [1-4], electric and magnetic materials [5-8], solid oxide fuel cells [9, 10], catalysis and photocatalysis [11-13]. The fascinating properties of this group of materials stems from the chemistry of the perovskite structure (ABO_3), which is flexible and allows for substitution and/or replacement of the ions on either of the sites (A-site which normally contains a large 12-fold coordinated (cuboctahedral) cations or B-site which is normally a smaller 6 fold coordinated (octahedral) cation) in a variety of combinations. The orthoferrites are members of the perovskite family in which the A-site is occupied by a rare earth metal and the B site by a smaller transition metal. They also display intriguing properties such as ferromagnetic and ferroelectric, pyro and piezoelectric [14-16], catalytic as well as photocatalytic properties [17-20]. Materials with novel properties can be made by introducing (doping or partial substitution on the A and/or B sites) ions with varied physical properties of interest into the lattice of the perovskite structure to impart on the material the required properties [21, 22]. The change in properties of doped perovskites can also arise from a change in the bond lengths in the lattice, the creation of defects in the lattice or the creation of oxygen deficiency, and transition metals with smaller ionic sizes (e.g. Ca^{2+}, Sr^{2+} and Ba^{2+}) have been used for this purpose [23-26]. In this work, we use a simple citric acid route to synthesize a novel perovskite-like material $(La_{0.5}Bi_{0.2}Ca_{0.2}Mn_{0.1})FeO_{(3-\delta)}$ and analyze the effect of annealing temperature on the structural and magnetic properties, as well as photocatalytic properties on the degradation of rhodamine B (RhB).

8.2 Experimental

8.2.1 Materials

$Fe(NO_3)_3.9H_2O$ (98%) (Saarchem), La_2O_3 (99.8%) (BDH Chemicals), $Bi(NO_3)_3.5H_2O$ (97%) (Saarchem), $Ca(NO_3)_2$ (99%) (Saarchem), $Mn(CH_3OO)_2$ (99%) $K_2Cr_2O_7$ (99%) Ag_2SO_4 (99%) (Saarchem), citric acid (99.7%) (BDH Chemicals), chemically pure concentrated H_2SO_4 (98%), $HgSO_4$ (99%) and $(NH_4)_2Fe(SO_4)_2.6H_2O$ (99%) (Merck), chemically pure concentrated HCl (37%) and HNO_3 (55%) (Promark Reagents), ethylene glycol (99%) (Promark Chemicals), rhodamine B (The Coleman and Bell Co), and H_2O_2 30% vol. (100 vol) (Minema Chemicals) were used as received. Deionized water from a Millipore Milli-Q Elix 5 UV water purification system was used throughout and is hereafter referred to as Milli-Q water.

8.2.2 Synthesis of $(La_{0.5}Bi_{0.2}Ca_{0.2}Mn_{0.1})FeO_{(3-\delta)}$

$(La_{0.5}Bi_{0.2}Ca_{0.2}Mn_{0.1})FeO_{(3-\delta)}$ samples was prepared by a citric acid sol-gel process. $Fe(NO_3)_3.9H_2O$ (0.03 mol) was dissolved in Milli-Q water (20.00 cm^{-3}). La_2O_3 (0.0075 mol), $Ca(NO_3)_2$ (0.006 mol) $Mn(CH_3OO)_2$ (0.003 mol) and $Bi(NO_3)_3.5H_2O$ (0.006 mol) were dissolved in dilute nitric acid (about 15 cm^3, 6 mol dm^{-3}) solution to give the amount of metals required to fulfil the material's stoichiometry. The two solutions were mixed thoroughly, made up to 200 cm^3 with water (Milli-Q) and then gradually poured into a burette. The solution was then added (drop-wise) to a citric acid solution (400 cm^3, 0.15 mol) in a beaker which was continuously stirred by magnetic stirrer at room temperature to form a clear solution. Once the addition was completed and still stirring, the temperature of the mixture was raised to 90 ^oC and allowed to stand until the volume of the solution was reduced to about 50 cm^3, ethylene glycol (100 cm^3) was added and

the heating and stirring continued until a thick gel was formed. The gel was then removed from the beaker and placed in a crucible in an oven at a temperature of 120 ^{o}C for 24 hrs to dry. The dry gel was subsequently pre-calcined at 400 ^{o}C for 4 hrs to remove all the organic components. Separate sample portions of the precalcined dry gel were subsequently annealed in a muffle furnace for 4 hrs at annealing temperatures (T_A) of 500, 600, 700, 800 and 900 ^{o}C respectively.

8.2.3 Characterisation

Transmission electron microscopy (TEM) micrographs were collected on a JEOL JEM 1010 instrument. Scanning electron microscopy (SEM) data were also collected on a ZEISS Ultra plus field emission gun scanning electron microscope for the analysis of the morphology of the crystals. The crystals lattice structures were determined by powder X-ray diffraction (PXRD) analysis by using a Bruker Advance D8 diffractometer equipped with a Cu K_α radiation source. Crystallite sizes (D) were calculated by using the Scherrer equation, $D = k\lambda/\beta\cos\theta$ (where k is the Scherrer constant, λ is the wavelength of the radiation and β is the full width at half maximum). Specific surface areas and pore sizes were determined by nitrogen adsorption and the BET equation method with a Micromeritrics Tristar II 3020 fully automated three station surface area and porosity analyzer. The magnetic properties were analysed by using a LakeShore model 735 vibrating sample magnetometer (VSM) which had been calibrated with a standard Ni sphere of saturation magnetization 54.7 emu g^{-1}. The maximum applied magnetic field was 14 kOe and analyses were done at room temperature. The thermal stability of the powders were analysed on a thermogravimetric analysis (TGA) and differential scanning calorimetry (DSC) instrument (TA Instruments SDT-Q600 thermal analyzer). Data were collected in air

for the sample between 25 and 1000 °C. Surface characterization of the powders was carried out on a PerkinElmer FTIR Spectrum 100 spectrometer fitted with an attenuated total reflectance (ATR) accessory. The photoluminescence spectra were monitored at two excitation wavelengths (390 and 400 nm) by means of a PerkinElmer LS 55 spectrofluorimeter equipped with a high energy pulsed xenon source for excitation.

8.2.4 Photocatalytic screening

The photocatalytic activity of each sample was tested on Rhodamine B dye in the absence and presence of H_2O_2 at room temperature. A 26 W fluorescent lamp (Osram Dulux D, 26 W, 1800 lm) placed in a quartz jacket and held at about 7 cm above the RhB dye solution (which was continuously being stirred with a magnetic stirrer) was used for the irradiation. The system contained 1.5 g dm^{-3} of synthesized materials and H_2O_2 (3.0×10^{-5} mol dm^{-3}). A period of 30 min was allowed for equilibration in the dark before the lamp was turned on. Aliquots of the dye solution were withdrawn at intervals of 20 min to monitor the photodegradation process by measuring the absorbance of the withdrawn aliquot at a λ_{max} of 556 nm on a Biochrom Libra S6 UV spectrophotometer. The extent of mineralization was also investigated by determining the chemical oxygen demand (COD) of the degraded solution after 180 min of degradation activity by means of standard method as described in the literature [27].

8.3 Results and discussion

A dry brown powder of the material $(La_{0.5}Bi_{0.2}Ca_{0.2}Mn_{0.1})FeO_{(3-\delta)}$ was obtained after the precalcination process. The colour of the powders changed gradually from brown to black as the annealing temperature increased. The samples were labelled LaCa

followed by the temperature at which they were annealed (LaCa400, LaCa500 and LaCa600 for samples annealed at 400, 500 and 600 °C respectively).

8.3.1 Crystal phase characterization

The PXRD diffractograms for the samples prepared at annealing temperatures (T_A) of 400-900 °C are shown in Figure 8.1. The perovskite peaks can be seen growing at T_A = 400 °C. This indicates that the nucleation and growth of the perovskite phase may have started at a lower temperature. Peaks corresponding to the 100, 110, 111, 200, 210 and 211 perovskite planes can be clearly identified in the diffractogram at T_A = 400 °C, but the presence of other prominent peaks indicates that for this T_A, the powder contains largely mixed oxides and probably some amorphous materials. The perovskite peak intensities increase for higher T_A, indicating an increase in crystallinity and also an increase in the phase purity of the powders. The powders crystallize in a pure rhombohedral perovskite phase of space group R 3c at higher T_A (i.e. 600 °C). The absence of impurity peaks indicates that the ions have all been incorporated into the perovskite lattice. The nanoparticulate nature of the particles leads to the broadening of the peaks, a reduction in the broadening of the peaks for higher T_A indicates an increase in crystallite sizes which is confirmed by crystallite size values obtained by applying the Scherrer equation to the 110 planes (Table 8.1). Higher T_A, is therefore, accompanied by an increase in phase purity, crystallinity as well as crystallite sizes. The tiny peaks that appear at T_A = 700 and 800 °C (indicated by an *) maybe due to phase separation or the formation of a secondary orthorhombic perovskite phase. Another explanation could be that it indicates the beginning of a phase transition from the rhombohedral to the orthorhombic lattice. These peaks disappear at T_A 900 °C but a shoulder can now be observed at the 110 planes. Table 8.1 also shows the calculated lattice parameters

obtained by using the Diffrac^{plus} software and matching the peaks with that of $(La_{0.4}Sr_{0.6})FeO_3$ (PDF 01-082-1963). The cell volumes were only slightly affected by increasing T_A. A slight decrease was observed in the cell volume between T_A = 500 and 600 °C. This could be attributed to a stabilization of higher oxidation states for the transition metals which will lead to a decrease in the ionic sizes (e.g. Fe^{4+} is smaller in size than Fe^{3+}) of the ions. A sudden increase in cell volume is noticed at T_A = 700 °C. This could be the point at which the ions are maximally incorporated into the perovskite lattice. The decrease in the cell volume which is observed afterwards may be as a result of phase separation.

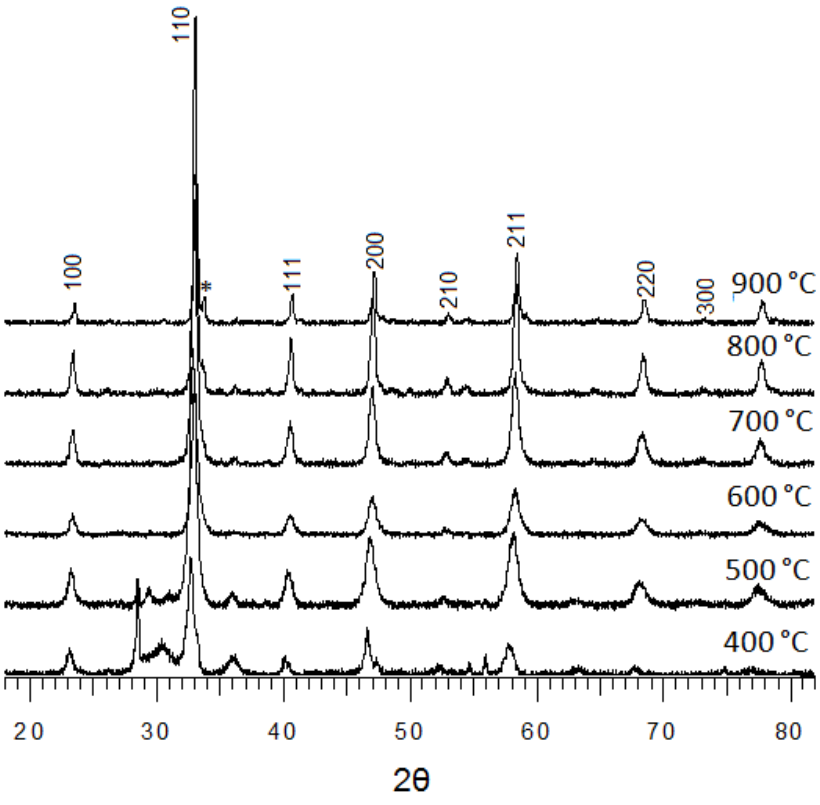

Figure 8.1: Powder X-ray diffractograms for the powders showing the evolution of the perovskite peaks as the annealing temperatures increased from 400 to 900 °C.

Table 8.1: Variation in cell parameters and specific surface areas for samples annealed between 500 and 900 °C.

Samples	Cell parameters				Space group	Lattice system	R/R_0	SSA/m^2 g^{-1} (± 0.01)
	a /Å	b /Å	c /Å	V /$Å^3$				
LaCa500	5.510	5.510	13.355	405.45	*R3C*	Rhomb.	9.52	27.37
LaCa600	5.505	5.505	13.347	404.46	*R3C*	Rhomb.	6.01	26.82
LaCa700	5.528	5.528	13.446	410.94	*R3C*	Rhomb.	8.51	16.93
LaCa800	5.507	5.507	13.428	407.29	*R3C*	Rhomb.	8.28	8.32
LaCa900	5.502	5.502	13.411	405.93	*R3C*	Rhomb.	6.04	2.77

8.3.2 Morphology

Figure 8.2 shows the TEM micrographs for samples LaCa400, LaCa700 and LaCa900. Perovskite crystals of size range between 13 to 16 nm can be seen clearly among other undifferentiated amorphous substances (Figure 8.2 (a)). This implies that the duration of the calcination (4 hrs) is long enough for the crystals to begin to evolve at this temperature. At 700 °C, the crystals have grown in size and are more spherical or cylindrical in shape (Figure 8.2 (b)). The crystallite sizes observed at this stage range between 17 and 25 nm. At 900 °C the crystals become even bigger and opaque due to increased density (Figure 8.2 (c)). At this stage the powder consists more of large aggregates of crystals with widely varied crystal sizes. Figure 8.3 displays SEM micrographs of crystals of LaCa600, LaCa700 and LaCa900. The increase in crystallite sizes and the clustering of the crystals can be seen clearly.

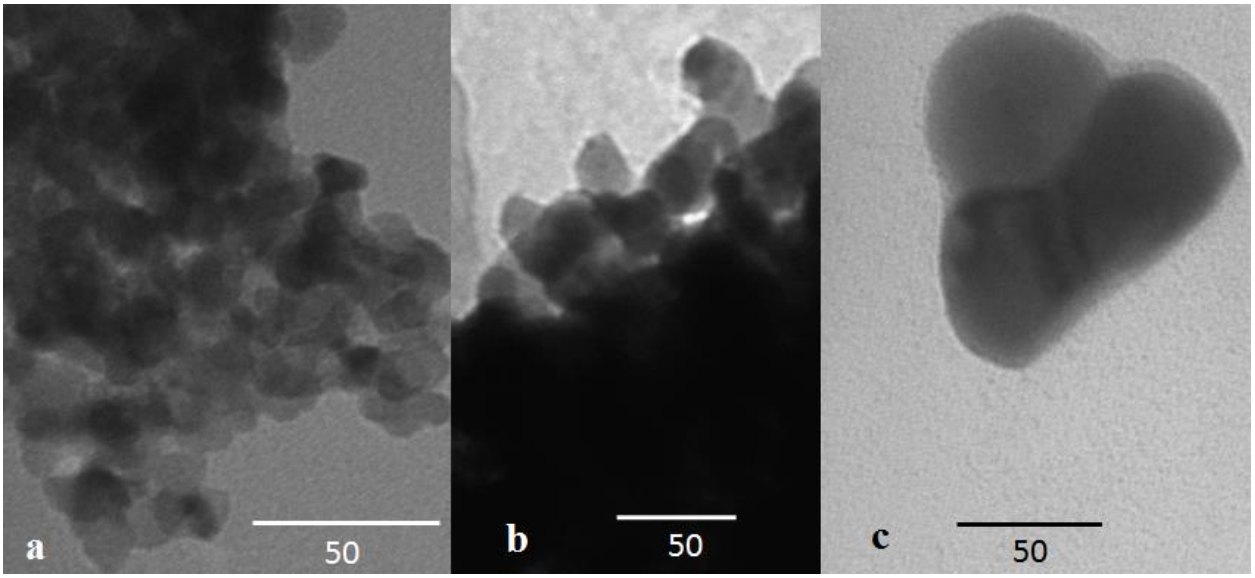

Figure 8.2: TEM images for (a) LaCa400, (b) LaCa700 and (c) LaCa900 showing the increase in crystallite size as T_A increases.

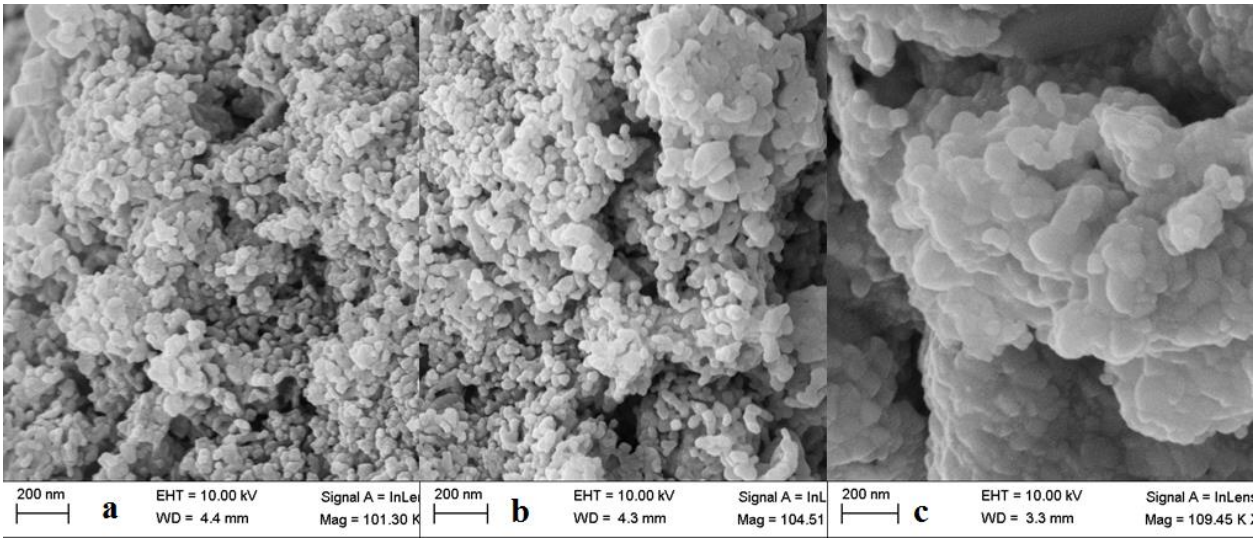

Figure 8.3: Scanning electron microscopy micrographs for (a) LaCa600, (b) LaCa700 and (c) LaCa900.

8.3.3 BET surface areas

Figure 8.4 shows the nitrogen adsorption-desorption isotherms for the powders. The isotherms conform to the type II isotherm on the IUPAC scale [28]. The BET specific surface areas range between 2.77 and 27.37 m^2 g^{-1} (Table 8.1) and decrease as T_A is

increased. Figure 8.5 shows the decreasing specific surface area as T_A increases. The hysteresis loop is pushed much closer to 1 at higher T_A indicating a preponderance of macropores at higher T_A. The inset in Figure 8.4 shows the pore size distribution of the powders. The pores are mostly mesopores at low T_A value. The sharpness of the peaks indicates a sort of uniformity or a narrow pore size distribution in the powders. As the T_A increases, however, the pore area drops rapidly and shifts towards larger pore sizes in agreement with the adsorption-desorption hysteresis loop until it finally disappears at T_A = 900 °C. The decrease in the mesopore areas, and the increase in particle sizes, is responsible for the decrease in the values of the specific surface areas of the powders. Figure 8.6 shows the Arrhenius fit for the relationship between the natural log of the BET specific surface area (ln S_{BET}) and the reciprocal of the T_A (K^{-1}) given by

$$ln\, S_{BET} = ln\, A - \frac{E_A}{R}(1|T). \qquad (8.1)$$

where S_{BET} is the BET specific surface area, E_A is the activation energy for surface reduction, R is the universal gas constant (value 8.314 J K^{-1} mol^{-1}), T is the annealing temperature, and A is a constant. The calculated value for the E_A from the slope of the graph is 41±12 kJ mol^{-1}. This value is much higher than values reported for pure $LaFeO_3$ (between 20 kJ mol^{-1} [29] and 28 kJ mol^{-1} [30]). This higher value for E_A may be as a result of the substitutions that have been made in the $LaFeO_3$ lattice as well as the difference in the synthesis method applied.

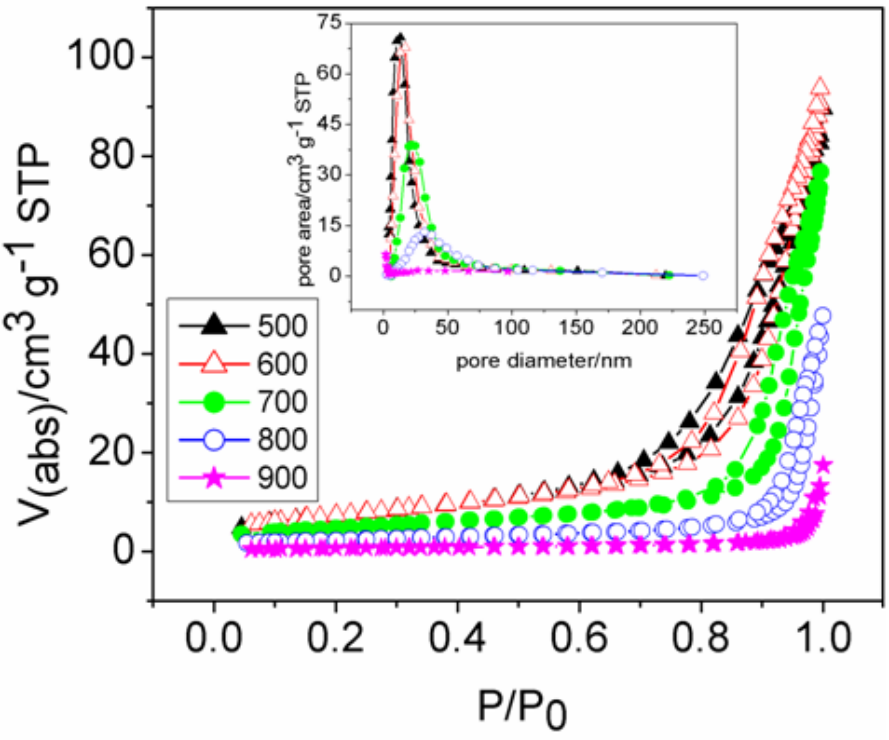

Figure 8.4: Adsorption-desorption isotherms for LaCa500-900. The hysteresis loop moves towards higher relative pressure as the annealing temperature increases. The inset shows plots of the pore size distribution for LaCa500-900 showing the decrease in the mesoporous peak area as the annealing temperature increases.

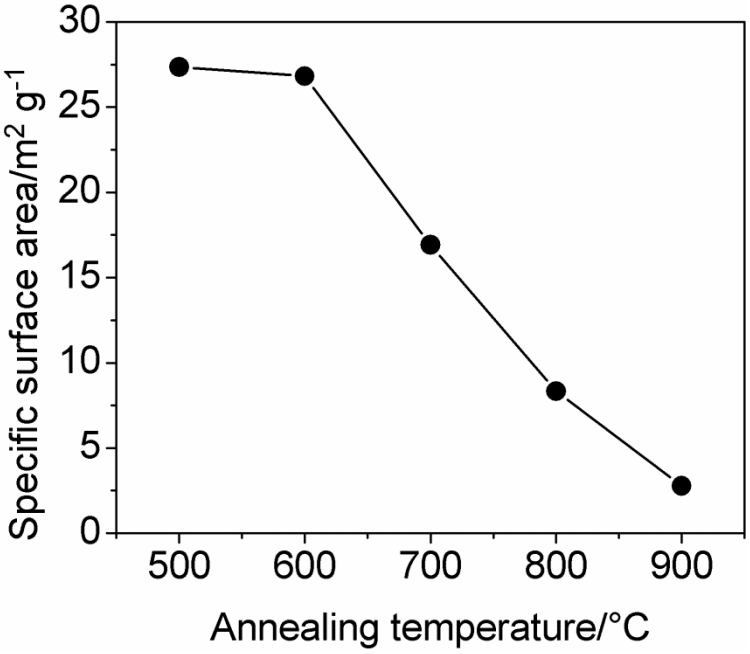

Figure 8.5: Decrease in specific surface area as annealing temperature increases.

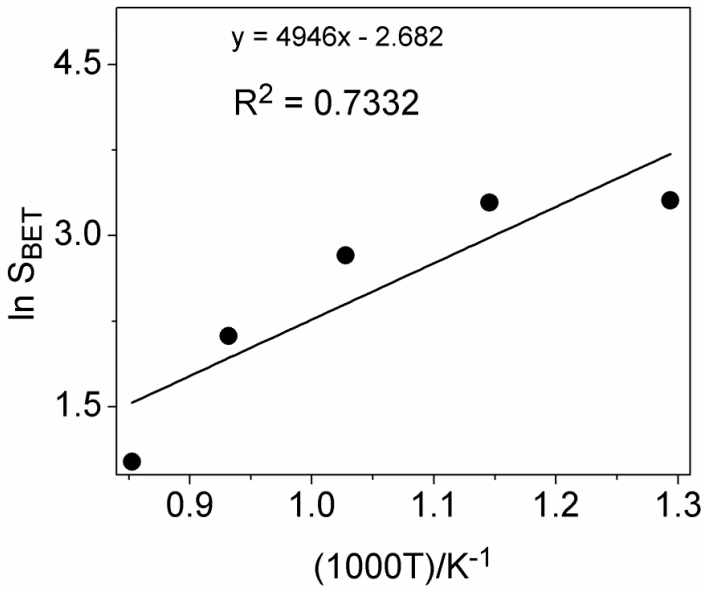

Figure 8.6: Arrhenius plot for LaCa500-900 from which the activation energy for surface reduction was obtained.

8.3.4 Surface characterization

Figure 8.7 shows the Fourier transform infrared spectra of the samples collected between wavelengths 380 and 4000 cm^{-1}. The spectra show two important peaks, one at about 1400 cm^{-1} and the other at around 600 cm^{-1}. The peak at 1400 cm^{-1} is assigned to stretching vibrations of OH groups from water molecules adsorbed on the surface of the crystals. The intensity of this peak decreases as T_A increases, indicating the removal of the water molecules at the surface of the material. It could also be an indication of a reduction in surface area as T_A increases. The peak at 600 cm^{-1} is assigned to stretching modes for O-Fe-O bonds. This is an indication of the progress of the formation of the perovskite lattice as was observed in the PXRD diffractograms.

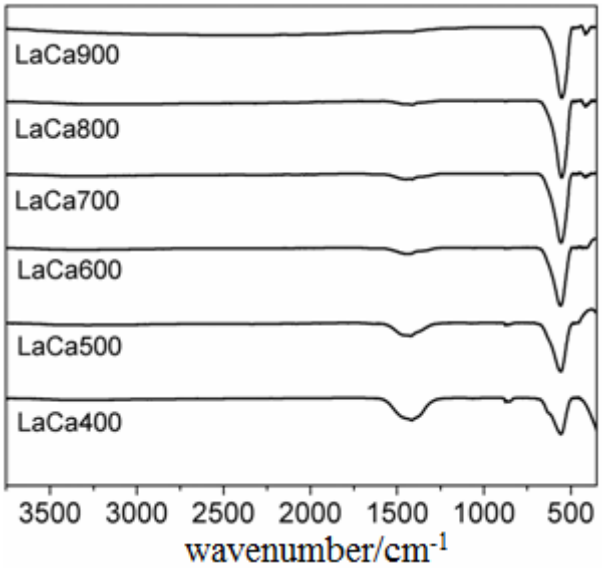

Figure 8.7: Fourier transform infrared spectra for LaCa400-900 showing the reduction in peak intensity at 1400 cm^{-1} and an increase in peak intensity at 600 cm^{-1} with increase in annealing temperature.

8.3.5 Thermal stability

The TGA-DSC results for LaCa400 are shown in Figure 8.8 with thermal decomposition occurring in two different stages. The first stage, which involves the decomposition proceeding gradually between the range 25-380 °C, represents loss of small adsorbed molecules like H_2O and CO_2. The sharp drop in weight between 380-650 °C is attributed to the decomposition of oxalates to carbonates and the subsequent decomposition of the carbonate and other organic materials present. The powder appears to stabilize thereafter with no further loss of weight. The crystallization process (which is exothermic) is unfortunately not captured on the DSC.

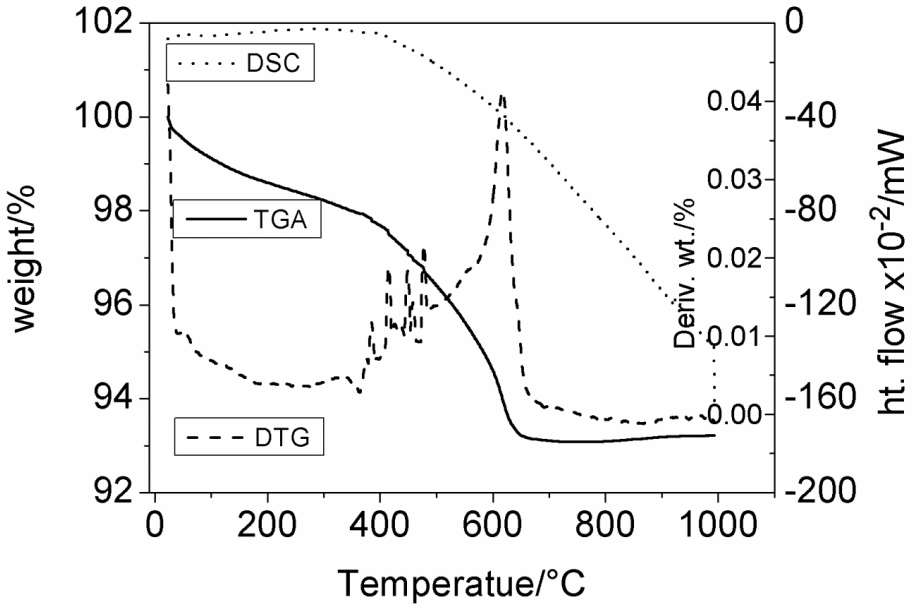

Figure 8.8: Thermal stability of the pre-calcined LaCa400 powder between 25 and 1000 °C obtained in air.

8.3.6 Magnetic properties

Perovskite solid solution ferrites have been reported to have antiferromagnetic properties due to the formation of bond overlaps between Fe ions and the p orbitals of oxygen ions which leads to the formation of Fe^{3+}–O–M^{3+} bonds (where M^{3+} is Bi^{3+}, $Fe^{3+}$and Mn^{3+}). The introduction of an M^{2+} ion into the lattice would lead to a distortion in the bond angle of the Fe–O–Fe. Furthermore, the introduction of Ca^{2+} into the lattice would either lead to the formation of Fe^{4+} in order to fulfill the requirements of charge compensation or result in the creation of oxygen vacancies and these contribute to the ferromagnetic characteristics [31-34]. The result of the room temperature (RT) magnetization measurements of the powders is presented in Figure 8.9. The highest magnetization of 7.67 emu g^{-1} was obtained for LaCa400. A general decrease in magnetization is observed for powders annealed at higher T_A. This decrease

in M_S corresponds to the increase in crystallinity as can be seen from the PXRD (Figure 8.1). At T_A = 400 °C, the powders are composed mainly of mixed oxides. As the T_A is increased, more ions are incorporated into the perovskite lattice and Fe^{2+} ions are oxidized to Fe^{3+} in the perovskite octahedral site. This leads to the formation of more of the antiferromagnetic Fe^{3+}-O-M^{3+} superexchange which results in a reduction in the value of M_S as T_A increased. The reverse, however, is the case for values of the coercive fields. The coercive field values increase for powders annealed at higher T_A (Table 8.2). Figure 8.10 shows the dependence of M_S and H_C on the T_A. The increase in H_C can be attributed to the increase in sizes of the crystals and is related to the magnetocrystalline anisotropy [35], as the crystallite sizes increased with T_A. The squareness values (M_R/M_s) all remain low, indicating soft magnetic properties and do not show any discernible variation with the changing T_A.

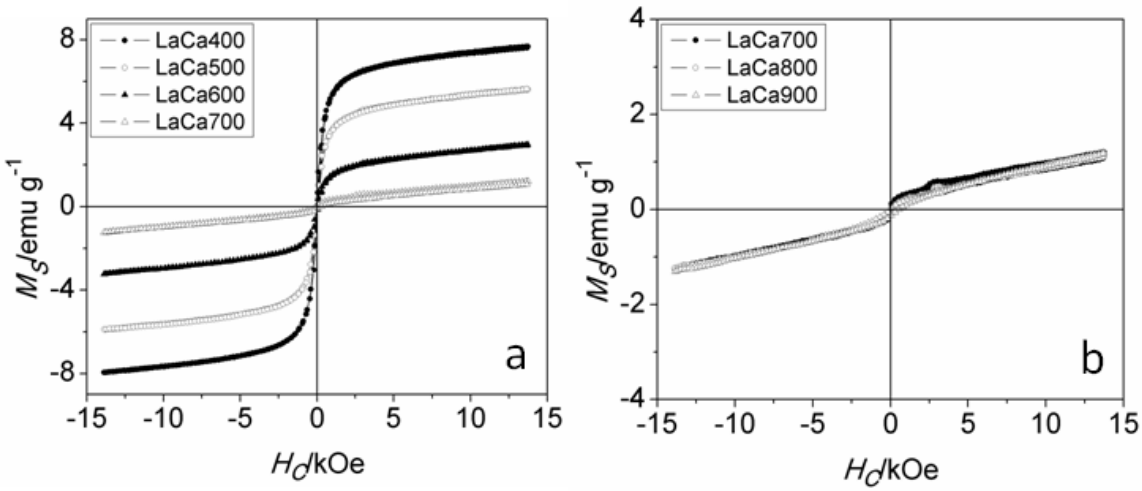

Figure 8.9: Magnetization hysteresis loops for (a) decreasing saturation magnetization for powders annealed at temperatures between 400 and 700 °C, and (b) powders annealed at 700 to 900 °C.

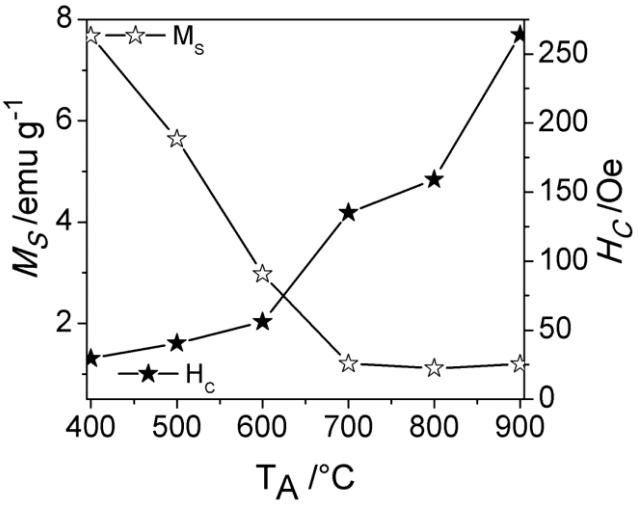

Figure 8.10: Variation of M_S and H_C with increasing T_A for LaCa400-900.

Table 8.2: Magnetization parameters for LaCa400-900. Crystallite sizes were calculated from PXRD by using the Scherrer equation.

Samples	M_S/emu g^{-1} (± 0.4)	M_R/emu g^{-1} (± 0.02)	H_C/Oe (± 1)	M_R/M_S	Crystallite sizes/nm (± 2)
LaCa400	7.70	0.27	29.56	0.049	15.99
LaCa500	5.64	0.23	40.59	0.061	16.52
LaCa600	3.00	0.06	56.02	0.064	17.69
LaCa700	1.20	0.02	135.08	0.053	22.35
LaCa800	1.11	0.03	159.11	0.025	31.84
LaCa900	1.19	0.003	263.87	0.054	37.91

8.3.7 Photoluminescence

Figure 8.11 shows the room temperature emission of the powders LaCa400-600 showing a T_A dependent photoluminescence (PL) spectral intensity. The spectra show

an initial decrease in the PL intensity as T_A increases from 400 to 600 °C for an excitation wavelength (λ_{ex}) of either 390 or 400 nm. Two peaks, each, shifting correspondingly with the excitation wavelength were obtained with the emissions excited at 390 nm having the higher intensity. The decrease in the PL peak intensities here appear to reflect the increase in order as observed from the magnetization measurements as well as the PXRD patterns. The peak intensities then begin to increase as T_A increases (Figure 8.12). Figure 8.12 shows the PL spectra for powders annealed at T_A values from 600 to 900 °C. The powders were excited at 390 and 400 nm as is the case for Figure 8.11 and the emissions were monitored between 530 to 660 nm. Two emission peaks are observed with λ_{em} shifting correspondingly with the shift in λ_{ex}. These increases in intensity appear to correspond to the increase in crystallinity as can also be observed from the PXRD peaks.

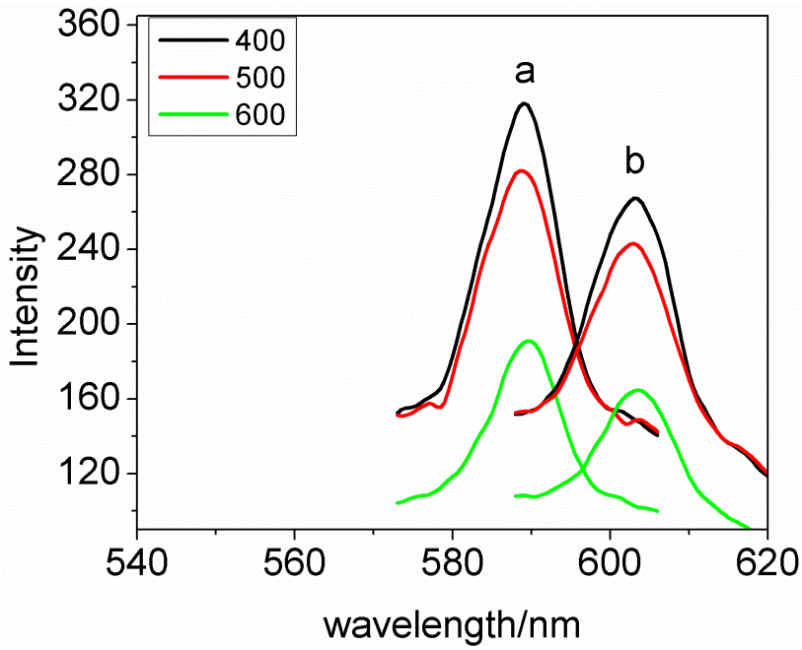

Figure 8.11: PL spectra showing the shifting emission peak intensities for the samples LaCa400, LaCa500 and LaCa600 which decrease with increasing T_A. The excitation and emission wavelengths are (a) λ_{ex} = 390 nm and λ_{em} = 589, and (b) λ_{ex} = 400 nm and λ_{em} = 603 nm.

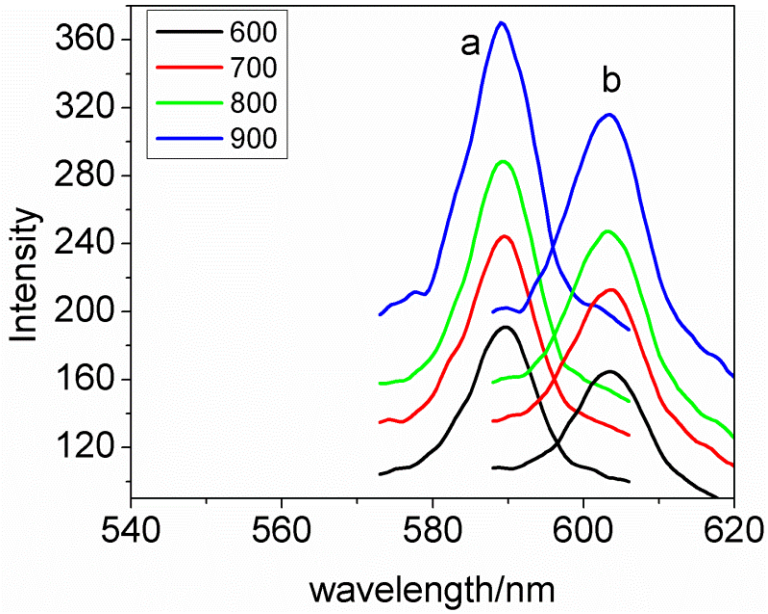

Figure 8.12: PL spectra showing shifts in the emission peak positions as the excitation wavelength is varied. The excitation and emission wavelengths are as follows (a) λ_{ex} = 390 nm and λ_{em} = 589, and (b) λ_{ex} = 400 nm and λ_{em} = 603 nm.

8.3.8 Photocatalytic screening

The results of the photocatalytic screening of LaCa400-900 on RhB dye are shown in Figure 8.13. The results show only slight activity for LaCa700, LaCa800 and LaCa900 in the absence of H_2O_2, while LaCa400, LaCa500 and LaCa600 appear not to have a significant effect on the dye solution Figure 8.13a. In the presence of H_2O_2, however, a significant impact is noticed in the photocatalytic activities of the powders LaCa600, LaCa700, LaCa800 and LaCa900 with the later three being the most active (Figure 8.13(b)). Organic and amorphous materials blocking the dye molecules from reaching the surface of the photocatalysts may explain the reason for the low or inactivity of powders annealed at lower T_A (400-600 °C see Section 8.3.5). The powders annealed at T_A between 700 and 900 °C, however, do not have such barriers and therefore were able to degrade the dye solution faster. Figure 8.14 shows the pseudo first-order kinetics of

the photocatalytic processes and the values of the observed rate constants and the calculated percent efficiency (E/%) (given by E% = (((A$_0$ - A)/A$_0$) × 100) where A$_0$ and A are the initial and final absorbance of the dye solution respectively) are shown in Table 8.3. The LaCa700-900/H_2O_2 systems showed very high efficiency in decolourizing the RhB dye solution, suggesting that the materials are excellent photocatalysis.

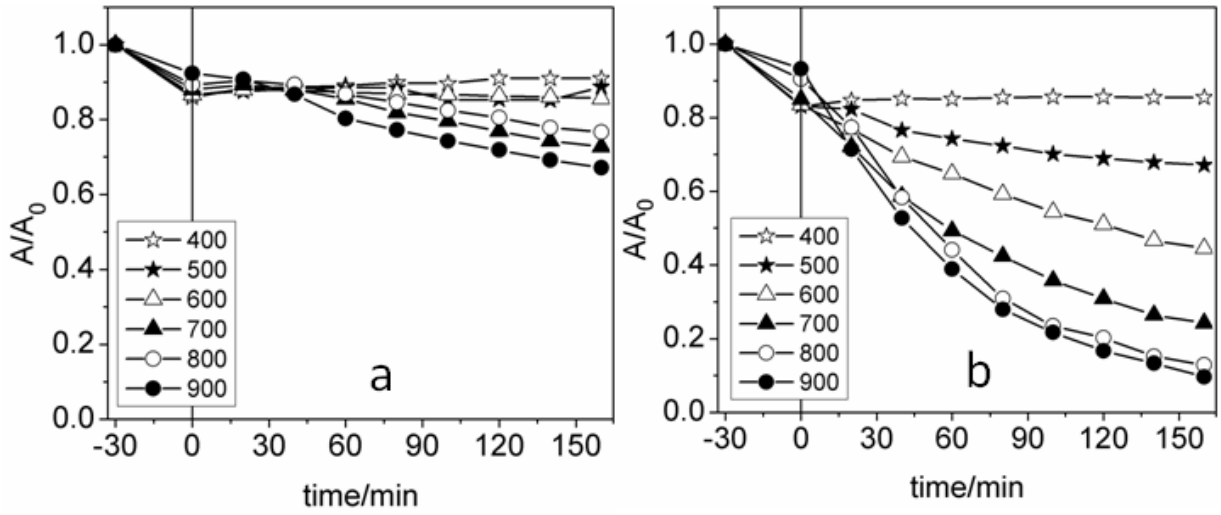

Figure 8.13: Photodegradation of RhB when irradiated with visible light for the photocatalysts LaCa400-900 (1.5 g dm^{-1}) (a) in the absence of H_2O_2, and (b) in the presence of H_2O_2 (3.0 × 10^{-5} mol dm^{-3}).

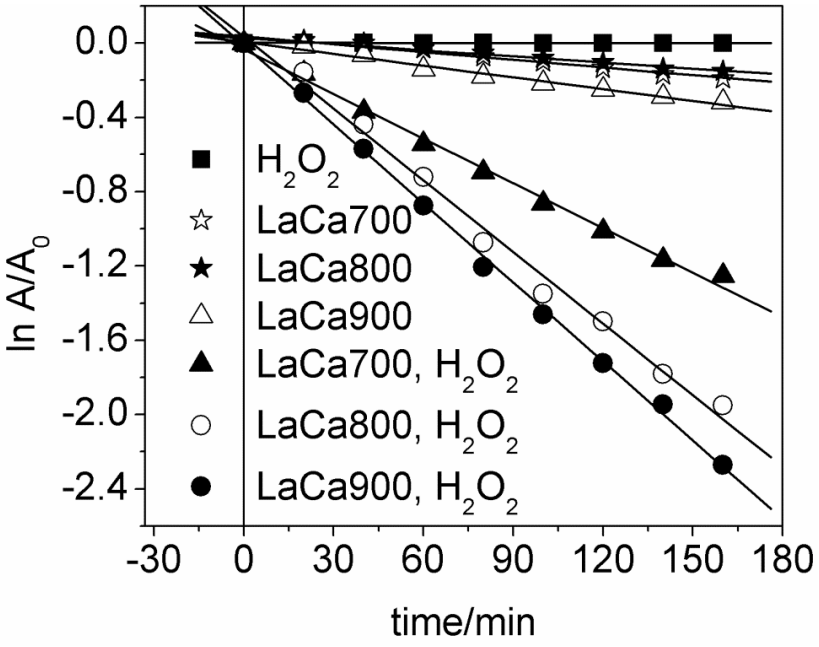

Figure 8.14: Pseudo-first-order rates for the degradation of RhB in the presence of 1.5 g dm^{-3} of photocatalyst and 3.0×10^{-5} mol dm^{-3} H_2O_2.

Table 8.3: Observed kinetics parameters for the photodegradation of RhB by 1.5 g dm^{-3} of photocatalysts (LaCa700-900) and 3.0×10^{-5} mol dm^{-3} H_2O_2.

Sample	**k_{obs}/min^{-1}**	**E/%**
H_2O_2	4.4×10^{-6}	0
LaCa700	1.4×10^{-3}	42.9
LaCa800	1.1×10^{-3}	39.8
LaCa900	2.1×10^{-3}	47.2
LaCa700 + H_2O_2	8.0×10^{-3}	79.6
LaCa800 + H_2O_2	1.2×10^{-2}	89.2
LaCa900 + H_2O_2	1.4×10^{-2}	99.1

8.3.8.1 Mineralisation of the RhB dye

Figure 8.15 shows the results for the chemical oxygen demand (COD) analysis of the dye solution over a period of 180 min of photodegradation activity in the presence of LaCa900 (1.5 g dm^{-1}) and H_2O_2 (3.0×10^{-5} mol dm^{-3}). A gradual decrease in the value

of the COD of the dye solution shows that the dye is being effectively mineralized. Figure 8.16 shows the COD results of the mineralisation of the dye solution by LaCa700, LaCa800 and LaCa900 after 180 min of phocatalytic activity. The COD values obtained are 52, 48 and 36 mg dm^{-3} for LaCa700, LaCa800 and LaCa900, which represents an efficiency of 56.67, 60.00 and 70% mineralisation respectively. This shows that the photocatalyst can be used to effectively degrade organic pollutants and convert them into harmless substances like CO_2 and H_2O.

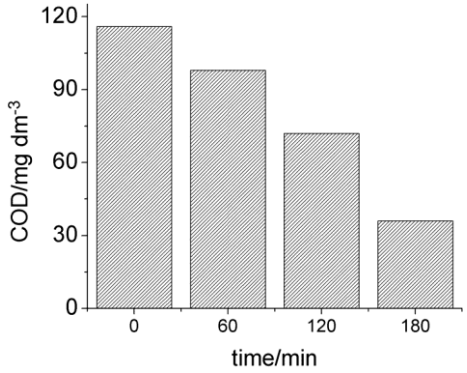

Figure 8.15: The carbon oxygen demand (COD) analyses at intervals of 1 hour for three hours for LaCa900.

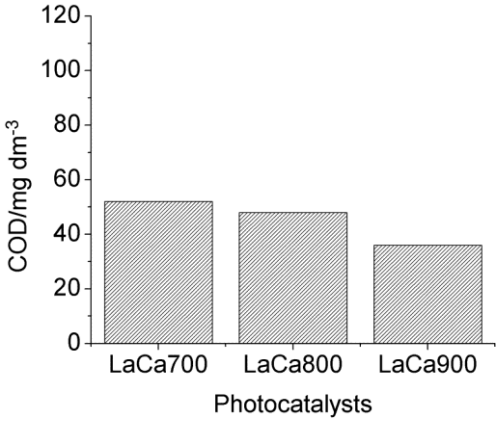

Figure 8.16: Analysis of the chemical oxygen demand (COD) for LaCa700, LaCa800 and LaCa900 after a period of 3 hours of photodegradation. The mineralization efficiency is 56.67, 60 and 70% respectively.

8.3.8.2 Mechanism of the photodegradation process

The photodegradation of RhB dye solution in this work is driven by the generation of hydroxyl radical. We propose the following mechanism for the generation of the hydroxyl radicals and the subsequent photodegradation processes of the dye solution.

The electron-hole pair is generated in the photocalyst (PC) material.

$$\mathrm{PC} + h\nu \rightarrow e^- + \mathrm{h}^+ \qquad (8.2)$$

Generated electrons in the conduction band are then trapped by H_2O_2 to produce the hydroxyl radicals:

$$\mathrm{H_2O_2} + e^- \rightarrow {}^{\cdot}\mathrm{OH} + \mathrm{OH}^- \qquad (8.3)$$

More radicals are generated from a reaction between the hole h^+ and the adsorbed H_2O molecules:

$$\mathrm{H_2O} + \mathrm{h}^+ \rightarrow \mathrm{H}^+ + {}^{\cdot}\mathrm{OH} \qquad (8.4)$$

A Fenton-like mechanism involving the Fe^{3+} ions in the B-site of the perovskite lattice and H_2O_2 can also produce more hydroxyl radicals:

$$\mathrm{H_2O_2} + \mathrm{Fe}^{3+} \rightarrow \mathrm{Fe} - \mathrm{OOH}^{2+} + \mathrm{H}^+ \qquad (8.5)$$

$$\mathrm{Fe}-\mathrm{OOH}^{2+} \rightarrow \mathrm{Fe}^{2+} + \mathrm{HO}_2^{\bullet} \qquad (8.6)$$

$$\mathrm{H_2O_2} + \mathrm{Fe}^{2+} \rightarrow \mathrm{Fe}^{3+} + 2\mathrm{HO}^{\bullet} \qquad (8.7)$$

The degradation process then proceeds as follows:

$$\mathrm{RhB} + \mathrm{HO}^{\bullet} \rightarrow \mathrm{RhB}^{\bullet} \qquad (8.8)$$

$$RhB^{\bullet} \rightarrow R^{\bullet} \rightarrow \text{smaller organic molecules} + CO_2 + H_2 \quad (8.9)$$

leading to complete mineralization of the rhodamine B dye.

8.4 Conclusions

Perovskite-like $(La_{0.5}Bi_{0.2}Ca_{0.2}Mn_{0.1})FeO_{(3-\delta)}$ powders of crystallite size range from 15.98 to 37.91 nm were synthesized via a citric acid route. The PXRD results show that the powders crystallized in a rhombohedral lattice with crystallite sizes increasing with T_A. The BET specific surface areas decreased with increase in T_A. The activation energy for the reduction of the material surface calculated from the Arrhenius plot is 41 kJ mol^{-1}. The saturation magnetization decreased gradually as T_A increased. The materials also showed good photoluminescence activities within the visible region of the electromagnetic spectrum. The powders annealed at 700, 800 and 900 °C showed slight photocatalytic activities for RhB degradation, but the activities were drastically improved by addition of H_2O_2 and up to 99% decolourization of RhB was achieved for LaCa900 and 70 % mineralization after 3 hours of exposure to visible light. The author recommends these materials for use in degrading toxic organic dyes and pharmaceutical waste. They are easy to prepare and are capable of achieving a higher degree of mineralization of organic molecules.

Acknowledgements

IA is grateful to the College of Agriculture, Engineering and Science at the University of KwaZulu-Natal for the award of a PhD bursary and a Doctoral Scholarship. The vibrating sample magnetometer used in this work was provided by the National Research Foundation of South Africa.

References

[1] N. Toan, S. Saukko, V. Lantto, N.S. Hieu, Physica Scripta 2004 (2004) 167.
[2] V. Lantto, S. Saukko, N. Toan, L. Reyes, C. Granqvist, Journal of Electroceramics 13 (2004) 721-726.
[3] T.G. Ho, T.D. Ha, Q.N. Pham, H.T. Giang, T.A.T. Do, N.T. Nguyen, Advances in Natural Sciences: Nanoscience and Nanotechnology 2 (2011) 015012.
[4] J.W. Fergus, Sensors and Actuators B: Chemical 123 (2007) 1169-1179.
[5] Z. Zhou, L. Guo, H. Yang, Q. Liu, F. Ye, Journal of Alloys and Compounds 583 (2014) 21-31.
[6] K. Sardar, J. Hong, G. Catalan, P.K. Biswas, M.R. Lees, R.I. Walton, J.F. Scott, S.A. Redfern, Journal of Physics: Condensed Matter 24 (2012) 8.
[7] H. Lahmar, S. Habouti, C.-H. Solterbeck, M. Dietze, M. Es-Souni, Journal of Applied Physics 107 (2010) 8.
[8] A. Lahmar, K. Zhao, S. Habouti, M. Dietze, C.-H. Solterbeck, M. Es-Souni, Solid State Ionics 202 (2011) 1-5.
[9] S.J. Skinner, International Journal of Inorganic Materials 3 (2001) 113-121.
[10] E. Maguire, B. Gharbage, F. Marques, J. Labrincha, Solid State Ionics 127 (2000) 329-335.
[11] S. Rousseau, S. Loridant, P. Delichere, A. Boreave, J.P. Deloume, P. Vernoux, Applied Catalysis B: Environmental 88 (2009) 438-447.
[12] W. Luo, L. Zhu, N. Wang, H. Tang, M. Cao, Y. She, Environmental Science & Technology 44 (2010) 1786-1791.
[13] C.-C. Hu, Y.-L. Lee, H. Teng, Journal of Materials Chemistry 21 (2011) 3824-3830.
[14] M.D. Peel, S.E. Ashbrook, P. Lightfoot, Inorganic Chemistry 52 (2013) 8872-8880.
[15] D.S. Paik, S.E. Park, T.R. Shrout, W. Hackenberger, Journal of Materials Science 34 (1999) 469-473.
[16] V. Bedekar, O.D. Jayakumar, J. Manjanna, A.K. Tyagi, Materials Letters 62 (2008) 3793-3795.
[17] H. Yang, J.X. Zhang, G.J. Lin, T. Xian, J.L. Jiang, Advanced Powder Technology 24 (2013) 242-245.
[18] X. Li, Z.-Q. Duan, Materials Letters 89 (2012) 262-265.
[19] L. Li, X. Wang, Y. Zhang, Materials Research Bulletin 50 (2014) 18-22.
[20] L. Li, X. Wang, Y. Lan, W. Gu, S. Zhang, Industrial & Engineering Chemistry Research 52 (2013) 9130-9136.
[21] J. Van Den Brink, D.I. Khomskii, Journal of Physics: Condensed Matter 20 (2008) 12.
[22] D.I. Khomskii, Journal of Magnetism and Magnetic Materials 306 (2006) 1-8.
[23] J. Yang, W. Yelon, W. James, Z. Chu, M. Kornecki, Y. Xie, X. Zhou, H. Anderson, A.G. Joshi, S. Malik, Physical Review B 66 (2002) 184415-184423.
[24] K. Takahashi, M. Tonouchi, Journal of Magnetism and Magnetic Materials 310 (2007) 1174-1176.
[25] J. Li, X. Kou, Y. Qin, H. He, Physica Status Solidi (a) 191 (2002) 255-259.
[26] M.B. Bellakki, V. Manivannan, J. Das, Materials Research Bulletin 44 (2009) 1522-1527.

[27] I. Williams, Wiley, 1 ed., John Wiley & Son, Ltd, UK, 2001, p. 276-279.
[28] K. Sing, D. Everett, R. Haul, L. Moscou, R. Pierotti, J. Rouquerol, T. Siemieniewska, Pure and Applied Chemistry 54 (1982) 603-619.
[29] R. Andoulsi, K. Horchani-Naifer, M. Férid, Cerâmica 58 (2012) 126-130.
[30] R. Köferstein, L. Jäger, S.G. Ebbinghaus, Solid State Ionics 249–250 (2013) 1-5.
[31] L. Wang, D. Wang, H. Huang, Z. Han, Q. Cao, B. Gu, Y. Du, Journal of Alloys and Compounds 469 (2009) 1-3.
[32] Y.-Q. Liang, N.-l. Di, Z.-h. Cheng, Physical Review B 72 (2005) 134416.
[33] M. Li, M. Ning, Y. Ma, Q. Wu, C. Ong, Journal of Physics D: Applied Physics 40 (2007) 1603-1607.
[34] V. Khomchenko, D. Kiselev, J. Vieira, L. Jian, A. Kholkin, A. Lopes, Y. Pogorelov, J. Araujo, M. Maglione, Journal of Applied Physics 103 (2008) 024105-024110.
[35] G. Herzer, IEEE Transactions on Magnetics 26 (1990) 1397-1402.

Chapter 9

Summary and conclusions

9.1 Summary

In summary, we have investigated the effect of synthesis route and annealing temperature on the magnetic and photocatalytic properties of hematite and some novel perovskite-like solid solutions. The characterization and analysis of these properties was carried out by using standard chemical methods of analysis as well as instrumentation which allowed us to describe the variation in the material properties as the synthesis route and annealing temperatures were varied.

In Chapter 3, we investigated the effect of synthesis method on the structure and magnetic and photocatalytic properties of α-Fe_2O_3. We synthesized α-Fe_2O_3 nanoparticles via three different wet chemical routes namely: coprecipitation, citric acid sol-gel route, and a sol-gel route, in Tween 20 and analysed their crystallite sizes and morphology, surface area, magnetic properties as well photocatalytic activities on the degradation of RhB. Tween 20, was able to produce α-Fe_2O_3 nanoparticle with crystallite sizes below 20 nm with improved magnetic properties. A saturation magnetisation of up to 19 emu g^{-1} was obtained for the Hem_TW400 which gradually reduced as annealing temperature was increased and crystallite sizes increased. Hem_TW400 also presented the highest activities in the photodegradation of RhB indicating that the synthetic medium (Tween 20, a polysorbate surfactant), can be a very good additive to the precursor solution in a Pechini type sol-gel synthesis of α-Fe_2O_3 in order to effectively impact on the properties of the synthesized powders.

In Chapter 4, we synthesized novel perovskite-type materials with a general formula $(Nd_{0.5}Bi_{0.2}X_{0.2}Mn_{0.1})FeO_{3-\delta}$, where X = Ca, Sr and Ba, by using a simple citric acid sol-gel method. The powders were precalcined at 400 °C and annealed at 750 and 900 °C in a muffle furnace for four hours. PXRD analysis showed that all the samples crystallized in an orthorhombic lattice with crystallinity increasing as annealing temperature increased. Crystallite sizes calculated by using the Scherrer equation also increased as annealing temperature increased. The BET surface area analysis showed a decrease in specific surface area as annealing temperature increased. The room temperature magnetisation hysteresis loops revealed high coercive fields for powders annealed at 750 and 900 °C for Sr and Ba substituted samples (up to 5.24 and 5.58 Oe for Sr- and Ba- substituted powders respectively) while the Ca substituted sample showed a predominance of antiferromagnetic properties. ^{57}Fe room temperature Mössbauer spectra were fitted with two sextet subspectra revealing the presence of two different Fe^{3+} environments, and also that the magnetism in the powders originates from the distortion of the bond angle of the O-Fe-O superexchange and therefore depends on the size of the substituent (i.e. Ca, Sr and Ba). The photoluminescence excitation energies fall within the visible region of the electromagnetic spectrum. The photocatalytic activities of the powders in the presence of H_2O_2 show that the powders function as good photocatalysts for the degradation of dyes in the visible light range over a wide range of pH conditions. The Ca- and Sr- substituted powders exhibited very good catalytic activity towards photodegradation and mineralisation of the model dye, RhB.

In Chapter 5, we synthesized novel perovskite-type materials with a general formula $(Eu_{0.5}Bi_{0.2}X_{0.2}Mn_{0.1})FeO_{3-\delta}$, where X = Ca, Sr and Ba, by using a simple citric acid sol-gel method. The powders were precalcined at 400 °C and annealed at 600, 700, 800 and 900 °C in a muffle furnace for four hours. PXRD analysis showed that all the samples crystallized in an orthorhombic lattice with crystallinity increasing as annealing temperature increased. The Sr- and Ba- substituted powders required a higher temperature for the orthorhombic peaks to fully form. Crystallite sizes calculated by using the Scherrer equation also increased as annealing temperature increased. The BET surface area analysis showed a decrease in specific surface area as annealing temperature increased. The room temperature magnetisation hysteresis loops revealed an increasing coercive field as the annealing temperature increased. A very high coercive field was recorded for powders annealed at 800 and 900 °C for Sr- and Ba-substituted samples (up to 5.78 and 5.05 Oe for Sr- and Ba- substituted powders respectively) while the Ca-substituted sample showed a predominance of antiferromagnetic properties. The photoluminescence excitation energies fall within the visible region of the electromagnetic spectrum. The photocatalytic activities of the powders in the presence of H_2O_2 showed that the powders function as good photocatalysts for the degradation of dyes in the visible light range over a wide range of pH conditions. The Ca- and Sr-substituted powders exhibited very good catalytic activity towards photodegradation and mineralisation of the model dye, RhB.

In Chapter 6, we synthesized novel perovskite-type materials with a general formula $(La_{0.5}Bi_{0.2}Sr_{0.2}Mn_{0.1})FeO_{3-\delta}$, by using a simple citric acid sol-gel method. The powders were precalcined at 400 °C and annealed at 500, 600, 700, 800 and 900 °C in a muffle furnace for four hours. PXRD analysis showed that all the samples crystallized in an

rhombohedral lattice with crystallinity increasing as annealing temperature increased. Crystallite sizes calculated by using the Scherrer equation also increased as annealing temperature increased (crystallite size range was 19.62 to 40.56 nm). The BET surface area analysis showed a decrease in specific surface area as annealing temperature increased (BET SSA range 2.26-22.34 $m^2 g^{-1}$). The activation energy for the reduction of surface area obtained from an Arrhenius plot is 43±7 kJ mol^{-1}. Cell parameters, however, were not drastically affected but a slight decrease due to stabilization of higher oxidation states was observed. The room temperature magnetisation hysteresis loops reveal two distinct stages. One characterized by a decrease in saturation magnetisation (between T_A = 400 and 600 °C), and the other by drastic increase in the coercive field. A very high coercive field was recorded for powders annealed at 800 and 900 °C (4.89 and 5.50 Oe respectively). The photoluminescence excitation energies fall within the visible region of the electromagnetic spectrum and showed a trend in two directions. The first, a decrease in intensity for LaSr400-600, and then an increase in intensity from LaSr600 to LaSr900. We have attributed the first stage to the ordering of the sites in the perovskite structure and the second to a subsequent increase in crystallinity of the lattice. The photocatalytic activities of the powders in the presence of H_2O_2 showed that the powders function as good photocatalysts for the degradation of dyes in the visible light range over a wide range of pH conditions. The powders annealed at 700 °C and above exhibited very good catalytic activities towards photodegradation and mineralisation of the model dye, RhB.

In Chapter 7, we synthesized novel perovskite-type materials with a general formula $(La_{0.5}Bi_{0.2}Ba_{0.2}Mn_{0.1})FeO_{3-\delta}$, by using citric acid sol-gel method. The powders were precalcined at 400 °C and annealed at 500, 600, 700, 800 and 900 °C in a muffle

furnace for four hours. PXRD analysis showed that all the samples crystallized in an rhombohedral lattice with crystallinity increasing as annealing temperature increased. Crystallite sizes calculated by using the Scherrer equation also increased as annealing temperature increased (crystallite size range was 18.49 to 32.42 nm). The BET surface area analysis showed a decrease in specific surface area as annealing temperature increased (BET SSA range 4.19-27.75 m^2 g^{-1}). The activation energy for the reduction of surface area obtained from an Arrhenius plot is 37±7 kJ mol^{-1}. Cell parameters, however, were not drastically affected but a slight decrease due to stabilization of higher oxidation states was observed. The room temperature magnetisation hysteresis loops revealed an increasing coercive field as the annealing temperature increases. A very high coercive field was recorded for powders annealed at 800 and 900 °C (5.16 and 5.60 Oe respectively). The photoluminescence excitation energies fall within the visible region of the electromagnetic spectrum but showed no discernible trend. The photocatalytic activities of the powders in the presence of H_2O_2 showed that the powders function as good photocatalysts for the degradation of dyes in the visible light range over a wide range of pH conditions. The powders annealed at 700 °C and above exhibited very good catalytic activities towards photodegradation and mineralisation of the model dye, RhB.

In Chapter 8, we synthesized novel perovskite-type materials with a general formula $(La_{0.5}Bi_{0.2}Ca_{0.2}Mn_{0.1})FeO_{3-\delta}$, by using a simple citric acid sol-gel method. The powders were precalcined at 400 °C and annealed at 500, 600, 700, 800 and 900 °C in a muffle furnace for four hours. PXRD analysis showed that all the samples crystallized in a rhombohedral lattice with crystallinity increasing as annealing temperature increased. Crystallite sizes calculated by using the Scherrer equation also increased as annealing

temperature increased (crystallite size range was 19.62 to 40.56 nm). The BET surface area analysis showed a decrease in specific surface area as annealing temperature increased (BET SSA range was 2.76 to 27.37 m^2 g^{-1}). The activation energy for the reduction of surface area obtained from an Arrhenius plot is 41±12 kJ mol^{-1}. Cell parameters were not drastically affected, a general slight decrease due to stabilization of higher oxidation states was observed with the exception of LaCa700 where an increase in the cell volume was observed. The room temperature magnetisation hysteresis loops reveal two distinct stages. one characterized by a decrease in saturation magnetisation (between T_A = 400 and 600 °C), and the other by a gradual increase in the coercive field which is as a result of magnetic anisotropy due to crystallite size increase. The photoluminescence excitation energies fall within the visible region of the electromagnetic spectrum and showed a trend in two directions. The first, a decrease in intensity for LaCa400-600, and then an increase in intensity from LaCa600 to LaCa900. We have attributed the first stage to the ordering of the sites in the perovskite structure and the second to a subsequent increase in crystallinity of the lattice. The photocatalytic activities of the powders in the presence of H_2O_2 showed that the powders function as good photocatalysts for the degradation of dyes in the visible light range over a wide range of pH conditions. The powders annealed at 700 °C and above exhibited very good catalytic activities towards photodegradation and mineralisation of the model dye, RhB in the presence of H_2O_2.

9.2 Conclusions

In conclusion:

- The properties of the synthesized materials depend on the route via which the material was prepared. The medium in which the synthesis takes place is also vital in determining such properties as surface area, crystallite size, magnetic as well as photocatlytic properties. α-Fe_2O_3 nanoparticles synthesized via a sol-gel type route in Tween20 (polysorbate surfactant) had a higher surface area, smaller crystallite sizes, improved magnetic as well as photocatalytic properties for RhB photodegradation. We propose Tween20 as a good additive to the precursor solution in a Pechini type sol-gel synthesis of α-Fe_2O_3 in order to effectively impact on the properties of the synthesized powders.
- Perovskite-type solid solutions with the general formula $((RE_{0.5}Bi_{0.2}X_{0.2}Mn_{0.1})FeO_{3-\delta}$ (where RE = La, Nd and Eu, X = Ca, Sr and Ba) can easily be synthesized via a simple citric acid sol-gel method. The perovskite crystal peaks for the La based materials were observed to form at a much lower temperature compared to those of Nd and Eu. This implies that higher annealing temperatures may be required for the perovskite peaks to form for RE with higher atomic mass.
- The prepared materials all showed improved magnetic properties relative to the weak ferromagnetic properties usually associated with perovskites-like materials. The Ca-substituted materials were an exception to this as all the Ca-substituted materials showed a paramagnetic or a predominance of an antiferromagnetic character. The high coercive fields observed for the materials annealed at high annealing temperatures (700-900 °C) could be of importance in making magnetic memory/recording devices.

- The materials showed very good photocatalytic properties in the degradation of RhB dye solution. Degradation efficiency of up to 99% were sometimes recorded. The same applies to the mineralization efficiencies (where up to 80 % efficiency has been observed). The trend in the photocatalytic efficiency in terms of the alkaline earth metal substitution as observed for all the synthesized perovskite-like materials is in the order Ca > Sr > Ba. The Sr- and Ba-substituted powders, however, have the advantage of the improved magnetic properties, which means they can easily be recovered from the dye solution after use by applying an external magnetic field.

9.3 Further work

- A more detailed analysis of the structural make-up of the materials is required in order to determine the actual types of cells, supercells and phases that are present in the structure. Neutron diffraction can be used to do a more thorough analysis on the structure as well as the source of the magnetism in the materials.
- The potential of these materials for use as solid oxide fuel cells (SOFC), as cathode materials and also as photovoltaic materials requires investigation.

Appendix

Supplementary materials

Chapter 3

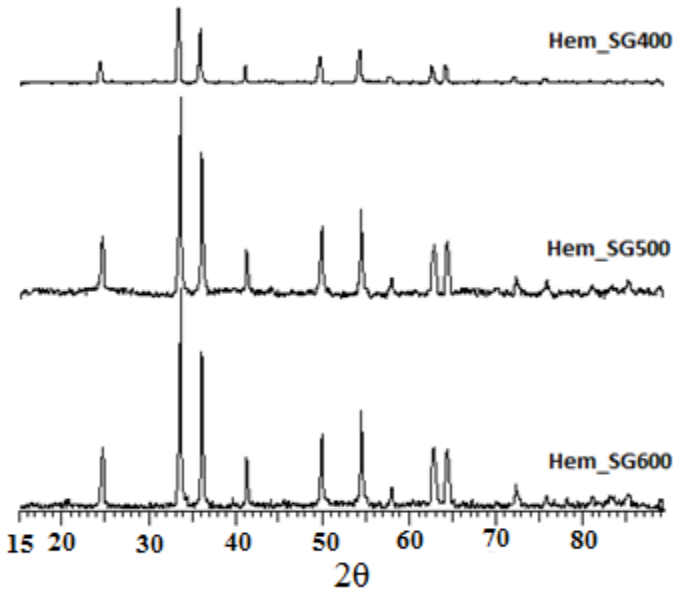

Figure 8: Powder X-ray diffractograms for Hem_SG400-600.

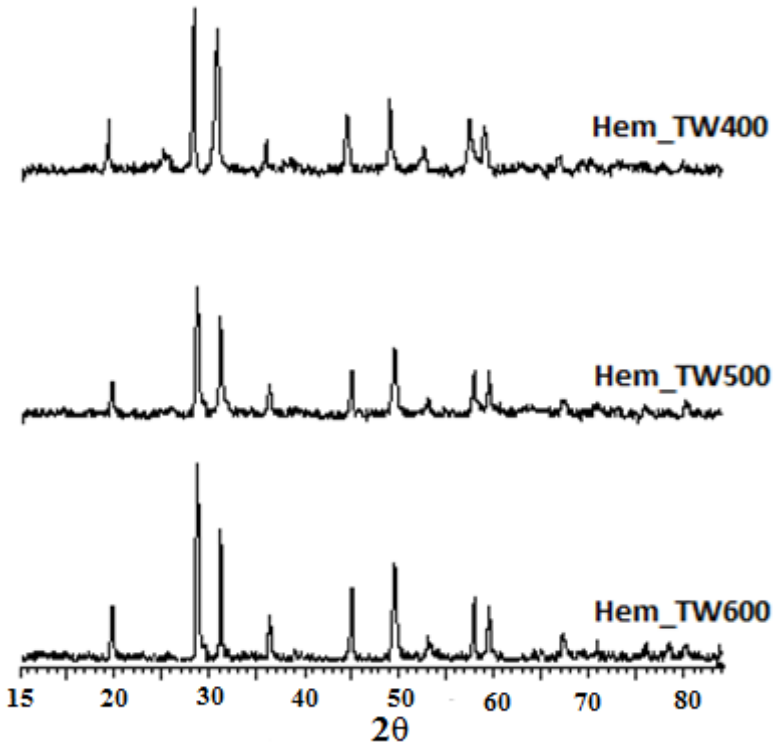

Figure 2: Powder X-ray diffractograms for Hem_TW400-600.

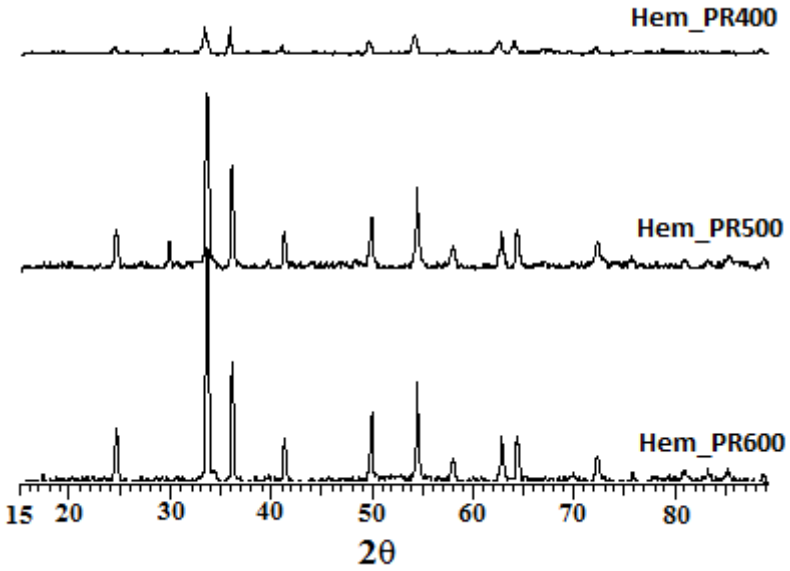

Figure 3: Powder X-ray diffractograms for Hem_PR400-600.

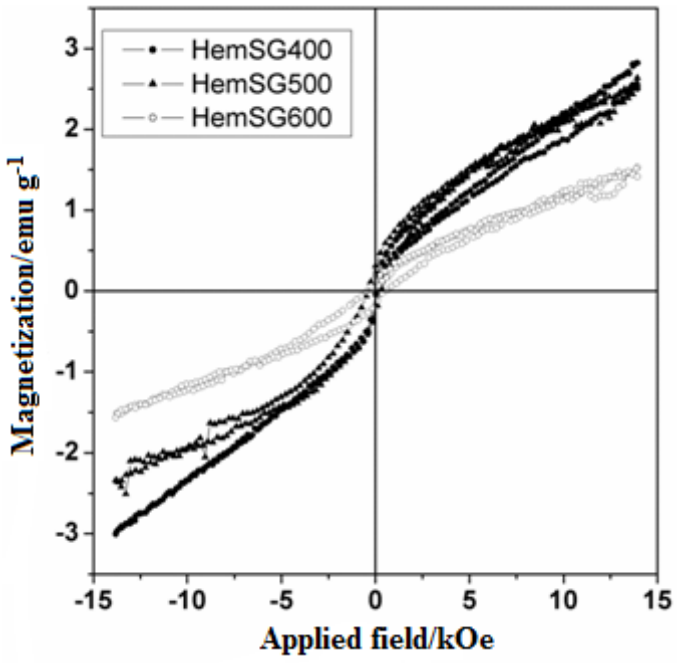

Figure 4: Magnetization hysteresis loop for Hem_SG400-600.

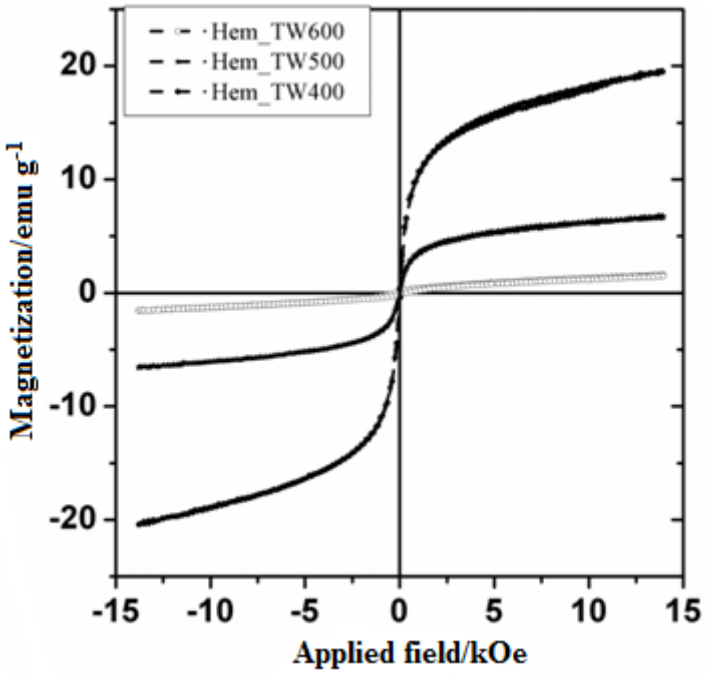

Figure 5: Magnetization hysteresis loop for Hem_TW400-600.

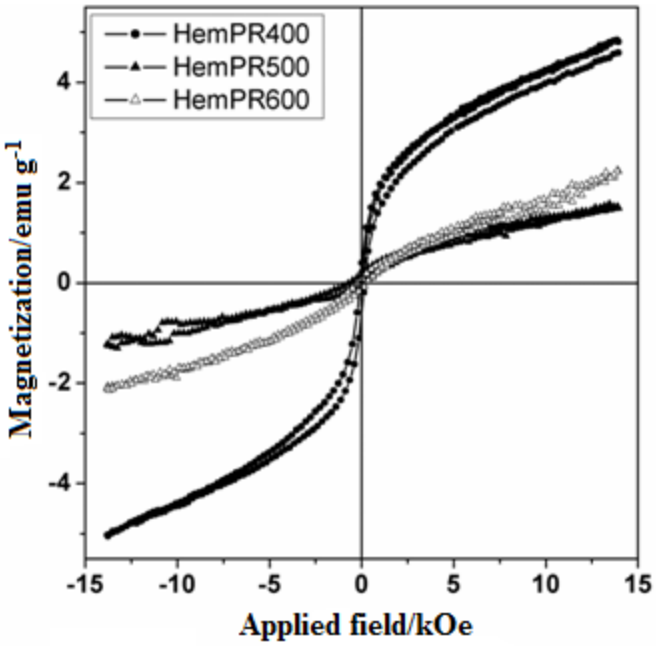

Figure 6: Magnetization hysteresis loop for Hem_PR400-600.

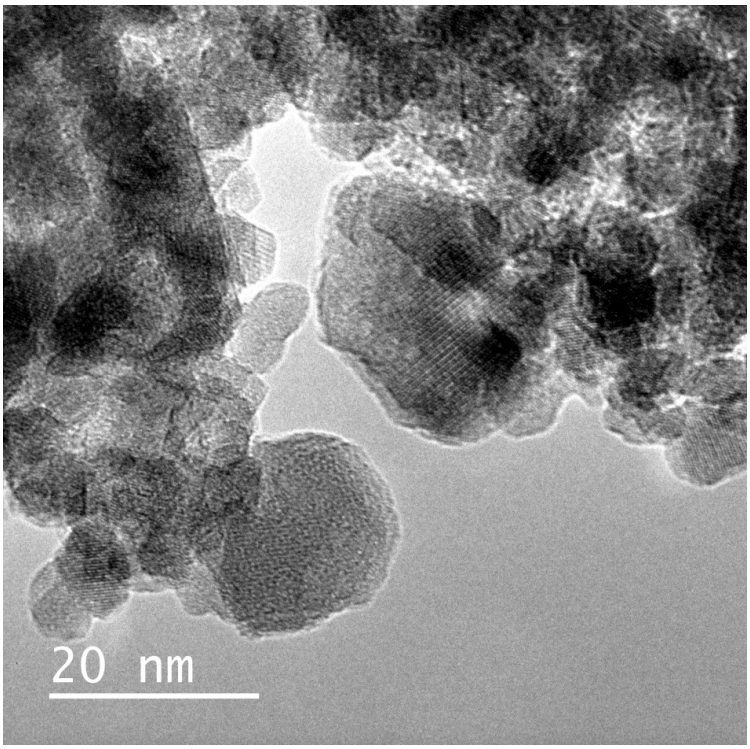

Figure 7: High resolution transmission electron microscopy for Hem_SG400 showing the lattice fringes of the crystals.

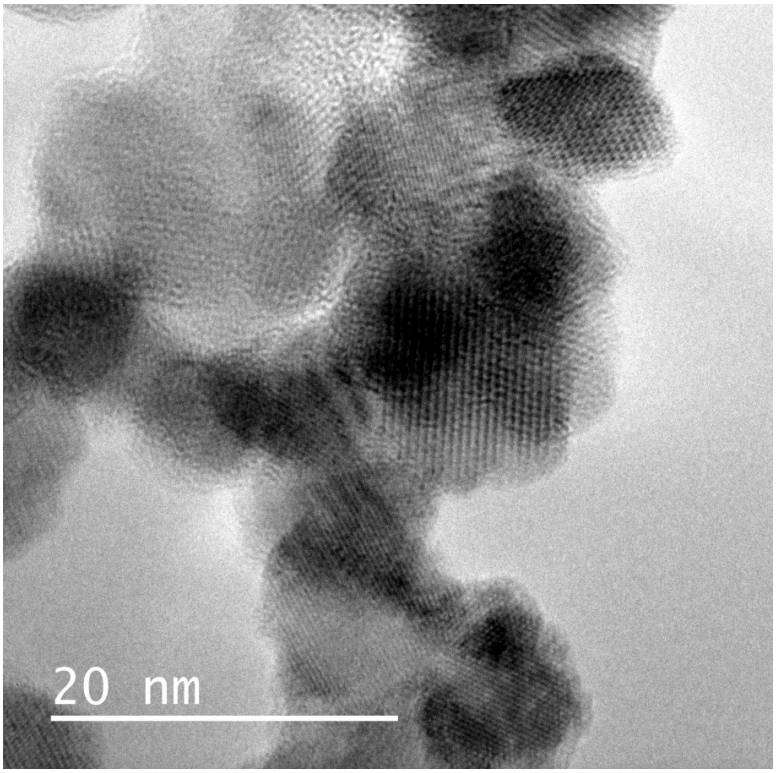

Figure 8: High resolution transmission electron microscopy for Hem_TW400 showing the lattice fringes of the crystals.

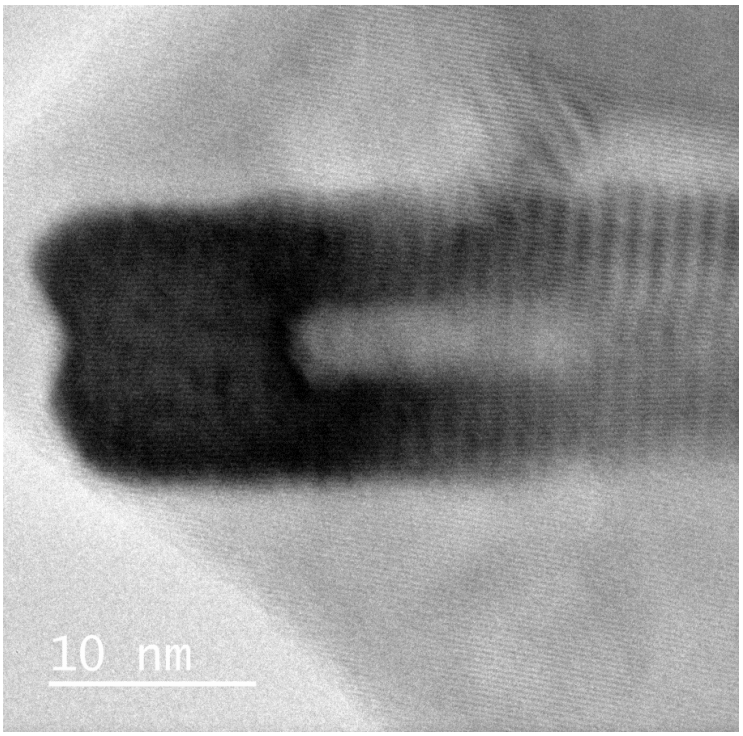

Figure 9: High resolution transmission electron microscopy for Hem_PR400 showing the lattice fringes of the crystals.

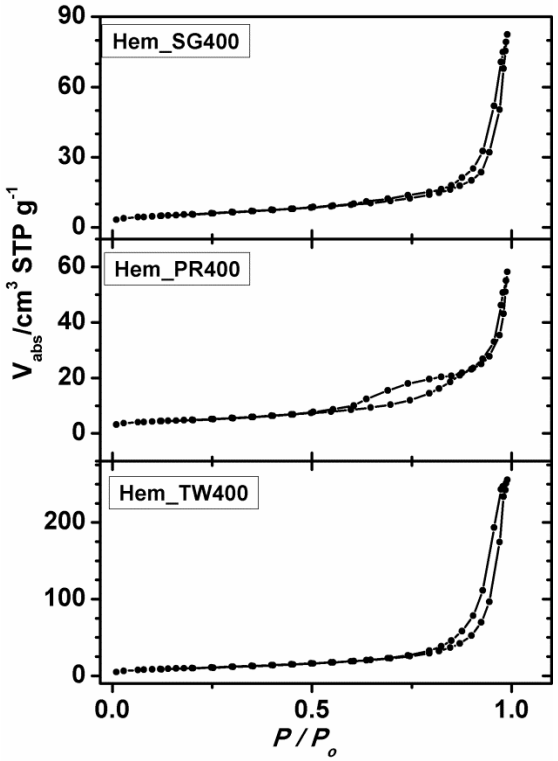

Figure 10: Adsorption-desorption isotherms the hematite powders calcined at 400 °C.

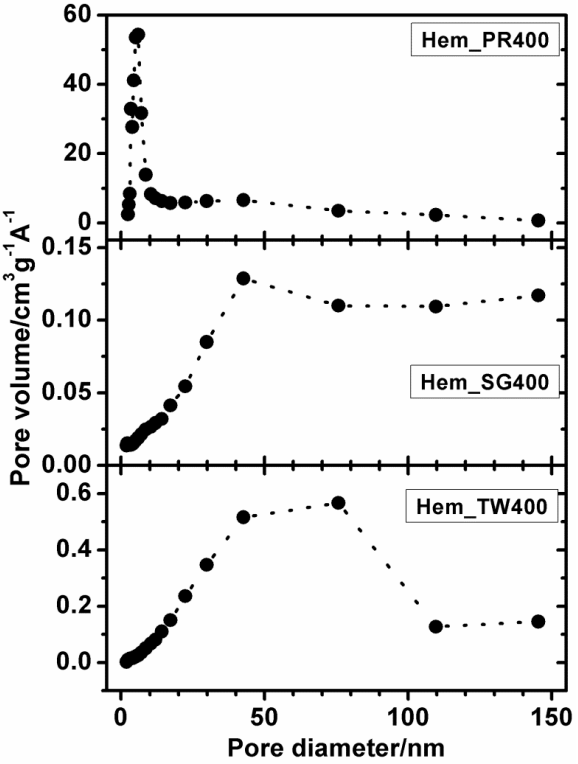

Figure 11: Pore size distribution for hematite powders calcined at 400.

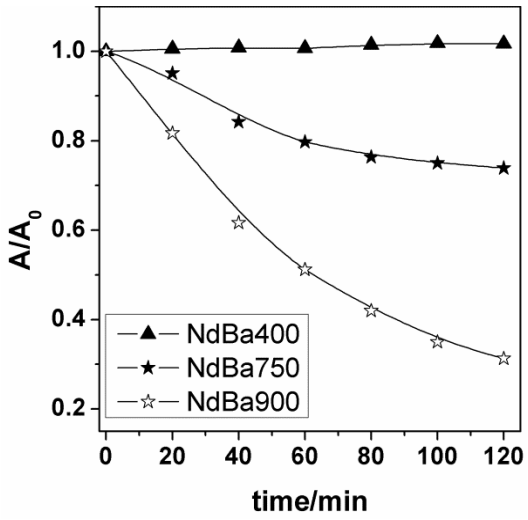

Figure 12: Photodegradation profile for RhB dye degradation by NdBa400-900 (1.5 g dm^{-3}) in the presence of 3.0×10^{-5} mol dm^{-3} H_2O_2.

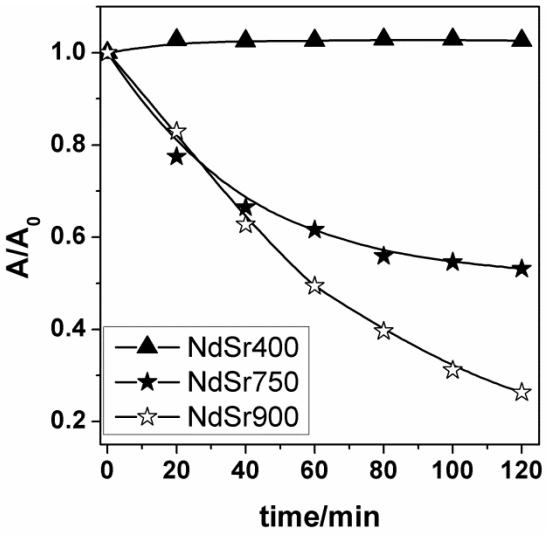

Figure 13: Photodegradation profile for RhB dye degradation by NdSr400-900 (1.5 g dm^{-3}) in the presence of 3.0×10^{-5} mol dm^{-3} H_2O_2.

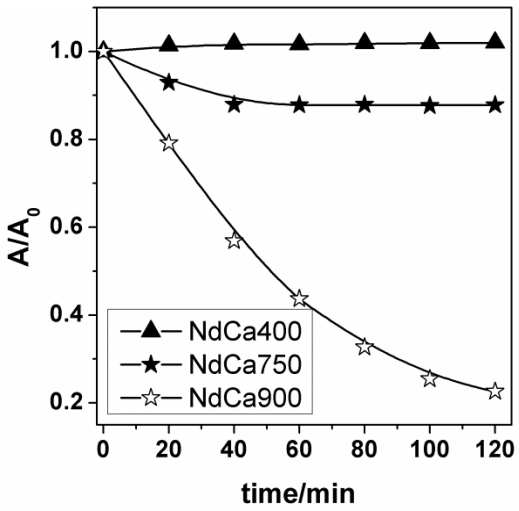

Figure 14: Photodegradation profile for RhB dye degradation by NdCa400-900 (1.5 g dm^{-3}) in the presence of 3.0×10^{-5} mol dm^{-3} H_2O_2**.**

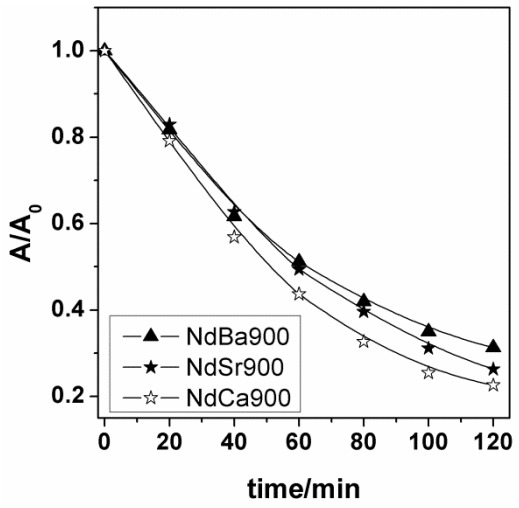

Figure 15: Photodegradation profile for RhB dye degradation by 1.5 g dm^{-3} each of NdBa900, NdSr900 and NdCa900 in the presence of 3.0×10^{-5} mol dm^{-3} H_2O_2.

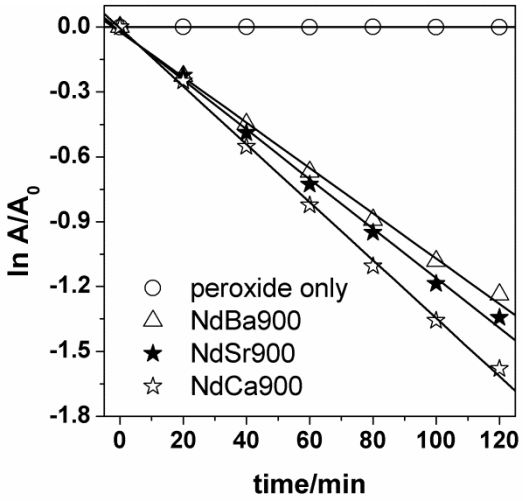

Figure 16: Photodegradation profile for RhB dye degradation by H_2O_2 only and 1.5 g dm^{-3} each of NdBa900, NdSr900 and NdCa900 in the presence of 3.0×10^{-5} mol dm^{-3} H_2O_2.

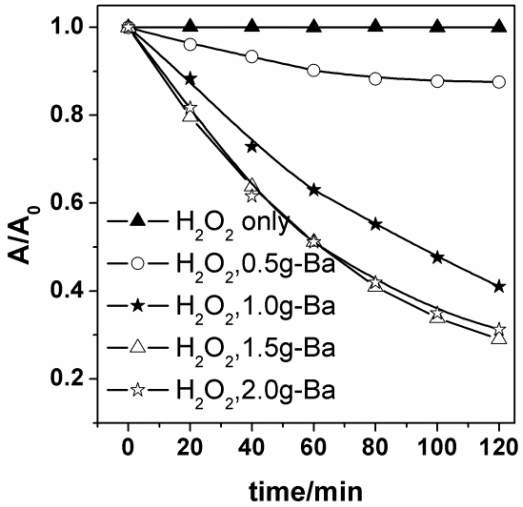

Figure 17: Photodegradation profile showing the effect of NdBa900 loading on the degradation of RhB dye in the presence of 3.0×10^{-5} mol dm^{-3} H_2O_2 and at the natural pH of the dye solution.

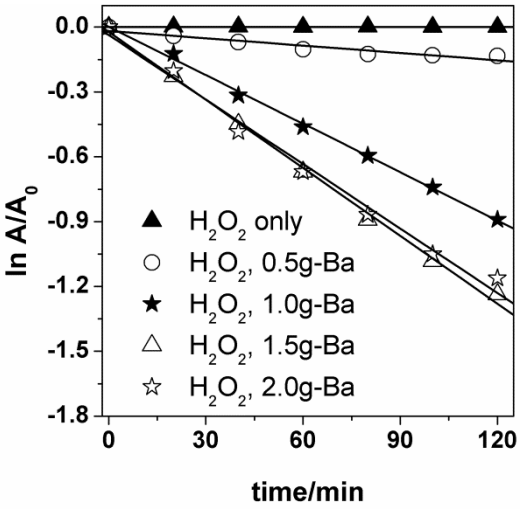

Figure 18: Pseudo first-order plots for the photodegradation profile showing the effect of NdBa900 loading of the degradation of RhB dye in the presence of 3.0×10^{-5} H_2O_2 mol dm^{-3} and at the natural pH of the dye solution.

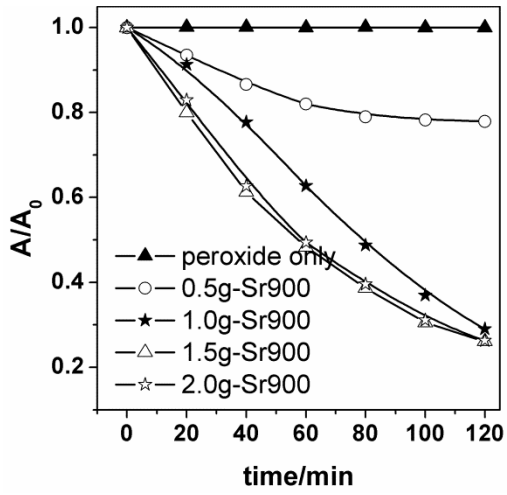

Figure 19: Photodegradation profile showing the effect of NdSr900 loading of the degradation of RhB dye in the presence of 3.0×10^{-5} mol dm^{-3} H_2O_2 and at natural pH of the dye solution.

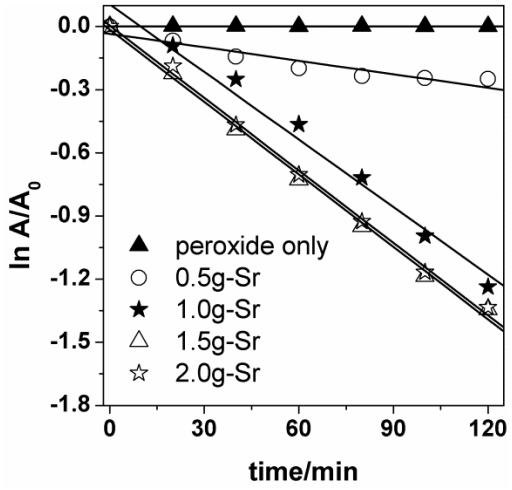

Figure 20: Pseudo first-order plots for the photodegradation profile showing the effect of NdSr900 loading of the degradation of RhB dye in the presence of 3.0×10^{-5} mol dm^{-3} H_2O_2 and at natural pH of the dye solution.

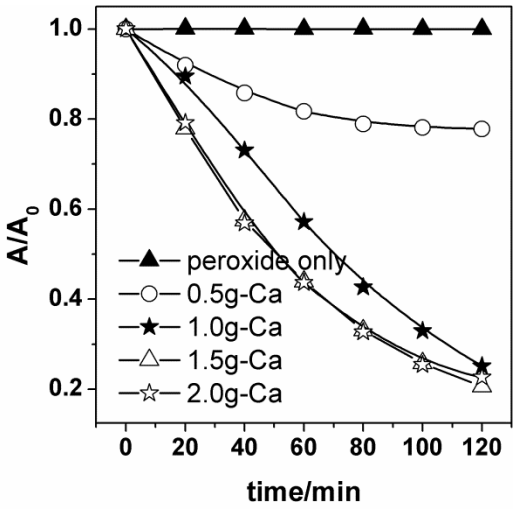

Figure 21: Photodegradation profile showing the effect of NdCa900 loading of the degradation of RhB dye in the presence of 3.0×10^{-5} mol dm^{-3} H_2O_2 and at natural pH of the dye solution.

.

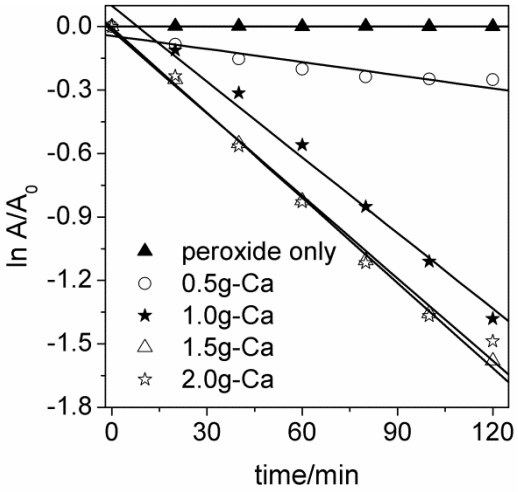

Figure 22: Pseudo first-order plots for the photodegradation profile showing the effect of NdCa900 loading of the degradation of RhB dye in the presence of 3.0×10^{-5} mol dm^{-3} H_2O_2 and at natural pH of the dye solution.

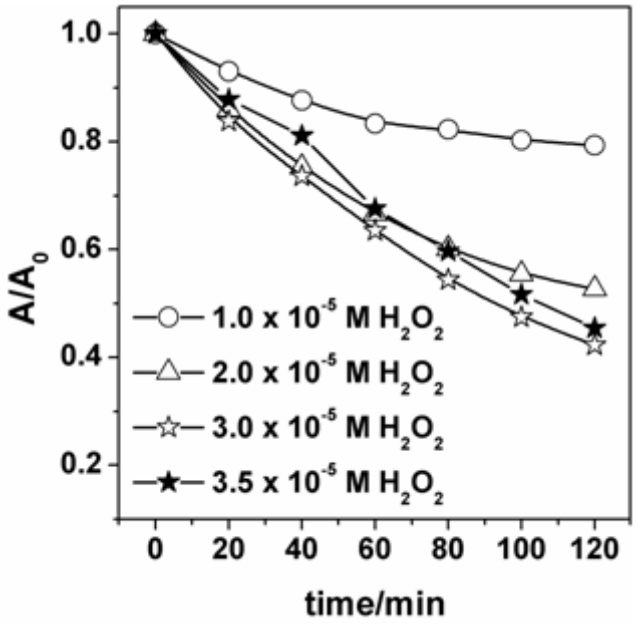

Figure 23: The Effect of H_2O_2 concentration on the rate of photodegradation of RhB dye solution in the presence of NdBa900 (1.5 g dm^{-3}), varying concebtrations of H_2O_2 and at natural pH of the dye solution.

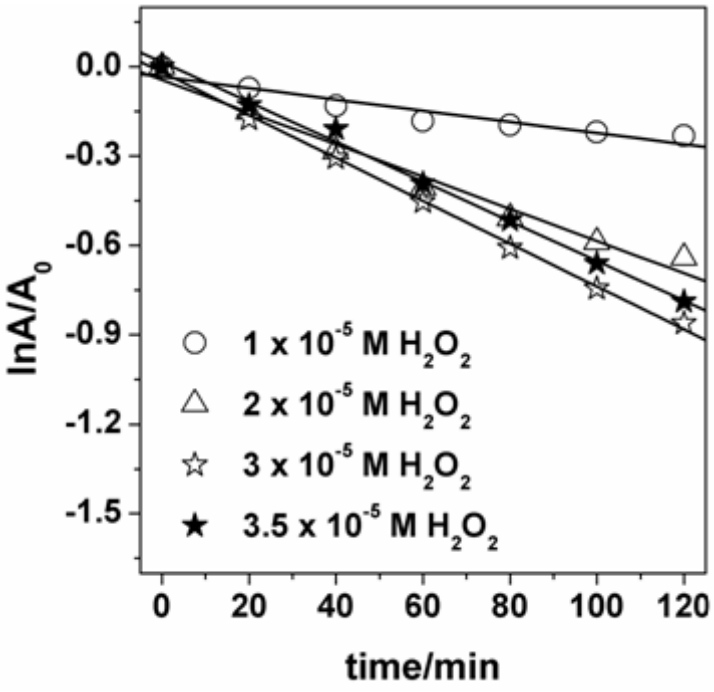

Figure 24: Pseudo first-order plots showing the effect of H_2O_2 concentration on the rate of photodegradation of RhB dye solution in the presence of NdBa900 (1.5 g dm^{-3}), varying concentrations of H_2O_2 and at natural pH of the dye solution.

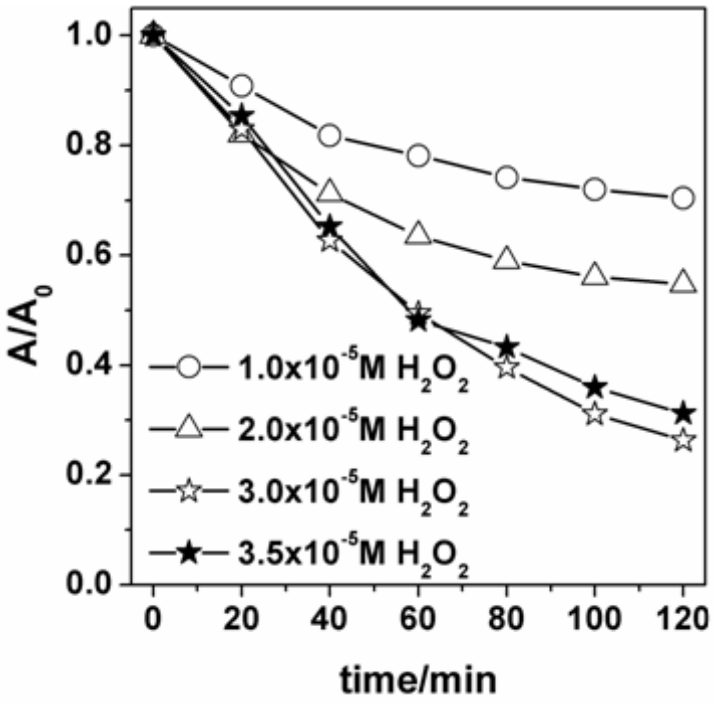

Figure 25: The effect of H_2O_2 concentration on the rate of photodegradation of RhB dye solution in the presence of NdSr900 (1.5 g dm^{-3}) and the natural pH of of RhB.

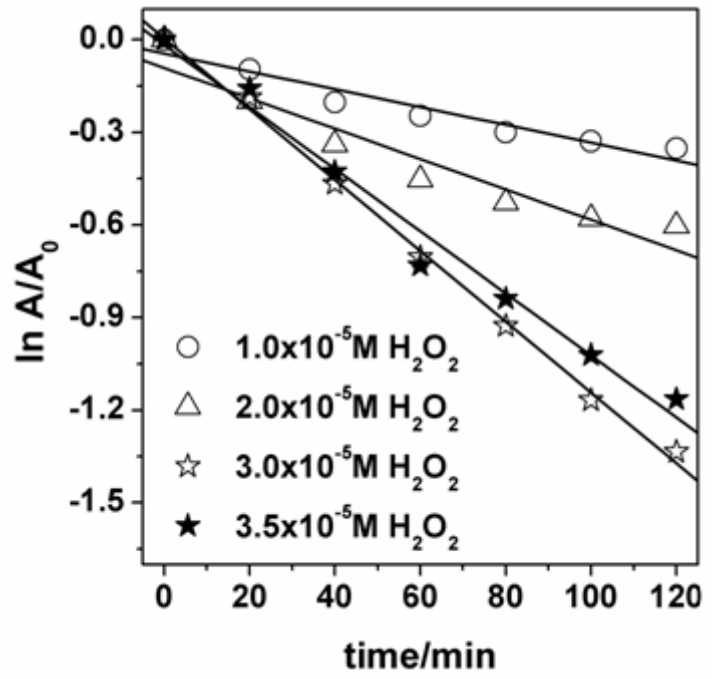

Figure 26: Pseudo-first-order plots showing the effect of H_2O_2 concentration on the rate of photodegradation of RhB dye solution in the presence of NdSr900 (1.5 g dm^{-3}) and constant pH of 5.

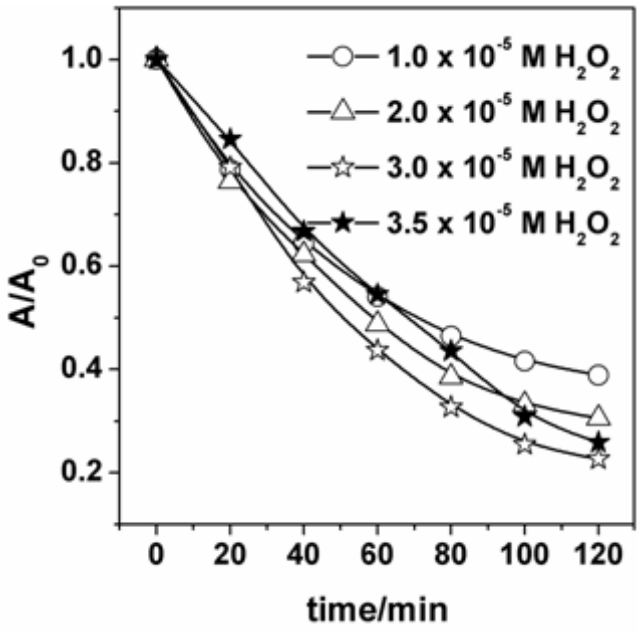

Figure 27: The effect of H_2O_2 concentration on the rate of photodegradation of RhB dye solution in the presence of NdCa900 (1.5 g dm^{-3}) and constant pH of 5.

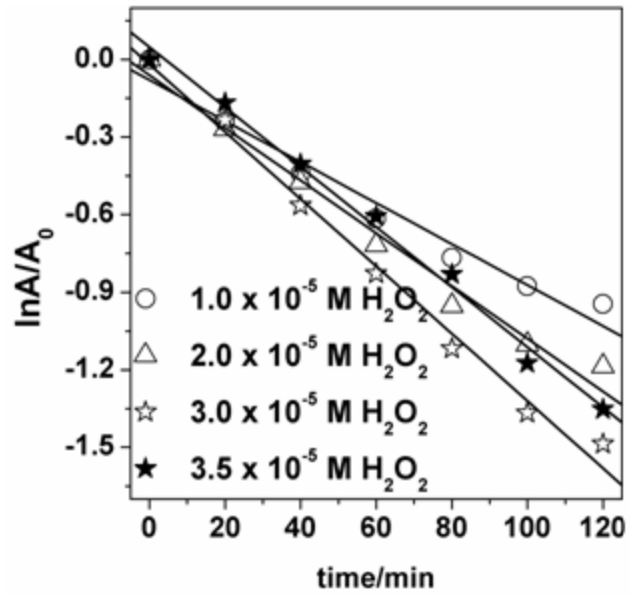

Figure 28: Pseudo-first-order plots showing the effect of H_2O_2 concentration on the rate of photodegradation of RhB dye solution in the presence of NdCa900 (1.5 g dm^{-3}) and at the natural pH of the dye.

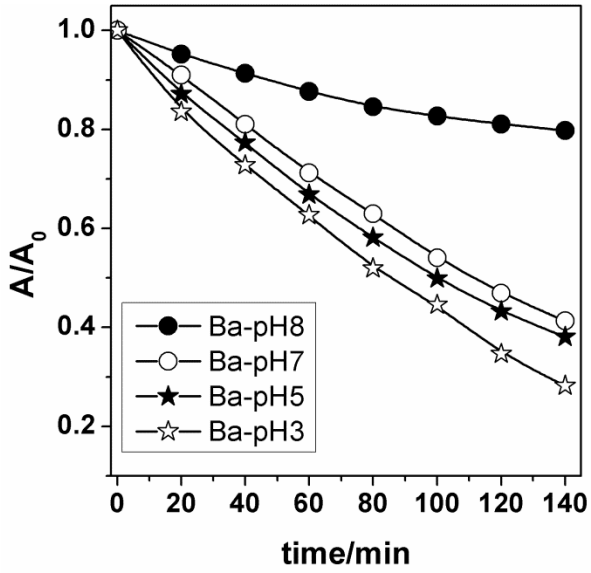

Figure 29: The effect of pH on the rate of photodegradation of RhB dye in the presence of NdBa900 (1.5 g dm^{-3}) and H_2O_2 (3.0×10^{-5} mol dm^{-3}).

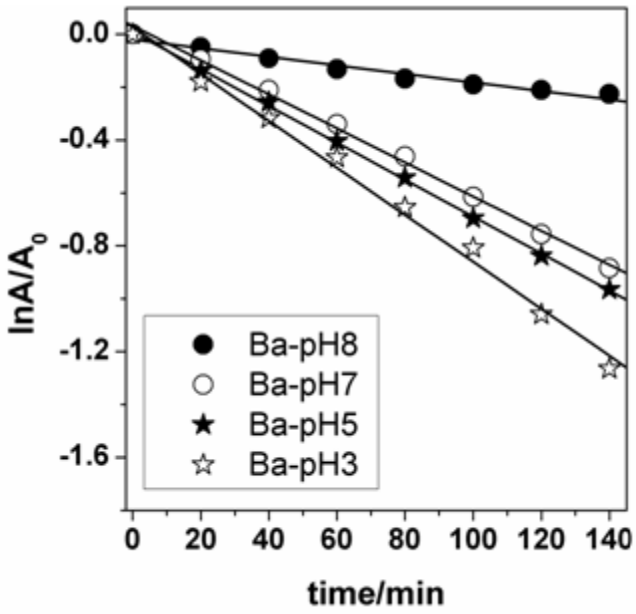

Figure 30: Pseudo-first-order plots showing the effect of pH on the rate of photodegradation of RhB dye in the presence of NdBa900 (1.5 g dm^{-3}) and H_2O_2 (3.0×10^{-5} mol dm^{-3}).

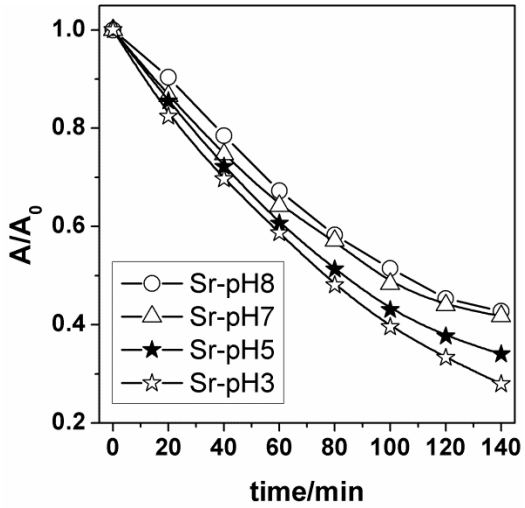

Figure 31: The effect of pH on the rate of photodegradation of RhB dye in the presence of NdSr900 (1.5 g dm^{-3}) and H_2O_2 (3.0 × 10^{-5} mol dm^{-3}).

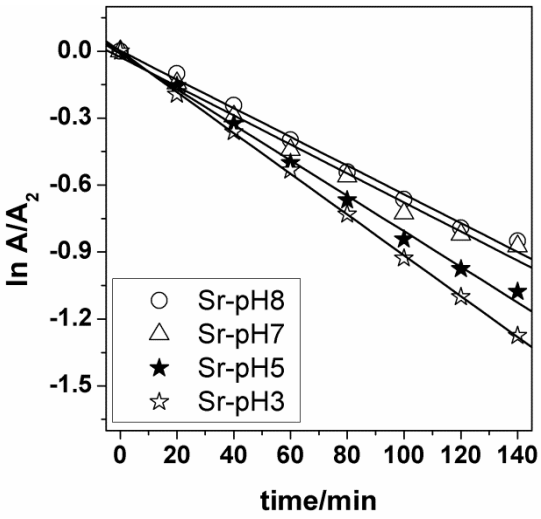

Figure 32: Pseudo-first-order plots showing the effect of pH on the rate of photodegradation of RhB dye in the presence of NdSr900 (1.5 g dm^{-3}) and H_2O_2 (3.0 × 10^{-5} mol dm^{-3}).

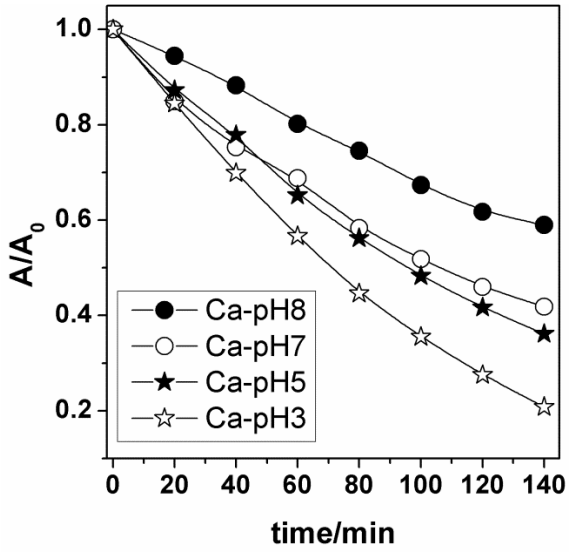

Figure 33: The effect of pH on the rate of photodegradation of RhB dye in the presence of NdCa900 (1.5 g dm^{-3}) and H_2O_2 (3.0 × 10^{-5} mol dm^{-3}).

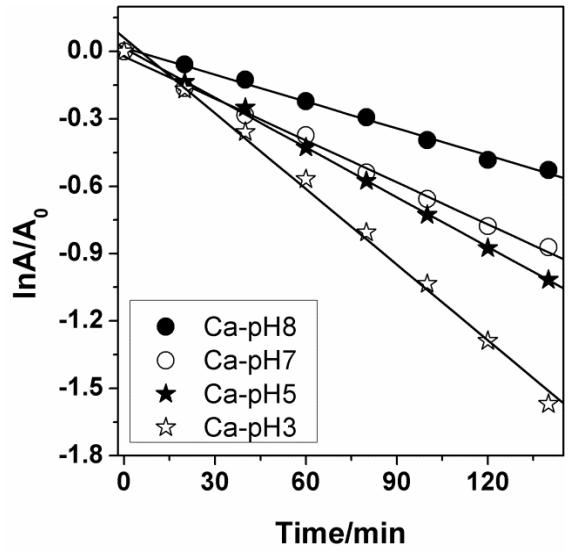

Figure 34: Pseudo-first-order plots showing the effect of pH on the rate of photodegradation of RhB dye in the presence of NdCa900 (1.5 g dm^{-3}) and H_2O_2 (3.0 × 10^{-5} mol dm^{-3})

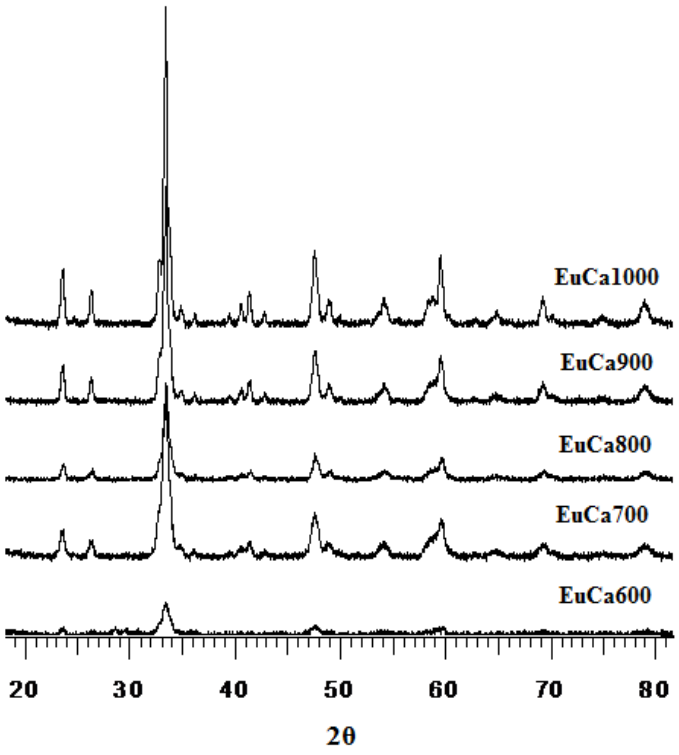

Figure 35: Powder X-ray diffractograms for EuCa600-900 showing the perovskite peak evolution at 600 °C.

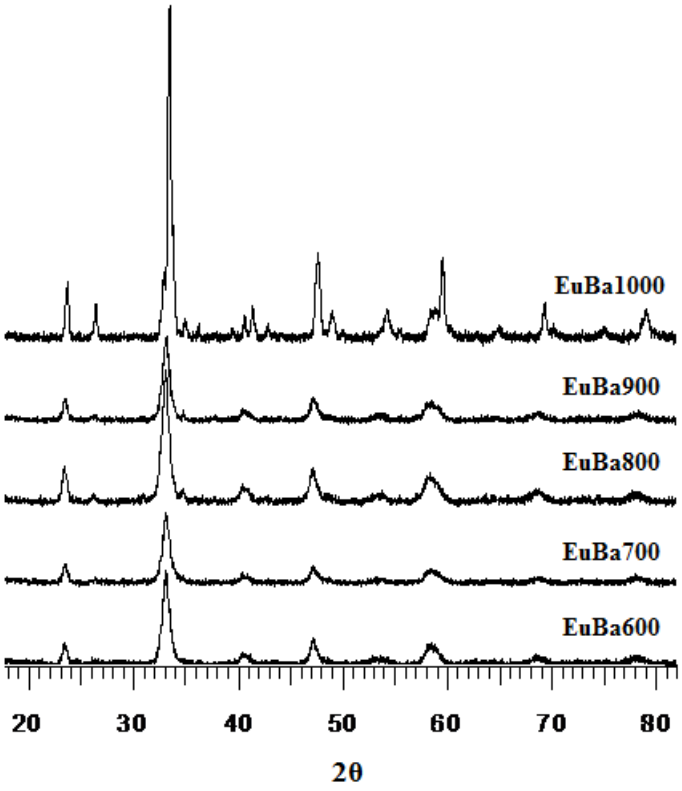

Figure 36: Powder X-ray diffractograms for EuBa600-900 showing the perovskite peak evolution at 600 °C.

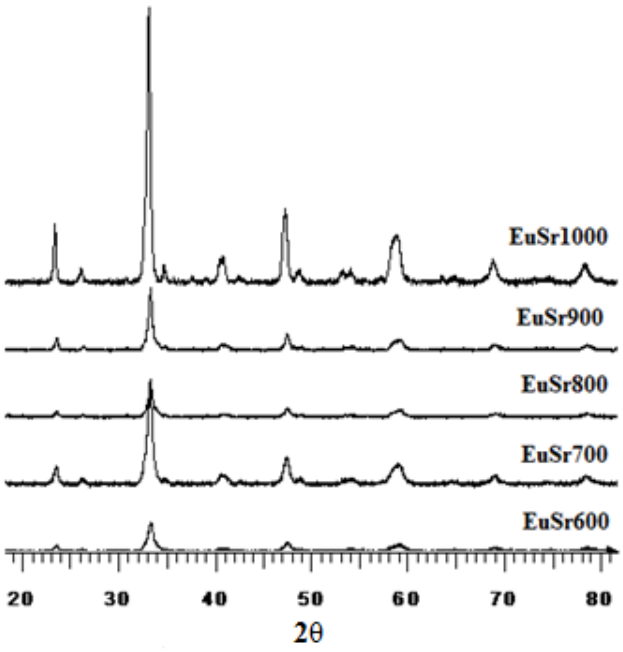

Figure 37: Powder X-ray diffractograms for EuSr600-900 showing the perovskite peak evolution at 600 °C.

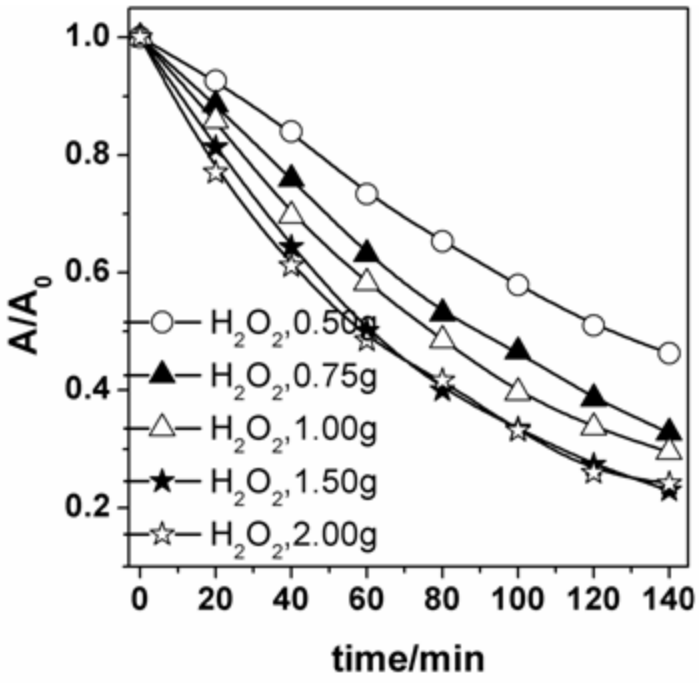

Figure 38: Effect of photocatalyst (EuBa900) loading on the degradation of RhB dye in the presence of 3.0×10^{-5} mol dm^{-3} H_2O_2 and at the natural pH of the dye.

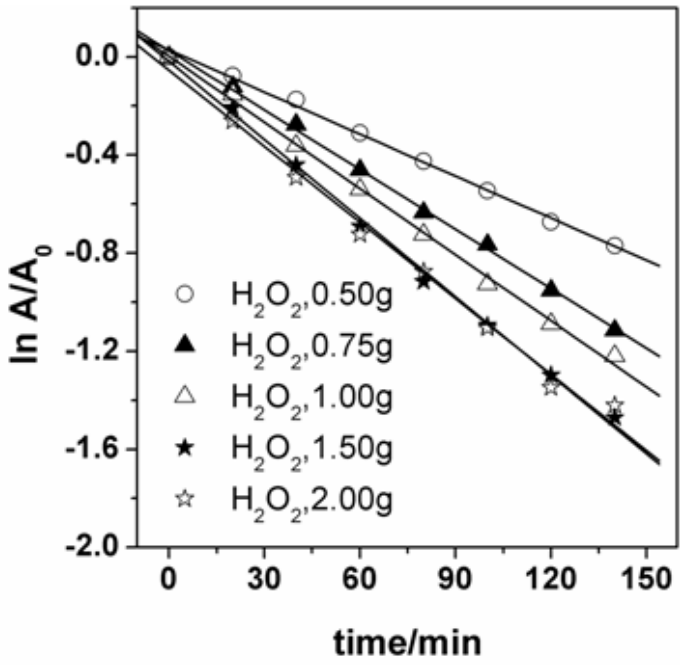

Figure 39: Pseudo-first-order plots for the effect of photocatalyst (EuBa900) loading on the degradation of RhB dye in the presence of 3.0×10^{-5} mol dm^{-3} H_2O_2 and at the natural pH of the dye.

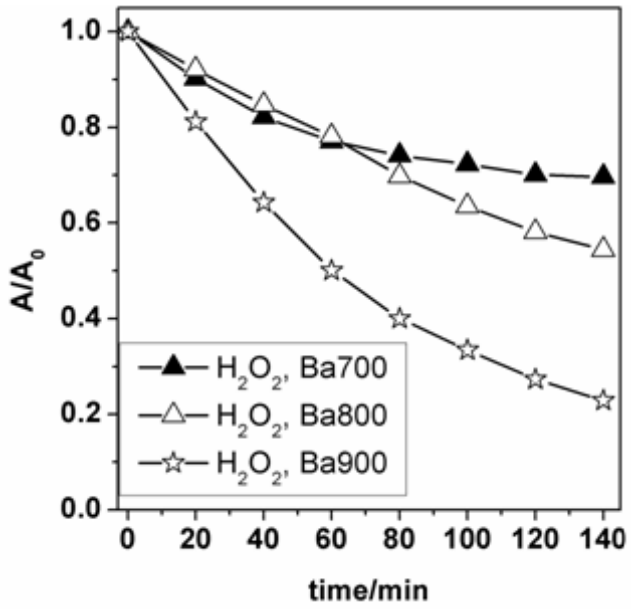

Figure 40: Effect of annealing temperature on the photocatalytic activities of Ba substituted powders.

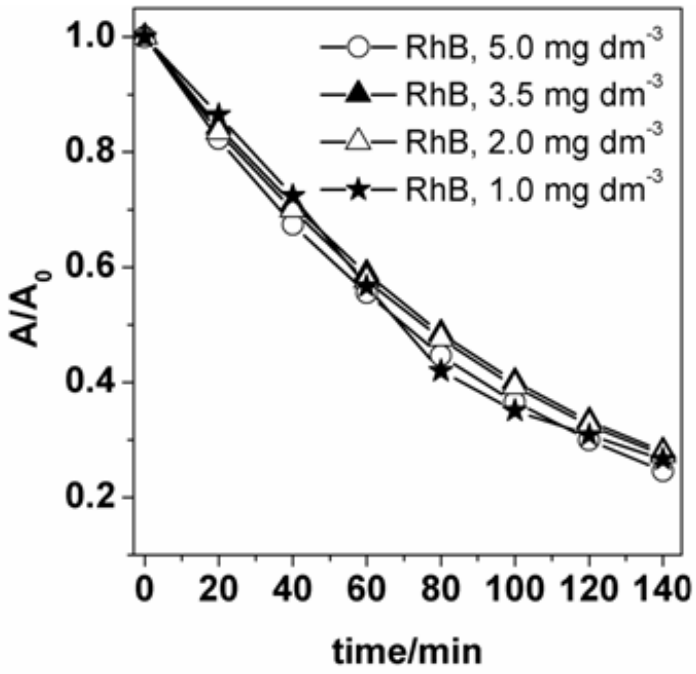

Figure 41: Effect of dye concentration on rates of RhB photodegradation in the presence of EuBa700-900 (1.5 g dm10^{-3}) and H_2O_2 (3.0×10^{-5} mol dm^{-3}).

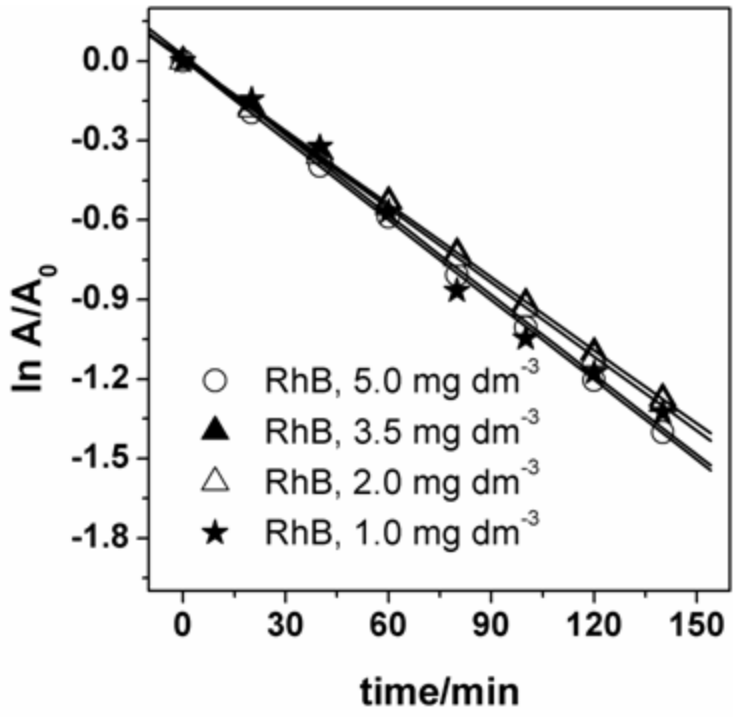

Figure 42: Pseudo-first-order plots for the effect of dye concentration on rates of the RhB dye degradation in the presence of EuBa700-900 (1.5 g dm^{-3}) and H_2O_2 (3.0×10^{-5} mol dm^{-3}).

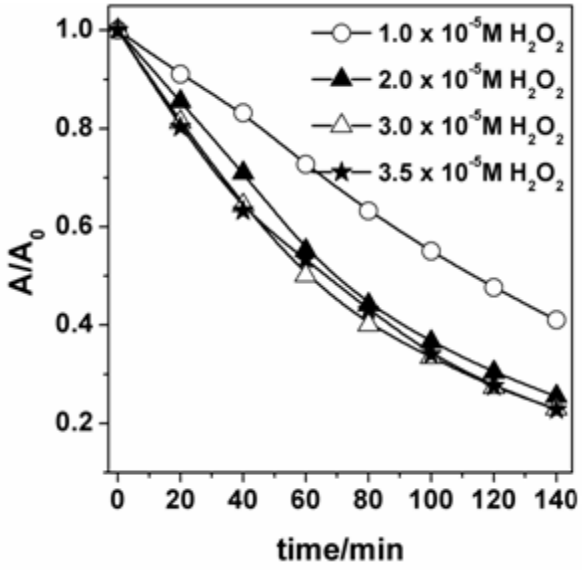

Figure 43: Effect of H_2O_2 concentration on rates of RhB photodegradation in the presence of EuBa900 (1.5 g dm^{-3}).

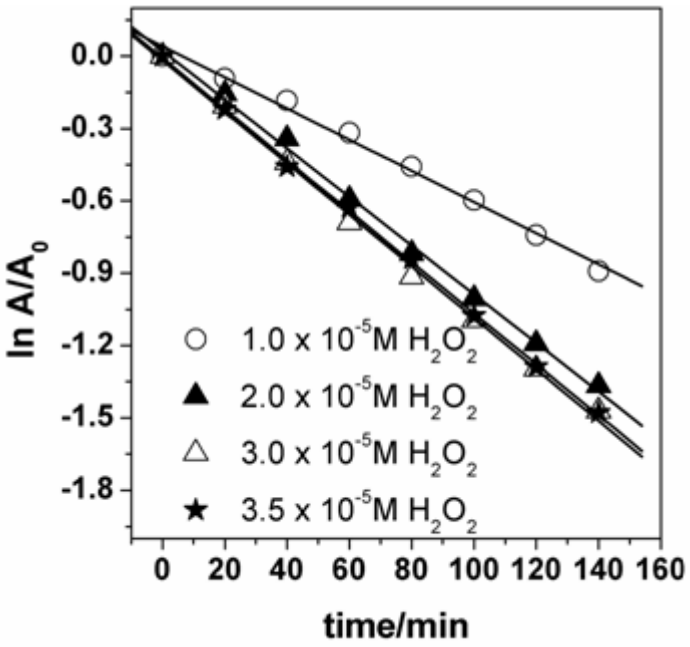

Figure 44: Linear plots showing the effect of H_2O_2 concentration on rates of RhB photodegradation in the presence of EuBa900 (1.5 g dm^{-3}).

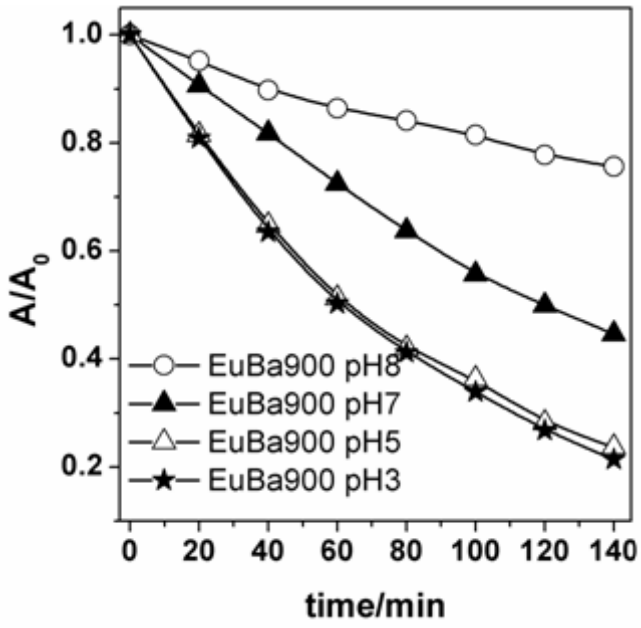

Figure 45: Effect of pH on rates of RhB photodegradation in the presence of EuBa900 (1.5 g dm^{-3}) and H_2O_2 (3.0×10^{-5} mol dm^{-3}).

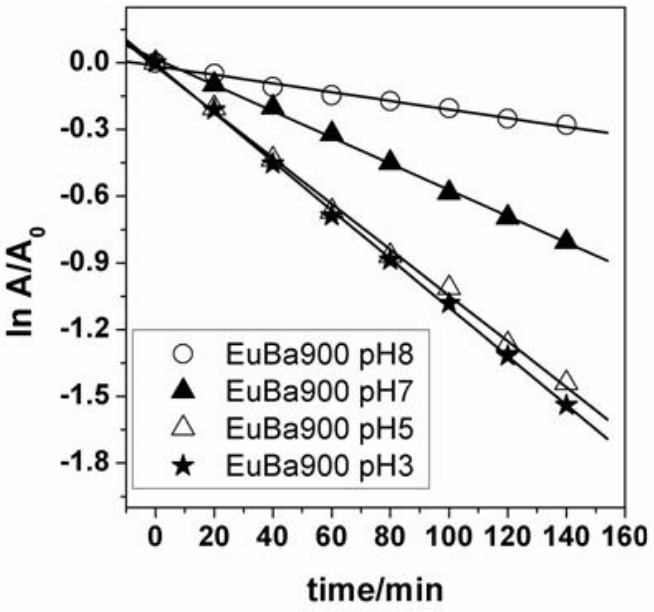

Figure 46: Linear plots showing the effect of pH on rates of RhB photodegradation in the presence of EuBa900 (1.5 g dm^{-3}) and H_2O_2 (3.0×10^{-5} mol dm^{-3}).

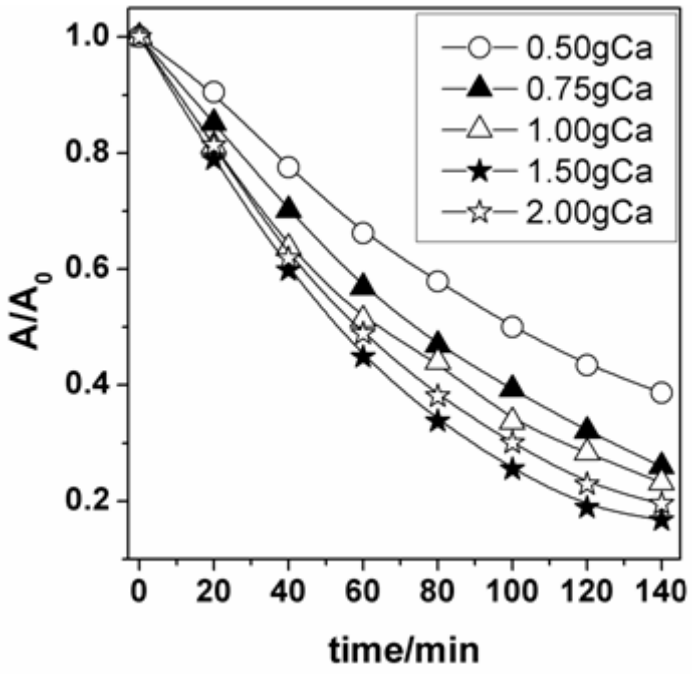

Figure 47: Effect of photocatalyst loading on the degradation of RhB dye for EuCa900 all other conditions remain constant.

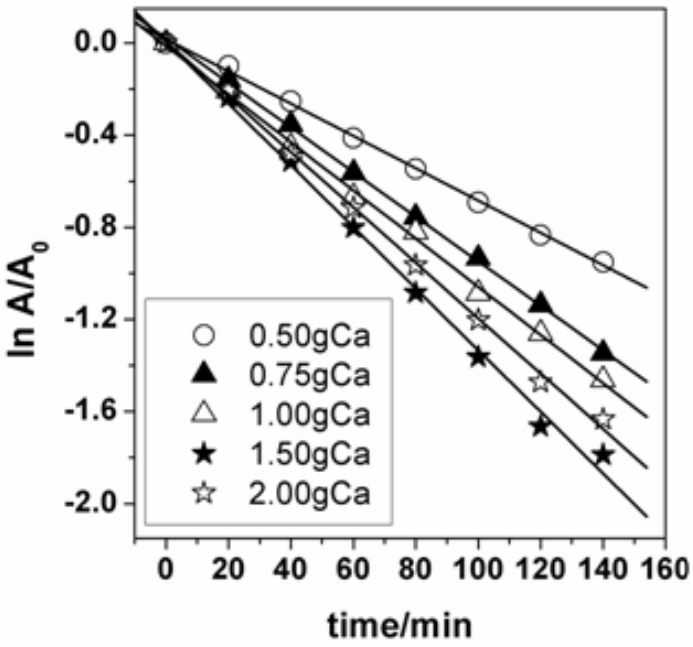

Figure 48: Peudo-first-oredr plots for the effect of photocatalyst loading on the degradation of RhB dye for EuCa900 all other conditions remain constant.

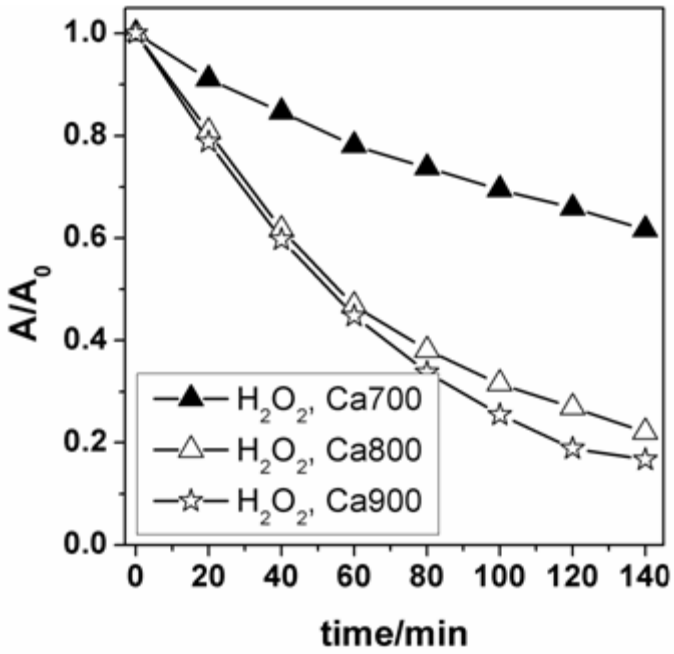

Figure 49: Effect of annealing temperature on the photocatalytic activities of EuCa700-900 in the presence of H_2O_2 (3.0×10^{-5} mol dm^{-3}) for the degradation of RhB.

.

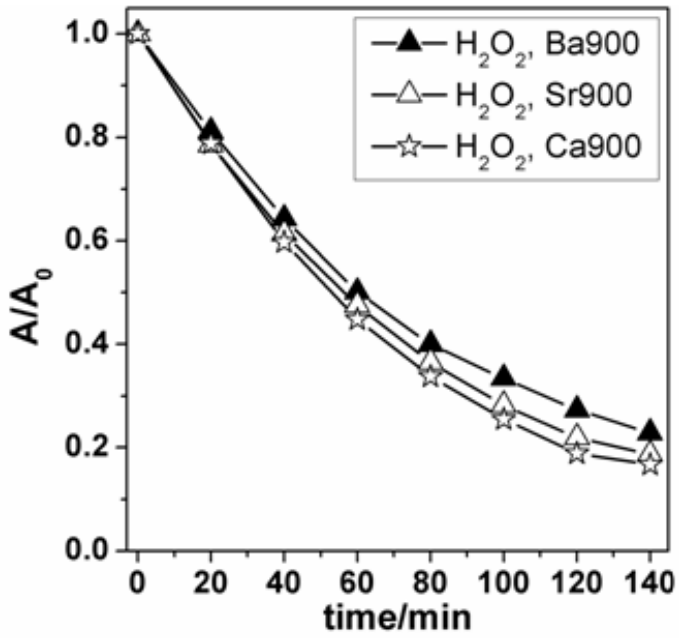

Figure 50: Photodegradation profile for EuCa900, EuSr900 and EuBa900 in the presence of H_2O_2 (3.0×10^{-5} mol dm^{-3}) for the degradation of RhB.

.

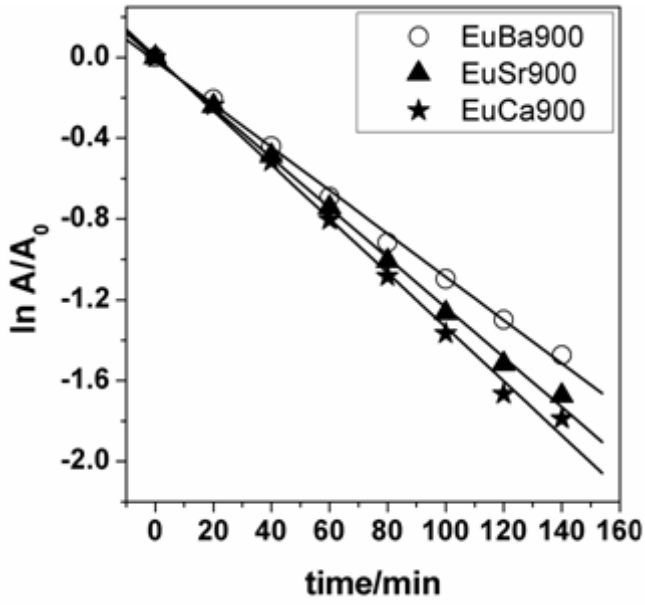

Figure 51: Pseudo-first-order plots for the photodegradation profile for EuCa900, EuSr900 and EuBa900 in the presence of H_2O_2 (3.0×10^{-5} mol dm^{-3}) for the degradation of RhB.

.

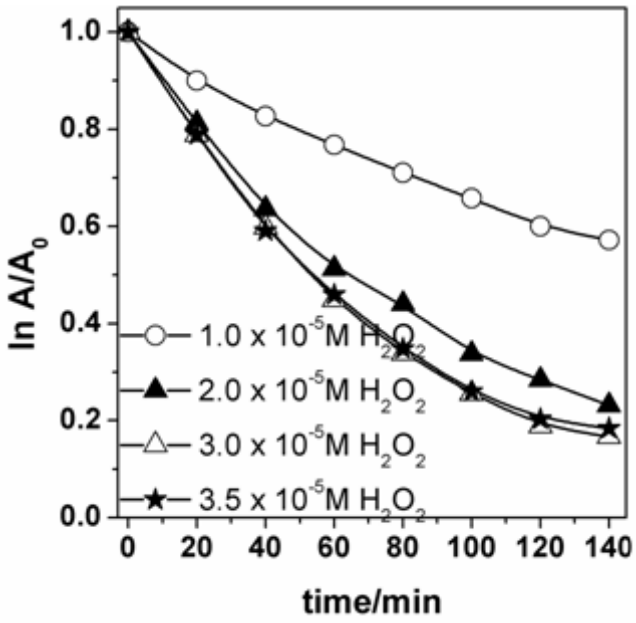

Figure 52: Effect of variation in peroxide concentration on the photodegradation of RhB dye by EuCa900 at the natural pH of the dye.

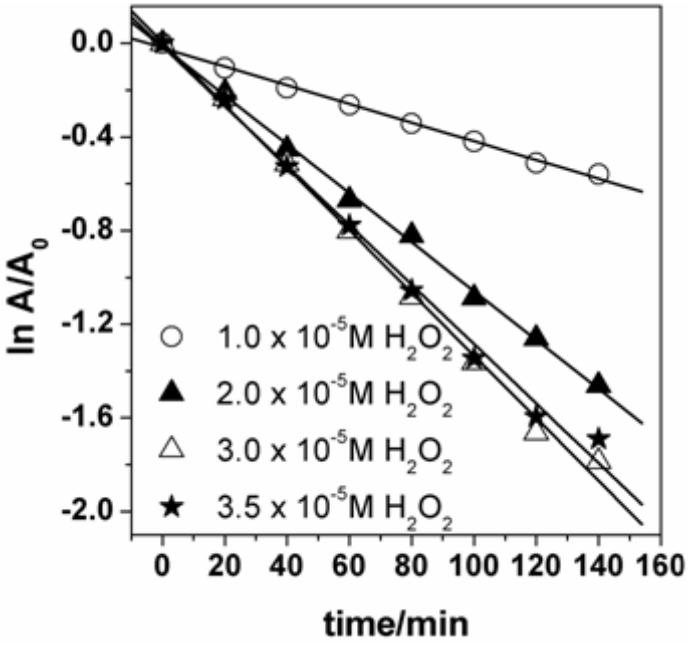

Figure 53: Pseudo-First-order plots for the effect of variation in peroxide concentration on the photodegradation of RhB dye in the presence of EuCa900 (1.5 g dm^{-3}) and at the natural pH of the dye.

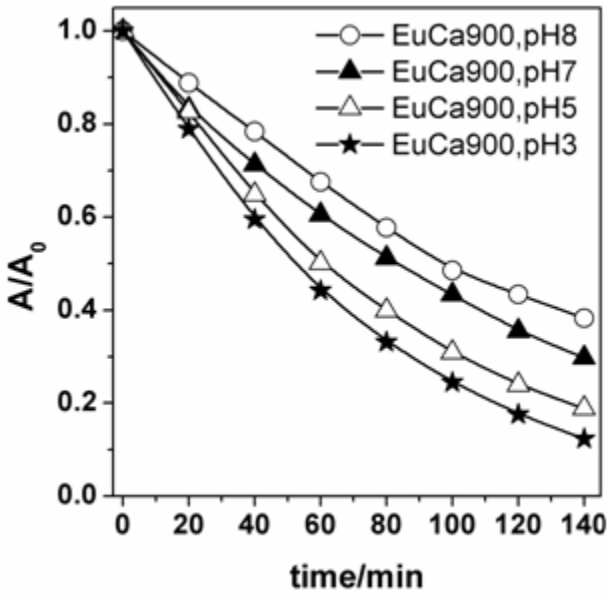

Figure 54: Effect of pH on the photodegradation of RhB dye by EuCa900 (1.5 g dm^{-3}) in the presence of H_2O_2 (3.0×10^{-5} mol dm^{-3}).

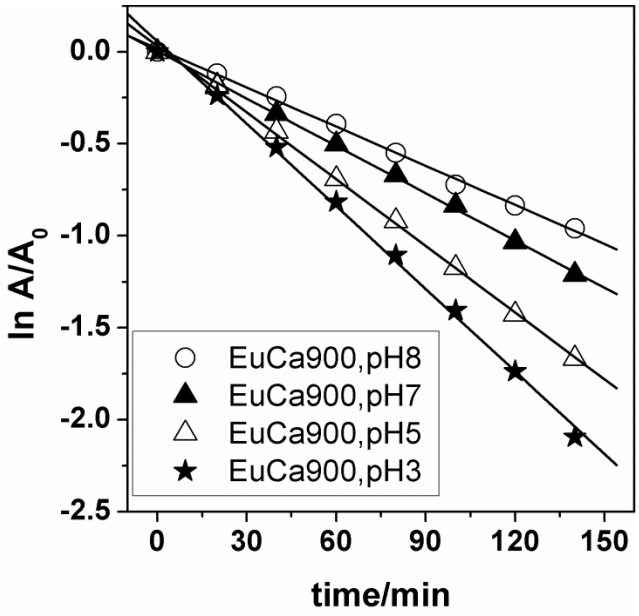

Figure 55: Pseudo-first-order plots of the effect of pH on the photodegradation of RhB dye by EuCa900 (1.5 g dm^{-3}) the presence of H_2O_2 (3.0×10^{-5} mol dm^{-3}).

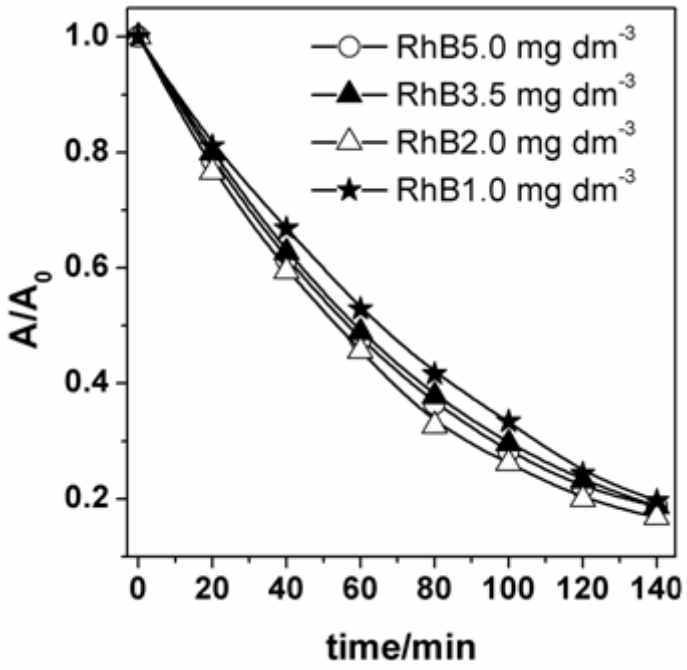

Figure 56: Effect of initial dye concentration on the rate of photodegradation of RhB by EuCa900 (1.5 g dm^{-3}).

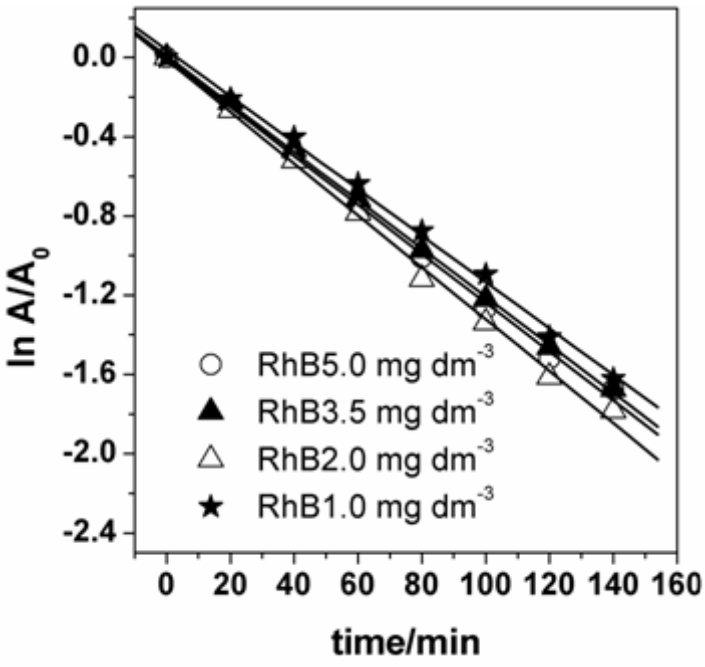

Figure 57: Linear plots of effect of variation in dye concentration on the rate of photodegradation of RhB by EuCa900 (1.5 g dm^{-3}).

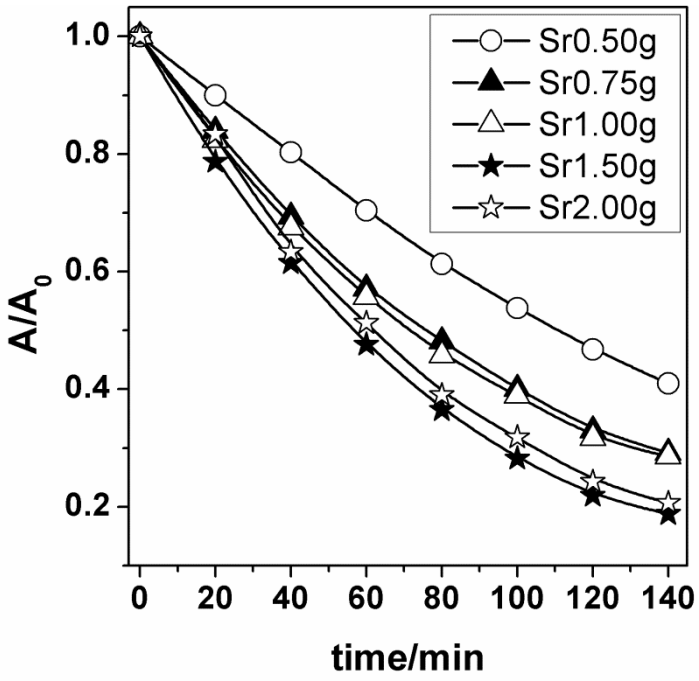

Figure 58: Degradation time dependence of RhB for different amounts of EuSr900 powders in the presence of 3.0×10^{-5} mol dm^{-3} H_2O_2.

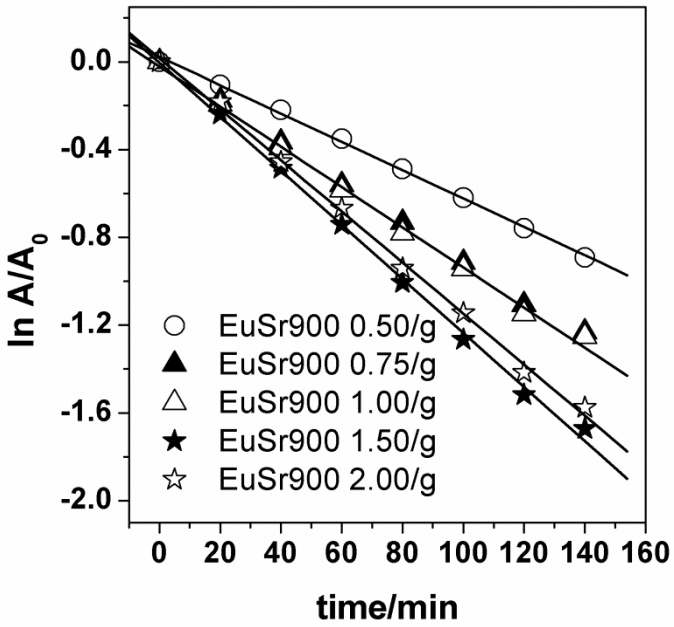

Figure 59: Degradation time dependence of RhB (5.0 mg dm^{-3}) for different amounts of EuSr900 powders in the presence of 3.0×10^{-5} mol dm^{-3} H_2O_2.

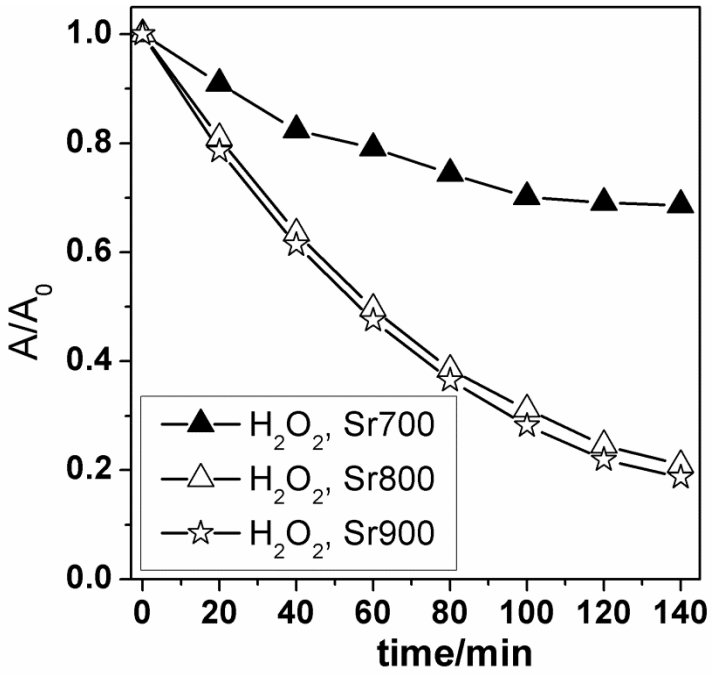

Figure 60: Time dependence of photodegradation of RhB for 1.5 g dm^{-3} EuSr700-900 in the presence of H_2O_2 (3.0×10^{-5} mol dm^{-3}).

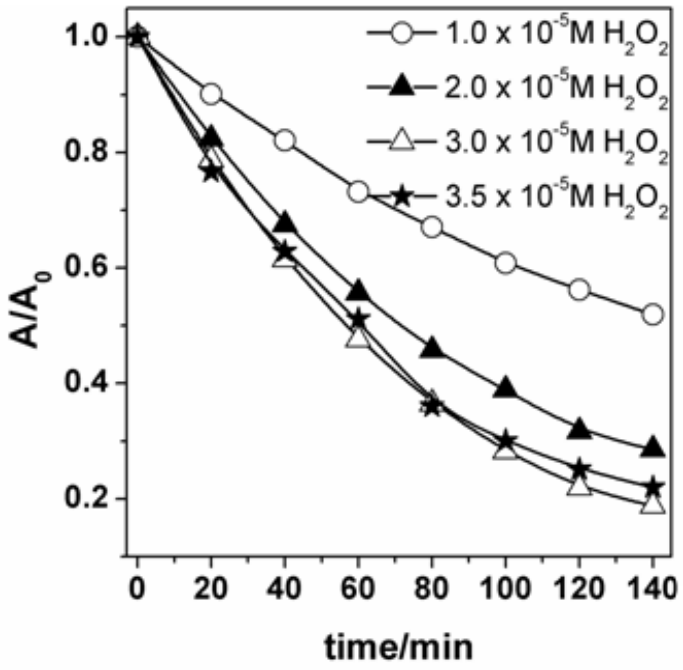

Figure 61: Effect of peroxide concentration on the rate of photodegradation of RhB dye by EuSr900 (1.5 g dm^{-3}) at the natural pH of the dye.

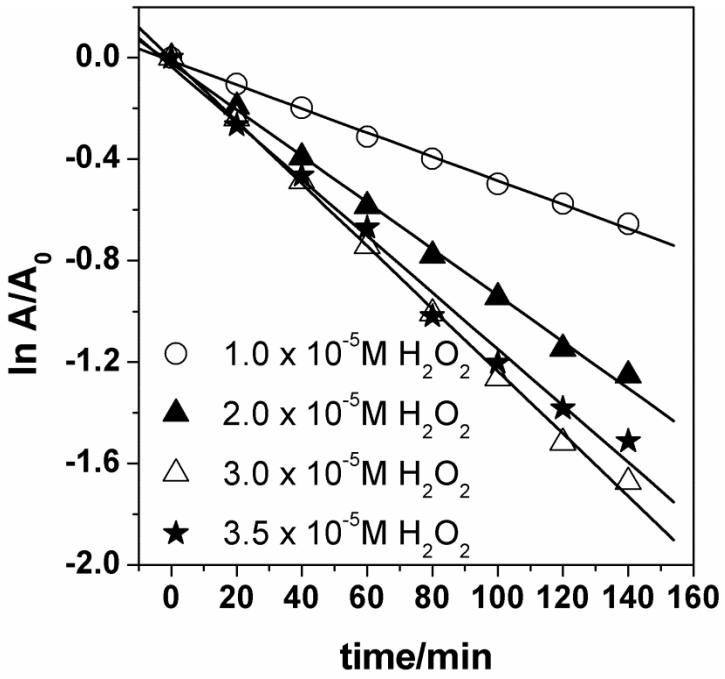

Figure 62: Pseudo-first-order plots of the effect of peroxide concentration on the rate of photodegradation of RhB dye by EuSr900 (1.5 g dm^{-3}) at the natural pH of the dye.

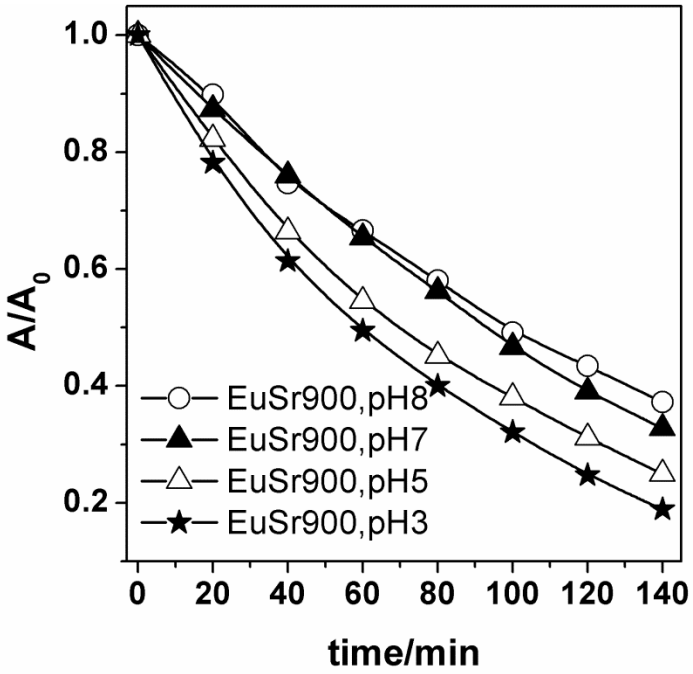

Figure 63: Effect of variation of initial solution pH on rates of RhB photodegradation in the presence of EuSr900 (1.5 g dm^{-3}) and H_2O_2 (3.0 × 10^{-5} mol dm^{-3}).

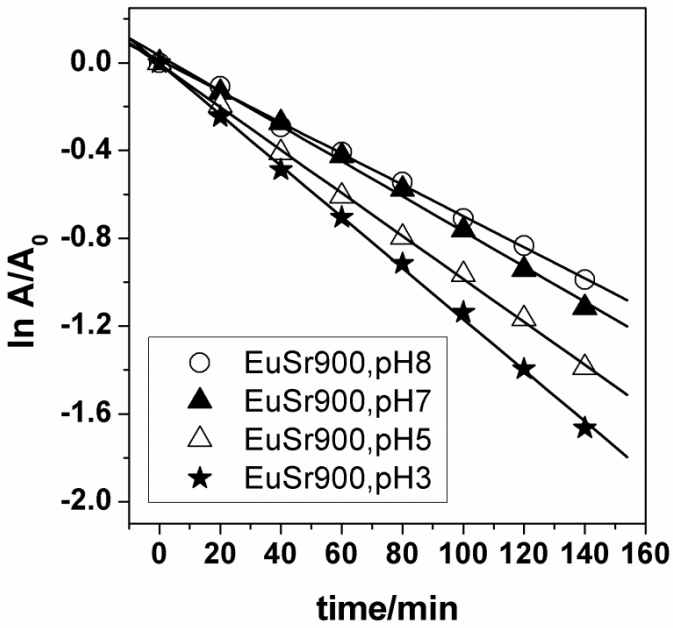

Figure 64: Pseudo-first-order plots showing the effect of initial pH on rates of RhB photodegradation in the presence of EuSr900 (1.5 g dm^{-3}) and H_2O_2 (3.0 × 10^{-5} mol dm^{-3}).

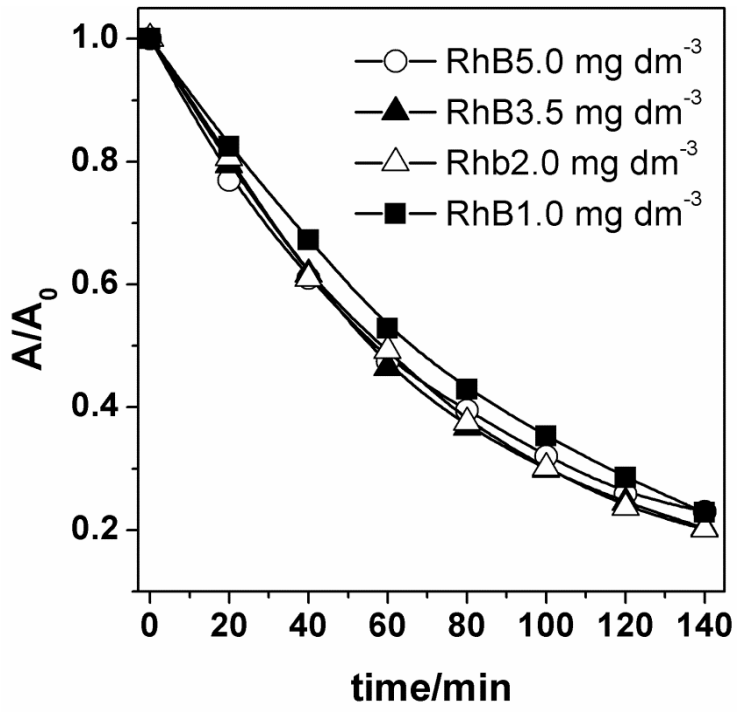

Figure 65: Effect of variation of dye concentration on rates of RhB photodegradation in the presence of EuSr900 (1.5 g dm10^{-3}) and H_2O_2 (3.0×10^{-5} mol dm^{-3}).

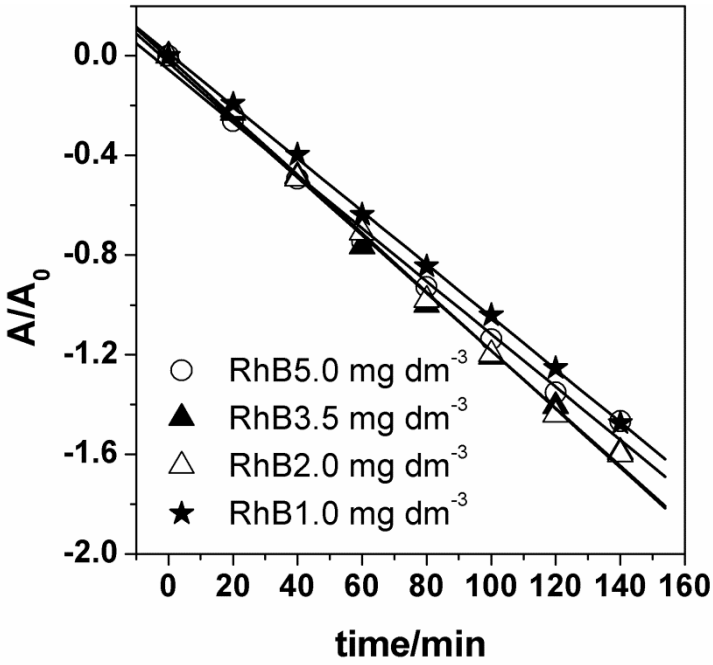

Figure 66: Pseudo first-order plots showing the effect of the variation of dye concentration on rates of RhB photodegradation in the presence of EuSr900 (1.5 g dm^{-3}) and H_2O_2 (3.0×10^{-5} mol dm^{-3}).